

In-situ stress analysis and fracture
characterization in oil reservoirs with complex
geological settings:

A multi-methodological approach in
the Zagros fold and thrust belt

2024

Nazir Mafakheri Bashmagh

Abstract

Subduction of the Arabian tectonic plate under the Eurasian plate has controlled the geological evolution of the Zagros suture zone and is considered one of Earth's most prominent regions of convergent deformation. The Zagros suture zone is bounded by the Zagros main reverse fault in the northeast, and the Zagros thrust front in the southwest. The study area represents a critical focal point for understanding tectonic processes and in-situ stress regimes due to its location along the Zagros suture zone. This zone is a key geological feature characterized by complex structural formations, active tectonic movements, and varied stress regimes. Complex structures with different stress regimes pose challenges in tectonic studies and affect the effective production and development of hydrocarbon resources. The unique tectonic setting not only presents challenges but also offers valuable insights into the mechanics of plate collision, stress distribution, and faulting patterns, which are essential for advancing our understanding of Earth's geodynamics. Therefore, research in this area holds immense significance for structural geology and petroleum engineering.

This dissertation presents a comprehensive study of in-situ stress analysis in the complex tectonic settings of the Kurdistan Region of Iraq and the Dezful Embayment in Iran, focusing on the Zagros suture zone. The first study area is in the Zagros fold and thrust of the Kurdistan region of Iraq, on the northwestern extension of the Zagros suture zone, where stress data derived from actual measurements is rare. The magnitudes and orientations of principal in-situ stresses were determined using well-logging data.

In the northwestern part of the Zagros suture zone, conventional and borehole image logs for two vertical wells were used, and several borehole breakouts were identified between 1600 and 2240 m depths. Two oil wells (wells A and B) were evaluated, and in well A, several breakouts occurred in eight distinct zones. The azimuth of maximum and minimum horizontal stresses was determined using breakout and six-arm caliper measurements, and lithological evaluation from wireline log data validated the results. The mean azimuth of maximum horizontal stress was N72°E, which showed relative consistency with the NE–SW to E–W direction of tectonic movement and

previous studies in the nearby Zagros suture zone. The magnitudes of the three principal in-situ stresses were determined by one direct method of breakout analysis and another indirect method of the poroelastic strain model.

The R-squared of linear regression between the maximum and minimum horizontal stress was 0.74 and 0.71, respectively. Even though there are different correlations in some depths, the consistency is generally significant, and stress regimes in both methods were consistent in almost all intervals. The results indicate that the direct and indirect methods for determining horizontal stresses are relatively consistent. Therefore, by employing the suggested empirical equation in this study, the gap between the breakout approach, which provides an intermittent stress profile in certain depths, and the poroelastic strain theory, which offers a continuous stress profile, can extend the breakout-based estimates of magnitudes of horizontal stresses to the intervals not directly determined by the breakout approach.

In the northwestern section of the Zagros suture zone area, the stress regime below the depth of 1600 m was a reverse faulting stress regime, and above this depth, it likely changed to a strike-slip faulting stress regime. The determined stress regime was consistent with the dynamics of the tectonic plate movement of the Arabian and Eurasian plates. Consequently, results suggest that the pattern of present-day tectonic stress is controlled mainly by the collision between the Arabian and Eurasian plates in the intermediate depths in the northwestern part of the Zagros suture zone.

The second study area is located in the Dezful Embayment in the Zagros fold and thrust belt (ZFTB), which is part of the Zagros Suture zone in Iran. This study analyses stress orientations, natural fractures, pore pressure, and stress regimes in two oil fields located in the Zagros foothills. The study utilized various data types, including conventional and image logs, to determine the in-situ stresses and their implications for energy field development. The results show that the mean azimuth of the maximum horizontal stress in Field A in the SW sector of Dezful embayment and Field B in the northeast sector are N32°E and N55°E, respectively. The analysis of natural fractures indicates that most tensional fractures are subparallel to the orientation of the maximum horizontal stresses, and the present stress state is responsible for these fractures. The analysis of stress magnitudes in deeper intervals below water-oil contact demonstrates that the stress regime in Field A changes from thrust faulting toward strike-slip faulting.

Meanwhile, no major change in the stress regime of Field B is detected. The azimuth of natural fractures suggests that horizontal wells drilled parallel to the orientation of maximum horizontal stress can optimize wellbore stability. In addition, the stress variations and complexities observed in Field A are attributed to factors such as folding degree, lateral deformability contrasts, and geological structures like faults. The stress regime analysis indicates the influence of regional tectonic forces and the proximity to the collision boundary. This study provided valuable insight into the exploration, development, and management of hydrocarbon resources in the complex geological structure regions of the Dezful Embayment and contributed to understanding stress variations and distribution patterns in similar geological settings elsewhere. Combining the results of both study areas reveals that Folding and faulting along the Zagros suture zone caused a disturbance in the stress regime and consequently changed the azimuth of maximum horizontal stress.

In another part of this dissertation, the importance of accurately identifying breakouts was emphasized throughout the study of the in-situ stress in the Zagros suture zone. Breakouts provide crucial information for evaluating in situ stresses and verifying the geomechanical model. One of the most common methods for identifying borehole breakouts is a combination of image logs and multiple pad Calipers. However, image logs are suitable for geomechanical studies but are usually unavailable in most drilled wells. On the other hand, conventional wireline logs are widely used in drilled wells. Therefore, a method that can use only conventional logs to identify breakouts would be significantly beneficial for geoscientists and geoengineers worldwide. This research investigated the possibility of predicting the occurrence of borehole breakouts only by conventional logs. The Machine learning classification models employed K-Nearest Neighbors (KNN), Decision Tree (DT), Random Forest (RF), Support Vector Machine (SVM), and Extreme Gradient Boosting (XGBoost). Conventional logs and their corresponding identified breakouts from the previous part of the study in the Zagros suture zone were used as the input values for training the classification models. The well-log data was considered the input variable, and breakout data was used as labeling parameters for the same interval. The results are promising, and the XGBoost and RF classification performance was proven more reliable than the other methods. Overall, this study shows that the application of machine learning classification models

demonstrated a reasonable and fast performance in identifying borehole breakouts from only conventional logs.

In summary, by providing a comprehensive analysis of tectonic and geomechanical dynamics, this dissertation enhances our understanding of the fields of structural geology and petroleum engineering in the Zagros suture zone. This study integrates various methodologies to analyze stress regimes, fracture patterns, and wellbore stability in the Zagros suture zone. These methodologies include direct and indirect methods for determining in situ stresses, utilizing conventional and image logs, and advanced machine learning techniques. In addition, it evaluates the magnitude and orientation of in situ stresses to understand the complexity of the collision of Arabian and Eurasian plates. Understanding the variability of stress patterns, influenced by geological complexity and tectonic plate interactions, is crucial for efficient and safe hydrocarbon production in the Zagros suture zone. Furthermore, this study conducted a successful machine learning classification model to predict borehole breakouts by conventional well logs.

Acknowledgments

This dissertation encapsulates the culmination of my extensive Three-year academic journey through my doctoral studies at Kyoto University. Throughout the development and composition of this dissertation, I have been fortunate to receive an immense amount of support and assistance, which has been invaluable to my work.

First, I want to express my deepest gratitude to Prof. Weiren Lin, my dissertation supervisor, for his unwavering support, guidance, and invaluable advice throughout this research journey. He gave me fruitful pieces of advice and helped with my research. I learned a lot from him, and I appreciate the opportunities he provided for me.

I would like to extend my sincere gratitude to my dissertation examiners, Prof. Eiichi Fukuyama and Prof. Sumihiko Murata, for their invaluable insights and constructive critiques that greatly enhanced the quality of this work.

I want to acknowledge Assoc. Prof. Kazuya Ishitsuka and Asst. Prof. Nana Kamiya for helping me through my thesis and providing me with many insightful comments and suggestions.

I would like to thank Assoc. Prof. Ahmed E. Radwan from Jagiellonian University and Mr. Foad Yousefi from Soran University for reviewing my research and providing me with a lot of valuable comments.

My heartfelt appreciation goes to my academic colleagues and peers, especially Yutaro Shigemitsu and Shuai Feng, for the stimulating discussions, encouragement, and camaraderie that enriched my Ph.D. experience. I am deeply thankful to all lab members of Earth and Resource System, whose contributions were vital to the success of this research.

JSPS, Japan supported this work, and I am grateful for their financial assistance. I also wish to acknowledge SLB Japan for providing the Techlog software.

I appreciate Maki Kataoka's encouragement and support of my life in the Katsura Campus. I want to thank all the past and present members of the laboratory for giving me a wonderful time.

I cannot express enough thanks to my family and friends, particularly my father, mother, sister, and best friends, Dr. Foad Salehenia and Dr. Muhammad Karimkhan for their endless love, patience, and support.

I want to express my deepest gratitude to my wife Mariam Wanli, who supported me all along the way, and without her, I could not have accomplished my goals.

My gratitude also goes to the support staff at the HSE division of Kyoto University, especially Emi Mori, for their assistance throughout my studies.

Lastly, I would like to acknowledge anyone who has played a significant role in my academic journey but has not been mentioned above. Your support has not gone unnoticed.

Nazir Mafakheri Bashmagh

2024

Contents

Abstract.....	i
Acknowledgment.....	v
Contents.....	vii
List of Figures.....	xi
List of Tables.....	xiii
List of Abbreviations	xiv
Chapter 1 INTRODUCTION	1
1.1 Motivation	1
1.2 Outline of the thesis	2
References	6
Chapter 2 GEOLOGY AND TECTONIC BACKGROUND	9
2.1 Study Area	9
2.2 Northwestern part of Zagros suture zone	11
2.3 Southeastern part of Zagros suture zone.....	19
References	31
Chapter 3 REVIEW OF DETERMINING IN SITU STRESS.....	40
3.1 Background.....	40
3.2 Direct Methods	43

3.2.1	Wellbore measurements.....	43
3.2.2	Anelastic strain recovery (ASR).....	45
3.2.3	Borehole deformation	46
3.3	Indirect Methods.....	48
3.3.1	Poroelastic strain model.....	48
3.3.2	Kaiser Effect method	48
3.3.3	Earthquake focal mechanism	50
3.4	Method selection	52
	References	53

Chapter 4 STRESS STATE OF NORTHWESTERN ZAGROS SUTURE ZONE 59

4.1	Background.....	59
4.2	Methodology.....	61
4.2.1	Data preparation and workflow	61
4.2.2	Orientation of maximum horizontal stress.....	66
4.2.3	Magnitude of principal in situ stresses	67
4.3	Results of in situ stress analysis (NW Zagros suture zone).....	71
4.3.1	Maximum horizontal stress orientation	71
4.3.2	Breakout quality classification.....	71
4.3.3	In-situ stress magnitude and stress regimes	73
4.3.4	Links to regional stress state and tectonic setting.....	75
4.3.5	Regional and local origin of present-day stress field.....	78
4.3.6	Implications for petroleum exploration and development.....	80
4.4	Comparison between breakout and poroelastic strain theory method.....	82
4.5	Summary.....	87
	References	88

Chapter 5 STRESS STATE OF SOUTHEASTERN ZAGROS SUTURE ZONE 94

5.1	Background.....	94
5.2	Methodology.....	95
5.2.1	Workflow	95
5.2.2	Lithology.....	97
5.2.3	Data Preparation	97
5.2.4	Fracture analysis	99
5.2.5	Breakout and Drilling Induced Tensile Fracture Quality Ranking.....	99
5.2.6	Magnitudes of In-Situ Principal Stresses.....	101
5.3	Results of stress analysis	103
5.3.1	Borehole Failure	103
5.3.2	Maximum horizontal stress orientation	106
5.3.3	Natural Fracture Analysis	108
5.3.4	Pore pressure.....	108
5.3.5	Stress Magnitude.....	113
5.3.6	Stress Regime	113
5.4	Interpretation of in situ stress analysis (SE Zagros suture zone).....	116
5.4.1	Horizontal stress magnitude and orientation	116
5.4.2	Links to regional stress state and tectonic setting.....	119
5.4.3	Regional and local origin of present-day stress field.....	121
5.4.4	Implications for field development and wellbore stability	122
5.5	Integration of two study area.....	124
5.6	Summary.....	126
	References	127

Chapter 6 APPLICATION OF AI IN BOREHOLE BREAKOUT ANALYSIS..... 133

6.1	Background.....	133
-----	-----------------	-----

6.2	ML Classification Methodology.....	136
6.2.1	Workflow	136
6.2.2	Petrophysical logs correspond to borehole geometry.....	139
6.3	Classification Models	144
6.3.1	Model selection.....	144
6.3.2	K-Nearest Neighbors (KNN):.....	146
6.3.3	Decision Tree (DT):.....	147
6.3.4	Random Forest (RF):	149
6.3.5	Support Vector Machine (SVM).....	150
6.3.6	Extremely Gradient boosting (XGBoost)	153
6.4	Evaluation metrics	155
6.5	Results and interpretation of classification models	157
6.5.1	Overview.....	157
6.5.2	Analysis of Input Parameters	161
6.5.3	Tuning hyperparameters	164
6.5.4	Robustness	168
6.5.5	Well log selection for future cases.....	170
6.6	Summary.....	172
	References	173
	Chapter 7 CONCLUSION.....	177

List of Figures

Figure 1-1. Structure of dissertation.....	5
Figure 2-1. Study area shown on world stress map.	10
Figure 2-2. Tectonic plates in the Middle East	12
Figure 2-3. Ongoing Arabian-Eurasian collision.....	13
Figure 2-4. Regional tectonic map of Kurdistan region, Iraq.	14
Figure 2-5. Structural map of the Kurdistan region, Iraq.....	15
Figure 2-6. Stratigraphic column and oil and gas reservoir.	18
Figure 2-7. Digital elevation map of study area	19
Figure 2-8. Field location and main tectonic and structural features.....	20
Figure 2-9. Study areas, Fields A and B, are plotted on a digital elevation map.....	22
Figure 2-10. Structural cross-section of the Dezful Embayment.....	23
Figure 2-11. Stratigraphic column of well A in Dezful Embayment.....	25
Figure 2-12. Schematic seismic profile of Fields A and B	27
Figure 3-1. Stress sources composing the tectonic stress.	41
Figure 3-2. Classification of in situ stress measurement methods.....	42
Figure 3-3. Hydraulic fracturing test.....	44
Figure 3-4. Elastic strain recovery caused by in situ stress release.	46
Figure 3-5. Example of breakouts and DIFT in an acoustic borehole image log	47
Figure 3-6. Schematic model of acoustic Kaiser effect test.....	49
Figure 3-7. Illustration of EFM for different stress regimes.....	51
Figure 4-1. Workflow of image log data preparation.	61
Figure 4-2. Workflow of determining magnitude and orientation of in situ stress....	62
Figure 4-3. Dynamic borehole image log, detected breakout in the wellbore.	63
Figure 4-4. Variation of breakout width, height, and azimuth.....	65
Figure 4-5. Magnitude of principal in situ stresses.	74
Figure 4-6. Schematic of breakout analysis parameters.....	75
Figure 4-7. Schematic Structural geology of study area.	76
Figure 4-8. Comparison of maximum horizontal stress.....	83
Figure 4-9. Comparison between the breakout and poroelastic strain method.....	84
Figure 4-10. Comparison of the maximum and minimum horizontal stress.....	86

Figure 5-1. Workflow of determining magnitude and orientation of in situ stress....	96
Figure 5-2. Lithology identification of Asmari formation for well A2.....	98
Figure 5-3. Presentation of image logs in wells A5 and B1.....	100
Figure 5-4. Underground contour map of top formation of Asmari in Filed A.	105
Figure 5-5. Rose diagram presents the breakouts and DITF for each well.....	107
Figure 5-6. Results of image log analysis for facture identification in well A2.	109
Figure 5-7. Profile of in situ stresses and pore pressure Pp for both fields	110
Figure 5-8. Stress polygon for two different depths in Well A2.....	115
Figure 5-9. The mean azimuth of maximum horizontal stress.....	117
Figure 5-10. Schematic anticline folding degree scale.	118
Figure 5-11. Integration of two study areas.	126
Figure 6-1. Workflow of a systematic supervised machine learning (ML).	137
Figure 6-2. Visual observation of resistivity image log to identify breakouts.....	138
Figure 6-3. Effect of the presence of breakout zones on petrophysical well logs. ..	140
Figure 6-4. KNN classification conceptual image..	147
Figure 6-5. Illustration of a simple DT algorithm.....	148
Figure 6-6. Schematic illustration of RF algorithm	150
Figure 6-7. SVM classification conceptual image.	152
Figure 6-8. Schematic illustration of XGBoost algorithm.	154
Figure 6-9. Visualized results of predicted breakouts for the studied intervals.....	159
Figure 6-10. Model evaluation metrics for training data.	160
Figure 6-11. Combinations of well logs for classification models	163
Figure 6-13. Tuning K value hyperparameter for the KNN classification model. ..	165
Figure 6-13. Tuning hyperparameters for DT classification model.....	165
Figure 6-14. Tuning hyperparameters for RF classification model.	166
Figure 6-15. Tuning gamma hyperparameter for the SVM classification model. ...	167
Figure 6-16. Tuning hyperparameters for XGBoost classification model.	168
Figure 6-17. Evaluation of Accuracy of test and train data.	169

List of Tables

Table 2-1. Previous tectonic studies in the nearby Kurdistan region of Iraq.....	17
Table 2-2. Previous tectonic studies in the nearby area of Dezful Embayment.	29
Table 2-3. Lithology and reservoir data for well A5 from Field A.....	30
Table 4-1. Average rock properties and geomechanical parameters.	70
Table 4-2. World Stress Map quality ranking criteria.....	72
Table 5-1. Data catalogue and results of breakout and DIFT for all wells..	103
Table 5-2. World Stress Map quality ranking criteria.....	104
Table 5-3. Magnitude of in situ stress and pore pressure for well A2.	118
Table 6-1. Comparison between image logs and conventional logs.....	134
Table 6-2. List of input variables and dependent variables..	143
Table 6-3. Comparison between the supervised machine learning classification....	145
Table 6-4. Four parameters define the evaluation metrics.	157

List of Abbreviations

BFZ	Balarood fault zone
BO	Breakout (Breakout zone)
CAL	Caliper
DEM	Digital elevation model
DITF	Drilling induced tensile fracture
DRHO	Density correction log
DT	Decision tree
EFM	Earthquake focal mechanism
FMI	Fullbore formation microimager
GR	Gamma ray log
InSAR	Interferometric synthetic aperture radar
K	Pottasium log
KFZ	Kazerun fault zone
KNN	K nearest neighbor
LLD	Resistivity lateral log deep
LLS	Resistivity lateral log shallow
MFF	Mountain front fault
MSFL	Micro-spherical focused log
NBO	Non-breakout zone
NE	Northeast
NF	Normal fault
NPHI	Neutron porosity log
NS	Predominantly normal faulting with strike slip components
NW	Northwest
OBMI	Oil-based microimager
OWC	Oil water contact
PEF	Photoelectric factor log
RF	Random forest
RFT	Repeated formation test
RHOB	Density log
RS	Remote sensing
SE	Southeast
SS	Strike-slip fault
SVM	Support vector machine
SW	Southwest
TF	Thrust fault
THOR	Thorium log
TS	Predominantly thrust faulting with strike slip components

TVD	True vertical depth
U	Uranium log
UBI	Ultrasonic borehole imager
UF	Oblique fault (Unknown fault)
WSM	World stress map
XGBoost	Extreme gradient boosting
ZFTB	Zagros fold and thrust belt
ZMTF	Zagros main thrust fault
UCS	Unconfined compressive strength

Chapter 1

Introduction

1.1 Motivation

Zagros suture zone is located on the borders of the collision between the Arabian, Eurasian (Iranian), and Anatolian plates. The suture zone marks the location of the subduction, while the Zagros fold and thrust belt (ZFTB) is the present-day expression of this ongoing tectonic collision. Consequently, this region is considered one of the most prominent regions of convergent deformation on the Earth, and understanding the stress state is crucial for geoscientists and geoengineers (Agard et al., 2011; Mouthereau et al., 2012). Research on in-situ stress orientations and magnitudes is mandatory for various fields of geosciences and geoengineering, including petroleum engineering (Abdelghany et al., 2021; Brudy and Zoback, 1999). Previous research studies prove the importance of in-situ stress studies in drilling, well completion, production optimization, wellbore stability, and hydraulic fracturing (Baouche et al., 2020; Karatela et al., 2016; Lakirouhani et al., 2016; Radwan and Sen, 2021). Several methods have been proposed for determining in-situ stress. The direct methods include core-based methods such as anelastic strain recovery (ASR), wellbore measurement such as hydraulic fracturing methods, and borehole deformation such as breakout and drilling induced tensile fractures (DITF). On the other hand indirect methods are based on theoretical approaches such as poroelastic strain theory, earthquake focal mechanism (EFM), and acoustic methods (Bell, 1996; Lee and Ong, 2018; Lin et al., 2006; Ljunggren et al., 2003; Nagano et al., 2015; Zoback et al., 2003, 1985). Acquiring core samples and running hydraulic fracturing methods are usually more expensive than other methods and they have several technical complexities. Therefore, they are often unavailable in many regions, including this study's region of interest. On the other hand, earthquake focal mechanisms are not highly accurate and usually represent a deeper crust stress state and cannot be easily correlated to the stress state in medium to shallow depths (Tingay et al., 2008). Therefore, using the well log data, including image logs, in combination with empirical approaches to determine the orientation and magnitude

of horizontal in situ stresses in the extension of the Zagros suture zone, where present-day stress data derived from actual measurements is rare, is valuable for geoscientists (Abdelghany et al., 2022; Haghi et al., 2018; Li et al., 2019; Rajabi and Tingay, 2014).

1.2 Outline of the thesis

This dissertation consists of seven chapters as follows (Figure 1-1):

In Chapter One, the motivation and objectives of the study are described. In addition, the summary of each chapter is presented in this chapter.

Chapter Two summarizes the geology and tectonic settings of the Zagros suture zone, drawing from previous studies. This zone represents a major convergent plate boundary where the Arabian and Eurasian tectonic plates meet, forming the Zagros fold and thrust belt (ZFTB). The area's geology is characterized by a mix of sedimentary, igneous, and metamorphic rocks, indicating a diverse and dynamic geological history. This region has experienced significant tectonic activities, including folding and faulting, due to the ongoing collision between the Arabian and Eurasian plates. These processes have shaped the physical landscape and profoundly impacted regional seismicity, making the Zagros suture zone a key area of interest for geoscientists studying plate tectonics. The study area's location and its geological structures are described briefly. The Geological structures, lithologies, and other significant aspects of the ZFTB are also described.

Chapter Three reviews the existing measurement and determining methods of the magnitude and orientation of in situ stresses. A wide range of in-situ stress measurement and empirical equations methods have been proposed by previous studies. There are several perspectives to categorize stress measurements and determining methods, and in this dissertation, the methods are categorized based on direct and indirect methods. The direct methods include core-based, borehole deformation such as breakout and field measurements that measure the rock deformation and properties parameters to estimate the magnitude and orientation of in situ stresses and provide the stress state for certain depths. On the other hand, indirect methods based on empirical equations, such as poroelastic strain theory, provide a continuous profile of stress state based on well-

logging data. Since estimating in situ stress is challenging and accuracy is a significant concern for geoscientists and geoengineers, combining two methods based on indirect and direct methods can be beneficial. Therefore, it is desirable to combine different methods. In this study, two methods of breakout and poroelastic strain theory have been selected. Subsequently, this chapter describes these two methods' basic principles, hypotheses, and theoretical equations in more detail.

Chapter Four discusses the methodology and results of the stress state of the northwestern part (NW) of the Zagros suture zone. The study area is in the Kurdistan Region of Iraq, where present-day stress data derived from actual measurements is rare. This chapter explains a systematic approach to determining the magnitudes and orientations of principal in-situ stresses using well-logging data, including image logs and conventional logs, based on the breakout approach and poroelastic strain theory. Then, the correlation between the two methods is assessed to compare the two methods and also find an empirical equation to relate these two methods. The five principal components of the geomechanical study, including the magnitude of the three principal in-situ stresses, distribution of formation pore pressure (P_p), and the azimuth of maximum horizontal stresses, were estimated for the depth interval of 1600 m to 2240 m in two oil wells. The stress regime below the depth of 1600 m was a reverse faulting stress regime, and above this depth, it likely changed to a strike-slip faulting stress regime. In this chapter multiple reasons were discussed that likely dominate the stress twisting at different depths. The determined stress regime was consistent with the nature and dynamics of the tectonic plate movement of the Arabian and Eurasian (Iranian) plates. Consequently, results suggest that the pattern of present-day tectonic stress is controlled mainly by the collision between the Arabian and Eurasian plates.

Chapter Five describes the methodology and analysis of the in-situ stress state and natural fractures in the Dezful Embayment, the southeastern (SE) part of the ZFTB in Iran, which is the extension of the study area of chapter four at the northwestern part of ZFTB. This study utilized various data types, including images and conventional logs, to determine the in-situ stresses and their implications for the region's energy field development and other relevant geoscience studies. This chapter analyzes magnitudes and orientations of principal in-situ stresses, natural fractures, pore pressure, and stress

regimes in fields A and field B with seven oil wells in the Zagros foothills. The results show that the azimuth of maximum horizontal stress in Asmari formation in Dezful Embayment varies from N32°E to N55°E. Deeper formations with a ductile nature can cause stress decoupling between upper and lower structures. Tectonic forces due to the collision of the Arabian and Eurasian plates dominate the current stress regime in Dezful embayment. Due to long-term oil production, pore pressure drawdown in oil fields affects the stress state in the Asmari Formation. The analysis of natural fractures indicates that most tensional fractures are subparallel to the orientation of the maximum horizontal stresses, and the present stress state is responsible for these fractures.

Chapter Six emphasizes the importance of borehole deformation, such as breakout, in geomechanics and several other geosciences disciplines. As discussed in chapters Four and Five, identifying breakout is vital in geomechanical studies. However, using image logs and multiple pad calipers is a common method for identifying the breakouts and has been used for this dissertation, but image logs are unavailable in many cases, and they have high time consumption and need human supervision during the process. Therefore, the application of supervised machine learning (ML) classification models to identify borehole breakouts in carbonate reservoirs, merely based on conventional log data, was investigated. This study used conventional wireline logs, including gamma-ray, neutron porosity, density, resistivity, and single-pad caliper, to identify the depth and length of breakout zones. The ML models employed K-nearest neighbors (KNN), decision tree (DT), and random forest (RF), support vector machine (SVM) and extremely gradient boosting (XGBoost). Overall, this study shows that the application of ML classification models demonstrated a reasonable and fast performance in identifying borehole breakouts from conventional logs.

Finally, in Chapter Seven, this dissertation is summarized in conclusion. This chapter summarizes analyzing the present-day stress state of the northwestern and southeastern parts of ZFTB and other relevant outcomes, such as the application of ML in identifying breakouts based on conventional log.

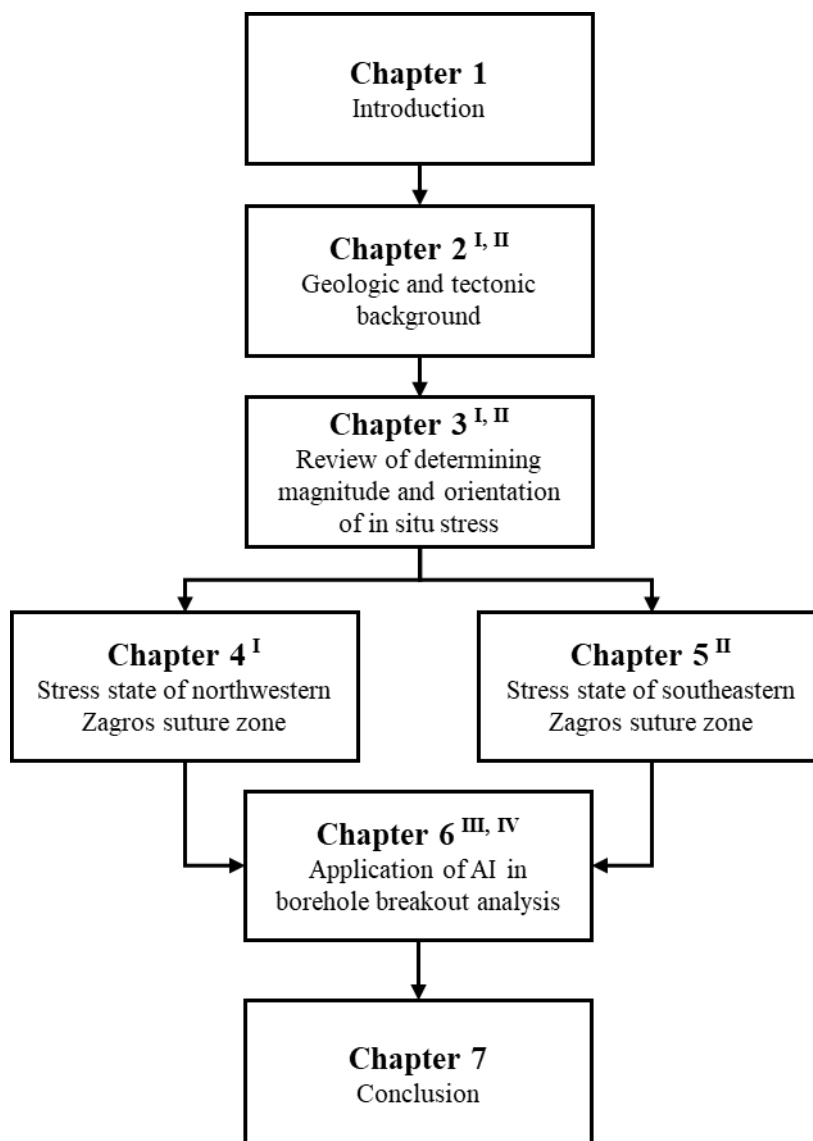


Figure 1-1. Structure of this dissertation. Roman numbers shown in this figure indicate the published, submitted (Under review) and in-preparation papers on these topics mentioned in each chapter (I: Mafakheri B. et al., 2022; II: Mafakheri B. et al., 2024; III: Mafakheri B. et al., Under revision; IV: Mafakheri B. et al., in-preparation.)

References

- Abdelghany, W.K., Ahmed, M.S.H., Nassar, E.R., 2022. Implications of machine learning on geomechanical characterization and sand management : a case study from Hilal field , Gulf of Suez. *J Pet Explor Prod Technol*. <https://doi.org/10.1007/s13202-022-01551-9>
- Abdelghany, W.K., Radwan, A.E., Elkhawaga, M.A., Wood, D.A., Sen, S., Kassem, A.A., 2021. Geomechanical modeling using the depth-of-damage approach to achieve successful underbalanced drilling in the Gulf of Suez rift basin. *J Pet Sci Eng* **202**, 108311. <https://doi.org/10.1016/j.petrol.2020.108311>
- Agard, P., Omrani, J., Jolivet, L., Whitechurch, H., Vrielynck, B., Spakman, W., Monié, P., Meyer, B., Wortel, R., 2011. Zagros orogeny: A subduction-dominated process. *Geol Mag* **148**, 692–725. <https://doi.org/10.1017/S001675681100046X>
- Baouche, R., Sen, S., Sadaoui, M., Boutaleb, K., Ganguli, S.S., 2020. Characterization of pore pressure, fracture pressure, shear failure and its implications for drilling, wellbore stability and completion design – A case study from the Takouazet field, Illizi Basin, Algeria. *Mar Pet Geol* **120**, 104510. <https://doi.org/10.1016/j.marpetgeo.2020.104510>
- Bell, J.S., 1996. Petro geoscience 1. In situ stresses in sedimentary rocks (part 1): Measurement techniques. *Geoscience Canada* **23**. <https://journals.lib.unb.ca/index.php/GC/article/view/3902>
- Brudy, M., Zoback, M.D., 1999. Drilling-induced tensile wall-fractures: Implications for determination of in-situ stress orientation and magnitude. *International Journal of Rock Mechanics and Mining Sciences* **36**, 191–215. [https://doi.org/10.1016/S0148-9062\(98\)00182-X](https://doi.org/10.1016/S0148-9062(98)00182-X)
- Haghi, A.H., Chalaturnyk, R., Ghobadi, H., 2018. International Journal of Rock Mechanics and Mining Sciences The state of stress in SW Iran and implications for hydraulic fracturing of a naturally fractured carbonate reservoir. *International Journal of Rock Mechanics and Mining Sciences* **105**, 28–43. <https://doi.org/10.1016/j.ijrmms.2018.03.002>
- Karatela, E., Taheri, A., Xu, C., Stevenson, G., 2016. Study on effect of in-situ stress ratio and discontinuities orientation on borehole stability in heavily fractured rocks

- using discrete element method. *J Pet Sci Eng* **139**, 94–103. <https://doi.org/10.1016/j.petrol.2015.12.016>
- Lakirouhani, A., Detournay, E., Bungler, A.P., 2016. A reassessment of in situ stress determination by hydraulic fracturing. *Geophys J Int* **205**, 1859–1873. <https://doi.org/10.1093/gji/ggw132>
- Lee, H., Ong, S.H., 2018. Estimation of In Situ Stresses with Hydro-Fracturing Tests and a Statistical Method. *Rock Mech Rock Eng* **51**, 779–799. <https://doi.org/10.1007/s00603-017-1349-1>
- Li, H., Tang, H., Qin, Q., Wang, Q., Zhong, C., 2019. Effectiveness evaluation of natural fractures in Xujiahe Formation of Yuanba area, Sichuan basin, China. *Arabian Journal of Geosciences* **12**. <https://doi.org/10.1007/s12517-019-4292-5>
- Lin, W., Kwaśniewski, M., Imamura, T., Matsuki, K., 2006. Determination of three-dimensional in situ stresses from anelastic strain recovery measurement of cores at great depth. *Tectonophysics* **426**, 221–238. <https://doi.org/10.1016/j.tecto.2006.02.019>
- Ljunggren, C., Chang, Y., Janson, T., Christiansson, R., 2003. An overview of rock stress measurement methods. *International Journal of Rock Mechanics and Mining Sciences* **40**, 975–989. <https://doi.org/10.1016/J.IJRMMS.2003.07.003>
- Mafakheri B., N., Lin, W., Ishitsuka, K., 2024a. Application of supervised machine learning classification models to identify borehole breakouts in carbonate reservoirs based on conventional log data. *International Journal of the JSRM* (Under review).
- Mafakheri B., N., Lin, W., Ishitsuka, K., 2024b. Utilizing artificial intelligence algorithms for detecting borehole breakouts by conventional logging data. in preparation.
- Mafakheri B., N., Lin, W., Murata, S., Yousefi, F., Radwan, A.E., 2022. Magnitudes and orientations of present-day in-situ stresses in the Kurdistan region of Iraq: Insights into combined strike-slip and reverse faulting stress regimes. *J Asian Earth Sci* **239**, 105398. <https://doi.org/10.1016/j.jseaes.2022.105398>
- Mafakheri B., N., Lin, W., Radwan, A.E., Manshad, A.K., 2024c. Comprehensive analysis of stress magnitude and orientations and natural fractures in complex structural regimes oil reservoir: Implications for tectonic and oil field development

- in the Zagros suture zone. *Mar Pet Geol* **160**, 106615.
<https://doi.org/10.1016/J.MARPETGEO.2023.106615>
- Mouthereau, F., Lacombe, O., Vergés, J., 2012. Building the Zagros collisional orogen: Timing, strain distribution and the dynamics of Arabia/Eurasia plate convergence. *Tectonophysics* **532–535**, 27–60. <https://doi.org/10.1016/j.tecto.2012.01.022>
- Nagano, Y., Lin, W., Yamamoto, K., 2015. In-situ stress analysis using the anelastic strain recovery (ASR) method at the first offshore gas production test site in the eastern Nankai Trough, Japan. *Mar Pet Geol* **66**, 418–424.
<https://doi.org/10.1016/J.MARPETGEO.2015.02.027>
- Radwan, A., Sen, S., 2021. Characterization of in-situ stresses and its implications for production and reservoir stability in the depleted El Morgan hydrocarbon field, Gulf of Suez rift basin, Egypt. *J Struct Geol* **148**, 104355.
<https://doi.org/10.1016/j.jsjg.2021.104355>
- Rajabi, M., Tingay, M., 2014. The Present-day stress pattern in the Middle East and Northern Africa and their importance, Paper presented at the International Petroleum Technology Conference, *World stress map*.
<https://doi.org/10.2523/IPTC-17663-MS>
- Tingay, M., Reinecker, J., Müller, B., 2008. Borehole breakout and drilling-induced fracture analysis from image logs. *World stress map* 1–8. http://dc-app3-14.gfz-potsdam.de/pub/guidelines/WSM_analysis_guideline_breakout_image.pdf
- Zoback, M.D., Barton, C.A., Brudy, M., Castillo, D.A., Finkbeiner, T., Grollimund, B.R., Moos, D.B., Peska, P., Ward, C.D., Wiprut, D.J., 2003. Determination of stress orientation and magnitude in deep wells. *International Journal of Rock Mechanics and Mining Sciences* **40**, 1049–1076.
<https://doi.org/10.1016/j.ijrmms.2003.07.001>
- Zoback, M.D., Moos, D., Mastin, L., Anderson, R.N., 1985. Well bore breakouts and in situ stress. *J Geophys Res Solid Earth* **90**, 5523–5530.
<https://doi.org/10.1029/JB090IB07P05523>

Chapter 2

Geology and Tectonic Background

2.1 Study Area

The Middle East has complex geology, significantly influenced by the dynamics of the Arabian, Eurasian, Anatolian, and African tectonic plates. The Arabian-Eurasian tectonic boundary is primarily a convergent plate boundary where the Arabian Plate moves northwards beneath the Eurasian Plate (Figure 2-1). The interaction between these plates has led to significant regional seismic activity, including frequent earthquakes such as the 7.8 Mw Kahramanmaras earthquake in 2023 in southern Turkey and northern Syria (Karabulut et al., 2023; Mousavi, 2017; Onur et al., 2016). One of this region's most significant geological features is the Zagros suture zone, located at the border between Iran and Iraq. This zone was formed after the collision of the Arabian and Eurasian plates. The zone is characterized by complex geological structures, including folded and faulted rock formations. The collision of these plates has profoundly influenced the geological history of the Middle East, contributing to the formation of various mountain ranges and basins.

Kurdistan is the most tectonically active region in the northwestern part of the Zagros suture zone. This region is located along the northeastern boundary of the Arabian Plate with the Anatolian and Eurasian plates (Figure 2-1). In addition, in terms of seismicity, the area is an active seismic zone, and the 7.3 Mw earthquake in 2017 on the border of Iran and Iraq is a recent event (Gombert et al., 2019). On the other hand, this area is one of the new important and prolific oil-rich zones with several oil and gas-producing fields. This region borders the collision area between the Arabian and Eurasian (Iranian) plates in the northeast and the Arabian and Anatolian plates in the north (Agard et al., 2011a).

The Dezful Embayment, located in the southern part of Zagros suture zone in southwestern Iran, is another one of significant geological importance due to its unique tectonic setting, in situ stress dynamics, seismicity, and abundant oil reservoirs. This embayment is characterized by distinct in situ stress patterns, influenced by the ongoing

tectonic compression, which affects the distribution and orientation of faults and fractures. Moreover, the Dezful Embayment is known for its hydrocarbon resources, which makes it a focal point for hydrocarbon exploration and production.

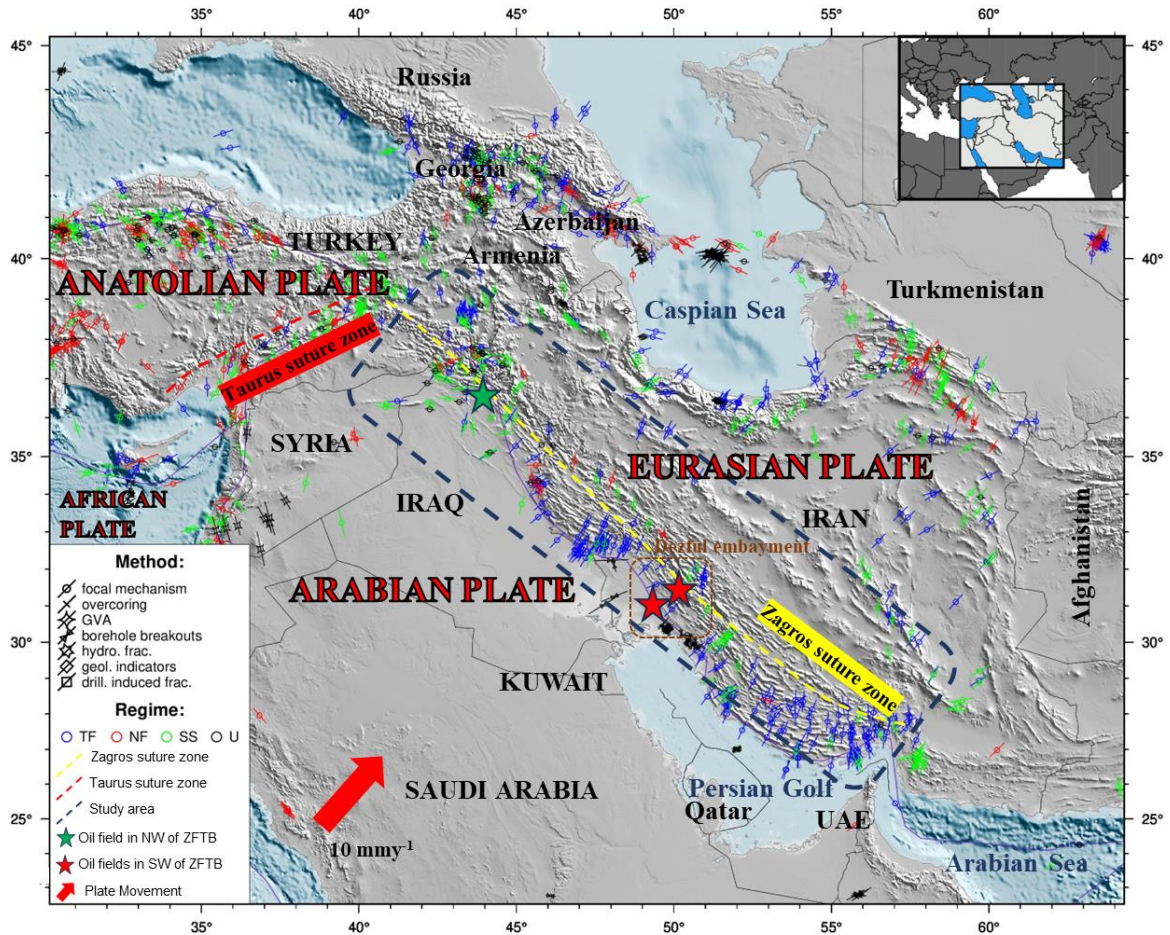


Figure 2-1. Study area shown on world stress map database in the middle east (Data from Heidbach et al., 2018). The Dark blue dashed line box shows the area of interest presented in chapter Four and Five. The subduction indicates the Arabian plate moving beneath the Eurasian plate. Stars are showing the field locations.

2.2 Northwestern part of Zagros suture zone

The entire country of Iraq is located on the northeastern part of the Arabian Plate, except for a small area in the farthest northeast, located on the Eurasian Plate (Figure 2-2). Different tectonic forces have affected Iraq in different eras, but the recent tectonic setting of Iraq is controlled by the collision between the Arabian and Eurasian plates (Abdulnaby, 2019). After the closure of the Neo-Tethys Ocean in the Miocene, the collision between these plates began. The northeastern margin of the Arabian Plate was initially formed by mid-Permian rifting, the Triassic break-up of Pangaea, and the opening of the Neo-Tethys Ocean. This collision continues and causes strong tectonic forces in the region (Ali et al., 2014, 2013; Al-Qayim et al., 2012; Numan, 1997). The tectonic evolution of the Zagros suture zone formed in a sequence of upper Proterozoic, Permian–Triassic (250 million years ago (Ma)), and Mesozoic rift events, which led to the closure of the ancient continental margin and ultimately caused a continental collision in the Cenozoic (Alavi, 2007, 2004; de Vera et al., 2009).

However, some slightly different scenarios for the tectonic evolution of the Zagros suture zone have been proposed in different studies based on different areas along the border, although most have agreed on seven distinct stages (Agard et al., 2011a; Alavi, 2007; Ali et al., 2019; Al-Qayim et al., 2012; Khadivi, 2010; Le Garzic et al., 2019; Regard et al., 2004). According to Al-Qayim et al. (2012) and Agard et al. (2011a), the beginning of this tectonic evolution was middle Triassic rifting at the Afro-Arabian plate margin; then, during the Jurassic, a radiolarite trough formed.

Consequently, in the next step in the upper Cretaceous, radiolarite–ophiolite obduction and formation of a foreland basin occurred. Afterward, during the Eocene and lower Oligocene, a fore-arc basin developed. Eventually, the collision of the Arabian Plate with the Sanandaj-Sirjan block in the Miocene caused a shortening of the Arabian plate margin during the Pliocene. Finally, the development of the Zagros orogenic belt, including the Zagros suture zone, reached the situation illustrated in Figure 2-3. As shown in Figures 2-3, the focus of this study was the Zagros fold and thrust belt. Overall, the Zagros orogenic belt has two distinct trends: an NW–SE trend

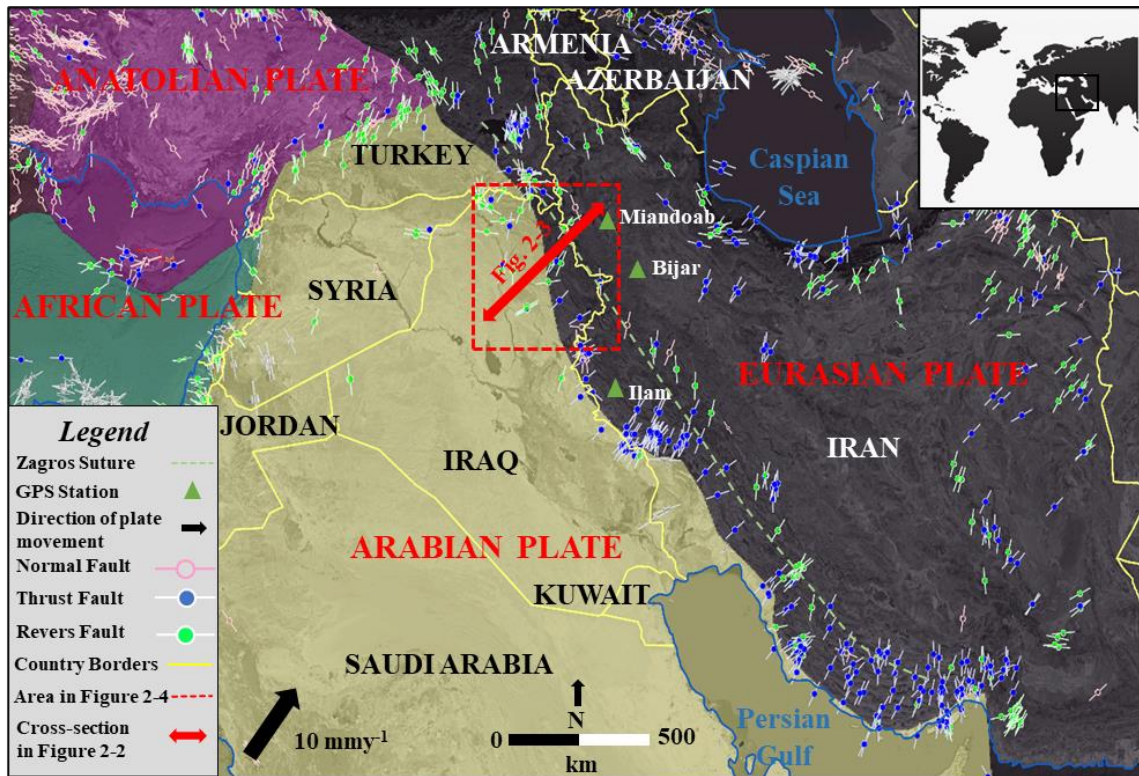


Figure 2-2. Tectonic plates and World Stress Map database in the Middle East (Data from Heidbach et al., 2018). The red dashed box shows the area of interest presented in the northwest area of the Zagros suture zone in Figure 2-3. Illustrations of Eurasian, Arabian, Anatolian, and African Plate collisions are shown in different colors. Green triangles show the closest GPS stations from (Vernant, 2004) near the study area. After Mafakheri B. et al. (2022).

along the Arabian and central Eurasian plates and an E–W trend between the Arabian and southern Anatolian plates. This orogenic belt results from the formation of the Bitlis–Zagros fold and thrust belt that extends from Turkey and Iraq in the north to the Strait of Hormuz in Iran (Alavi, 1994; Falcon, 1974; Khadivi, 2010; Vernant et al., 2004). Several studies have determined different convergence rates between the Arabian, Eurasia, and Anatolian plates in tectonic plate movement. There are significant differences up to 20 mm y^{-1} in some cases; however, overall, between the Arabian and Eurasian plates, a convergence rate of 10 to 15 mm y^{-1} is accepted among scientists. According to Vernant et al. (2004), there is a wide range of convergence rates along the boundary of collision of the Arabian and Eurasian plates. It varies from 1 mm y^{-1} to 2 mm y^{-1} in the Yazd-Iran and $9 \pm 2 \text{ mm y}^{-1}$ in the southeastern Zagros to $19.5 \pm 2 \text{ mm y}^{-1}$ in the Makran subduction zone (Vernant et al., 2004). For central Zagros, the shortening rate is approximately $6.5 \pm 2 \text{ mm y}^{-1}$. However, the overall convergence rate

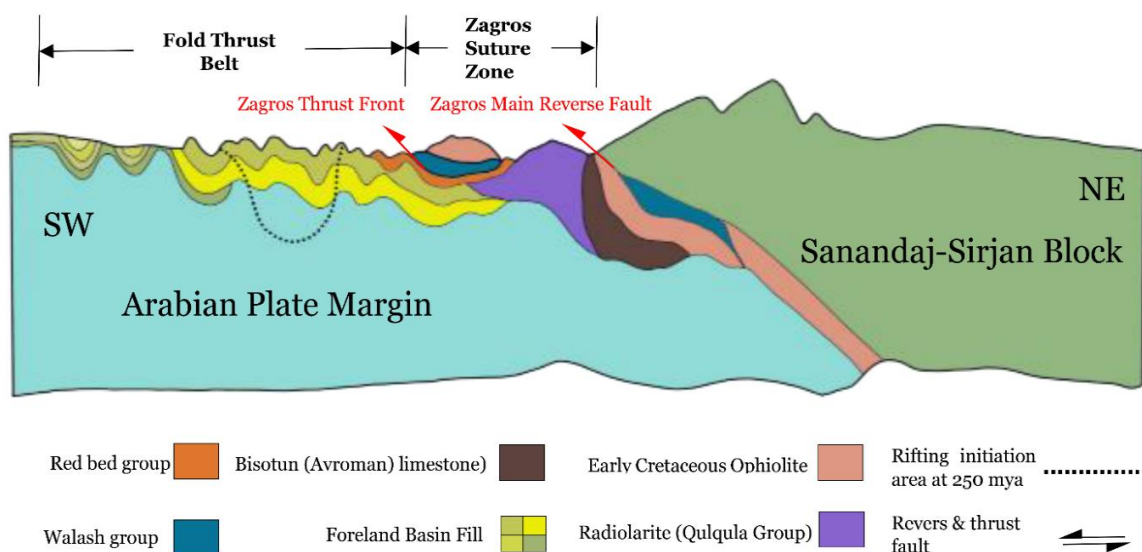


Figure 2-3. Ongoing Arabian-Eurasian collision (double side arrow in Figure 2-2). Middle Miocene-present situation of the Zagros orogenic belt, including the Zagros suture zone. At 250 Ma a rift started in the dotted line area and caused the collision of Arabian plate and Eurasian plate (Sanandaj Sirjan Block) which led to the subduction between the plates. After Al-Qayim et al. (2012) and Mafakheri B. et al. (2022).

is 10 mm y^{-1} for the Zagros fold and thrust belt. The nearest GPS-measured convergence rates in Iran along the current study area in Iraq are 13.3 mm y^{-1} , 17.8 mm y^{-1} , and 14.6 mm y^{-1} in Miandoab, Ilam, and Bijar, respectively (Vernant et al., 2004) (Figure 2-2).

The collision between these plates created three major fault systems in Iraq: the N–S Nabitah system, the NW–SE Najd system, and the NE–SW or E–W transversal system (Doski, 2021; Jassim, S.Z., and Goff, 2006). Iraq's western Zagros fold and thrust belt are divided into three major blocks: Sinjar, Mosul, and Kirkuk (Abdulnaby, 2019; Numan, 1984). The NW–SE-oriented Zagros fold and thrust belt extends approximately 2,000 km from the Anatolian fault of southeastern Turkey to the Makran zone in southern Iran (Alavi, 2004; Al-Qayim et al., 2012; Sharland et al., 2004). This fold and thrust belt formed under the structural deformation of the Zagros proforeland system, which is currently known as the Persian Gulf and continental Mesopotamia Basin. In

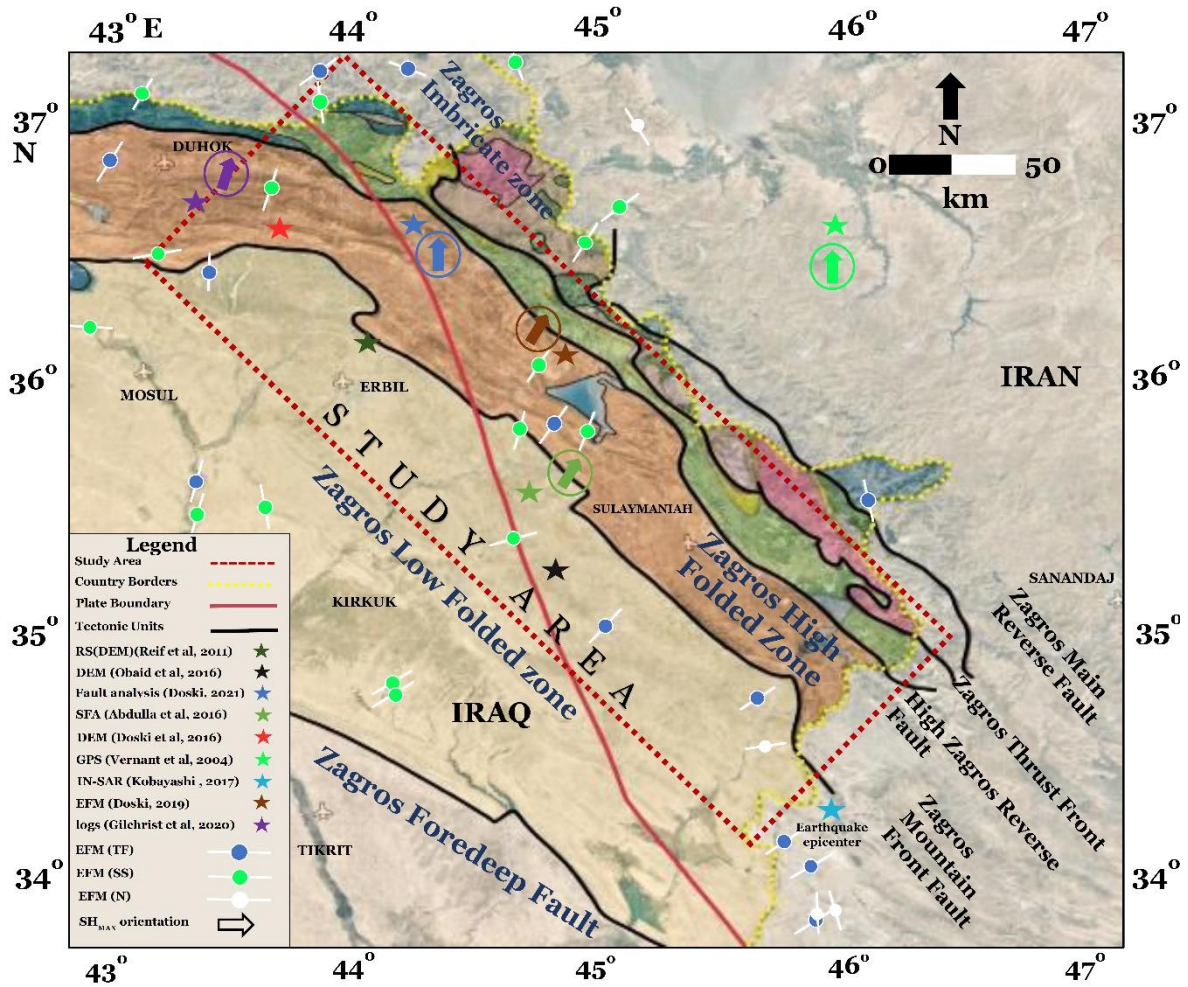


Figure 2-4. Regional tectonic map of Kurdistan region, Iraq. Major tectonic subdivisions, including Zagros high folded zone, Zagros low folded zone, and Zagros imbricated zone have been illustrated. Several studies shown in Table 2-1 have been placed on different tectonic subdivisions on the map. The orientation of maximum horizontal stresses for some previous studies has been placed on the map. Modified from Al-Qayim et al (2012) and after Mafakheri B. et al. (2022).

the outer part of the southwest Zagros orogenic wedge, the belt's structure evolved as an overlaid thrust sheet, including a sedimentary succession approximately 7 to 12 km thick (Alavi, 2004). According to Alavi (2007, 2004, 1994) and Al-Qayim et al. (2012), the entire Zagros region is subdivided into three tectonic units from northeast to southwest. The first is the Urumieh–Dokhtar magmatic assemblage, the second is the Sanandaj–Sirjan zone (the Zagros imbricate zone), and the last is the Zagros fold-thrust belt, which is the area of interest in this study. As shown in Figure 2-3, major components of the Zagros suture zone (collision between Arabian and Eurasian plates) include an ophiolite–radiolarite obduction related to the Coniacian–Campanian, which

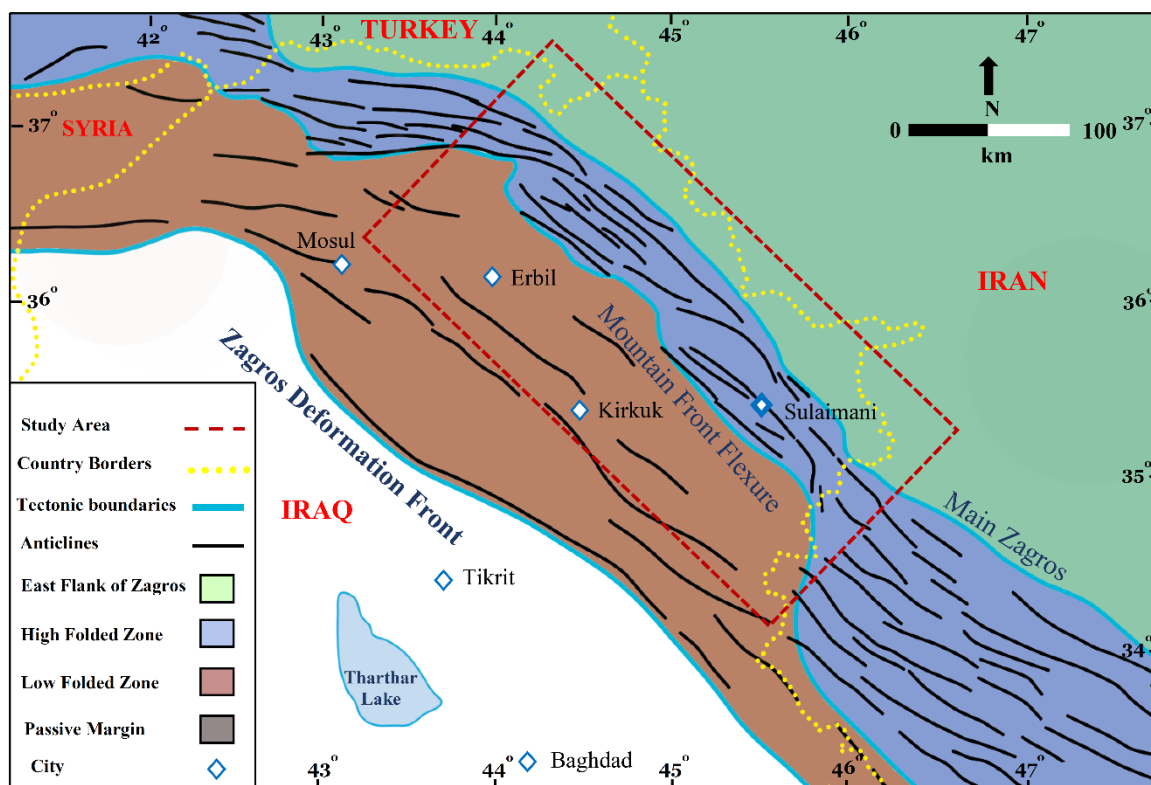


Figure 2-5. Structural map of the Kurdistan region, Iraq. Orientations of the anticlines in this part of the Zagros Orogen is presented, as well as zone boundaries of the belt. Modified from Zebari and Burberry (2015) and taken from Mafakheri B. et al. (2022).

is composed of sedimentary mélangé (Qulqula Group), radiolarites, and Triassic platform carbonate (Avroman Limestone Formation) (Alavi, 2004; Al-Qayim et al., 2012). The northwestern part of the Zagros orogenic belt in the Kurdistan region of Iraq includes the Zagros suture zone, which also includes allochthonous Tethyan Triassic–Eocene thrusts sheets. The suture zone is between the Zagros main reverse fault in the northeast and the Zagros thrust front in the southwest (Alavi, 2007, 2004; Al-Qayim et al., 2012) (Figures 2-2, 2-3, and 2-4).

Iraq's basic geological units are grouped according to the region's tectonic development and depositional history. Iraq can be considered as a large anticline (Zebari and Burberry, 2015) (Figures 2-3 and 2-5) with a trend of NW–SE and many small folds (syncline and anticlines). Because of the collision of the Arabian and Eurasian plates, Iraq is now tectonically divided into the western desert, Mesopotamian (unfolded), low-folded, high- folded, imbricated, and thrust zones from southwest to

northwest (Kamal Haji Karim Ahmad, 2015). The stratigraphic column of the Zagros foreland basin is shown in Figure 2-6. Although the dominant lithological unit in this study is carbonate, there are significant shale, marl, and halite formations. There are several oil and gas reservoirs in carbonates, and limestone is the most abundant rock type among the carbonate rocks in this well. However, there are also traces of thin shale and marl layers along the carbonate rocks.

Table 2-1. Previous tectonic studies in the nearby Kurdistan region of Iraq. After Mafakheri B. et al. (2024).

Author	Approach	Content	Year	Area
Vernant et al.	GPS	Present-day crustal deformation and plate kinematics in the Middle East constrained by GPS measurements	2004	Iran and northern Oman
Reif et al.	Remote Sensing (Dems)	mapping and measuring the spatial orientation of finite planar geologic structure from digital elevation models	2011	Northeast of Erbil Kurdistan Region of Iraq
Kamal haji karim	Review Surface and Underground Geology	Basic Principles Description of stratigraphy, tectonics and boundary conditions of Rock units in Kurdistan region of Iraq	2011	Northern Iraq
Al-Qayim et al.	Tectonostratigraphic	Tectonostratigraphic overview of the Zagros Suture Zone, Kurdistan Region of Iraq	2012	Zagros Suture Zone, Kurdistan Region of Iraq
Awdal et al.	Oil Well Field Data Analysis	characterization of fracture networks using a combination of core, log, flowmeter, and surface observation by scanlines on bedding surfaces in the limbs and hinge of the anticlines.	2013	Taq Taq Field, Zagros, Kurdistan region of Iraq
Ali et al.	Tectonostratigraphic	Tectonic evolution of a Neo-Tethyan (Eocene-Oligocene) island-arc (Walsh and Naopurdan groups)	2014	Northwestern Zagros collision, Iran Iraq border
Abdulnaby et al.	Earthquake Focal Mechanism	Estimation of the principal stress orientations in Northern Iraq and Surrounding Regions by inversion of focal mechanism solutions.	2014	Thrust Zone of the Arabian Plate Northern Iraq
Awdal et al.	Fracture Patterns Characterization	Study the fracture patterns and petrophysical properties of carbonates undergoing regional folding	2016	Northern Iraq
Obaid and Allen	Digital Elevation Models (Dems) And Satellite Images	Combining landscape maturity analysis, fold growth sequence, and structural style to understand anticline growth in the Kirkuk Embayment of the Zagros	2017	Southwest of the Zagros fold-and-thrust belt, Kirkuk, Iraq
Kobayashi et al.	InSAR-Derived Crustal Deformation and Reverse Fault Motion	Applying an interferometric InSAR analysis using ALOS-2 SAR data and InSAR-derived Crustal Deformation and Reverse Fault Motion of the 2017 Earthquake (Iraq)	2018	Northwestern Part of the Zagros Orogenic Belt
Afra et al.	Earthquake Focal Mechanism	Deduce the stress regimes in northwestern Iran and surrounding regions from stress inversion of earthquake focal mechanisms	2017	Northwest Iran
Doski	Earthquake Focal Mechanism	Tectonic interpretation of the 2017 Raniya earthquake and determining the present-day stress field by inversion of the fault plane solution.	2019	Raniya, Northeast Iraq
Gilchrist et al.	Wireline Log, Image Log, and Leak of Test	Analysis of critically stressed fractures using oil field data and determining stress-field orientations.	2020	Sheikhan Field, Kurdistan Region of Iraq
Doski	Seismogenic Fault Analysis	Analyzing seismic activity caused by the Quaternary reactivation of a seismogenic blind basement fault in the Sheladiz area	2021	Sheladiz Northeast Iraq

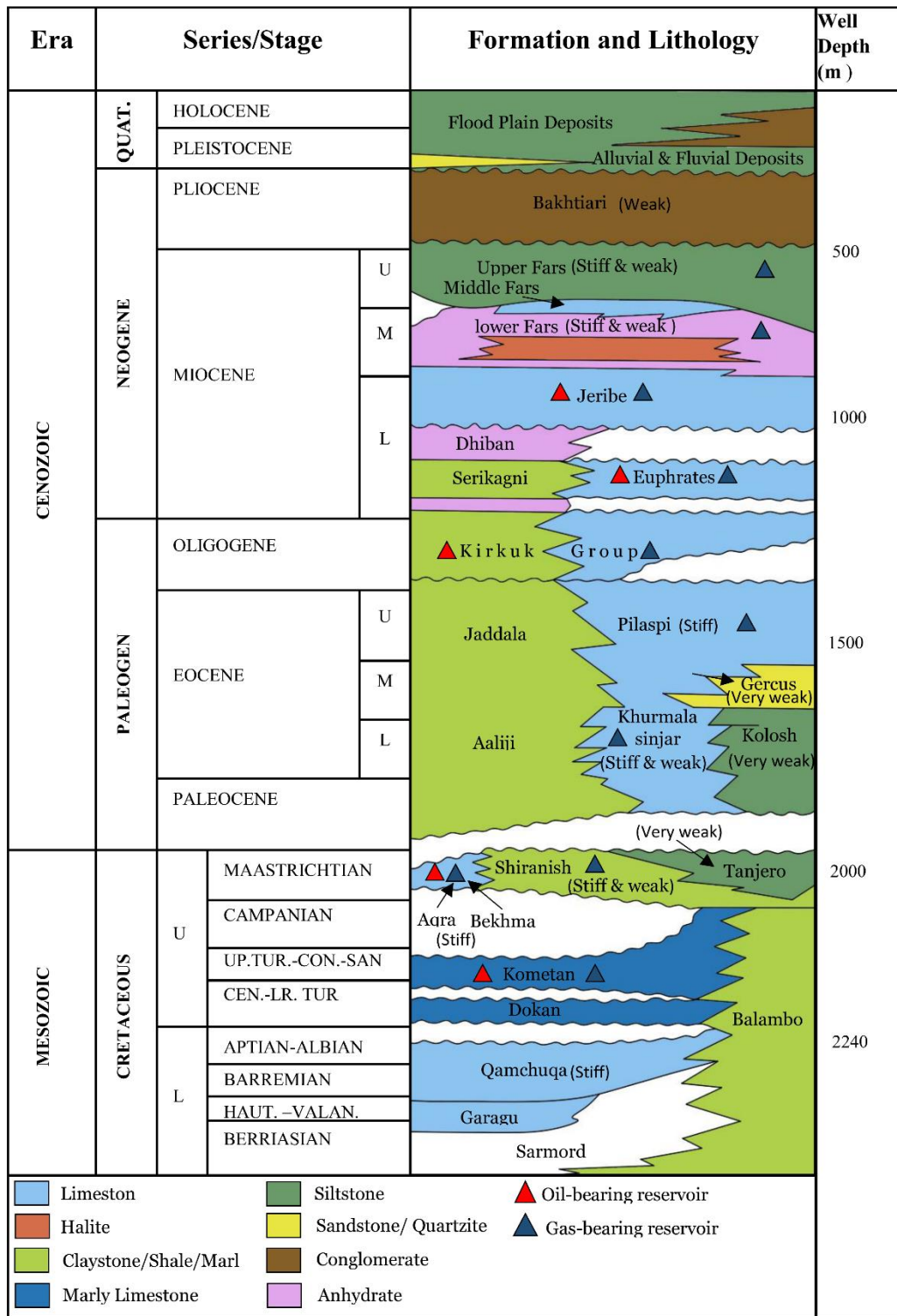


Figure 2-6. Stratigraphic column and oil and gas reservoir and drilled well depths. Modified from English (2015) and after Mafakheri B. et al. (2022).

2.3 Southeastern part of Zagros suture zone

In terms of tectonics, the study area is located in the Zagros fold-and-thrust belt (ZFTB), which is the result of the consequence of the oblique continental collision between the Eurasian and Arabian plates initiated at the Eocene (35 Ma) as the rifted Arabian lithosphere was under thrust beneath the Eurasian (Iranian) plate (Figure 2-7). The majority of collisions occurred in the Late Miocene and have continued until now (Agard et al., 2011b; Karimnejad Lalami et al., 2020; Khadivi, 2010; Lai et al., 2022; Mouthereau et al., 2012). The deformation is due to the relative convergence between Arabia and Eurasia's tectonic plates (Agard et al., 2005; Takin, 1972). The ZFTB is trending NW-SE (Figure 2-7, 2-8), is a part of the Alpine-Himalayan Mountain chain and extends for about 2000 km from the Taurus Mountains in Turkey, through northern Iraq and SW Iran, to the Strait of Hormuz (Figure 2-7, 2-8) (Alavi, 2007, 2004; Al-Qayim et al., 2012).

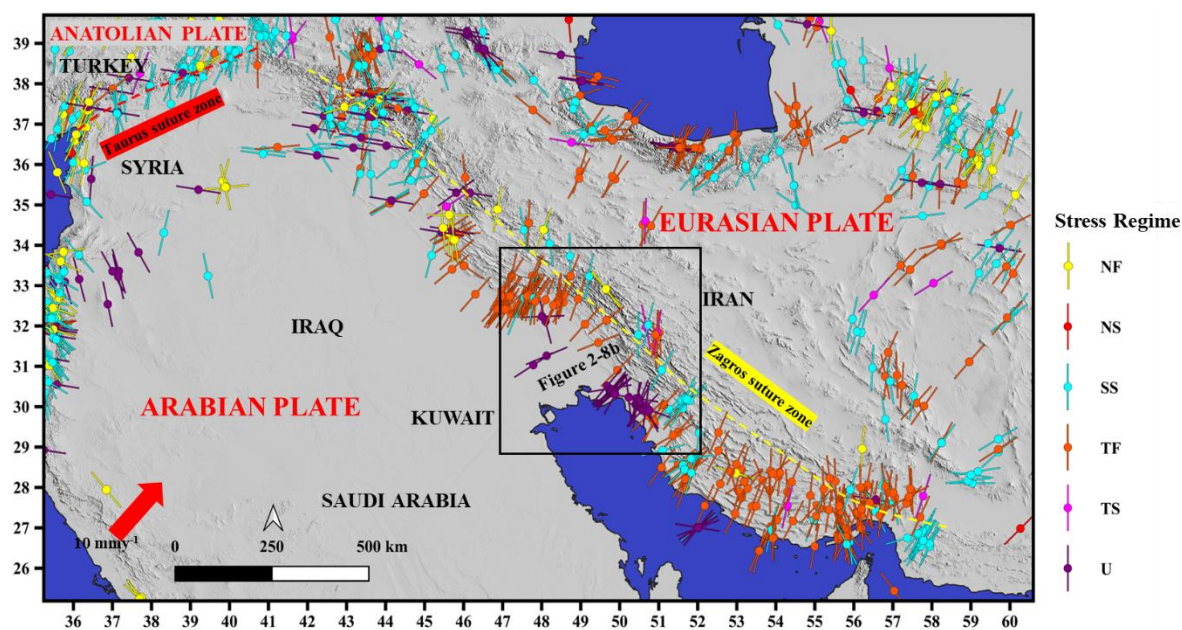


Figure 2-7. World stress map database in the middle east plotted on a digital elevation map (Heidbach et al., 2018). The black box shows the area of interest presented in Figure 2-8b. Colorful lines show the orientation of maximum horizontal stress in the region based on world stress map data. Different colors represent different stress regimes. The red arrow shows the estimated Arabian tectonic plate movement toward the Eurasian plate. The subduction indicates the Arabian plate moving beneath the Eurasian plate. After Mafakheri B. et al. (2024).

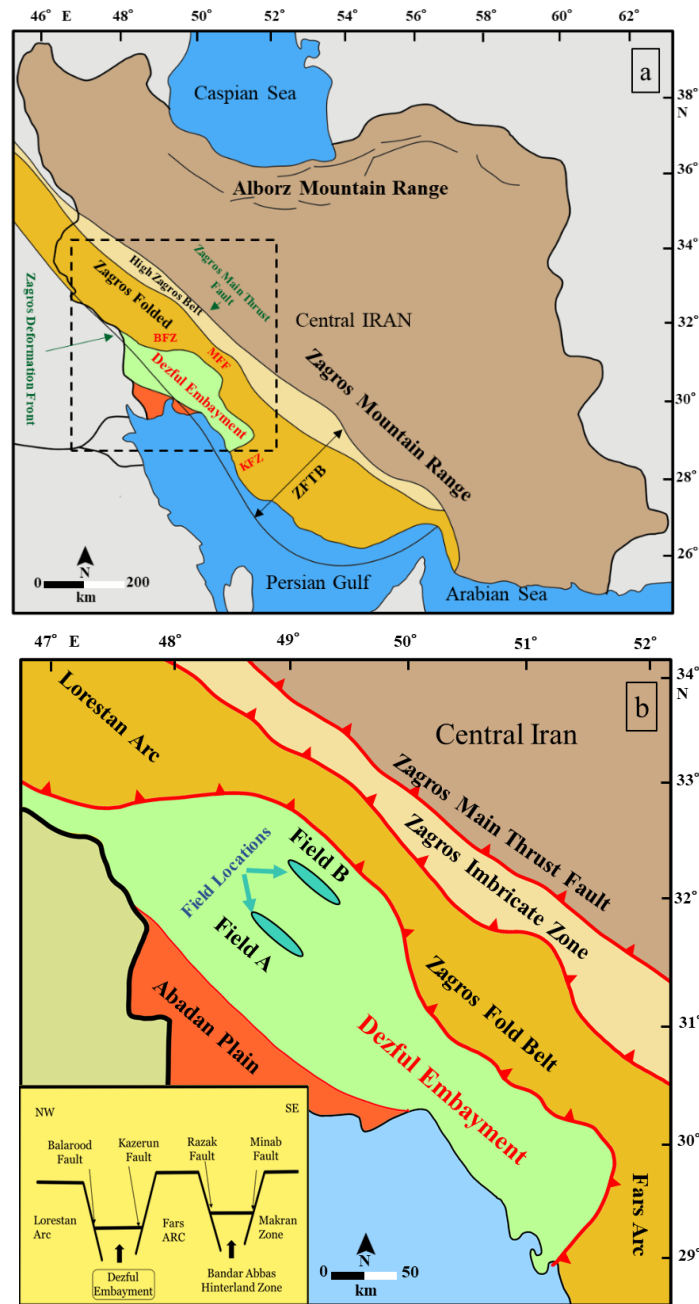


Figure 2-8. Field location and main tectonic and structural features related to the Dezful Embayment. Between the Zagros main thrust fault and Zagros deformation front is ZFTB. The study area is separated from the Lurestan and Fars arc by Balarood and Kazerun Faults, modified after Karimi et al. (2016). b) Main tectonic units of Iran, including Dezful Embayment, Zagros folded zone, high Zagros belt and the central block of Iran. The dashed line black box shows the area in Figure 2-8b. Modified from Ghasemi and Talbot (2006) and after Mafakheri B. et al. (2024).

The thrust system develops in a NE-dipping (foreland dipping), SW-dipping (hinterland dipping), or organized NW-trending configuration with SW displacements. The thrust system consists of physically, geometrically, and kinematically related faults formed sequentially during regional deformation and connected to thin-skinned deformation above a basal décollement horizon (Boyer and Elliott, 1982). The ZFTB is subdivided into two main zones: the high Zagros (imbricated zone) to the north and the ZFTB to the South. The main orogeny of foredeep basins in Zagros has occurred in Kirkuk and Dezful Embayment (Abdollahie Fard et al., 2011; Berberian and King, 1981). The depression of the foredeep started after the deposition of the lower part of the Asmari Formation, which is the target formation in this paper (Sherkati et al., 2006), and eventually extended to the southwest, near the Persian Gulf (Figure 2-9) (Abdollahie Fard et al., 2011). The ZFTB in Iran has been divided laterally into the Lurestan Arc, Dezful Embayment, and Fars Arc from the northwest to southeast (Figure 2-8). The Dezful Embayment is a 60,000 km² area situated between Lurestan Arc and Fars Arc in the southwest of the Zagros main thrust fault (ZMTF) (Figure 2-8) (Allen et al., 2004) and it is bounded by the Balarood fault zone (BFZ) to the north, the Kazerun fault zone (KFZ) to the South, and the Mountain Front Fault (MFF) to the East (Alavi, 1994; Berberian and King, 1981; Karimi et al., 2016; Mouthereau et al., 2012).

In the folding process, the carbonates of the Asmari, Khami, and Bangestan formations formed the main hydrocarbon reservoirs of the study area (Figure 2-10) (Abdollahie Fard et al., 2006; Derikvand et al., 2018). Along the Lower Cambrian Hormuz Salt Formation and Paleozoic strata, the sedimentary cover of the ZFTB is most likely decoupled from its underlying basement (Kent, 1979). The Early Miocene (Gachsaran Formation) evaporite sequence in the cover plays a crucial role in the deformation of the cover (Figure 2-10) (Bird et al., 1975; Snyder and Barazangi, 1986). These faults governed the tecto-sedimentary evolution of this embayment during the Cenozoic. (Abdollahie Fard et al., 2006; Derikvand et al., 2019).

Comparing the Dezful Embayment to the nearby zones reveals significant geological and morphological variations. The MFF separates the Dezful Embayment from the Izeh zone (Figures 2-8 and 2-10). On the other hand, the Dezful Embayment was divided into the NE, SW, and Izeh zones based on geological characteristics. One of the study fields is located in the NE sector, and another is in the SW sector (Figures

2-9 and 2-10) (Derikvand et al., 2018). In both sectors where the study area is situated, the anticlines display slightly asymmetric geometry, suggesting that the southern flanks or both flanks were affected by thrust faults (Figures 2-9, 2-11 and 2-12). Most surface thrust faults in the NE sector are anchored deep inside the Gachsaran evaporites, but in the SW sector, most of them are blind thrust faults. Regarding the structure, the NE sector is more complex than the SW sector.

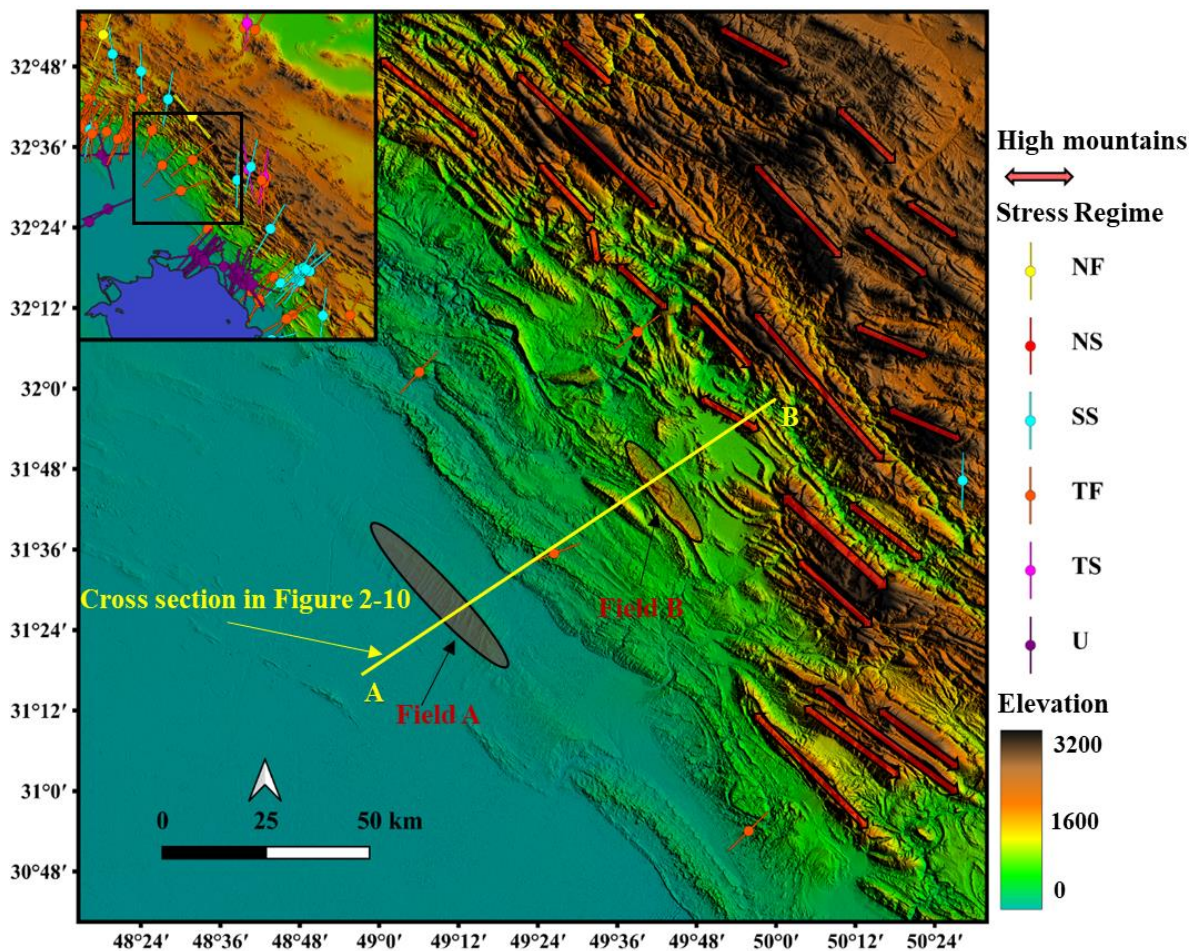


Figure 2-9. Study areas, including Fields A and B, are plotted on a digital elevation map. Red double-sided arrows show the high mountain string in the area, which is associated with the folding process of ZFTB. Colourful lines in the inset represent the orientation of maximum horizontal stress in the area based on the world stress map database (Data from Heidbach et al., 2018). Taken from Mafakheri B. et al. (2024).

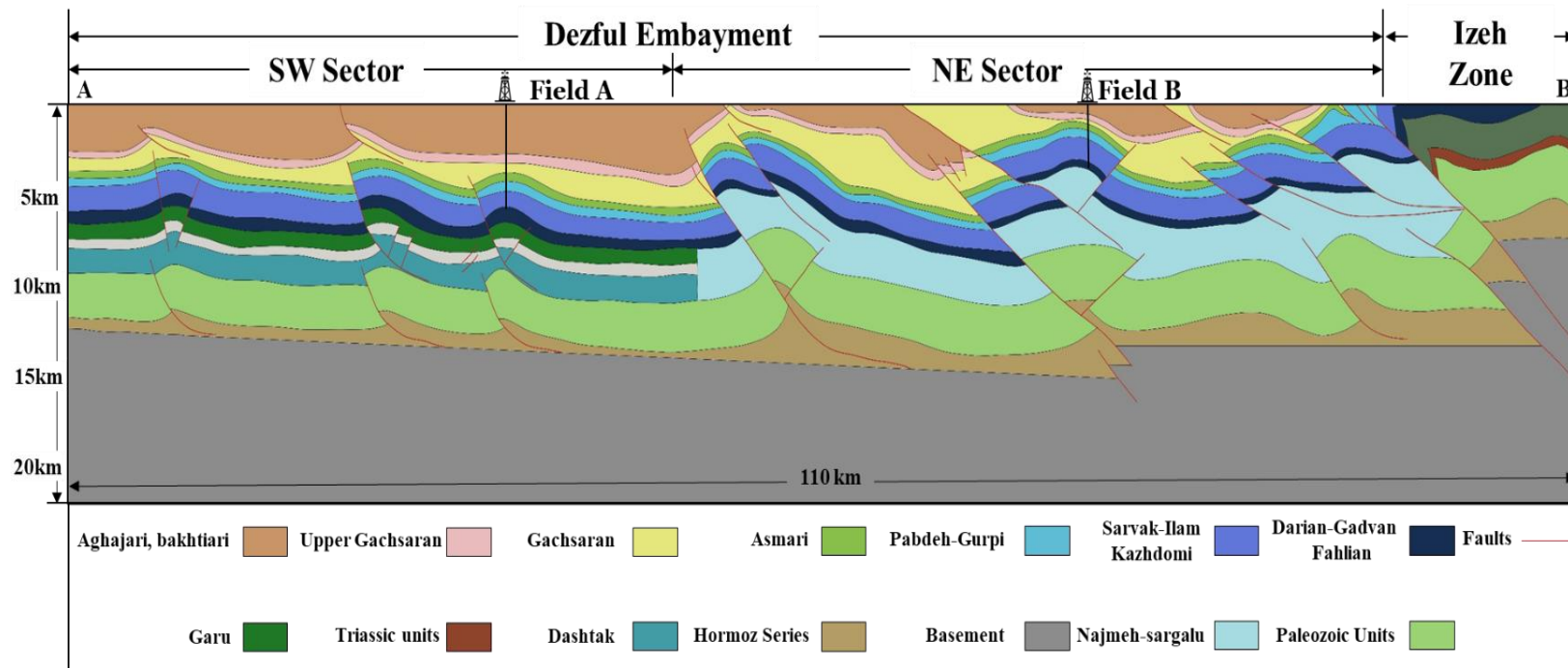


Figure 2-10. Structural cross-section of the Dezful Embayment for A-B line shown in Figure 2-9. Field A is located in the SW sector of Dezful Embayment, and Field B on the NE sector. The MFF separates the Dezful Embayment and Izeh zone. In both sectors, the anticlines display slightly asymmetric to asymmetric geometry that the southern flanks or both flanks were affected by thrust faults. Modified from Derikvand et al (2018) and taken from Mafakheri B. et al. (2024)

On the other hand, the thin-skinned tectonic regime is prevalent in the SW sector, where the synclines are wider, and the anticlines are comparatively more elongated than in the NE sector (Figure 2-10) (Derikvand et al., 2018). The sedimentary succession of the ZFTB is divided into four groups by Alavi (1994). The first group is the Proterozoic to the Early Cambrian evaporites of the Hormuz Series. These evaporites are covered by epicontinental sediments from the Cambrian through the Early Permian, including sandstones, carbonates, shales, and evaporites (Figure 2-10) (Alavi, 1994; Vergés et al., 2011). The high mobility of the evaporitic members of Gachsaran led to the development of disharmonic folding from surface to depth so that these units decoupled from larger subsurface folds. As a result, the salt and marl of the Gachsaran Formation formed a strong detachment horizon (Abdollahie Fard et al., 2011; Khodabakhshnezhad et al., 2016).

Technically, both fields are in the Zagros low-folded belt. The anticline axis shows torsion to the north at the two ends. The northern limb is slightly steeper than the southern limb, and no major fault has been detected in the image logs of the Asmari Formation in all the wells. Due to the complexity of the area, two oil fields in the southeastern and northeastern parts of the Dezful Embayment have been studied (Figures 2-9 and 2-10). The basement along the Infra-Cambrian Hormuz salt décollement horizon and four other shallower décollement horizons are detached from the Zagros thin-skinned tectonics. This part includes 7–12 km of thick-sedimentary sequences (Sarkarinejad and Goftari, 2019). Kinematic evolution during simultaneous folding and thrusting is due to several décollement horizons of the sedimentary cover sequence from the basement, a controlling factor contributing to the structural styles of folding and thrusting (Sarkarinejad et al., 2021). Several tectonic and geomechanical studies in the Zagros suture zone near the study area have been presented in Table 2-2.

The stratigraphy of the Dezful Embayment is characterized by a thick sequence of sedimentary rocks, ranging from the Early Cambrian to the recent Quaternary (Nabavi, 2016). The Embayment hosts a variety of sedimentary rock formations that have been subjected to tectonic processes throughout geological time. These formations can be broadly divided into several key formations. In this study, as shown in Figures 2-10, 2-11, and 2-12, the Bakhtiari Formation primarily comprises of eroded conglomerates, sandstones, and shales from the Late Cretaceous to the Early Miocene.

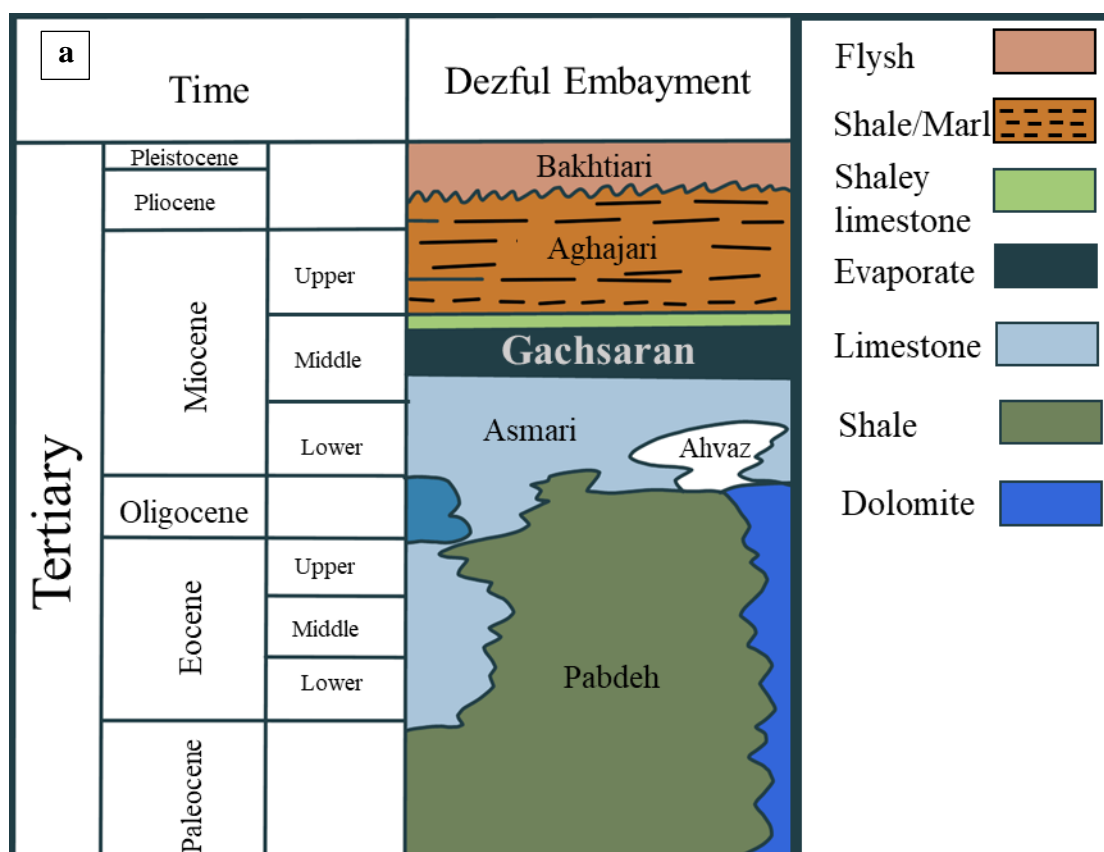


Figure 2-11. a) The stratigraphic column of the Dezful Embayment shows lateral lithology changes from NW-SE. After Albooyeh et al. (2018) and Mafakheri B. et al. (2024).

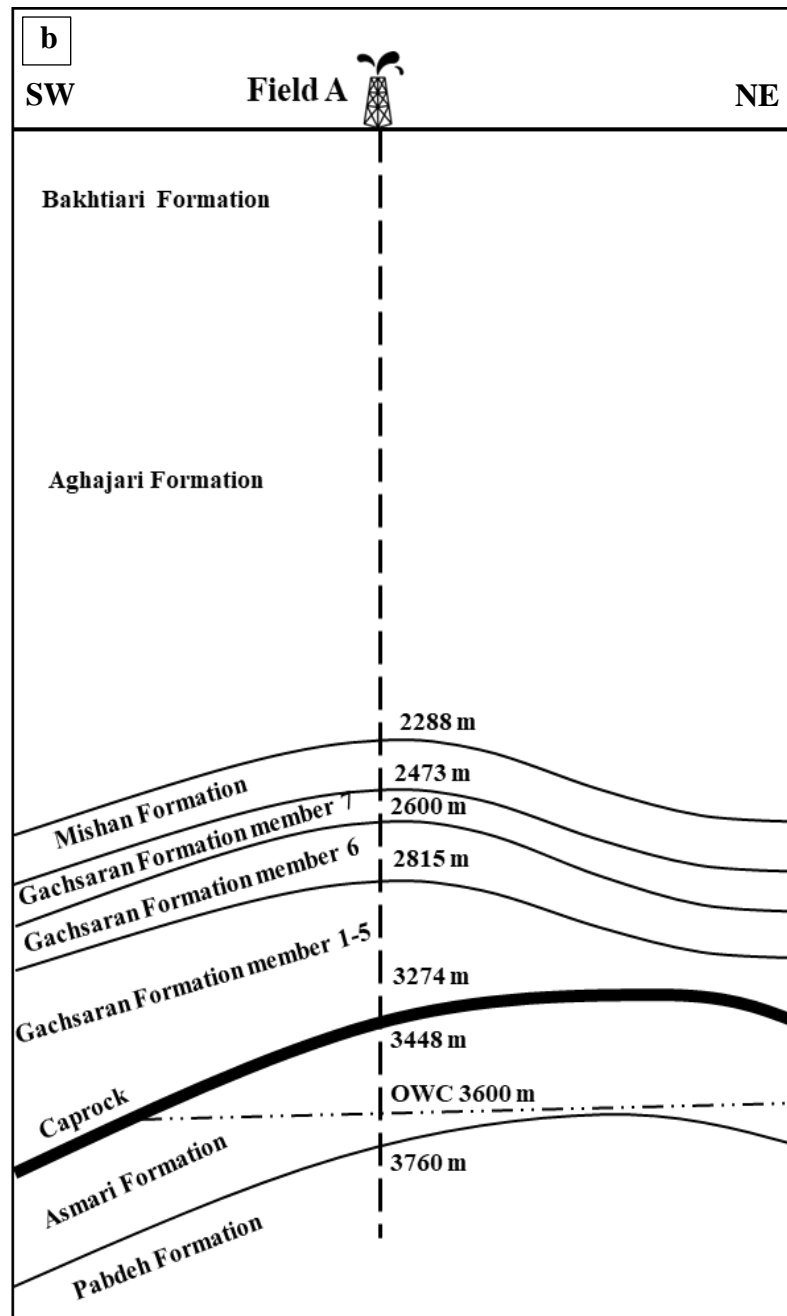


Figure 2-11. Continued. b) Shows the schematic lithological column and top formations of Well A5 from Field A. Well A5 penetrates Asmari Formation at 3348 m, and oil water contact (OWC) is at a depth of 3600 m. After Mafakheri B. et al. (2024)

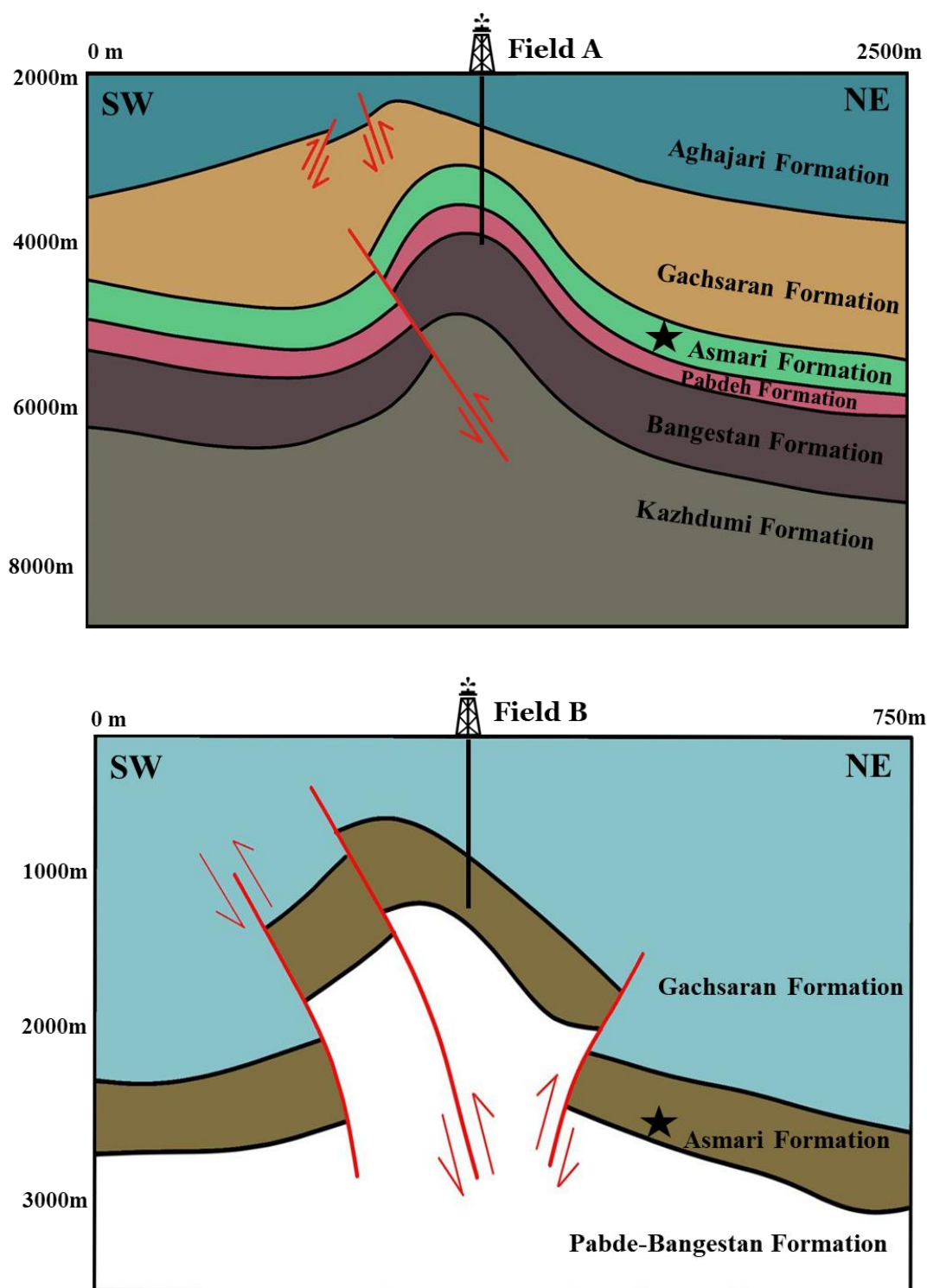


Figure 2-12. Schematic seismic profile of Fields A and B. Several thrust faults are detected in both cases. Red lines are faults and black stars show the target formation. After Mafakheri B. et al. (2024).

Then there is the Aghajari Formation, which exists in the Zagros Mountains' foothills and consists of shales, marl, and siltstones, with deposits dating back to the Oligocene and Miocene. Next, the lithology of the Mishan Formation primarily consists of marine marls with some thin limestone intercalations and shales from the Late Eocene to the Early Oligocene. Below this Formation, the Gachsaran Formation comprises evaporites from the Miocene, including anhydrite, gypsum, halite, marls, and shales. In the Dezful Embayment, the fractured Asmari reservoirs are covered by the Gachsaran evaporites (Figures 2-10, 2-11, and 2-12). The Oligo-Early Miocene Asmari Formation, which is situated in the depths between 3348–3760 m (true vertical depth) in Field (A) and 1020–1210 m (true vertical depth) in Field (B), is the main oil reservoir formation, followed by the Cenomanian limestones of the Pabdeh-Bangestan Formation (Figures 2-10, 2-11, and 2-12) (Bordenave and Hegre, 2005; Mouthereau et al., 2012).

According to Honarmand and Amini (2012), due to variations in depositional conditions and environments, the reservoir quality of the limestones of the Asmari Formation varies significantly, as shown in Table 2-3 for this study. Most of the Eocene-Oligocene Pabdeh Formation is thin-bedded deep-marine pelagic calcareous shale, marl, and limestone abundant in pelagic microfauna (Alavi, 2004; Karimi et al., 2016). Below the Asmari, the Pabdeh Formation is predominantly composed of marl, shales, and limestone, with deposits dating back to the Paleocene and Eocene epochs.

Table 2-2. Previous tectonic studies in the nearby area of Dezful Embayment. After Mafakheri B. et al. (2024).

Author	Approach	Content	Year	Area
Yaghoubi and Zeinali	Borehole image logs	Determination of magnitude and orientation of the in-situ stress from borehole breakout and borehole stability	2009	Cheshmeh Khush-Iran
Sanaee et al.	conventional logs	Stress profile in a deep borehole in a naturally fractured reservoir	2010	Southwestern Iran
Haghi et al.	Borehole image logs	Present-day stress of the central Persian Gulf: Implications for drilling and well performance	2013	Central Persian gulf
Elyasi et al.,	Borehole image logs	Stress determination and geomechanical stability analysis by numerical modelling	2014	Southwestern Iran
Molaghab et al.	Borehole image and conventional logs	Determination of minimum and maximum stress profile	2017	Southwestern Iran
Mousavi	earthquake focal mechanisms	Spatial variation in the frequency-magnitude distribution of earthquakes under the tectonic framework	2017	Middle east
Haghi et al.	Borehole image and conventional logs	State of stress and implications for hydraulic fracturing of naturally fractured carbonate reservoir	2018	Southwestern Iran
Abdideh and Alisamir	Borehole image and conventional logs	Deep stress Field using well log and wellbore breakout in cretaceous oil reservoir, southwest iran	2018	Southwestern Iran
Ranjbar-Karami et al.	Borehole image logs	Contemporary tectonic stress pattern of the Persian Gulf Basin	2019	Central Persian gulf
Yousefi et al.	Borehole image logs	Fracture systems development using image logs at Asmari Formation	2019	Rag Sefid- Iran
Jalili et al.	Borehole image logs	Fracture characteristics and borehole instability in the Asmari reservoir of Zagros folded belt zone	2020	Kuh-e-Kamarab, Marun and Aghajari
Mousavipour et al.	Conventional logs	In situ stresses, mud window, and overpressure zone in the South Pars Field	2020	South Pars-persian gulf
Yaghoubi et al.	Conventional logs and EFM	Seismicity and the State of Stress in the Dezful Embayment	2021	Dezful Embayment- Iran
Taghipour et al.	Borehole image and conventional logs	Geomechanical Evaluation of Fault Reactivation Using Analytical Methods	2021	Southwestern Iran
Abdideh and Dastyaft	Laboratory data and conventional well logs	Stress Field analysis and its effect on the selection of optimal well trajectory in directional drilling	2022	Southwestern Iran
Mafakheri et al.	Borehole image and conventional logs	Present-day in-situ stresses in the Kurdistan region of Iraq	2022	Kurdistan Region of Iraq

Table 2-3. Lithology and reservoir data, including porosity and water saturation for well A5 from Field A. After Mafakheri B. et al. (2024).

Zone	TVD (m)	Lithology	Total porosity (%)	Average Porosity (%)	Average water Saturation (%)
Zone 1	3348 – 3405	Calcareous dolomite	3 – 25	12.2	28.8
Zone 2	3405 – 3443	dolomitic limestone with a sand stringer	2 – 24	10.2	28.5
Zone 3	3443 – 3490	dolomitic limestone	1 – 20	12.5	28.6
Zone 4	3490 – 3529	dolomitic limestone with a little sand	2 – 19	12.7	22.3
Zone 5-1	3529 – 3557.5	dolomitic limestone	2 – 18	11.6	26.3
Zone 5-2	3557.5 – 3584	dolomitic limestone	2 – 16	12.4	36.4
Zone 6	3584 – 3760	shaly sand with clean sand stringers	2 – 18	10.8	49.8

References

- Abdideh, M., Alisamir, S., 2018. Analysis of deep stress field using well log and wellbore breakout data: A case study in cretaceous oil reservoir, southwest Iran. *Geodesy and Cartography* **44**, 113–128. <https://doi.org/10.3846/gac.2018.4152>
- Abdideh, M., Dastyaft, F., 2022. Stress field analysis and its effect on selection of optimal well trajectory in directional drilling (case study: southwest of Iran). *J Pet Explor Prod Technol* **12**, 835–849. <https://doi.org/10.1007/s13202-021-01337-5>
- Abdollahie Fard, I., Braathen, A., Mokhtari, M., Alavi, S.A., 2006. Interaction of the Zagros Fold–Thrust Belt and the Arabian-type, deep-seated folds in the Abadan Plain and the Dezful Embayment, SW Iran. *Petroleum Geoscience* **12**, 347–362. <https://doi.org/10.1144/1354-079305-706>
- Abdollahie fard, I., Sepehr, M., Sherkati, S., 2011. Neogene salt in SW Iran and its interaction with Zagros folding. *Geol Mag* **148**, 854–867. <https://doi.org/10.1017/S0016756811000343>
- Abdulnaby, W., 2019. Structural Geology and Neotectonics of Iraq, Northwest Zagros. *Development in structural geology and tectonics* **3**, 53–73. <https://doi.org/10.1016/b978-0-12-815048-1.00004-4>
- Abdulnaby, W., Mahdi, H., Al-Shukri, H., Numan, N.M.S., 2014. Stress Patterns in Northern Iraq and Surrounding Regions from Formal Stress Inversion of Earthquake Focal Mechanism Solutions. *Pure Appl Geophys* **171**, 2137–2153. <https://doi.org/10.1007/s00024-014-0823-x>
- Afra, M., Moradi, A., Pakzad, M., 2017. Stress regimes in the northwest of Iran from stress inversion of earthquake focal mechanisms. *J Geodyn* **111**, 50–60. <https://doi.org/10.1016/j.jog.2017.08.003>
- Agard, P., Omrani, J., Jolivet, L., Mouthereau, F., 2005. Convergence history across Zagros (Iran): Constraints from collisional and earlier deformation. *International Journal of Earth Sciences* **94**, 401–419. <https://doi.org/10.1007/s00531-005-0481-4>
- Agard, P., Omrani, J., Jolivet, L., Whitechurch, H., Vrielynck, B., Spakman, W., Monié, P., Meyer, B., Wortel, R., 2011a. Zagros orogeny: A subduction-dominated process. *Geol Mag* **148**, 692–725. <https://doi.org/10.1017/S001675681100046X>

- Agard, P., Omrani, J., Jolivet, L., Whitechurch, H., Vrielynck, B., Spakman, W., Monié, P., Meyer, B., Wortel, R., 2011b. Zagros orogeny: A subduction-dominated process. *Geol Mag* **148**, 692–725. <https://doi.org/10.1017/S001675681100046X>
- Alavi, M., 2007. Structures of the Zagros fold-thrust belt in Iran. *Am J Sci* **307**, 1064–1095. <https://doi.org/10.2475/09.2007.02>
- Alavi, M., 2004. Regional stratigraphy of the Zagros fold-thrust belt of Iran and its proforeland evolution. *Am J Sci* **304**, 1–20. <https://doi.org/10.2475/ajs.304.1.1>
- Alavi, M., 1994. Tectonics of the zagros orogenic belt of iran: new data and interpretations. *Tectonophysics* **229**, 211–238. [https://doi.org/10.1016/0040-1951\(94\)90030-2](https://doi.org/10.1016/0040-1951(94)90030-2)
- Albooyeh, M., Rahimzadeh, I., Ameri, M., 2018. Promoting wellbore stability in active shale formations by water-based muds: A case study in Pabdeh shale , Southwestern Iran. *J Nat Gas Sci Eng* **56**, 166–174. <https://doi.org/10.1016/j.jngse.2018.05.040>
- Ali, S.A., Buckman, S., Aswad, K.J., Jones, B.G., Ismail, S.A., Nutman, A.P., 2013. The tectonic evolution of a Neo-Tethyan (Eocene-Oligocene) island-arc (Walash and Naopurdan groups) in the Kurdistan region of the Northeast Iraqi Zagros Suture Zone. *Island Arc* **22**, 104–125. <https://doi.org/10.1111/iar.12007>
- Ali, S.A., Mohajjel, M., Aswad, K., Ismail, S., Buckman, S., 2014. Tectono-stratigraphy and structure of the northwestern Zagros collision zone across the Iraq-Iran border. First *EAGE* Workshop on Iraq - Hydrocarbon Exploration and Field Development. <https://doi.org/10.3997/2214-4609.20143580>
- Ali, S.A., Nutman, A.P., Aswad, K.J., Jones, B.G., 2019. Overview of the tectonic evolution of the Iraqi Zagros thrust zone: Sixty million years of Neotethyan ocean subduction. *J Geodyn* **129**, 162–177. <https://doi.org/10.1016/j.jog.2019.03.007>
- Allen, M., Jackson, J., Walker, R., 2004. Late Cenozoic reorganization of the Arabia-Eurasia collision and the comparison of short-term and long-term deformation rates. *Tectonics* **23**. <https://doi.org/10.1029/2003TC001530>
- Al-Qayim, B., Omer, A., Koyi, H., 2012. Tectonostratigraphic overview of the Zagros Suture Zone, Kurdistan Region, Northeast Iraq. *GeoArabia* **17**, 109–156. <https://doi.org/10.2113/geoarabia1704109>

- Awdal, A., Healy, D., Alsop, G.I., 2016. Fracture patterns and petrophysical properties of carbonates undergoing regional folding: A case study from Kurdistan, N Iraq. *Mar Pet Geol* **71**, 149–167. <https://doi.org/10.1016/j.marpetgeo.2015.12.017>
- Awdal, A.H., Braathen, A., Wennberg, O.P., Sherwani, G.H., 2013. The characteristics of fracture networks in the Shiranish formation of the Bina Bawi Anticline; comparison with the Taq Taq Field, Zagros, Kurdistan, NE Iraq. *Petroleum Geoscience* **19**, 139–155. <https://doi.org/10.1144/petgeo2012-036>
- English, J.M., Lunn, C.A., Ferreira, L., Yacu, G., 2015. Geologic evolution of the Iraqi Zagros, and its influence on the distribution of hydrocarbons in the Kurdistan region. *Am Assoc Pet Geol Bull* **99**, 231–272. <https://doi.org/10.1306/06271413205>
- Berberian, M., King, G.C.P., 1981. Towards a paleogeography and tectonic evolution of Iran. *Can J Earth Sci* **18**, 210–265. <https://doi.org/10.1139/e81-019>
- Bird, P., Toksöz, M.N., Sleep, N.H., 1975. Thermal and mechanical models of continent-continent convergence zones. *Journal of Geophysical Research* **80**, 4405–4416. <https://doi.org/10.1029/JB080i032p04405>
- Bordenave, M.L., Hegre, J.A., 2005. The Influence of Tectonics on The Entrapment of Oil in the Dezful Embayment, Zagros Foldbelt, Iran. *Journal of Petroleum Geology* **28**, 339–368. <https://doi.org/10.1111/j.1747-5457.2005.tb00087.x>
- Boyer, S.E., Elliott, D., 1982. Thrust Systems. *Am Assoc Pet Geol Bull* **66**, 1196–1230. <https://doi.org/10.1306/03B5A77D-16D1-11D7-8645000102C1865D>
- de Vera, J., Ginés, J., Oehlers, M., McClay, K.R., Doski, J.A.H., 2009. Structure of the Zagro fold and thrust belt in the Kurdistan region, northern Iraq. *Trabajos de Geologia* **29**, 213–217. <https://geol00.geol.uniovi.es/TDG/Volumen29/TG29-39.PDF>
- Derikvand, B., Alavi, S.A., Fard, I.A., Hajialibeigi, H., 2018. Folding style of the Dezful Embayment of Zagros Belt: Signatures of detachment horizons, deep-rooted faulting and syn-deformation deposition. *Mar Pet Geol* **91**, 501–518. <https://doi.org/10.1016/j.marpetgeo.2018.01.030>
- Derikvand, B., Alavi, S.A., Fard, I.A., Jalali, L., 2019. Changing in fold geometry from faulted detachment fold to fault-bend fold, a case study: The Zeloi Anticline in the

- Dezful Embayment, southwest of Iran. *J Pet Sci Eng* **173**, 381–401. <https://doi.org/10.1016/j.petrol.2018.10.033>
- Doski, J.A.H., 2021. Active tectonics along the Sheladiz seismogenic fault in the Western Zagros fold-thrust belt, Kurdistan, Northern Iraq. *International Journal of Earth Sciences* **110**, 595–608. <https://doi.org/10.1007/s00531-020-01973-y>
- Doski, J.A.H., 2019. Tectonic interpretation of the Raniya earthquake, Kurdistan, northern Iraq. *J Seismol* **23**, 303–318. <https://doi.org/10.1007/s10950-018-9807-0>
- Elyasi, A., Goshtasbi, K., Saeidi, O., Torabi, S.R., 2014. Stress determination and geomechanical stability analysis of an oil well of Iran. *Sadhana - Academy Proceedings in Engineering Sciences* **39**, 207–220. <https://doi.org/10.1007/S12046-013-0224-3/FIGURES/7>
- Falcon, N.L., 1974. Southern Iran: Zagros Mountains. In: Spencer, A., Ed., Mesozoic-Cenozoic Orogenic Belts, Data for Orogenic Studies: Alpine-Himalayan Orogens. *Geological Society Special Pu*, 199–211.
- Ghasemi, A., Talbot, C.J., 2006. A new tectonic scenario for the Sanandaj–Sirjan Zone (Iran). *J Asian Earth Sci* **26**, 683–693. <https://doi.org/10.1016/J.JSEAES.2005.01.003>
- Gilchrist, C.J.D., Cosgrove, J.W., Parmassar, K.J., 2020. Critically stressed fractures: analysis of the Shaikan Field, Kurdistan Region of Iraq. *J Geol Soc London* **177**, 1315–1328. <https://doi.org/10.1144/jgs2019-136>
- Gombert, B., Duputel, Z., Shabani, E., Rivera, L., Jolivet, R., Hollingsworth, J., 2019. Impulsive Source of the 2017 MW=7.3 Ezgeleh, Iran, Earthquake. *Geophys Res Lett* **46**, 5207–5216. <https://doi.org/10.1029/2018GL081794>
- Haghi, A.H., Chalaturnyk, R., Ghobadi, H., 2018. The state of stress in SW Iran and implications for hydraulic fracturing of a naturally fractured carbonate reservoir. *International Journal of Rock Mechanics and Mining Sciences* **105**, 28–43. <https://doi.org/10.1016/j.ijrmms.2018.03.002>
- Haghi, A.H., Kharrat, R., Asef, M.R., Rezazadegan, H., 2013. Present-day stress of the central Persian Gulf: Implications for drilling and well performance. *Tectonophysics* **608**, 1429–1441. <https://doi.org/10.1016/j.tecto.2013.06.001>
- Heidbach, O., Rajabi, M., Cui, X., Fuchs, K., Müller, B., Reinecker, J., Reiter, K., Tingay, M., Wenzel, F., Xie, F., Ziegler, M.O., Zoback, Mary Lou, Zoback, Mark,

2018. The World Stress Map database release 2016: Crustal stress pattern across scales. *Tectonophysics* **744**, 484–498. <https://doi.org/10.1016/j.tecto.2018.07.007>
- Honarmand, J., Amini, A., 2012. Diagenetic processes and reservoir properties in the ooid grainstones of the Asmari Formation, Cheshmeh Khush Oil Field, SW Iran. *J Pet Sci Eng* **81**, 70–79. <https://doi.org/10.1016/j.petrol.2011.12.022>
- Jalili, Y., Yassaghi, A., Khatib, M.M., Golalzadeh, A., 2020. Effect of transverse faults on fracture characteristics and borehole instability in the Asmari reservoir of Zagros folded belt zone, Iran. *J Pet Sci Eng* **188**, 106820. <https://doi.org/10.1016/j.petrol.2019.106820>
- Jassim, S.Z., and Goff, J.C., 2006. Geology of Iraq. Brno Museum, Czech Republic, Dolin, Prague and Moravian Museum. https://books.google.co.jp/books/about/Geology_of_Iraq.html?id=LLH8aygMJFwC&redir_esc=y
- Kamal Haji Karim Ahmad, 2015. Geology of Iraq : Basic Principles Description of. <https://doi.org/10.13140/2.1.3052.6245>
- Karabulut, H., Güvercin, S.E., Hollingsworth, J., Konca, A.Ö., 2023. Long silence on the East Anatolian Fault Zone (Southern Turkey) ends with devastating double earthquakes (6 February 2023) over a seismic gap: implications for the seismic potential in the Eastern Mediterranean region. *J Geol Soc London* **180**. <https://doi.org/10.1144/JGS2023-021>
- Karimi, A.R., Rabbani, A.R., Kamali, M.R., 2016. A bulk kinetic, burial history and thermal modeling study of the Albian Kazhdumi and the Eocene-Oligocene Pabdeh formations in the Ahvaz anticline, Dezful Embayment, Iran. *J Pet Sci Eng* **146**, 61–70. <https://doi.org/10.1016/j.petrol.2016.04.015>
- Karimnejad Lalami, H.R., Hajjalibeigi, H., Sherkati, S., Adabi, M.H., 2020. Tectonic evolution of the Zagros foreland basin since Early Cretaceous, SW Iran: Regional tectonic implications from subsidence analysis. *J Asian Earth Sci* **204**, 104550. <https://doi.org/10.1016/j.jseaes.2020.104550>
- Kent, P.E., 1979. The Emergent Hormuz Salt Plugs of Southern Iran. *Journal of Petroleum Geology* **2**, 117–144. <https://doi.org/10.1111/j.1747-5457.1979.tb00698.x>

- Khadivi, S., 2010. Tectonic evolution and growth of the Zagros Mountain Belt (Fars, Iran): constraints from magnetostratigraphy, sedimentology and low- temperature thermochronometry. *PhD Thesis Pierre and Marie Curie University*.
- Khodabakhshnezhad, A., Arian, M., Khodabakhshnezhad, A., Arian, M., 2016. Salt Tectonics in the Southern Iran. *International Journal of Geosciences* **7**, 367–377. <https://doi.org/10.4236/IJG.2016.73029>
- Kobayashi, T., Morishita, Y., Yurai, H., Fujiwara, S., 2018. InSAR-derived Crustal Deformation and Reverse Fault Motion of the 2017 Iran-Iraq Earthquake in the Northwest of the Zagros Orogenic Belt. *Bulletin of the Geospatial Information Authority of Japan*, **66**, 1–9.
- Lai, J., Wang, G., Fan, Q., Pang, X., Li, H., Zhao, F., Li, Y., Zhao, X., Zhao, Y., Huang, Y., Bao, M., Qin, Z., Wang, Q., 2022. Geophysical Well-Log Evaluation in the Era of Unconventional Hydrocarbon Resources: A Review on Current Status and Prospects. *Surveys in Geophysics* **43**, 913–957. <https://doi.org/10.1007/S10712-022-09705-4>
- Le Garzic, E., Vergés, J., Sapin, F., Saura, E., Meresse, F., Ringenbach, J.C., 2019. Evolution of the NW Zagros Fold-and-Thrust Belt in Kurdistan Region of Iraq from balanced and restored crustal-scale sections and forward modeling. *J Struct Geol* **124**, 51–69. <https://doi.org/10.1016/j.jsg.2019.04.006>
- Mafakheri B., N., Lin, W., Murata, S., Yousefi, F., Radwan, A.E., 2022. Magnitudes and orientations of present-day in-situ stresses in the Kurdistan region of Iraq: Insights into combined strike-slip and reverse faulting stress regimes. *J Asian Earth Sci* **239**, 105398. <https://doi.org/10.1016/j.jseaes.2022.105398>
- Mafakheri B., N., Lin, W., Radwan, A.E., Manshad, A.K., 2024. Comprehensive analysis of stress magnitude and orientations and natural fractures in complex structural regimes oil reservoir: Implications for tectonic and oil field development in the Zagros suture zone. *Mar Pet Geol* **160**, 106615. <https://doi.org/10.1016/J.MARPETGEO.2023.106615>
- Molaghab, A., Taherynia, M.H., Mahmoud, S., Aghda, F., Fahimifar, A., 2017. Determination of minimum and maximum stress profiles using wellbore failure evidences : a case study — a deep oil well in the southwest of Iran. *J Pet Explor Prod Technol* **7**, 707–715. <https://doi.org/10.1007/s13202-017-0323-5>

- Mousavi, S.M., 2017. Spatial variation in the frequency-magnitude distribution of earthquakes under the tectonic framework in the Middle East. *J Asian Earth Sci* **147**, 193–209. <https://doi.org/10.1016/j.jseaes.2017.07.040>
- Mousavipour, F., Ali, M., Hamed, R., Moghanloo, G., 2020. Prediction of in situ stresses , mud window and overpressure zone using well logs in South Pars field. *J Pet Explor Prod Technol* **10**, 1869–1879. <https://doi.org/10.1007/s13202-020-00890-9>
- Mouthereau, F., Lacombe, O., Vergés, J., 2012. Building the Zagros collisional orogen: Timing, strain distribution and the dynamics of Arabia/Eurasia plate convergence. *Tectonophysics* **532–535**, 27–60. <https://doi.org/10.1016/j.tecto.2012.01.022>
- Numan, N., 1997. A Plate Tectonic Scenario for The Phanerozoic Succession in Iraq. *IRAQI GEOLOGICAL JOURNAL*.
- Numan, N.M.S., 1984. Basement control of stratigraphy sequences and structural pattern in Iraq. *Journal of the Geological Society of Iraq* **16**, 8–24.
- Obaid, A.K., Allen, M.B., 2017. Landscape maturity, fold growth sequence and structural style in the Kirkuk Embayment of the Zagros, northern Iraq. *Tectonophysics* **717**, 27–40. <https://doi.org/10.1016/j.tecto.2017.07.006>
- Onur, T., Gok, R., Abdulnaby, W., Mahdi, H., 2016. A Comprehensive Earthquake Catalogue for Iraq in Terms of Moment Magnitude.
- Ranjbar-Karami, R., Rajabi, M., Ghavidel, A., Afroogh, A., 2019. Contemporary tectonic stress pattern of the Persian Gulf Basin, Iran. *Tectonophysics* **766**, 219–231. <https://doi.org/10.1016/j.tecto.2019.06.017>
- Regard, V., Bellier, O., Thomas, J.C., Abbassi, M.R., Mercier, J., Shabanian, E., Feghhi, K., Soleymani, S., 2004. Accommodation of Arabia-Eurasia convergence in the Zagros-Makran transfer zone, SE Iran: A transition between collision and subduction through a young deforming system. *Tectonics* **23**, 1–25. <https://doi.org/10.1029/2003TC001599>
- Reif, D., Grasemann, B., Faber, R.H., 2011. Quantitative structural analysis using remote sensing data: Kurdistan, northeast Iraq. *Am Assoc Pet Geol Bull* **95**, 941–956. <https://doi.org/10.1306/11151010112>
- Sanaee, R., Reza Shadizadeh, S., Ali Riahi, M., 2010. Determination of the stress profile in a deep borehole in a naturally fractured reservoir. *International Journal of Rock*

- Mechanics and Mining Sciences* **47**, 599–605.
<https://doi.org/10.1016/j.ijrmms.2010.03.014>
- Sarkarinejad, K., Goftari, F., 2019. Thick-skinned and thin-skinned tectonics of the Zagros orogen, Iran: Constraints from structural, microstructural and kinematics analyses. *J Asian Earth Sci* **170**, 249–273.
<https://doi.org/10.1016/J.JSEAES.2018.10.021>
- Sarkarinejad, K., Mottahedi, M., Nori, M., 2021. Aseismic slip on the active Sabz-Pushan and Sepidar thrusts, Iran: microstructural and kinematics evidence of the slickenline fibre creep. *International Journal of Earth Sciences* **110**, 2831–2848.
<https://doi.org/10.1007/s00531-021-02081-1>
- Sharland, P.R., Casey, D.M., Davies, R.B., Simmons, M.D., Sutcliffe, O.E., 2004. Arabian Plate Sequence Stratigraphy – revisions to SP2. *GeoArabia* **9**, 199–214.
<https://doi.org/10.2113/geoarabia0901199>
- Sherkati, S., Letouzey, J., Frizon de Lamotte, D., 2006. Central Zagros fold-thrust belt (Iran): New insights from seismic data, field observation, and sandbox modeling. *Tectonics* **25**. <https://doi.org/10.1029/2004TC001766>
- Snyder, D.B., Barazangi, M., 1986. Deep crustal structure and flexure of the Arabian Plate Beneath the Zagros collisional mountain belt as inferred from gravity observations. *Tectonics* **5**, 361–373. <https://doi.org/10.1029/TC005i003p00361>
- Taghipour, M., Ghafoori, M., Lashkaripour, G.R., Hafezi Moghaddas, N., Molaghab, A., 2021. A Geomechanical Evaluation of Fault Reactivation Using Analytical Methods and Numerical Simulation. *Rock Mech Rock Eng* **54**, 695–719.
<https://doi.org/10.1007/s00603-020-02309-7>
- Takin, M., 1972. Iranian Geology and Continental Drift in the Middle East. *Nature* **235**, 147–150. <https://doi.org/10.1038/235147a0>
- Vergés, J., Goodarzi, M.G.H., Emami, H., Karpuz, R., Efstathiou, J., Gillespie, P., 2011. Multiple Detachment Folding in Pusht-e Kuh Arc, Zagros: Role of Mechanical Stratigraphy, in: McClay, K., Shaw, J., Suppe, J. (Eds.), Thrust Fault-Related Folding. *American Association of Petroleum Geologists*, **94**.
<https://doi.org/10.1306/13251333M942899>
- Vernant, P., Nilforoushan, F., Hatzfeld, D., Abbassi, M.R., Vigny, C., Masson, F., Nankali, H., Martinod, J., Ashtiani, A., Bayer, R., Tavakoli, F., Chéry, J., 2004.

- Present-day crustal deformation and plate kinematics in the Middle East constrained by GPS measurements in Iran and northern Oman. *Geophys J Int* **157**, 381–398. <https://doi.org/10.1111/j.1365-246X.2004.02222.x>
- Yaghoubi, A., Mahbaz, S., Dusseault, M.B., Leonenko, Y., 2021. Seismicity and the state of stress in the Dezful embayment, Zagros fold and thrust belt. *Geosciences* **11**, 254. <https://doi.org/10.3390/GEOSCIENCES11060254/S1>
- Yaghoubi, A., Zeinali, M., 2009. Determination of magnitude and orientation of the in-situ stress from borehole breakout and effect of pore pressure on borehole stability — Case study in Cheshmeh Khush oil field of Iran. *J Pet Sci Eng* **67**, 116–126. <https://doi.org/10.1016/j.petrol.2009.05.008>
- Yousefi, M., Moussavi, S.M., Khatib, M.M., 2019. Analysis of fold and fault-related fracture systems development using image logs at Asmari Formation in the Rag Sefid Anticline, SW Iran. *Geopersia* **9**, 279–292. <https://doi.org/10.22059/GEOPE.2019.264206.648410>
- Zebari, M.M., Burberry, C.M., 2015. 4-D evolution of anticlines and implications for hydrocarbon exploration within the Zagros Fold-Thrust Belt, Kurdistan Region, Iraq. *GeoArabia* **20**, 161–188. <https://doi.org/10.2113/geoarabia2001161>

Chapter 3

Review of determining magnitude and orientation of in situ stress

3.1 Background

Research on in-situ stress orientations and magnitudes is not mandatory for tectonic and structural studies only, but it plays a vital role in the oil and gas industry. Previous research studies prove that geomechanical modeling has become vital to any field development including drilling (Abdelghany et al., 2021; Brudy and Zoback, 1999) production optimization (Radwan and Sen, 2021a, 2021b), wellbore-stability (Gholami et al., 2015; Karatela et al., 2016; McLean and Addis, 1990), and hydraulic-fracturing (Lakirouhani et al., 2016; Nasehi and Mortazavi, 2013). Specifically, to analyze the instability of the oil and gas wells, it is necessary to determine the magnitude and orientation of in situ stress components (Manshad et al., 2014; Mousavipour et al., 2020; Cui & Radwan, 2022).

The five essential principal components of any geomechanical study are the magnitudes of the three principal in-situ stresses (vertical stress (S_v), minimum horizontal stress (S_h), and maximum horizontal stress (S_H)), the distribution of formation pore pressure (P_p), and the orientation of S_H (Baouche et al., 2020b, 2020a; Bell, 1996; Buseti and Reches, 2014; Rajabi et al., 2016a, 2016b; Tingay, 2015; Zoback, 2007). Gravitational and tectonic forces dominate the in-situ stresses and are particularly associated with horizontal tectonic movements (Kang et al., 2010). Vertical stress is mainly influenced by the overlying rocks and can be estimated reasonably accurately by calculating the weight of the overlying layers. Nevertheless, tectonic forces play an essential role in horizontal stress and are extremely complex with irregular spatial distributions. In addition, tectonic movements greatly influence tectonic forces during the geological history of the region, and they can be explained by several forces (Figure 3-1) (Bell, 1996; Heidbach et al., 2018; Ju and Wang, 2018; Lin et al., 2020; Rebaï et al., 1992; Zoback, 2007).

Previous authors have proposed several methods for determining orientations and magnitudes of in-situ stress. There are several perspectives to categorize stress measurements and determining methods. This chapter categorizes the methods based on direct and indirect methods (Figure 3-2). The direct methods include core-based, wellbore measurement, and borehole deformation. On the other hand, indirect methods are based on theoretical approaches, earthquake focal mechanism (EFM), and acoustic methods (Ljunggren et al., 2003; Zoback, 2007).

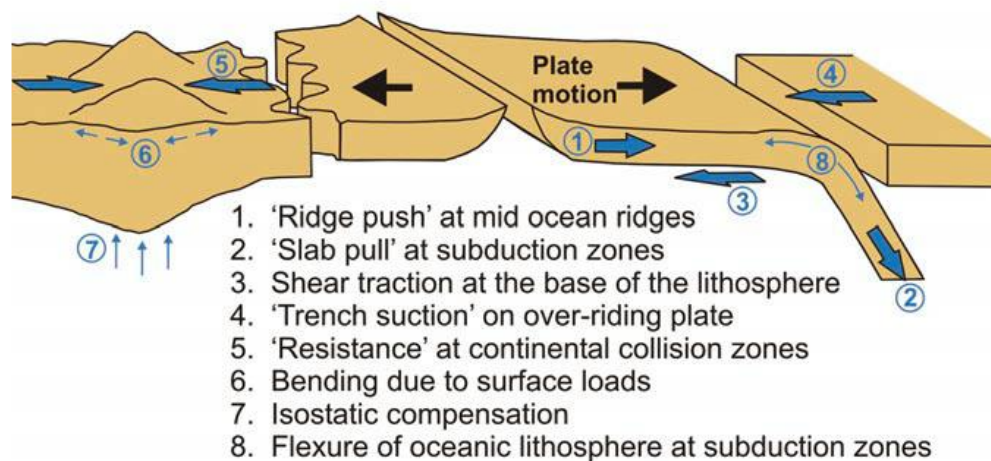


Figure 3-1. Stress sources composing the tectonic stress. (After Tingay et al., 2012; Zoback et al., 1989)

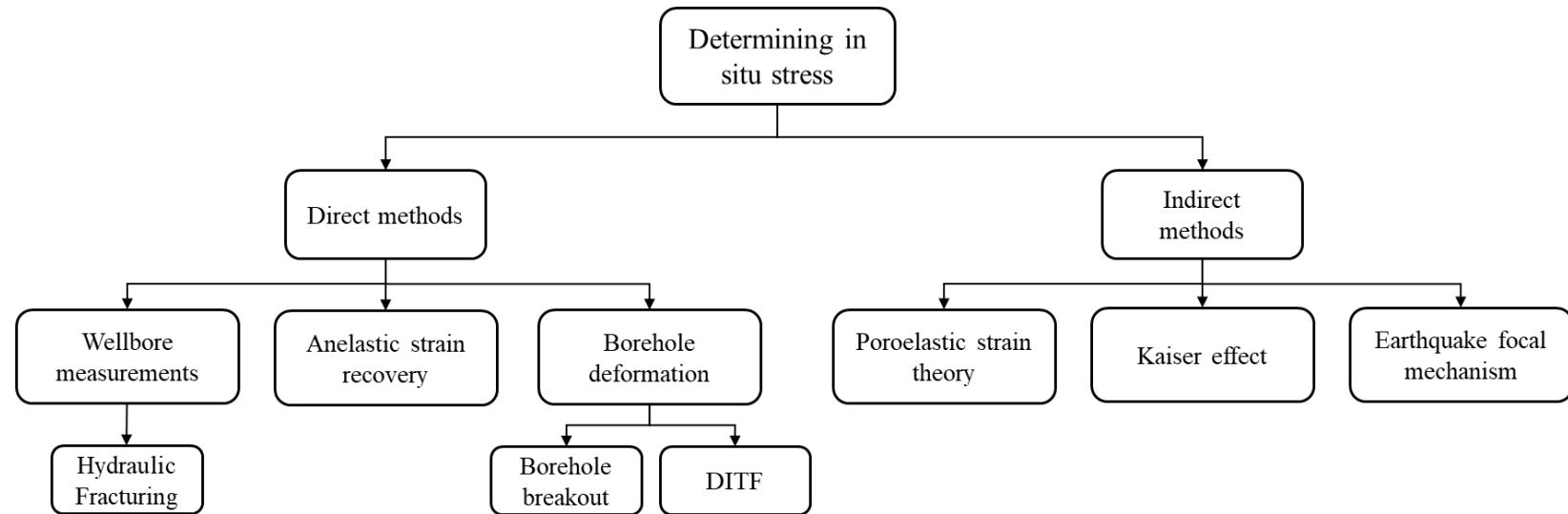


Figure 3-2. Classification of in situ stress measurement methods.

3.2 Direct methods

3.2.1 Wellbore measurements

The concentration stress around a wellbore can explain the relationships among in situ stress magnitudes, rock strength, and the nature of compressive and tensile failures. There are several wellbore measurements, including hydraulic fracturing, mini frac test, and leak off test (LOT). Hydraulic methods are among the most widely used techniques for measuring in-situ stress. With this technique, a pre-existing fracture in a rock formation is injected with pressured liquids, which causes the fracture to widen and produce new fractures. The stress levels of the rock formation can be evaluated by observing how these cracks respond to pressure (Sazid et al., 2023). Usually, a set of packers is used to seal off a section of the borehole, with the sealed interval around one meter. Hydraulic fracturing is used to measure the in-situ stress of subsurface rock by propagating a fracture in the rock. The direction of the fracture is identified by looking at the traces of fracture on the borehole wall, and it spreads in the direction of least resistance. The components recorded in a vertical borehole are two of the primary stresses, and this orientation is related to the direction of the maximum horizontal stress in vertical or sub-vertical boreholes (Ljunggren et al., 2003). On the other hand, hydraulic fractures will always propagate perpendicular to the minimum principal stress (Zoback, 2007). One advantage of hydraulic methods is that they can determine the in-situ stress without knowing the rock's deformation properties.

A schematic pressure–time history illustrating a hydraulic fracturing test is shown in Figure 3-3. The pumping rate into the well is constant. Therefore, the pressure should increase linearly with time. Then, a linear increase of wellbore pressure with time causes a distinct change in the volume rate, considered the leak-off point (LOP) and an indicator that hydraulic fracture must have formed. A clear LOP is approximately equal to the minimum principal stress. Next, the peak pressure reaches the formation breakdown pressure (FBP), which means the fluid flows into the fracture faster from the wellbore than the pump. Finally, if pumping continues at a constant rate, the pumping pressure will drop to a relatively constant value called the fracture propagation pressure (FPP), which is very close to the minimum principal stress (Zoback, 2007).

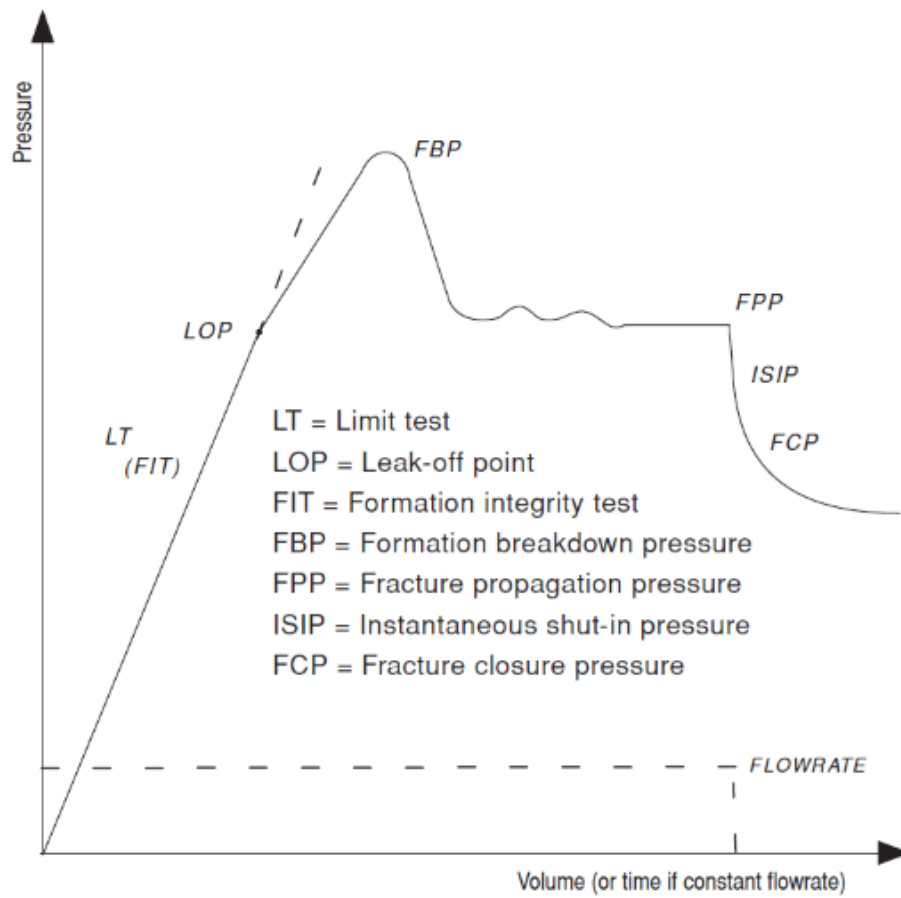


Figure 3-3. A hydraulic fracturing test showing pressure as a function of injection volume. (After Zoback, 2007)

The main disadvantage of the hydraulic fracturing method is that it has the potential to cause damage to the surrounding rock. Additionally, the measurements obtained may be affected by factors such as temperature, pore pressure, and fractures in the rock.

3.2.2 Anelastic strain recovery (ASR)

In this section, the anelastic strain recovery (ASR) method, a stress measurement method based on the strain recovery of the rock, is described. Usually, core samples recovered from deep wells cannot maintain in-situ stress once removed from the formation. However, structural changes in sediment fabrics caused by the release of in-situ stress are thought to be detectable. Thus, information about in situ stress may remain in the recovered sediments (Lin et al., 2010a; Nagano et al., 2015). According to Amadei and Stephansson (1997), when a piece of rock is removed from the in-situ state of stress, it tends to relax and deform. There is an instantaneous elastic component and a time-dependent recovery component to relaxation. According to field observations, preferred microcracks are typically open and spread in drilled cores following drilling and coring, indicating the occurrence of anelastic strain recovery.

The ASR method evaluates stress by measuring the ASR of a core sample after stress release by drilling. ASR is relatively small and requires high measurement accuracy. One feature of this method is that the three-dimensional stress can be determined with a single rock core sample (Amadei and Stephansson, 1997). This method applies to rock types with large ASR. Its inapplicability to rock types with a great anisotropy is the issue. Furthermore, the measurement is contingent upon the drilling schedule since it must be carried out at or near the site right after the stress release. A Schematic diagram of ASR and illustration of Strain gauge layout are presented in Figure 3-4.

Overall, the ASR method analyzes the three-dimensional stress fields using the isotropic viscoelastic model by measuring anelastic strain restorations of core samples.

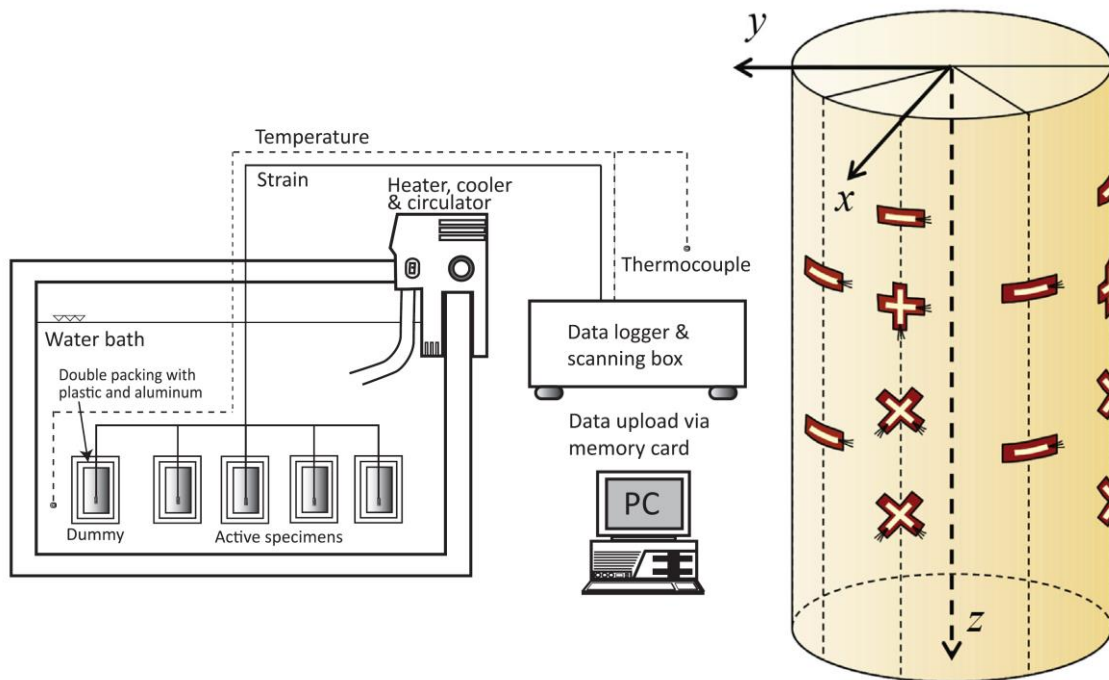


Figure 3-4. Schematic diagram of ASR and illustration of Strain gauge layout. (After Nagano et al., 2015)

3.2.3 Borehole deformation

After drilling a well, wellbore instability causes several deformations and fractures in the borehole. Borehole breakouts and drilling-induced tensile fractures (DITF) are among the most important features that interest geoscientists. Borehole breakout is a local enlargement of the borehole diameter usually associated with in-situ stress and formation strength. Breakouts occur when the circumference stress exceeds the strength of the rock surrounding the borehole, causing rock failure (Zoback et al., 1985).

The most reliable way to observe wellbore breakouts is through image logs. As shown in Figure 3-5, a standard borehole image log shows breakouts and DITF. Using image logs to identify wellbore deformation and failure, particularly the breakouts and fractures, is among the most frequently used methods for determining the orientation and magnitude of horizontal in situ stresses and has shown valuable results (Cui et al., 2009; Han, 2021; Li et al., 2019; Lin et al., 2010b; Riedel et al., 2016). Digital processing allows cross-sections of a well to determine orientation of the breakouts and DITF and also width of the breakout. As shown in figure 3-5, breakouts and DITFs

form symmetrically on both sides of the well. Using the breakouts and DITF properties enables scientists to determine both orientation and magnitude of horizontal stresses.

The DITF occurs when the wellbore wall experiences a tension. The area around the wellbore wall in which tensional stresses exist is at the azimuth of the maximum horizontal stress. Under normal circumstances, DITF are not expected to propagate more than a cm from the wellbore wall. Thus, identifying DITF is only possible by observation of the image logs. A detailed explanation of using breakout and DITF to determine orientation and magnitude of horizontal stresses is presented in chapter Four section 4.2.2 and 4.2.3.

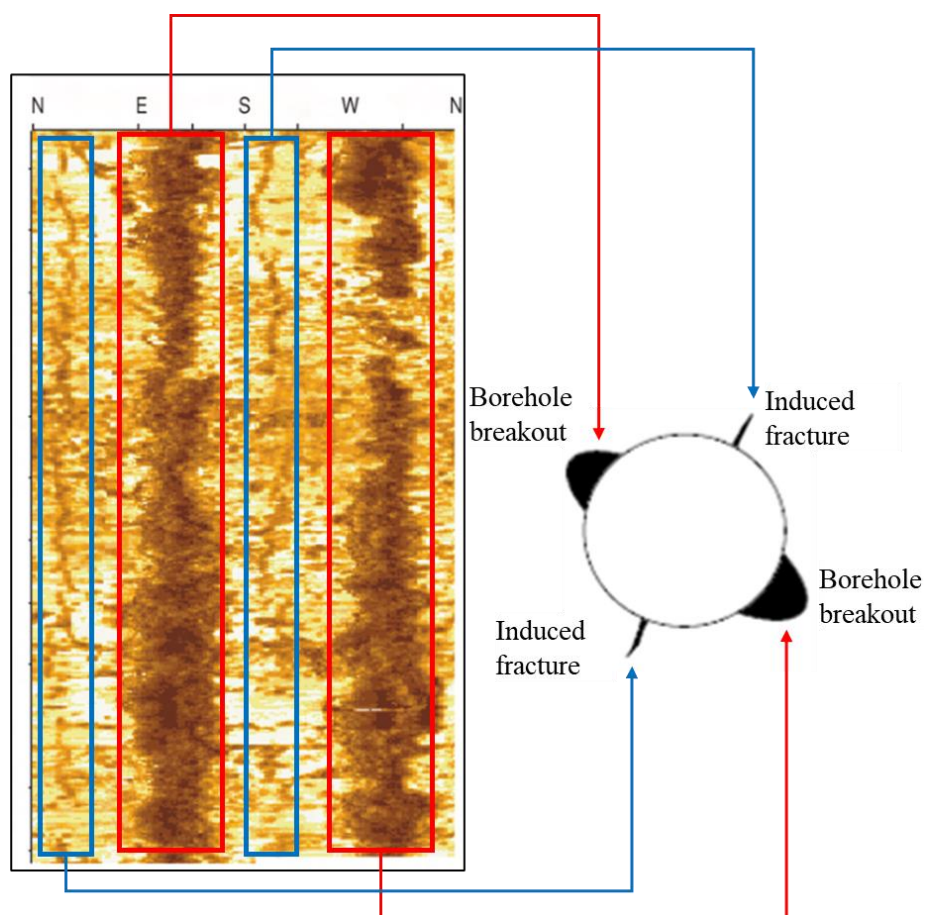


Figure 3-5. Example of breakouts and DITF appear in an acoustic borehole image log. (After Zoback, 2007)

3.3 Indirect Methods

3.3.1 Poroelastic strain model

Another approach for determining the in-situ stresses is using fundamentals of rock mechanics in porous media. In this approach rock properties such as bulk modulus, young modulus, Biot's coefficient, and poisson's ratio are used to determine the magnitude of horizontal stresses. The constitutive behavior of rock is described by the notion of poroelasticity in a porous elastic solid saturated with a fluid. The theory of linear elasticity deals with situations where there are linear relationships between applied stresses and resulting strains. While most rocks exhibit a nonlinearly behavior when large stresses is applied on them and their behavior can be described by linear relations for sufficiently small changes in stress (Fjær et al., 2008).

Poroelastic strain model suggested by Fjær et al. (2008) can determine the anisotropic magnitude of horizontal stresses via the rock properties. On the other hand several empirical equations are developed to determine the rock properties from well logs (Bailin, 2001; Najibi et al., 2015; Wang, 2017). Therefore a continuous stress profile can be created for entire well logged intervals. In comparison to the other stress determining methods in this chapter which determine the magnitude of stress in a certain depth, this method provides stress profile in a longer range. A detailed explanation of poroelastic strain theory to determine magnitude of horizontal stresses is presented in chapter Four section 4.2.3.

3.3.2 Kaiser Effect method

Determining in situ stresses using the acoustic Kaiser Effect method is another technique in determining in situ stresses. This method is based on the principle discovered by Kaiser in the 1950s. This method is based on a phenomenon where materials, particularly rocks, exhibit acoustic emissions at stress levels that correspond to their maximum previous stress (Holcomb, 1993). This phenomenon, known as the Kaiser Effect, indicates that materials hold a memory of their stress history. When rocks are subjected to stress, they develop micro-cracks, leading to the emission of acoustic signals (Figure 3-6). If the rock is unloaded and then reloaded, significant acoustic emissions do not occur until the stress exceeds the maximum stress level previously

experienced. In a controlled laboratory setting, these samples are subjected to loading, and high-precision acoustic emission sensors are employed to detect and record the acoustic signals emitted from the rock. By analyzing this data and considering the geological history and conditions of the site, an estimation of the in-situ stresses can be conducted.

In this method, samples should closely represent the in-situ conditions and ensuring this consideration can be challenging. The accuracy of the Kaiser Effect in predicting in situ stress is highly dependent on the correct interpretation of acoustic emissions, which requires significant expertise. Moreover, in areas with complex geological histories, the interpretation of acoustic emissions can become complicated, which may reduce the accuracy of the stress estimations.

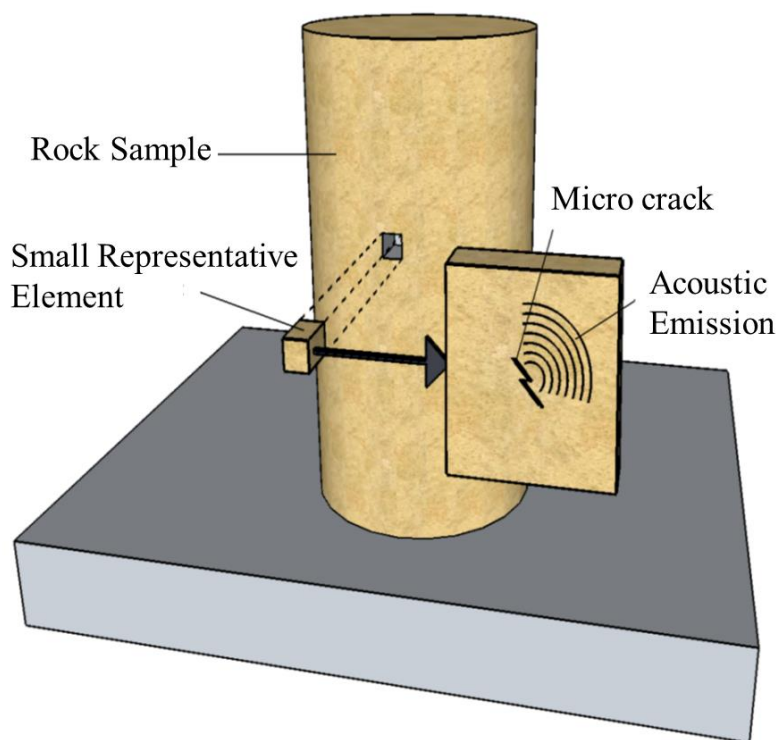


Figure 3-6. Schematic model of acoustic Kaiser effect test. (After Blanksma, 2011)

3.3.3 Earthquake focal mechanism

In seismically active regions, from earthquake focal mechanisms (EFM) important information can be obtained about the stress state. This method is crucial to seismology and provides insights into the orientation and movement on fault planes during an earthquake (Zoback, 2007). EFM is dependent on the study of seismic waves generated by an earthquake. These waves are recorded by seismometers placed around the globe. By analyzing the patterns of these waves, seismologists can determine the direction of slip on the fault plane and the orientation of the fault itself (Frohlich and Apperson, 1992).

The primary assumption is that the direction of the largest compressive stress is perpendicular to the fault plane where slip occurs most easily. This means that by analyzing multiple earthquake focal mechanisms in a region, it is possible to predict the general stress regime of an area. In this method, small earthquake data can be used to calculate the first motion of seismic waves in different directions. In a normal fault, for instance, one block of rock slips downward relative to another, while in a reverse fault, a block moves upwards. In a strike-slip fault, blocks of rock slide past each other horizontally. The patterns of the first motion indicate whether the waves are compressing or not, which reveals the nature of the fault movement. This information is typically represented in a beachball diagram, which visually displays the type of fault movement such as normal, reverse, or strike-slip and the orientation of the fault plane (Figure 3-7). The beachball is a two-dimensional projection of a sphere, representing the seismic waves radiating out from the earthquake's focal point (hypocenter). Typically, the diagram is divided into quadrants by two intersecting circles, creating four lobes or segments. These segments are colored in contrasting colors, often black and white, to represent different types of motion. The intersecting circles represent two possible fault planes along which the earthquake could have occurred. These planes divide the sphere into four quadrants (Frohlich and Apperson, 1992).

However, interpreting focal mechanism data is a challenging task. The accuracy of the interpretations heavily depends on the quality and quantity of seismic data available. In remote or under-monitored regions, data may be sparse, leading to less reliable

interpretations. Moreover, complex fault systems can produce intricate seismic patterns, which can be difficult to interpret.

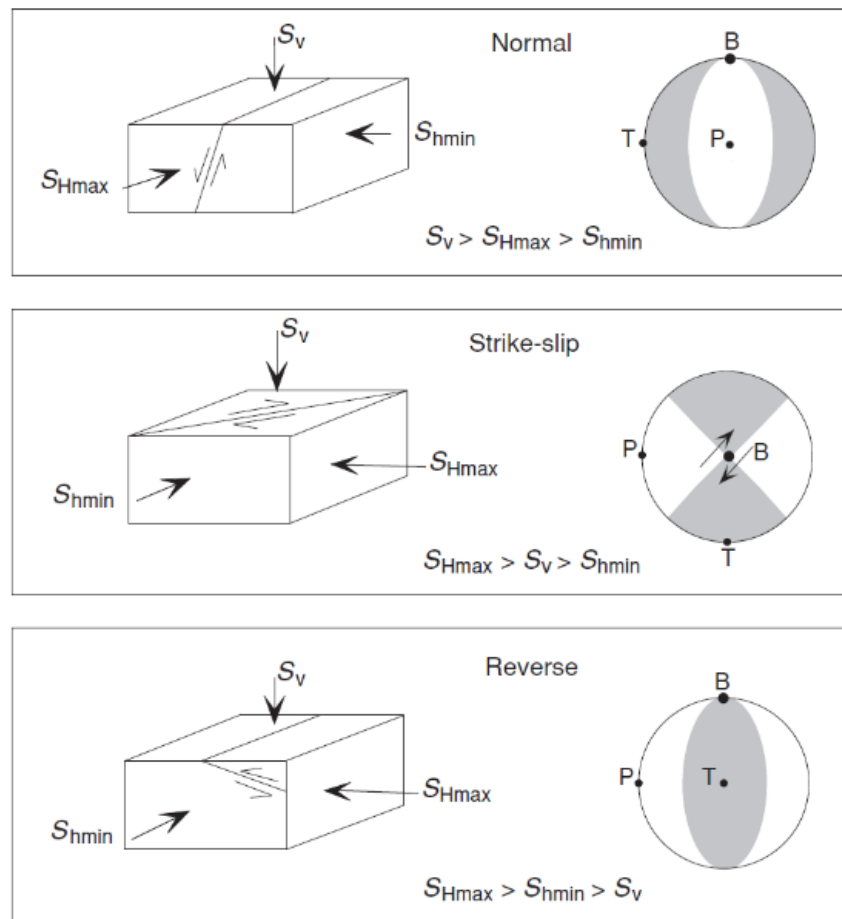


Figure 3-7. Illustration of EFM for different stress regimes by the beach balls.
(After Zoback, 2007)

3.4 Method selection

In the studied area in Figures 2-1 and 2-2 the majority of previous studies for orientation of maximum horizontal stress are based on EFM which investigate the deeper depths sand according to Tingay et al. (2008), despite high availability of EFM data in this area, at intermediate depths, borehole deformations such as breakout and DITF data from image logging are better indicators of orientation of horizontal stresses than EFMs. Therefore, these studies most likely do not represent the intermediate depths between 1 and 5 km, and typically cannot be used to explain and study the complexity of the stress state in these depths. Accordingly, breakout data can provide more accurate orientation of horizontal stresses for the petroleum industry and geothermal systems and consequently has been selected for this study (Cui et al., 2009).

For determining magnitude of in-situ stresses each method presented in this chapter has merits and disadvantages, but in this area most direct and indirect methods including hydraulic fracturing, core-based and acoustic methods were not available due to lack of core samples and complexity of operation of advanced hydraulic fracturing method. However image logs for identifying borehole deformation for a total of 10 wells were available. In addition, breakout approach is a one of the common and well-established methods for determining horizontal stresses. Furthermore, theoretical methods such poroelastic strain model by using the oil field data such as well logs from actual measurements in the wellbore can provide continuous stress profile and offer valuable information for intermediate depths in this active tectonic region.

Therefore, in chapter Four and Five, breakouts analysis combined with multiped caliper has been selected as the primary indicator of orientation of maximum horizontal stresses. In addition, for determining the magnitude of maximum horizontal stress as the most challenging parameter among geomechanical parameters, poroelastic strain theory and breakout approach has been employed in this study.

References

- Abdelghany, W.K., Radwan, A.E., Elkhawaga, M.A., Wood, D.A., Sen, S., Kassem, A.A., 2021. Geomechanical modeling using the depth-of-damage approach to achieve successful underbalanced drilling in the Gulf of Suez rift basin. *J Pet Sci Eng* **202**, 108311. <https://doi.org/10.1016/j.petrol.2020.108311>
- Amadei, B., Stephansson, O., 1997. Strain Recovery Methods. *Rock Stress and Its Measurement* 289–302. https://doi.org/10.1007/978-94-011-5346-1_7
- Bailin, W., 2001. Boit's Effective Stress Coefficient Evaluation: Static And Dynamic Approaches. *ISRM International Symposium - 2nd Asian Rock Mechanics Symposium*, 82.
- Baouche, R., Sen, S., Boutaleb, K., 2020a. Present day In-situ stress magnitude and orientation of horizontal stress components in the eastern Illizi basin, Algeria: A geomechanical modeling. *J Struct Geol* **132**, 103975. <https://doi.org/10.1016/j.jsg.2019.103975>
- Baouche, R., Sen, S., Ganguli, S.S., 2020b. Pore pressure and in-situ stress magnitudes in the Bhiret Hammou hydrocarbon field, Berkine Basin, Algeria. *Journal of African Earth Sciences* **171**, 103945. <https://doi.org/10.1016/j.jafrearsci.2020.103945>
- Bell, J.S., 1996. Petro geoscience 2. In situ stresses in sedimentary rocks (part 2): Applications of stress measurements. *Geoscience Canada* **23**, 135-153.
- Blanksma, D.J., 2011. Investigation of In-Situ Stresses in Rocks via Acoustic Emission Investigation of In-Situ Stresses in Rocks via Acoustic Emission and the Kaiser Effect. *Thesis, University of North Dakota*.
- Brudy, M., Zoback, M.D., 1999. Drilling-induced tensile wall-fractures: Implications for determination of in-situ stress orientation and magnitude. *International Journal of Rock Mechanics and Mining Sciences* **36**, 191–215. [https://doi.org/10.1016/S0148-9062\(98\)00182-X](https://doi.org/10.1016/S0148-9062(98)00182-X)
- Buseti, S., Reches, Z., 2014. Geomechanics of hydraulic fracturing microseismicity: Part 2. Stress state determination. *Am Assoc Pet Geol Bull* **98**, 2459–2476. <https://doi.org/10.1306/05141413124>

- Cui, J. wen, Wang, L. jie, Li, P., Tang, Z. min, Sun, D. sheng, 2009. Wellbore breakouts of the main borehole of Chinese Continental Scientific Drilling (CCSD) and determination of the present tectonic stress state. *Tectonophysics* **475**, 220–225. <https://doi.org/10.1016/j.tecto.2009.03.021>
- Fjær, E., Holt, R.M., Horsrud, P., Raaen, A.M., Risnes, R., 2008. Petroleum Related Rock Mechanics, 2nd Edition. ed, Mar. Environ. Res. *Elsevier* . [https://doi.org/10.1016/S0376-7361\(07\)53013-X](https://doi.org/10.1016/S0376-7361(07)53013-X)
- Frohlich, C., Apperson, K.D., 1992. Earthquake focal mechanisms, moment tensors, and the consistency of seismic activity near plate boundaries. *Tectonics* **11**, 279–296. <https://doi.org/10.1029/91TC02888>
- Gholami, R., Rasouli, V., Aadnoy, B., Mohammadi, R., 2015. Application of in situ stress estimation methods in wellbore stability analysis under isotropic and anisotropic conditions. *Journal of Geophysics and Engineering* **12**, 657–673. <https://doi.org/10.1088/1742-2132/12/4/657>
- Han, Y., 2021. Refined equations for estimating maximum horizontal stress from borehole breakouts in vertical wells. *Geomechanics and Geophysics for Geo-Energy and Geo-Resources* **7**, 1–12. <https://doi.org/10.1007/s40948-021-00251-8>
- Heidbach, O., Rajabi, M., Cui, X., Fuchs, K., Müller, B., Reinecker, J., Reiter, K., Tingay, M., Wenzel, F., Xie, F., Ziegler, M.O., Zoback, Mary Lou, Zoback, Mark, 2018. The World Stress Map database release 2016: Crustal stress pattern across scales. *Tectonophysics* **744**, 484–498. <https://doi.org/10.1016/j.tecto.2018.07.007>
- Holcomb, D.J., 1993. Observations of the Kaiser Effect under multiaxial stress states: Implications for its use in determining in situ stress. *Geophys Res Lett* **20**, 2119–2122. <https://doi.org/10.1029/93GL01270>
- Ito, T., Funato, A., Lin, W., Doan, M.L., Boutt, D.F., Kano, Y., Ito, H., Saffer, D., McNeill, L.C., Byrne, T., Moe, K.T., 2013. Determination of stress state in deep subsea formation by combination of hydraulic fracturing in situ test and core analysis: A case study in the IODP Expedition 319. *J Geophys Res Solid Earth* **118**, 1203–1215. <https://doi.org/10.1002/jgrb.50086>
- Ju, W., Wang, K., 2018. A preliminary study of the present-day in-situ stress state in the Ahe tight gas reservoir, Dibeig Gasfield, Kuqa Depression. *Mar Pet Geol* **96**, 154–165. <https://doi.org/10.1016/j.marpetgeo.2018.05.036>

- Kang, H., Zhang, X., Si, L., Wu, Y., Gao, F., 2010. In-situ stress measurements and stress distribution characteristics in underground coal mines in China. *Eng Geol* **116**, 333–345. <https://doi.org/10.1016/j.enggeo.2010.09.015>
- Karatela, E., Taheri, A., Xu, C., Stevenson, G., 2016. Study on effect of in-situ stress ratio and discontinuities orientation on borehole stability in heavily fractured rocks using discrete element method. *J Pet Sci Eng* **139**, 94–103. <https://doi.org/10.1016/j.petrol.2015.12.016>
- Lakirouhani, A., Detournay, E., Bungler, A.P., 2016. A reassessment of in situ stress determination by hydraulic fracturing. *Geophys J Int* **205**, 1859–1873. <https://doi.org/10.1093/gji/ggw132>
- Li, H., Tang, H., Qin, Q., Zhou, J., Qin, Z., Fan, C., Su, P., Wang, Q., Zhong, C., 2019. Characteristics, formation periods and genetic mechanisms of tectonic fractures in the tight gas sandstones reservoir: A case study of Xujiahe Formation in YB area, Sichuan Basin, China. *J Pet Sci Eng* **178**, 723–735. <https://doi.org/10.1016/j.petrol.2019.04.007>
- Lin, H., Kang, W.H., Oh, J., Canbulat, I., Hebblewhite, B., 2020. Numerical simulation on borehole breakout and borehole size effect using discrete element method. *Int J Min Sci Technol* **30**, 623–633. <https://doi.org/10.1016/j.ijmst.2020.05.019>
- Lin, W., Byrne, T.B., Tsutsumi, A., Yamamoto, Yuhji, Sakaguchi, A., Yamamoto, Yuzuru, Chang, C., 2010. Applications of Anelastic Strain Measurements In Scientific Ocean Deep Drillings. *Proceedings of the EUROCK*, 749-758.
- Lin, W., Doan, M.L., Moore, J.C., McNeill, L., Byrne, T.B., Ito, T., Saffer, D., Conin, M., Kinoshita, M., Sanada, Y., Moe, K.T., Araki, E., Tobin, H., Boutt, D., Kano, Y., Hayman, N.W., Flemings, P., Huftile, G.J., Cukur, D., Buret, C., Schleicher, A.M., Efimenko, N., Kawabata, K., Buchs, D.M., Jiang, S., Kameo, K., Horiguchi, K., Wiersberg, T., Kopf, A., Kitada, K., Eguchi, N., Toczko, S., Takahashi, K., Kido, Y., 2010b. Present-day principal horizontal stress orientations in the Kumano forearc basin of the southwest Japan subduction zone determined from IODP NanTroSEIZE drilling Site C0009. *Geophys Res Lett* **37**, 1–6. <https://doi.org/10.1029/2010GL043158>

- Ljunggren, C., Chang, Y., Janson, T., Christiansson, R., 2003. An overview of rock stress measurement methods. *International Journal of Rock Mechanics and Mining Sciences* **40**, 975–989. <https://doi.org/10.1016/J.IJRMMS.2003.07.003>
- Manshad, A.K., Jalalifar, H., Aslannejad, M., 2014. Analysis of vertical, horizontal and deviated wellbores stability by analytical and numerical methods. *J Pet Explor Prod Technol* **4**, 359–369. <https://doi.org/10.1007/s13202-014-0100-7>
- McLean, M.R., Addis, M.A., 1990. Wellbore Stability Analysis: A Review of Current Methods of Analysis and Their Field Application. *IADC/SPE Drilling Conference*. <https://doi.org/10.2118/19941-MS>
- Mousavipour, F., Ali, M., Hamed, R., Moghanloo, G., 2020. Prediction of in situ stresses , mud window and overpressure zone using well logs in South Pars field. *J Pet Explor Prod Technol* **10**, 1869–1879. <https://doi.org/10.1007/s13202-020-00890-9>
- Nagano, Y., Lin, W., Yamamoto, K., 2015. In-situ stress analysis using the anelastic strain recovery (ASR) method at the first offshore gas production test site in the eastern Nankai Trough, Japan. *Mar Pet Geol* **66**, 418–424. <https://doi.org/10.1016/J.MARPETGEO.2015.02.027>
- Najibi, A.R., Ghafouri, M., Lashkaripour, G.R., Asef, M.R., 2015. Empirical relations between strength and static and dynamic elastic properties of Asmari and Sarvak limestones, two main oil reservoirs in Iran. *J Pet Sci Eng* **126**, 78–82. <https://doi.org/10.1016/J.PETROL.2014.12.010>
- Nasehi, M.J., Mortazavi, A., 2013. Effects of in-situ stress regime and intact rock strength parameters on the hydraulic fracturing. *J Pet Sci Eng* **108**, 211–221. <https://doi.org/https://doi.org/10.1016/j.petrol.2013.04.001>
- Radwan, A., Sen, S., 2021a. Stress Path Analysis for Characterization of In Situ Stress State and Effect of Reservoir Depletion on Present-Day Stress Magnitudes: Reservoir Geomechanical Modeling in the Gulf of Suez Rift Basin, Egypt. *Natural Resources Research* **30**, 463–478. <https://doi.org/10.1007/s11053-020-09731-2>
- Radwan, A., Sen, S., 2021b. Characterization of in-situ stresses and its implications for production and reservoir stability in the depleted El Morgan hydrocarbon field, Gulf of Suez rift basin, Egypt. *J Struct Geol* **148**, 104355. <https://doi.org/10.1016/j.jsg.2021.104355>

- Rajabi, M., Tingay, M., Heidbach, O., 2016a. The present-day stress field of New South Wales, Australia. *Australian Journal of Earth Sciences* **63**, 1–21. <https://doi.org/10.1080/08120099.2016.1135821>
- Rajabi, M., Tingay, M., King, R., Heidbach, O., 2016b. Present-day stress orientation in the Clarence-Moreton Basin of New South Wales, Australia: a new high density dataset reveals local stress rotations. *Basin Research* **29**, 622–640. <https://doi.org/10.1111/bre.12175>
- Rebäi, S., Philip, H., Taboada, A., 1992. Modern tectonic stress field in the Mediterranean region: evidence for variation in stress directions at different scales. *Geophys J Int* **110**, 106–140. <https://doi.org/10.1111/j.1365-246X.1992.tb00717.x>
- Riedel, M., A, Malinverno., Wang, K., D., G., Guerin G., 2016. *Geochemistry, Geophysics, Geosystems*. **17**, 1312–1338. <https://doi.org/10.1002/2015GC006205>. Received
- Sazid, M., Hussein, K., Abudurman, K., Sazid, M., Hussein, K., Abudurman, K., 2023. Rock Stress Measurement Methods in Rock Mechanics—A Brief Overview. *World Journal of Engineering and Technology* **11**, 252–272. <https://doi.org/10.4236/WJET.2023.112018>
- Tingay, M., 2015. Initial pore pressures under the Lusi mud volcano, Indonesia. *Interpretation* **3**, SE33–SE49. <https://doi.org/10.1190/INT-2014-0092.1>
- Tingay, M., Müller, B., Reinecker, J., Heidbach, O., Wenzel, F., Fleckenstein, P., 2012. Understanding tectonic stress in the oil patch: *The World Stress Map Project* **24**, 1276–1282. <https://doi.org/10.1190/1.2149653>
- Tingay, M., Reinecker, J., Müller, B., 2008. Borehole breakout and drilling-induced fracture analysis from image logs. *World stress map 1–8. Guidelines: Image Logs*
- Wang, H., 2017. Theory of linear poroelasticity with applications to geomechanics and hydrogeology. *Princeton University Press*. <https://doi.org/10.1515/9781400885688>
- Zoback, M., Zoback, M.D., Adams, J., Assumpção, M., Bell, S., Bergman, E.A., Blümling, P., Brereton, N.R., Denham, D., Ding, J., Fuchs, K., Gay, N., Gregersen, S., Gupta, H.K., Gvishiani, A., Jacob, K., Klein, R., Knoll, P., Magee, M., Mercier, J.L., Müller, B.C., Paquin, C., Rajendran, K., Stephansson, O., Suarez, G., Suter,

M., Udias, A., Xu, Z.H., Zhizhin, M., 1989. Global patterns of tectonic stress. *Nature* **341**, 291–298. <https://doi.org/10.1038/341291a0>

Zoback, M.D., 2007. Reservoir Geomechanics, 1st edition, *Cambridge University Press*. <https://doi.org/10.1017/CBO9780511586477>

Zoback, M.D., Moos, D., Mastin, L., Anderson, R.N., 1985. Well Bore Breakouts and in Situ Stress. *J Geophys Res* **90**, 5523–5530. <https://doi.org/10.1029/JB090iB07p05523>

Chapter 4

Stress state of northwestern Zagros suture zone

4.1 Background

Several studies in the region could be beneficial for determining the regional stress regime and horizontal stress orientation. The most commonly performed type of study conducted in this area previously is earthquake focal mechanism (EFM) analysis. EFM studies on the foreland and hinterland of the Zagros suture zone presented slightly different results. For example, Afra et al. (2017) divided northern Iran (east flank of the Zagros suture zone) into nine zones and investigated based on the similarity of horizontal GPS velocities. The determined stress regime in the region varies from thrust faulting to strike-slip faulting. According to Afra et al. (2017), in eastern Anatolia, the direction of maximum horizontal stress is nearly north–south, but it changes to east–west in the Talesh region in northern Iran. Abdalnaby et al. (2014a, 2014b) suggested that on the left flank, the pattern of present-day tectonic stress fields in northern Iraq and the surrounding regions is controlled by the dynamics of the collision between the Arabian and Eurasian plates. Based on the world stress map (WSM)(Heidbach et al., 2018) and Abdalnaby et al. (2014a, 2014b), the most common tectonic regimes in this study area are strike-slip (SS), followed by thrust faulting (TF), as well as combinations of these types (Figure 2-4,1-1). Doski (2021, 2019; 2016) used EFM analysis to evaluate the tectonic and stress states of the Sheladiz, Raniya, and Sheikhan earthquakes, respectively. In the Sheikhan area, the average trend of maximum compressive stress was reported to be N20°E. In the Sheladiz area, EFM results indicated N–S maximum compressive stress, which Doski (2021) suggested could be related to the anticlockwise rotation of the Arabian plate with respect to the Eurasian plate. According to an EFM study of the Raniya earthquake, this region is subjected to present-day compressional deformation, with a NE–SW maximum horizontal stress axis (N47°E).

Additional sources of data for study are remote sensing and satellite images. Using digital elevation models (DEMs), Reif (2011) studied geological structures of northern Erbil; the average azimuth of the trend of anticline hinge lines was NW–SE (Figure 2-

5). In the Kirkuk Embayment of the Zagros fold-and-thrust belt, the folds grew at different times and out of sequence; on average, they are oriented N–S to NW–SW. The Kirkuk Embayment is located southwest of the Zagros fold-and-thrust belt of Iraq, includes the surface structures of the simply folded zone in northern Iraq, and is commonly included as a subdivision of the Zagros orogenic belt. (Obaid and Allen, 2017). In addition, after the 2017 earthquake with a moment magnitude (M_w) of 7.3, Kobayashi (2018) combined Interferometric Synthetic Aperture Radar (InSAR) derived crustal deformation and reverse fault motion data to study the tectonics of the Zagros orogenic belt. In the western part of the epicenter region (Iraq), uplift of 90 cm upward occurred, whereas most of the epicenter region moved westward overall by 50 cm. Pure reverse fault motion was detected with slight dextral motion toward the NE (Table 2-1 and Figure 2-4). Regard (2004) and Vernant (2004) used GPS data to study the surface displacement. Regard (2004) performed tectonic and fault slip vector analyses and determined that compression tectonic regimes had occurred trending NE–SW in the Arabian Plate, and Vernant (2004) suggested 10 mm y^{-1} average displacement along the N–S direction (Table 2-1 and Figure 2-4). Gilchrist et al. (2020) studied well logs around the depth of 1500 m, whereas Awdal et al. (2016, 2013) studied surface fractures and well logs. The overall orientation of maximum horizontal stress was found to be NE–SW, with slightly different results between studies (Table 2-1 and Figure 2-4).

4.2 Methodology

4.2.1 Data preparation and workflow

In this study (Mafakheri B. et al., 2021; Mafakheri B. et al., 2022), a combination of conventional logs such as natural gamma-ray, density, porosity, compressional and shear acoustic wave, and resistivity logs, in addition to borehole image logs and six-arm mechanical caliper data, was used to determine the magnitudes and orientations of in-situ principal stresses. For confidentiality and security reasons, the data presented in this analysis has been generously provided by a prominent oil company, though specific details regarding the exact fields and locations remain undisclosed to protect proprietary and sensitive information. The specific borehole image logs consisted of data from six pads of resistivity sensors assisted with six-arm calipers, which provided high-quality images. Coverage of the wellbore of 58% for an 8 ½ inch well and of 43% for a 12 ½ inch well was sufficient for geomechanical and stress analysis. Data preparation is a crucial element of breakout analysis, and in the present study, this preparation was conducted in seven steps (Figure 4-1). The used workflow and general steps in this work are presented in Figure 4-2. Each component was required to meet the corresponding standards to lead to successful interpretation. In this study, two wells were evaluated: well A, with an overall true depth of 2240 m, and well B, with a depth of 1400 m. After data quality control, dynamic and static borehole images were created to inform interpretation using the processing software Techlog developed by Schlumberger. As

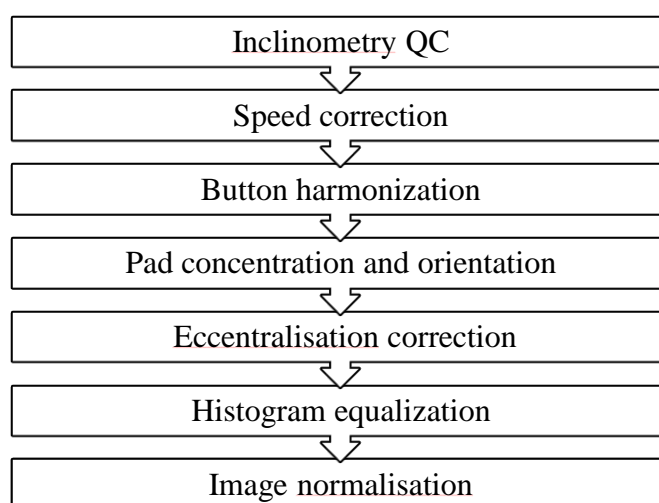


Figure 4-1. Workflow of image log data preparation. After Mafakheri B. et al. (2022).

shown in Figures 4-3a and 4-3b, several breakouts were detected in well A between 1600 m and 2000 m.

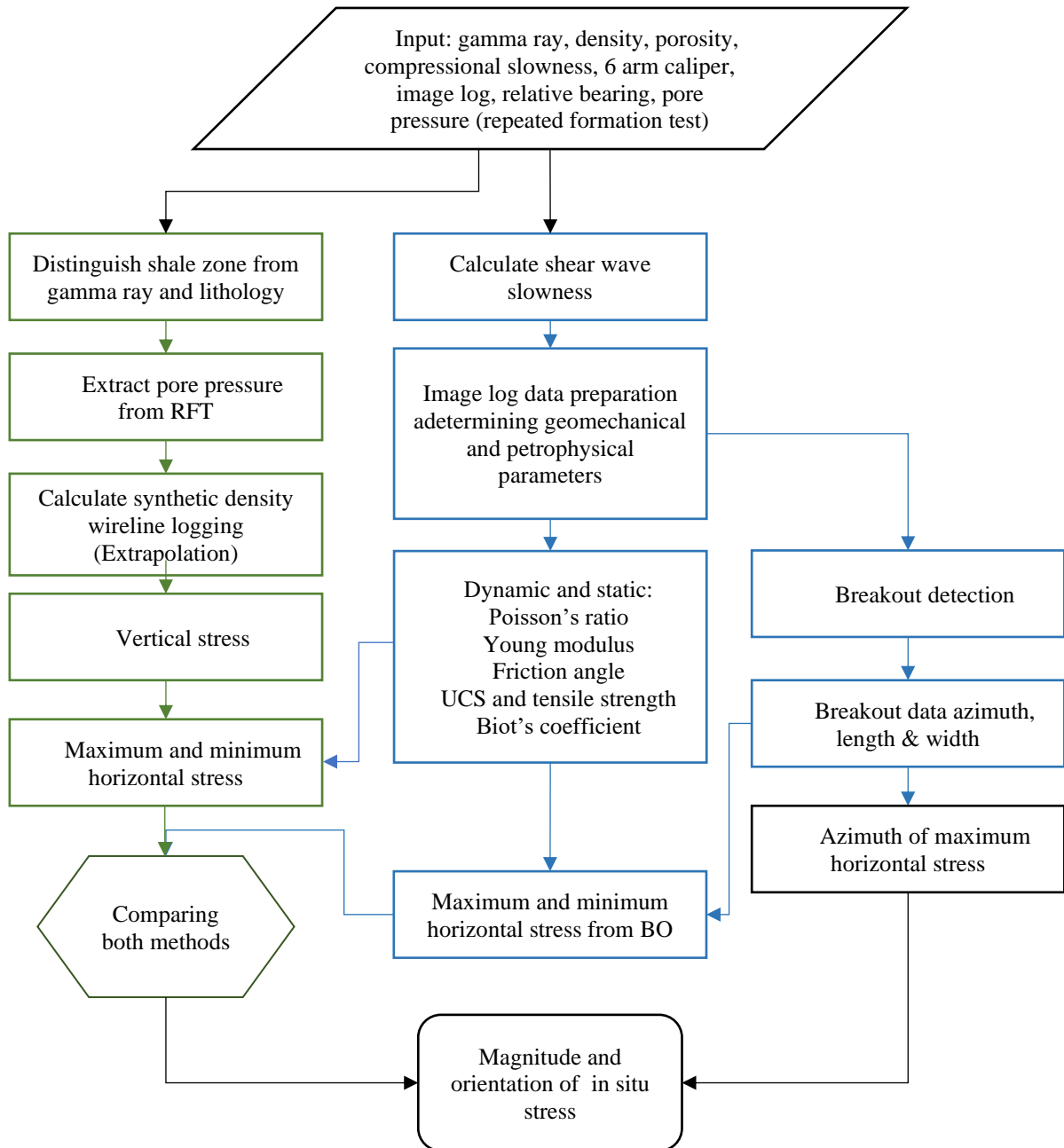


Figure 4-2. Workflow of determining magnitude and orientation of in situ stresses. Green boxes and arrows represent the method of Poroelastic strain theory and blue boxes and arrows are breakout analysis approach. Green squares and arrows represent the poroelastic strain model approach. Blue squares and arrows represent the methods based on breakout and black squares and arrows are common steps for both methods. After Mafakheri B. et al. (2022).

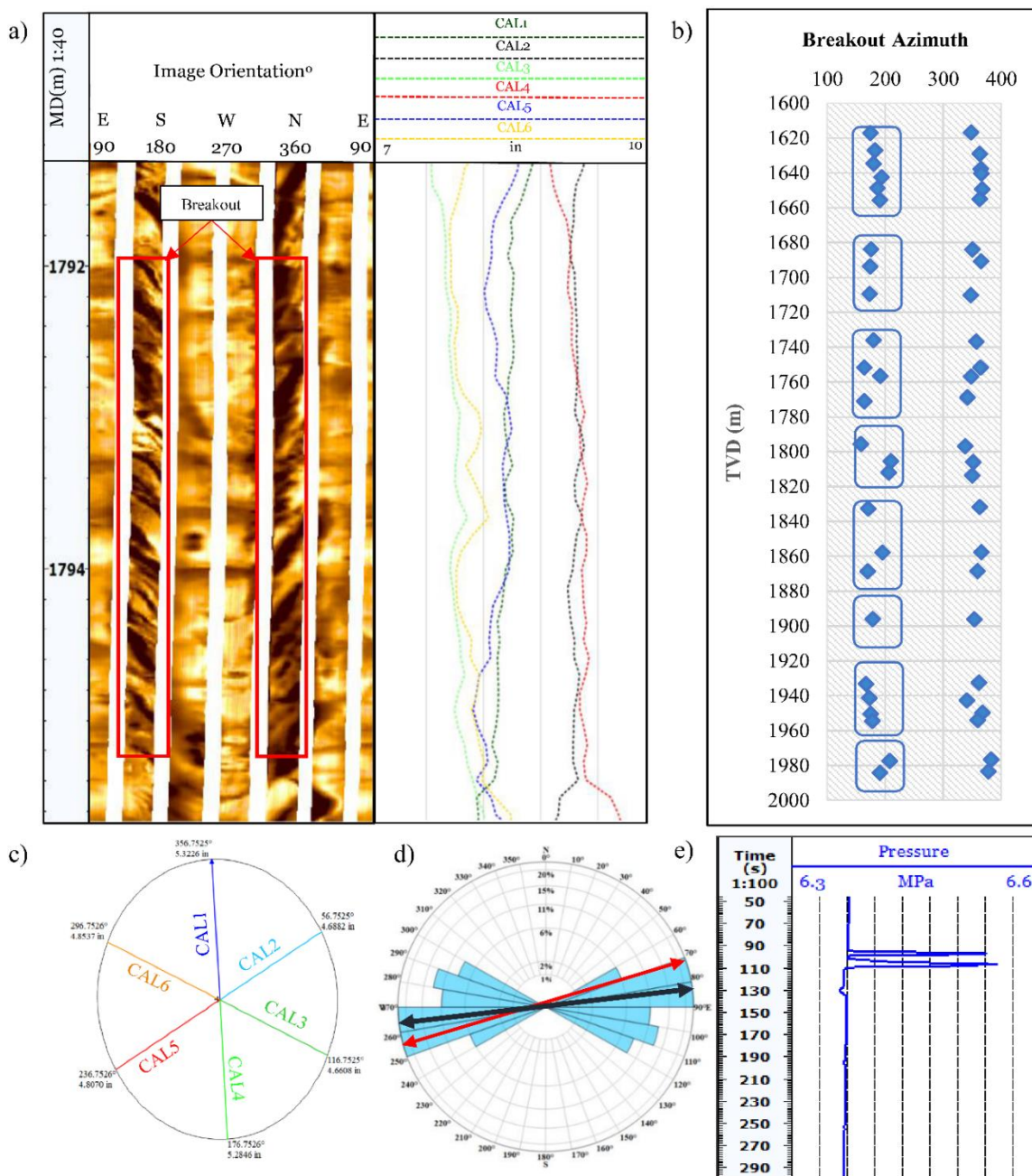


Figure 4-3. a) Dynamic borehole image log is presented on the left track. On the right track, six-arm calipers are illustrated to check the breakout detection from the image log. b) Detected breakout in the wellbore with eight distinct zones. c) Wellbore shape cross-section from Techlog to ensure the breakout detection analysis (TVD of 1620.51 m). d) Rose diagram of the azimuth of maximum horizontal stress. The black line is number weighted, and the red line is the length weighted mean azimuth. e) RFT graph for a certain depth (1720 m) to measure P_p . After Mafakheri B. et al. (2022).

The variation of the caliper also confirmed the occurrence of breakouts (Lin et al., 2010). To ensure the accuracy of breakout analysis, the borehole shape section in Techlog was used to create a horizontal section of the borehole, and it showed two distinct greater diameters from the center of the borehole in breakout zones (Figure 4-3c). Ultimately, the orientations of in-situ principal stresses were determined by combining the above-mentioned data and approaches (Figure 4-3d and Figure 4-4). In the workflow of this research, as shown in Figure 4-2, to determine the magnitudes of principal stresses, two approaches were applied and compared to ensure accuracy of the results. The first approach was the poroelastic horizontal strain theory method. This method was initially used to determine the lithology and shale zone based on wireline logging. The pore pressure was then extracted directly from a repeated formation test (RFT) (Figure 4-3e). Because the magnitudes of effective maximum and minimum horizontal stresses are dependent on pore pressure (P_p), this parameter is crucial in any geomechanical study. One principal stress that must be initially calculated is vertical stress. Therefore, minimum and maximum principal horizontal stresses were determined using pore pressure, vertical stress, and the physical properties of the rock. The other approach was used to detect breakout features, such as width and height, combined with physical properties, and the caliper log was used to determine the magnitudes of the minimum and maximum principal horizontal stresses. Ultimately, the breakout azimuth indicates the orientation of the minimum principal horizontal stress. The findings of both approaches were compared, and the results are presented in a subsequent section.

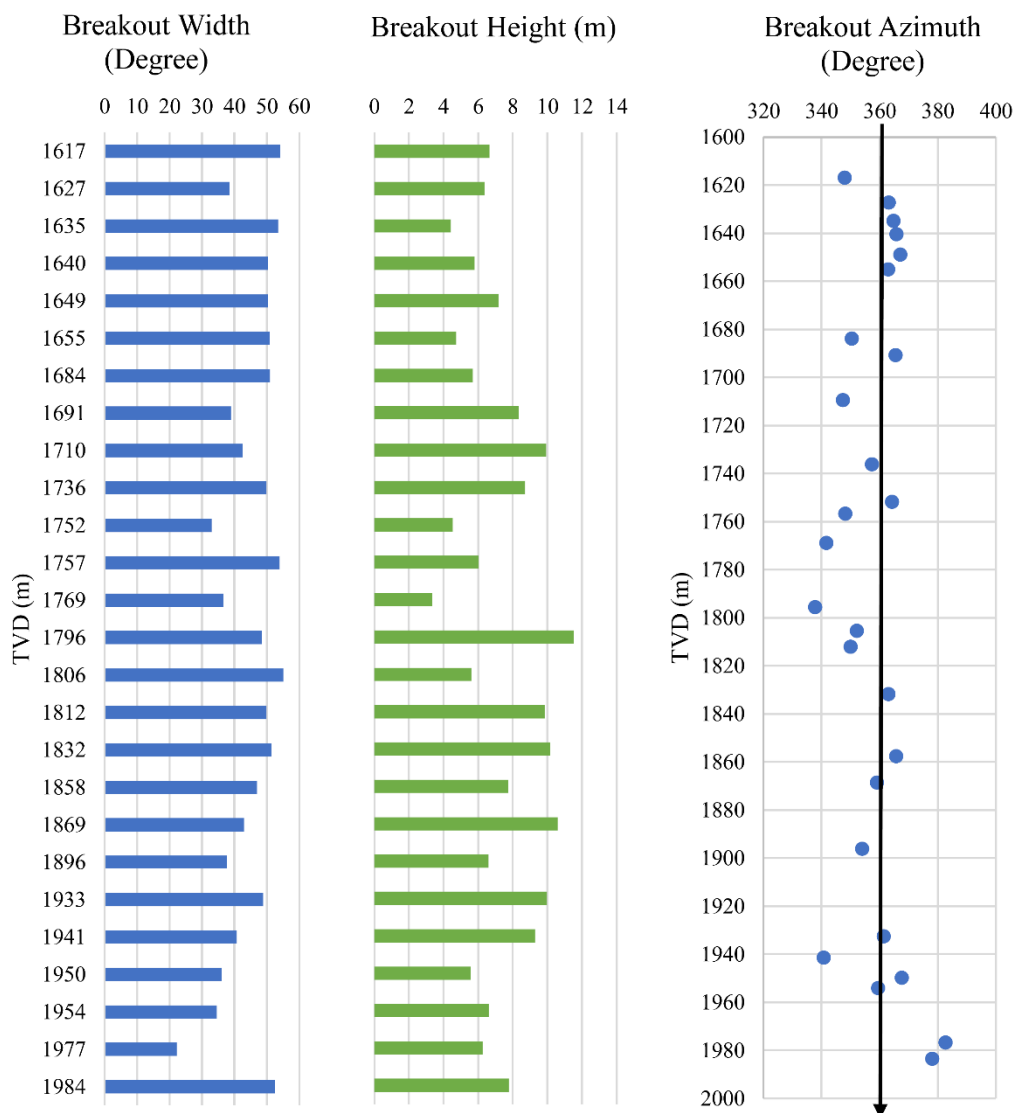


Figure 4-4. Variation of breakout width, height, and azimuth with respect to depth. After Mafakheri B. et al. (2022).

4.2.2 Orientation of maximum horizontal stress

In this section, the equations that were used to calculate the standard deviation and mean breakout azimuth are shown according to Tingay et al. (2008) and Mafakheri B. et al. (2022). The breakout orientations were mirrored on both sides of the wellbore. Therefore, breakouts between 180° and 360° are equivalent to those from the interval 0° – 180° . Thus, θ_i is the orientation of just one parallel breakout, and $\theta_i^* = 2 \theta_i$. The number-weighted and length (height)-weighted mean azimuths were calculated as below:

Number weighted:

$$C = \frac{1}{n} \sum_{i=1}^n \cos \theta_i^* \quad (4-1)$$

$$S = \frac{1}{n} \sum_{i=1}^n \sin \theta_i^* \quad (4-2)$$

Length weighted:

$$L = \sum_{i=1}^n l_i \quad (4-3)$$

$$C = \frac{1}{L} \sum_{i=1}^n l_i \cos \theta_i^* \quad (4-4)$$

$$S = \frac{1}{L} \sum_{i=1}^n l_i \sin \theta_i^* \quad (4-5)$$

where l_i is the length of each breakout and L is total length of the breakouts. The mean azimuth and standard deviation result from:

$$\theta_m = \frac{1}{2} \arctan(S/C) \quad (4-6)$$

$$R = (C^2 + S^2)^{1/2} \quad (4-7)$$

$$S_o = \frac{360}{2\pi(-\frac{1}{2} \log_e R)^{1/2}} \quad (4-8)$$

where, θ_m is the mean azimuth of the breakout and S_o is the standard deviation. The azimuth of maximum horizontal stress is an essential parameter for any geomechanical

study and one method to determine is the breakout azimuth method. The azimuth of maximum horizontal stress is perpendicular to the mean azimuth of the breakout (Zoback, 2007).

4.2.3 Magnitude of principal in situ stresses

In order to determine the magnitude of horizontal stresses, first, the breakout approach was applied in this study. Then, using the approach of (Cui et al., 2009) and (Zoback et al., 1985), horizontal stresses were determined for breakout intervals. In this method, horizontal stress depends on the borehole shape deformation caused by wellbore failure and rock physical properties. In these equations,

$$S_H = \frac{2[(d_1 + d_2)(S_c - e\Delta P) - (b_1 + b_2)(S_c - f\Delta P)]}{[(a_1 + a_2)(d_1 + d_2) - (b_1 + b_2)(c_1 + c_2)]} \quad (4-9)$$

$$S_h = \frac{2[(a_1 + a_2)(S_c - f\Delta P) - (c_1 + c_2)(S_c - e\Delta P)]}{[(a_1 + a_2)(d_1 + d_2) - (b_1 + b_2)(c_1 + c_2)]} \quad (4-10)$$

Where S_H is the maximum horizontal stress and S_h is the minimum horizontal stress. All parameters depend on rock physical properties and wellbore deformation caused by wellbore breakout. They are explained below.

The input parameters were determined using conventional logs such as sonic, natural gamma-ray, and porosity logs, as well as empirical correlations. The variable S_c represents cohesion, and was determined using the following equation from (Almalikee, 2019):

$$S_c = \frac{UCS}{2 * [(\sqrt{(1 + (\tan\phi)^2}) + \tan\phi)}]} \quad (4-11)$$

Where, UCS is unconfined compressive strength in megapascals, and ϕ is the angle of internal friction in degrees. The angle of internal friction (ϕ) (Almalikee, 2019) and the coefficient of friction (μ) (Fjær et al., 2008) were determined using the below equations which are calibrated for limestone in the study area:

$$\phi = (-0.1166*GR)+39.25 \quad (4-12)$$

$$UCS = 194.4 - 0.6072\Delta_T - 646.1\phi - 0.01644\Delta_T^2 + 8.792(\phi * \Delta_T) \quad (4-13)$$

$$\mu = \tan(\phi) \quad (4-14)$$

Here, GR is natural gamma rays in API units, Δ_T is the compressional sonic travel time in $\mu\text{sec}/\text{ft}$, and φ is the neutron porosity log (NPHI in fraction). The variables a_1 , a_2 , b_1 , b_2 , c_1 , c_2 , d_1 , d_2 , e , and f depend on several parameters as follow:

$$\begin{aligned}
 a_1 &= -\mu(1 - 2\cos 2\theta_b) \\
 a_2 &= \pm(1 + \mu^2)^{1/2}(-2\cos 2\theta_b) \\
 b_1 &= -\mu(1 + 2\cos 2\theta_b) \\
 b_2 &= \pm(1 + \mu^2)^{\frac{1}{2}}(1 + 2\cos 2\theta_b) \\
 c_1 &= -\mu\left(1 + 2\frac{a^2}{r_b^2}\right) \\
 c_2 &= \pm(1 + \mu^2)^{\frac{1}{2}}\left(1 - \frac{a^2}{r_b^2} + 3\frac{a^4}{r_b^4}\right) \\
 d_1 &= -\mu\left(1 - 2\frac{a^2}{r_b^2}\right) \\
 d_2 &= \pm(1 + \mu^2)^{\frac{1}{2}}\left(1 + 3\frac{a^2}{r_b^2} - 3\frac{a^4}{r_b^4}\right) \\
 e &= \pm(1 + \mu^2)^{\frac{1}{2}} \\
 f &= \pm(1 + \mu^2)^{\frac{1}{2}}\frac{a^2}{r_b^2}
 \end{aligned} \tag{4-15}$$

Other parameters are as follow: the coefficient of friction (μ), angle of breakout initiation with respect to the maximum horizontal stress (θ_b), depth of breakout initiation (r_b), azimuth between the direction of the maximum horizontal principal stress and the breakout region (θ), the radius of the well (a), and the difference between the borehole fluid pressure and formation pressure (ΔP). The coefficient of friction (μ) is determined by equation 4-14. In this study, borehole fluid pressure was determined based on the actual hydrostatic pressure of the mud column in the wellbore, and the formation pressure was determined directly by the extrapolation of pressure from RFT test points. The poroelastic horizontal strain model, presented by Fjær et al. (2008), considers the rock strains to determine anisotropic horizontal stresses. This approach has been used frequently to determine principal in-situ stresses (Amiri et al., 2019;

Baouche et al., 2020; Javani et al., 2017; Radwan and Sen, 2021a). The equations of vertical stress and maximum and minimum horizontal stresses are as follows:

$$S_v = \int_0^H RHOB * g dH \quad (4-16)$$

$$S_h = \frac{\nu}{1-\nu} (S_v - \alpha P_p) + \alpha P_p + \nu_s \frac{E_s}{1-\nu^2} \varepsilon_x + \frac{E_s}{1-\nu^2} \varepsilon_y \quad (4-17)$$

$$S_H = \frac{\nu}{1-\nu} (S_v - \alpha P_p) + \alpha P_p + \nu \frac{E_s}{1-\nu^2} \varepsilon_y + \frac{E_s}{1-\nu^2} \varepsilon_x \quad (4-18)$$

where S_v is the vertical in-situ stress (overburden pressure). In this study, the static Young's modulus (E_s), dynamic Young's modulus (E_d), and Poisson's ratio (ν) were estimated by the method of Wang (2017), and Biot's coefficient was estimated by the method of Wu et al. (2001):

$$E_s(GPa) = 0.4142 * E_d - 1.0593 , \quad (4-19)$$

$$E_d(GPa) = RHOB * V_s^2 \left[\frac{3V_p^2 - 4V_s^2}{V_p^2 - V_s^2} \right] \quad (4-20)$$

$$\nu = \left[\frac{V_p^2 - 2V_s^2}{2*(V_p^2 - V_s^2)} \right], \quad (4-21)$$

$$\alpha = 1 - (1 - \varphi)^{3.8}, \quad (4-22)$$

where $RHOB$ is the density from the density wireline log, V_p is the compressional wave velocity, and V_s is the shear wave velocity. In addition, P_p is pore pressure. In Equations 4-17 and 4-18, ε_x and ε_y are the strains in the S_H and S_h directions, respectively, and might be compressional or extensional according to the tectonic stresses. Therefore, they would account for calibration factors and would be expected to match estimations from rock failure observed in the image logs. The input data are presented in Table 4-1. The variables ε_y and ε_x are as given by Kidambi and Kumar (2016):

$$\varepsilon_x = S_v \frac{\nu}{E_s} \left(\frac{1}{1-\nu} - 1 \right) \quad (4-23)$$

$$\varepsilon_y = S_v \frac{\nu}{E_s} \left(1 - \frac{\nu^2}{1-\nu} \right) \quad (4-24)$$

Table 4-1. Average rock properties and geomechanical parameters for poroelastic strain theory method. After Mafakheri B. et al. (2022).

Interval number	Depth interval (m)	Density log (gr/cm³)	Porosity (%)	V_p (m/s)	V_s (m/s)	E_s (GPa)	Poisson's ratio (ν)
1	1500 - 1600	1.93	28.3	5557	2812	15.4	0.33
2	1600 - 1700	2.36	16.8	4650	2498	12.2	0.29
3	1700 - 1800	2.56	6.6	5214	2768	19.1	0.30
4	1800 - 1900	2.57	6.4	5730	2976	25.5	0.32
5	1900 - 2000	2.45	13.2	5981	3069	25.6	0.32
6	2000 - 2100	2.69	5.5	6374	3205	34.7	0.33
7	2100 - 2200	2.66	5.2	6202	3140	32.3	0.33
8	2200 - 2240	2.34	16.2	6196	3110	25.6	0.33

4.3 Results of in situ stress analysis (NW Zagros suture zone)

4.3.1 Maximum horizontal stress orientation

The entire logged depth ranges of wells A (2240 m) and B (1400 m) were evaluated, and in well B, neither breakout nor drilling-induced tensile fracture (DITF) was detected. In addition, for the same depths in well A, neither borehole breakout nor DITF was detected, and the results for both wells were consistent. However, below 1400 m in well A, breakout detection, assisted with derived lithology, six-arm caliper data, and the borehole shape cross-section, indicated a significant number of breakouts (Figure 4-3a and Figure 4-3b). Therefore, the caliper track in Figure 4-3a shows variation in the wellbore geometry, consistent with the image log. Some additional considerations were also investigated. For example, shale zones were evaluated to avoid misinterpretation among other deformations, such as washout and keyseat resulting from shale swelling with breakout. As shown in Figure 4-3b, overall, 52 distinct breakouts from 26 pairs of breakout sets were detected. In Figures 4-3a and 4-3c borehole shape section for a specific depth illustrates the borehole shape, differentiating between different forms of borehole deformation.

After all of the breakouts were detected and recorded, considering that the breakout azimuth is perpendicular to the azimuth of the principal maximum horizontal stress, a rose diagram was constructed, as illustrated in Figure 4-3d, showing the frequency of the azimuths of the principal maximum horizontal stress for a different set of azimuths. This rose diagram shows that the azimuth of the principal maximum horizontal stress was between NEE-SWW and NWW-SEE. The black arrow is the mean azimuth of the principal maximum horizontal stress based on the number weighted method, and the red arrow shows the length-weighted azimuth of the principal maximum horizontal stress.

4.3.2 Breakout quality classification

For each breakout interval, width, height, and azimuth were recorded, which would be essential later in breakout quality classification and stress analysis (Table 4-2 and Figure 4-4). Figure 4-3b, shows the overall detected breakouts for different depths. For the entire well, eight distinct breakout zones were detected.

Table 4-2. World Stress Map quality ranking criteria (Tingay et al., 2008) for breakouts interpreted from image logs. Characteristic of analyzed breakout data, including mean breakout azimuth and standard deviation (S_o). After Mafakheri B. et al. (2022).

A-Quality	B-Quality	C-Quality	D-Quality	E-Quality
≥ 10 distinct breakout zones and combined length ≥ 100 m in a single well with $S_o \geq 12^\circ$	≥ 6 distinct breakout zones and combined length ≥ 40 m in a single well with $S_o \geq 20^\circ$	≥ 4 distinct breakout zones and combined length ≥ 20 m in a single well with $S_o \geq 25^\circ$	< 4 distinct breakout zones or < 20 m combined length with $S_o \geq 40^\circ$	Wells without reliable breakouts or with $S_o > 40^\circ$
Length Weighted Mean Azimuth (degree)	Standard Deviation (degree)	Total length (m)	Number of distinct zones	
162°	11°	189	8	
-----	WSM A-quality	WSM A-quality	WSM B-quality	

According to Tingay et al. (2008), there are two methods for determining standard deviation and mean breakout azimuth: length (height) weighting and number weighting. Both methods were evaluated in this study, but because the standard deviation of breakout height (Length) was significant (3.7 m), length weighting was more likely to represent the mean azimuth. The breakout length-weighted mean azimuth was 162°; consequently, the azimuth of the principal maximum horizontal stress was 72°. In contrast, the breakout number-weighted mean azimuth was 173°, and the azimuth of the principal maximum horizontal stress was 83°.

Therefore, based on the World Stress Map standard (Tingay et al., 2008), several parameters, such as standard deviation and mean breakout azimuth, were calculated, as presented in Table 4-2. According to Figure 4-4 and Table 4-2, the standard deviation is 11°, which is lower than 12°, a criterion for quality assessment by Tingay et al. (2008). Therefore, with the total length of 189 m, the data quality could be considered as A-quality. However, the number of distinct breakout depths was less than ten and more than six, which would put the data in the category of B-quality. Nonetheless, because the distinct number of breakout zones was less than ten and considering the significant total lengths (approximately twice the minimum length for A-quality) with a low standard deviation, ultimately, the conclusion was reached that the breakout data are more likely to be of A-quality.

4.3.3 In-situ stress magnitude and stress regimes

Based on the approaches mentioned above in Methodology, the magnitudes of principal in-situ stresses, including vertical stress and the maximum and minimum horizontal stresses, were determined and plotted in Figure 4-5. Based on the breakout analysis approach, the black and blue square symbols indicate the magnitudes of the minimum and maximum horizontal stresses. In addition, continuous green and red lines indicate the minimum and maximum horizontal stresses, respectively, based on the poroelastic horizontal strain method. Linear regression from the breakout analysis approach showed correlations (R^2) of 0.7950 and 0.7889 for the maximum and minimum horizontal stresses, respectively. Both methods for determining the magnitudes of principal in-situ stresses showed relative consistency, and their trends were similar. In this study, the applied tool had caliper pads in which a single pad covered only 35° of the wellbores. However, because the average breakout width was above 50° , one of the pads was more likely to touch the bottom of the breakout, read the correct diameter of the well, and reasonably estimate breakout depth (Figure 4-6). Therefore, parameter a , which is the radius of the well, would be more accurate and could result in more accurate minimum and maximum principal horizontal stresses.

In the entire studied interval, the vertical stress varies from 2.3 to 2.5 MPa/100m. In the upper and middle Eocene formations above 1500 m, the maximum horizontal stress gradient value based on Poroelastic strain theory is 6.2 MPa/100m and gradually decreases to 5.8 MPa/100m at 1720m. While this number is varying from 5.3 to 6.3 MPa/100m for minimum horizontal stress (Figures 2-5 and 4-5). But a dramatic change in the stress is taking place in the lower Eocene around 1720 m which is most probably caused by different strength in weak Kolosh Formation compared to deeper and shallower formations. Then in the lower Paleocene, both maximum and minimum horizontal stress gradients indicate a significant increase at the level of the Khurmala Formations, where it is increased up to 38 MPa/100m and 33 MPa/100m respectively for maximum and minimum horizontal stress. The different rock physical properties including higher rock strength in Tanjero Formations could be one of the reasons for this dramatic change.

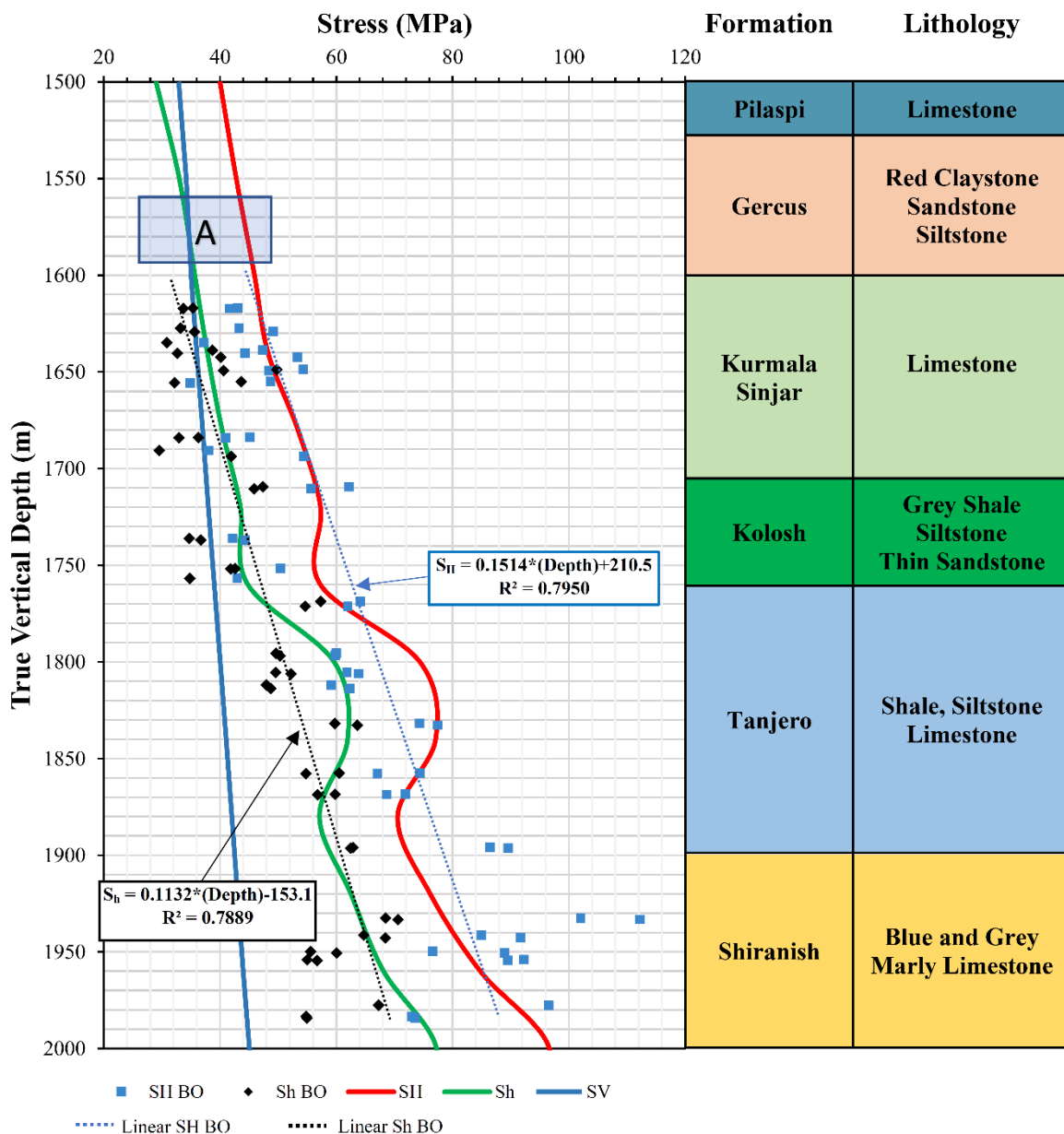


Figure 4-5. Magnitude of principal in situ stresses including vertical stress, minimum and maximum horizontal stresses. Blue line is vertical stress and Black and blue symbols illustrate the magnitudes of minimum and maximum horizontal stresses, based on the breakout analysis approach respectively. While continuous green and red lines are showing the minimum and maximum horizontal stresses respectively by using poroelastic strain theory. Straight dot blue and black lines show the linear regression for magnitudes of maximum and minimum horizontal stresses based on breakout approach respectively. Highlighted (A) is suspected depth for the stress regime change. right columns are indicating the formation and their dominant lithology. After Mafakheri B. et al. (2022).

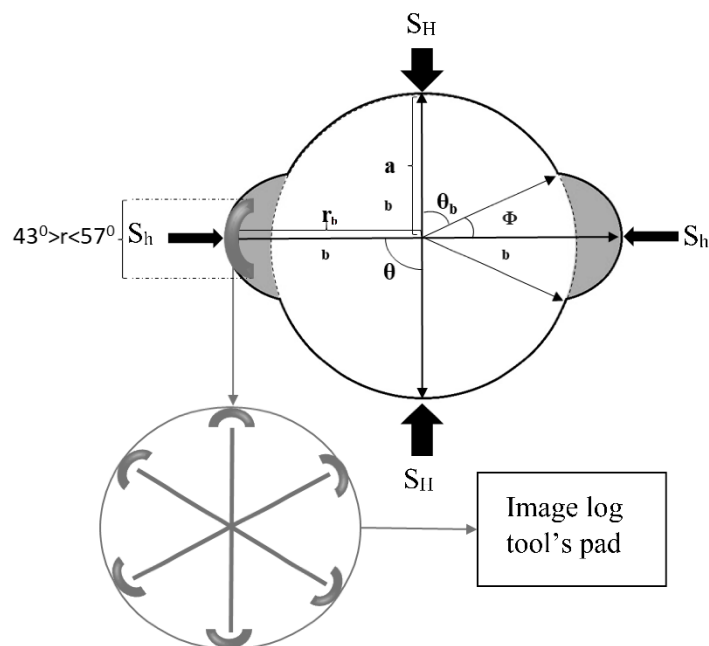


Figure 4-6. Schematic of breakout analysis parameters in the well and pads of image log tools. After Mafakheri B. et al. (2022).

In the post-Paleocene formations, the gradient rebalanced to its previous position around 6.7 MPa/100m and reach up to 10 MPa/100m in the upper Cretaceous in Shiranish formation (Table 4-1, Figures 2-6 and 4-5). Overall, the stress regime is the reverse fault stress regime ($S_H > S_h > S_v$), for middle Eocene to upper Cretaceous.

In contrast, as presented in Figure 4-5, for upper Eocene above the depth of 1600 m highlighted (A), vertical stress exceeded the minimum horizontal stress; therefore, the stress regime transformed to a strike-slip fault regime ($S_H > S_v > S_h$). In fact, the differences between all of the principal in-situ stresses became smaller. In general, the present in situ stress analysis in the studied area indicates the presence of a combined strike-slip faulting stress regime at the shallower sediments and a reverse fault stress regime at the deeper sediments.

4.3.4 Links to regional stress state and tectonic setting

The studied oilfield is located in the Kirkuk Embayment of the Zagros foothills. The oilfield is located on the crest of a slightly asymmetric anticline, which trending NW–SE towards the foreland in the Foothill Zone (Figure 4-7). There are several reservoirs but, in this study, the major reservoir is in the Shiranish Formation which is

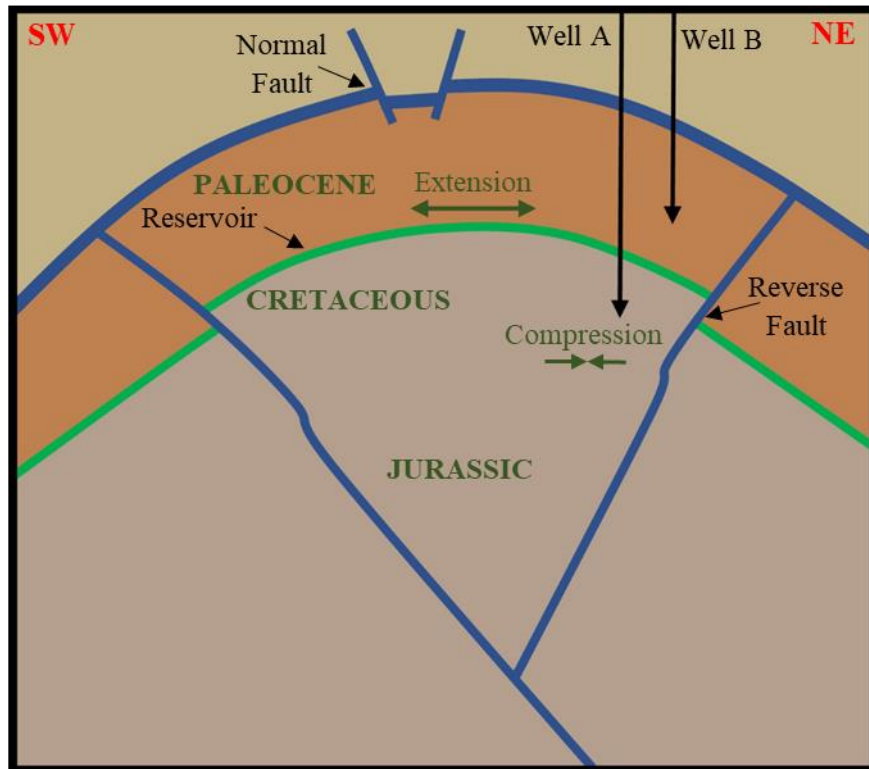


Figure 4-7. Schematic Structural geology of study area showing two major faults and geological events and stress state. After Mafakheri B. et al. (2022).

limestones and dolomites of the upper Cretaceous age. The reservoir placed between the two reverse faults isolated from the outer arc by decollement within the shales and siltstones of the Kolosh Formation (Figure 2-6 and 4-7). Jurassic reverse faulting in border between Zagros high folded and Zagros low folded zone was reported by Ameen et al. (1991) and Garland (2010) which indicate a compressional stress state and on the other hand normal faulting reported in the Cenozoic on the crest section, indicates extensional stress (Figure 4-7). Therefore, on the hinge line of the anticline normal stress regime is expected, and as it gets closer to the limbs the stress regime changes to reverse fault regime. However, in general, these anticlines are predicted to occur in an oblique orientation to a right-lateral fault. On the other hand, a regional unconformity covers the upper Cretaceous, lower Miocene, and Oligocene succession, and several hundred meters of the sedimentary section may have been eroded and removed, especially from anticlinal crests in northern Iraq (Ameen et al., 1991).

In this study, no major faults were observed from log data, and the two wells are placed on the hanging wall of one of the faults. These faults initially were suspected to play a critical role in the stress regime in different depths. But as shown in Figures 4-

3c, 4-4 and 4-5, there is no clear trend for alteration of maximum horizontal stress azimuth based on depth or even with the magnitude of in situ stresses. This fact brings us to the conclusion that there is no correlation between the orientation of in situ stress and regional geological structure including two reverse major faults. The variation of breakout azimuth most likely is local and is dependent on the rock's physical properties. Therefore, the reverse stress regime is most likely impacted by the far-field stress regime in the outer arc and is approximately consistent with the plate convergence vector reported in several studies (Doski, 2019; Regard et al., 2004; Vernant et al., 2004). In addition, in Figures 4-4 the breakout height (length) and width do not show a meaningful correlation with breakout azimuth.

A tectonic setting with a current oblique compression is a challenging and complicating factor, and possibly it causes activity on oblique structures that deviate from the regional structural patterns. The high folded zone and low folded zone are separated by the Zagros front fault (Al-Qayim et al., 2012; Berberian, 1995) (Figure 2-4) and a major morphotectonic discontinuity uplifted the high folded zone by 3–6 km with respect to the low folded zone (Le Garzic et al., 2019) (Figure 2-3). The Moho reported in depths of around 35 km in the low folded zone, and approximately 40 km in the high fold zone (Le Garzic et al., 2019). Therefore, probably the elevation of the low folded zone with respect to high folded zone can play an important role on the transformation of stress regime. Evidence for this strike-slip element has also been witnessed in the surface outcrop of sandstones and red shales of the upper Fars Formation (Awdal et al., 2016).

In the west Zagros of Iran, a major change reported in the stress state from a Miocene–Pliocene syn-folding reverse regime to a Pliocene–Recent post-folding strike-slip system, with a significant anticlockwise reorientation of the maximum horizontal stress from NE–SW to N–S (Navabpour et al., 2008). However, the change in the stress regime is consistent to the present study but there was no evidence for changing the orientation of maximum horizontal stress with respect to depth and age.

4.3.5 Regional and local origin of present-day stress field

The results of this study suggest a change in stress state from a strike-slip faulting regime at shallow depths to a reverse faulting regime at deeper levels. Therefore, probably the hanging wall of the decollement is strongly coupled between the overlying hanging wall and the subducting footwall. Even though there is not enough evidence for orientation of maximum horizontal stress above 1500m for a detailed discussion of the spatial distribution of stress, there are some hypothesis for this transformation as below: i- the stress regime variation is related to rock strength variation; ii- elevation of area with respect to high folded zone can cause different compressional effects.

Another hypothesis is the alteration of rock physical properties, including the compressive strength ductility of different geological formations, during the history of plate tectonic collision or regional unconformity caused a sudden change in physical property of rock. Furthermore, several dolomitization occurrences and hydrothermal streams formed in the carbonate formations, which likely caused the significant alteration of the physical properties of the rocks (Bretis et al., 2011; Burtscher et al., 2012). Another hypothesis is the difference in elevation between the low folded zone and high folded zone which is tightly related to presence of high mountains in the region or variations in the dip of the underlying blind thrusts, causing variable uplift and probably disturbed the stress distributions and generate complex stress patterns. In addition, above the depth of 1600 m, no breakout or drilling-induced tensile fracturing or other wellbore failures have been detected in either well A or well B in this study, which could be a reasonable clue for the occurrence of stress regime alteration.

On a regional scale as shown in Figures 2-2 and 2-5 the collision between Arabian, Eurasian and Anatolian Plate caused orogenic belt in Zagros and Taurus suture zone. As mentioned earlier the plate movement caused an oblique stress and created a compressional stress in the plate boundaries (Figure 2-4). From southeast of the study area in Figure 2-4, the azimuth of maximum horizontal stress is shifting from ENE-WSW to NE-SW in central study area and as it gets closer to the Taurus suture zone it changes to N-S. Doski (2021) suggests that according to EFM analysis the present-day tectonic stress regime in the Shiladiz area near to Taurus suture zone is reverse faulting and sinistral strike-slip faulting regime. This region displays open to gentle folding

similar to the study area of this study above blind thrusts, with a characteristic wavelength between 5 and 10 km (Reif et al., 2011) (Figure 2-4).

According to previous studies, different stress regimes have been detected in this study area based on different sources (Figure 2-4). As discussed in chapter 2 and section 4-1, because this region is seismically active, tectonic movement in the area is considerably high. According to GPS studies, the surface displacement is higher than average relative to nearby areas. Thus, the dominant source of horizontal stress in this region is most likely associated with the region's tectonics. Based on the results of this study, the range of azimuths of maximum horizontal stress is between NE–SW and NEE–SWW. Because the well is vertical, the azimuth of the maximum horizontal stress is perpendicular to the azimuth of the breakouts (162°), and consequently, the mean azimuth of the maximum horizontal stress would be 72° .

In terms of seismicity according to Garzic et al. (2019) the high relief topography with recent seismicity and various rock exposures indicate that the Kurdistan structure is controlled by the reactivation of basement faults. Furthermore, the Raniya earthquake of 2017 with a moment magnitude (M_w) of 5.1 and the epicenter is the closest to the location of the oil field (Doski, 2019). The results show that the Raniya earthquake was generated by the neotectonics reactivation of the upper Precambrian northeast-dipping blind basement thrust fault, with a small amount of strike–slip motion, at a focal depth of 8 km. This indicates that the Raniya region is subjected to a present-day compressional deformation, with a northeast-southwest-oriented maximum horizontal stress axis ($N47^\circ E$) (Doski, 2019). The result of this study is relatively consistent with the ($N72^\circ E$) for the current study.

Previous studies noted in Table 2-1 and Figure 2-4 reported that the azimuth of maximum horizontal stress varied from N–S to NE–SW. The determined $N72^\circ E$ azimuth of maximum horizontal stress was relatively consistent with the results of previous studies and tectonic movement shown in Figure 2-2 and 2-4 and was perpendicular to anticline hinges in the study area shown in Figure 2-5. However, the dominant stress regimes are reverse (thrust) faulting (TF) and strike-slip (SS) in the study area, although incidences of thrust faulting with a strike-slip component (TS) and oblique faulting (UF) have also been reported (Abdulnaby et al., 2014a).

Since the magnitudes of the three principal stresses were close to each other above 1600 m, the existence of TS and UF faulting stress regimes is likely reasonable. Another important point to consider is the depth of investigation. As discussed in previous sections, different methods were used with significantly different depths of investigation. For example, GPS, EFM, DEM, fault analysis (FA), surface fracture analysis (SFA), and InSAR have different approaches and different depths of investigation. For instance, in the EFM method, the depth of the earthquake's epicenter can affect the depth of investigation of the stress regime. Therefore, evaluating all mentioned hypotheses in the future may help engineers and geologists to understand the distribution and transformation of the stress regimes.

4.3.6 Implications for petroleum exploration and development

The orientations and magnitudes of present-day stresses, according to Zoback (2007), are critical to borehole stability, fracture stimulation, water flooding, and fault reactivation. Radwan and Sen (2021a, 2021b) refer to the stress changes and redistribution in subsurface sediments as a major challenge in oil drilling and production. In the study area, mechanical wellbore instability may be a significant issue for the drilling of hydrocarbon wells in the study area, based on the numerous wide and highly eccentric breakouts observed in this study. The observed variation of breakout width, height, and azimuth with respect to depth in figures 4-3 and 4-4 indicate drilling challenges across the entire sediments of the studied field. The redistribution of stresses and the transition from a strike-slip faulting stress regime to a reverse fault stress regime is critical and definitely will affect the hole stability in the drilled wells across the field, which should be taken into consideration during future well planning. According to Moos et al (1998), raising the mud weight and/or adjusting borehole deviation and azimuth to reduce circumferential stress acting on the wellbore can reduce the mechanical instability and number of breakouts along the drilled formations. The constructed model in this study could provide critical help for drilling engineers in terms of well planning and well trajectory. For example, in the studied field, considering drilling hydrocarbon wells in a strike-slip stress regime, horizontal wells drilled toward the maximum horizontal stress are the most stable because they have the least stress

anisotropy (Peska and Zoback, 1995). On the contrary, the least stable borehole is likely to be found in the vertical wells because it has the greatest stress anisotropy (Baouche et al., 2022). On the other hand, considering drilling hydrocarbon wells in reverse faulting stress regimes, drilling in the direction of the maximum horizontal stress will increase the borehole stability. Therefore, the safe azimuth of any future horizontal well should be along N72°E which is the azimuth of maximum horizontal stress. On the other hand, considering the complexities of reservoir exploration and development, it is vital to understand the geomechanical properties of the reservoir and well in the drilling operation. According to English et al. (2015), most of the exploration effort in the Kurdistan region of Iraq has focused on fractured dolomitic limestone formations. As a result, understanding the magnitude and orientation of in situ stresses will aid drillers and reservoir engineers in choosing the most appropriate safe trajectories to maximize productivity.

In addition, the Zagros is an orogen dominated by flexural processes making it ideal for hydrocarbon generation and storage. But on the other hand, many potential reservoirs in the Zagros belt experienced several tectonic stages and many fault systems changed the cap rock integrity and led to depletion of the reservoir or even in some cases conducted produced hydrocarbons to another oil trap. Although this study is mainly focused on the present-day stress state, for future work, the study of the evolution of stress patterns and tectonics could be beneficial for petroleum exploration and development and suggests possible locations for further exploration.

4.4 Comparison between breakout and poroelastic strain theory method

In this section, the result of empirical correlations introduced in section 4.2 will be compared to show their application in accurately estimating horizontal stresses according to Mafakheri B. et al. (2023). As shown in Figure 4-5 and 4-8, the magnitudes of principal in-situ stresses, including vertical stress and the maximum and minimum horizontal stresses, were determined, and plotted. As presented in Figure 4-5 and the stress polygon in Figure 4-9, around a depth of 1600 m, based on both approaches, the vertical stress likely exceeds the minimum horizontal stress, and the stress regime is strike-slip. However, below 1600 m, the dominant stress regime is a reverse (thrust) fault stress regime. Figures 4-8a and 4-8b plotted and compared maximum and minimum horizontal stresses from the poroelastic strain versus the breakout method. The up/down bars represent the differences between the two results. For most intervals, there are similarities between the change in up/down bars for both maximum and minimum horizontal stresses. No dramatic differences in the results have been observed.

Ideally, these empirical methods should be calibrated with direct measurements of horizontal stress, such as the leak-off test and mini-frac test. Unfortunately, in this study, such data was not available. However, there were no certain methods for calibrating the results, but calibrating these approaches together would enable us to improve the estimation in future cases. Therefore, the estimated value of horizontal stresses would be more reliable if a good match between the predicted horizontal in situ stresses from the poroelastic strain method and results from the breakout approach in the wellbore were observed. Figure 4-9 shows this field's stress polygon for four different approximate depths. However, the stress regime based on both methods is significantly consistent, but the data points are more scattered in deeper intervals. This fact opens the door for several hypotheses behind the inconsistencies.

As shown in Figures 4-5, 4-8a, and 4-8b, different depths show variation in average maximum and minimum horizontal differences. On the other hand, the limestone formation in the shallower depths shows the least difference. It probably indicates that the poroelastic strain theory is more consistent with the breakout approach in this interval.

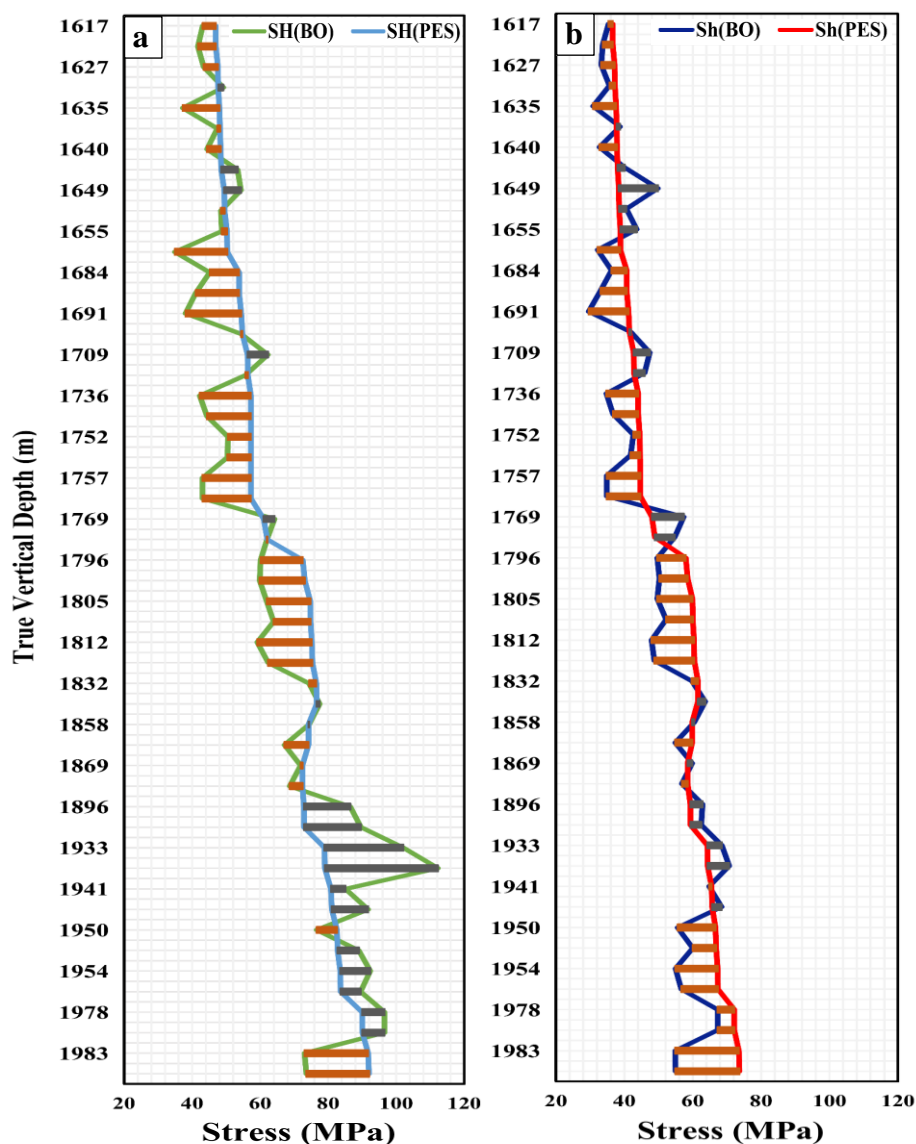


Figure 4-8. Comparison of maximum horizontal stress based on both approaches. Up/down bars indicate the differences between the results. Orange bars indicate that horizontal stress derived from Poroelastic strain theory is greater than the breakout method, and grey bars show the opposite. After Mafakheri B. et al. (2023).

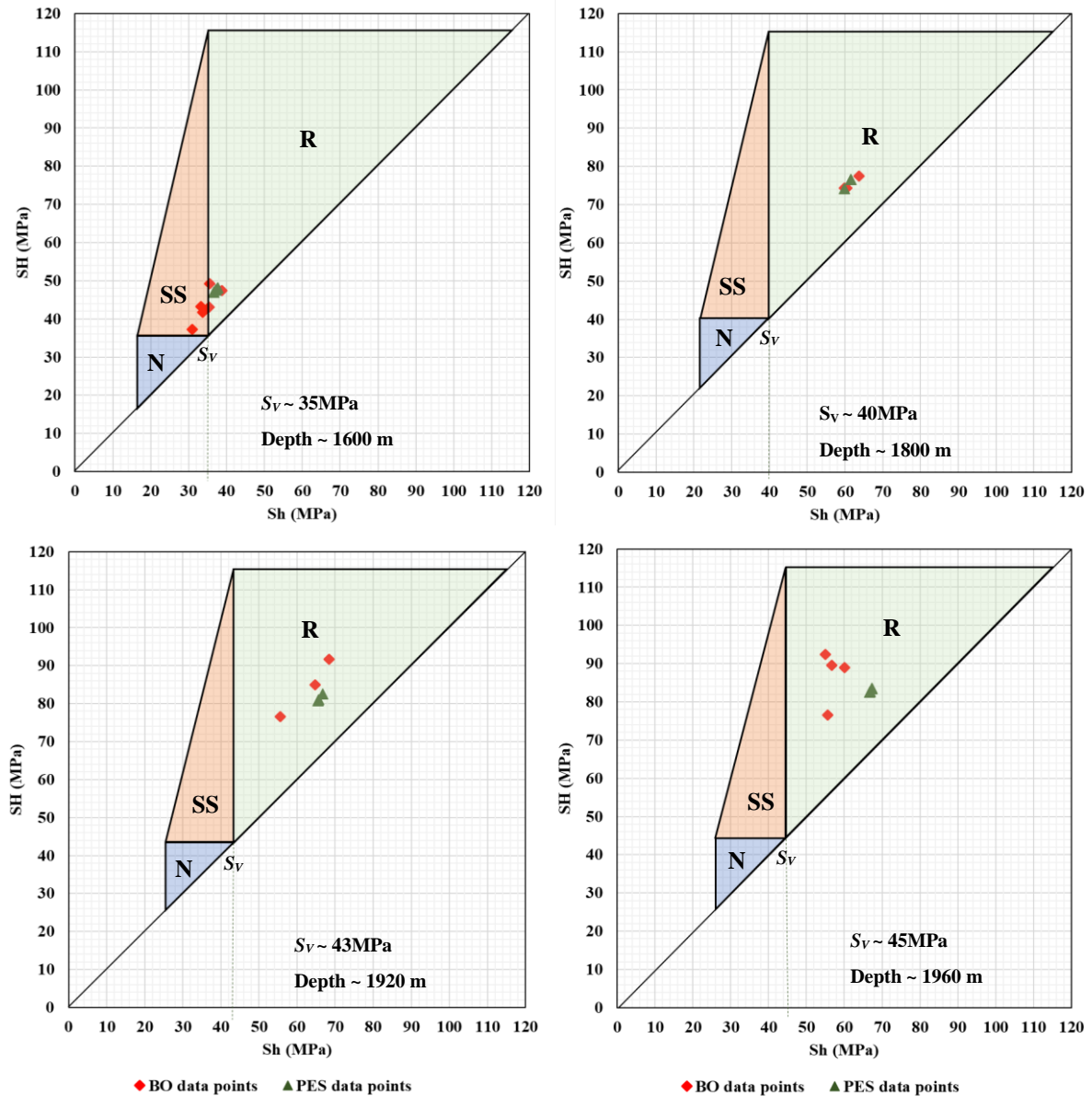


Figure 4-9. Comparison between the results of breakout and poroelastic strain method for maximum and minimum horizontal in situ stresses by stress polygon in well A. Red diamonds represent the estimated stress based on breakout approach and green triangles based on poroelastic strain model. Light green, brown and blue triangles show reverse stress regime (R), strike-slip regime (SS) and normal faulting stress regime (N), respectively. After Mafakheri B. et al. (2023).

There are several hypotheses for explaining these differences. First, as mentioned earlier, the average horizontal stress differences generally increase in deeper intervals, and consequently, the calibration would be less reliable. Second, the stress regime affects the consistency of results. For example, the intervals with a strike-slip regime show a

lower difference, and the reverse fault regime reveals a higher difference. Third, the lithology and physical properties of rock influence the differences between the results of the two methods. For example, pure limestone shows the lowest differences, and formations with higher clay content indicate relatively greater differences. It is well known that the physical properties of rock, such as rock strength, young modulus, and friction angle, play an important role in the mechanism of borehole breakout occurrence and make a greater difference in the results. Besides, in Equations 4-15, the accuracy of the depth of breakout initiation (r_b) greatly impacts the results of the horizontal stresses. Finally, the results could be misinterpreted since the mud cake thickness on the breakout surface is associated with lithology. Even though these hypotheses stand on a reasonable pillar, there are some counterexamples in some depths. For instance, based on the first hypothesis, the average horizontal stress differences in Figure 4-5, the shale-siltstone-limestone formation should have a higher difference than the grey shale formation, but the results are the opposite. In reality, a combination of mentioned reasons probably caused the differences between the two methods.

In the last step, the comparison was conducted between two sets of results in order to calibrate the poroelastic strain results with the breakout approach. As shown in figure 4-10, the minimum horizontal stress derived from the borehole breakout approach and poroelastic strain method has a slightly higher correlation than the maximum horizontal stress. The R-squared value for minimum and maximum horizontal stress is 0.73 and 0.71, respectively. Eventually, the following equations are suggested to calibrate the horizontal stresses based on the Poroelastic strain method:

$$S_{h(PES)}^* = 0.86S_{h(PES)} + 27 \quad (4-25)$$

$$S_{H(PES)}^* = 0.61S_{H(PES)} + 10.2 \quad (4-26)$$

where $S_{H(PES)}^*$ is calibrated maximum horizontal stress and $S_{h(PES)}^*$ is calibrated minimum horizontal stress.

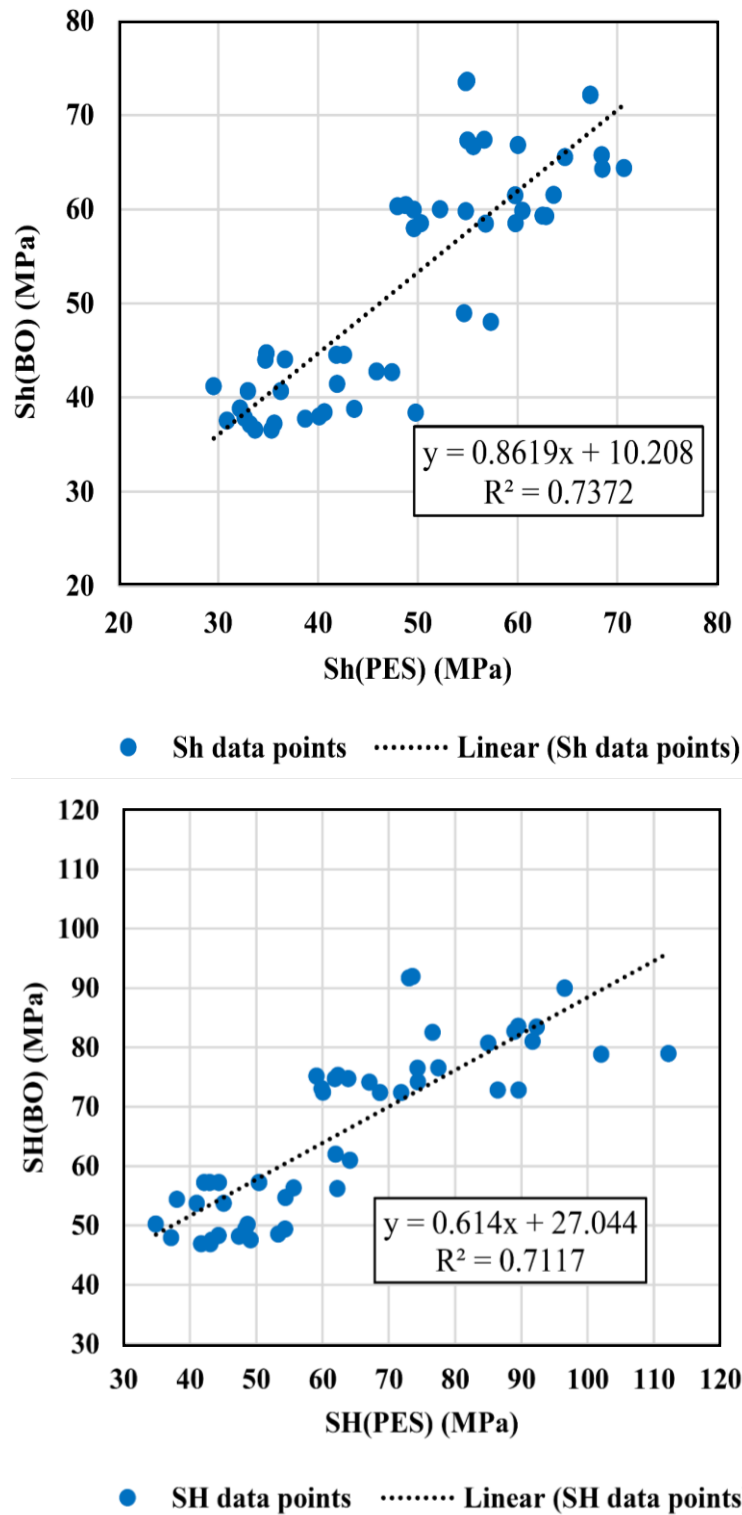


Figure 4-10. Comparison of the maximum and minimum horizontal stress derived from borehole breakout approach and poroelastic strain method. After Mafakheri B. et al. (2023).

4.5 Summary

This chapter primarily explores the regional stress regime and horizontal stress orientation in the northwestern Zagros suture zone. It highlights the varied stress regimes in the region, from thrust faulting to strike-slip faulting, influenced by tectonic activities such as the collision between the Arabian and Eurasian plates. To study the present-day stress state of the Zagros suture zone in the Kurdistan region of Iraq, two sets of well log data from actual measurements in the wellbore were analyzed.

The chapter methodologically explains how to determine principal in-situ stresses by combination of conventional logs, borehole image logs, and mechanical caliper data. The methodologies for determining the magnitude and orientation of stresses, as well as the analysis of breakout features and their implications on stress orientation, are elaborately discussed. The chapter also covers the mathematical models and empirical correlations used for the analyses. The chapter also conduct a comparison between breakout and poroelastic strain theory methods, analyzing their applications in estimating horizontal stresses.

The mean azimuth of the maximum horizontal in-situ stress, N72°E, is consistent with the tectonic movement and previous studies from different methods in the nearby Zagros suture zone. The pattern of tectonic stress fields was found to be mainly controlled by the collision between the Arabian and Eurasian plates, and our stress analysis revealed stress states that corresponded to regional tectonics.

Furthermore, it integrates regional tectonic settings with local stress fields, discussing the relationship between structural geology, fault systems, and stress states in the context of petroleum exploration and development. In terms of drilling implications, the redistribution of stresses and the transition from a strike-slip faulting stress regime to a reverse fault stress regime found to be critical and will undoubtedly affect hole stability in the drilled wells throughout the field, which should be considered during future well planning.

References

- Abdulnaby, W., Mahdi, H., Al-Shukri, H., Numan, N.M.S., 2014a. Stress Patterns in Northern Iraq and Surrounding Regions from Formal Stress Inversion of Earthquake Focal Mechanism Solutions. *Pure Appl Geophys* **171**, 2137–2153. <https://doi.org/10.1007/s00024-014-0823-x>
- Abdulnaby, W., Mahdi, H., Numan, N.M.S., Al-Shukri, H., 2014b. Seismotectonics of the Bitlis-Zagros Fold and Thrust Belt in Northern Iraq and Surrounding Regions from Moment Tensor Analysis. *Pure Appl Geophys* **171**, 1237–1250. <https://doi.org/10.1007/s00024-013-0688-4>
- Afra, M., Moradi, A., Pakzad, M., 2017. Stress regimes in the northwest of Iran from stress inversion of earthquake focal mechanisms. *J Geodyn* **111**, 50–60. <https://doi.org/10.1016/j.jog.2017.08.003>
- Almalikee, H.S., 2019. Predicting Rock Mechanical Properties from Wireline Logs in Rumaila Oilfield. *American Journal of Geophysics, Geochemistry and Geosystems* **5**, 69-77.
- Al-Qayim, B., Omer, A., Koyi, H., 2012. Tectonostratigraphic overview of the Zagros Suture Zone, Kurdistan Region, Northeast Iraq. *GeoArabia* **17**, 109–156. <https://doi.org/https://doi.org/10.2113/geoarabia1704109>
- Ameen, M., Solutions, O.G., Mohammed, S., 1991. Alpine geowarpings in the Zagros-Taurus Range: influence on hydrocarbon generation, migration and accumulation. *Journal of Petroleum Geology* **14**, 417-428. <https://doi.org/10.1111/j.1747-5457.1991.tb01034.x>
- Amiri, M., Lashkaripour, G.R., Ghabezloo, S., Moghaddas, N.H., Tajareh, M.H., 2019. Mechanical earth modeling and fault reactivation analysis for CO₂-enhanced oil recovery in Gachsaran oil field, south-west of Iran. *Environ Earth Sci* **78**, 1–22. <https://doi.org/10.1007/s12665-019-8062-1>
- Awdal, A., Healy, D., Alsop, G.I., 2016. Fracture patterns and petrophysical properties of carbonates undergoing regional folding: A case study from Kurdistan, N Iraq. *Mar Pet Geol* **71**, 149–167. <https://doi.org/10.1016/j.marpetgeo.2015.12.017>
- Awdal, A.H., Braathen, A., Wennberg, O.P., Sherwani, G.H., 2013. The characteristics of fracture networks in the Shiranish formation of the Bina Bawi Anticline;

- comparison with the Taq Taq Field, Zagros, Kurdistan, NE Iraq. *Petroleum Geoscience* **19**, 139–155. <https://doi.org/10.1144/petgeo2012-036>
- Bailin, W., 2001. Boit's Effective Stress Coefficient Evaluation: Static And Dynamic Approaches. *ISRM International Symposium - 2nd Asian Rock Mechanics Symposium*.
- Baouche, R., Sen, S., Ferial, H.A., Radwan, A.E., 2022. Estimation of horizontal stresses from wellbore failures in strike-slip tectonic regime: A case study from the Ordovician reservoir of the Tinzaouatine field, Illizi Basin, Algeria. *Interpretation* **10**, SF37–SF44. <https://doi.org/10.1190/INT-2021-0254.1>
- Baouche, R., Sen, S., Ganguli, S.S., 2020. Pore pressure and in-situ stress magnitudes in the Bhiret Hammou hydrocarbon field, Berkine Basin, Algeria. *Journal of African Earth Sciences* **171**, 103945. <https://doi.org/10.1016/j.jafrearsci.2020.103945>
- Berberian, M., 1995. Master “blind” thrust faults hidden under the Zagros folds: active basement tectonics and surface morphotectonics. *Tectonophysics* **241**, 193–224 . [https://doi.org/10.1016/0040-1951\(94\)00185-C](https://doi.org/10.1016/0040-1951(94)00185-C)
- Bretis, B., Bartl, N., Grasemann, B., 2011. Lateral fold growth and linkage in the Zagros fold and thrust belt (Kurdistan, NE Iraq). *Basin Research* **23**, 615–630. <https://doi.org/10.1111/j.1365-2117.2011.00506.x>
- Burtscher, A., Frehner, M., Grasemann, B., 2012. Tectonic geomorphological investigations of antiforms using differential geometry: Permian anticline, northern Iraq. *Am Assoc Pet Geol Bull* **96**, 301–314. <https://doi.org/10.1306/06141110204>
- Cui, J. wen, Wang, L. jie, Li, P., Tang, Z. min, Sun, D. sheng, 2009. Wellbore breakouts of the main borehole of Chinese Continental Scientific Drilling (CCSD) and determination of the present tectonic stress state. *Tectonophysics* **475**, 220–225. <https://doi.org/10.1016/j.tecto.2009.03.021>
- Doski, J.A.H., 2021. Active tectonics along the Sheladiz seismogenic fault in the Western Zagros fold-thrust belt, Kurdistan, Northern Iraq. *International Journal of Earth Sciences* **110**, 595–608. <https://doi.org/10.1007/s00531-020-01973-y>
- Doski, J.A.H., 2019. Tectonic interpretation of the Raniya earthquake, Kurdistan, northern Iraq. *J Seismol* **23**, 303–318. <https://doi.org/10.1007/s10950-018-9807-0>

- Doski, J.A.H., Mohammad, R.J., 2016. Tectonic analysis of the Shaikhan earthquakes, Kurdistan, Northern Iraq. *Arabian Journal of Geosciences* **9**, 1–12. <https://doi.org/10.1007/s12517-015-2023-0>
- English, J.M., Lunn, C.A., Ferreira, L., Yacu, G., 2015. Geologic evolution of the Iraqi Zagros, and its influence on the distribution of hydrocarbons in the Kurdistan region. *Am Assoc Pet Geol Bull* **99**, 231–272. <https://doi.org/10.1306/06271413205>
- Fjær, E., Holt, R.M., Horsrud, P., Raaen, A.M., Risnes, R., 2008. Petroleum Related Rock Mechanics, 2nd Edition. ed, Mar. Environ. Res. Elsevier. [https://doi.org/10.1016/S0376-7361\(07\)53013-X](https://doi.org/10.1016/S0376-7361(07)53013-X)
- Garland, C.R., Abalioglu, I., Akca, L., Cassidy, A., Chiffolleau, Y., Godail, L., Grace, M.A.S., Kader, H.J., Khalek, F., Legarre, H., Nazhat, H.B., Sallier, B., 2010. Appraisal and development of the Taq Taq field, Kurdistan region, Iraq. *Petroleum Geology Conference Proceedings* **7**, 801–810. <https://doi.org/10.1144/0070801>
- Gilchrist, C.J.D., Cosgrove, J.W., Parmassar, K.J., 2020. Critically stressed fractures: analysis of the Shaikhan Field, Kurdistan Region of Iraq. *J Geol Soc London* **177**, 1315–1328. <https://doi.org/10.1144/jgs2019-136>
- Heidbach, O., Rajabi, M., Cui, X., Fuchs, K., Müller, B., Reinecker, J., Reiter, K., Tingay, M., Wenzel, F., Xie, F., Ziegler, M.O., Zoback, Mary Lou, Zoback, Mark, 2018. The World Stress Map database release 2016: Crustal stress pattern across scales. *Tectonophysics* **744**, 484–498. <https://doi.org/10.1016/J.TECTO.2018.07.007>
- Javani, D., Aadnoy, B., Rastegarnia, M., Nadimi, S., Aghighi, M.A., Maleki, B., 2017. Failure criterion effect on solid production prediction and selection of completion solution. *Journal of Rock Mechanics and Geotechnical Engineering* **9**, 1123–1130. <https://doi.org/10.1016/j.jrmge.2017.07.004>
- Kidambi, T., Kumar, G.S., 2016. Mechanical Earth Modeling for a vertical well drilled in a naturally fractured tight carbonate gas reservoir in the Persian Gulf. *J Pet Sci Eng* **141**, 38–51. <https://doi.org/10.1016/j.petrol.2016.01.003>
- Kobayashi, T., Morishita, Y., Yurai, H., Fujiwara, S., 2018. InSAR-derived Crustal Deformation and Reverse Fault Motion of the 2017 Iran-Iraq Earthquake in the

- Northwest of the Zagros Orogenic Belt. *Bulletin of the Geospatial Information Authority of Japan* 1–9.
- Le Garzic, E., Vergés, J., Sapin, F., Saura, E., Meresse, F., Ringenbach, J.C., 2019. Evolution of the NW Zagros Fold-and-Thrust Belt in Kurdistan Region of Iraq from balanced and restored crustal-scale sections and forward modeling. *J Struct Geol* **124**, 51–69. <https://doi.org/10.1016/j.jsg.2019.04.006>
- Lin, W., Doan, M.L., Moore, J.C., McNeill, L., Byrne, T.B., Ito, T., Saffer, D., Conin, M., Kinoshita, M., Sanada, Y., Moe, K.T., Araki, E., Tobin, H., Boutt, D., Kano, Y., Hayman, N.W., Flemings, P., Huftile, G.J., Cukur, D., Buret, C., Schleicher, A.M., Efimenko, N., Kawabata, K., Buchs, D.M., Jiang, S., Kameo, K., Horiguchi, K., Wiersberg, T., Kopf, A., Kitada, K., Eguchi, N., Toczko, S., Takahashi, K., Kido, Y., 2010. Present-day principal horizontal stress orientations in the Kumano forearc basin of the southwest Japan subduction zone determined from IODP NanTroSEIZE drilling Site C0009. *Geophys Res Lett* **37**, 1–6. <https://doi.org/10.1029/2010GL043158>
- Mafakheri B., N., Lin, W., Khaksar Manshad, A., 2023. Determining the Magnitudes of Maximum and Minimum Horizontal Stresses from Borehole Data: Comparison Between Borehole Failure Approach and Poroelastic Strain Model, in: Proceedings of the *ISRM 15th International Congress on Rock Mechanics and Rock Engineering & 72nd Geomechanics Colloquium – Challenges in Rock Mechanics and Rock Engineering*, Schubert, W. & Kluckner, A. (Eds). ISRM , Salzburg, Austria , pp. 2128–2133.
- Mafakheri B., N., Lin, W., Murata, S., Yousefi, F., Radwan, A.E., 2022. Magnitudes and orientations of present-day in-situ stresses in the Kurdistan region of Iraq: Insights into combined strike-slip and reverse faulting stress regimes. *J Asian Earth Sci* **239**, 105398. <https://doi.org/10.1016/j.jseaes.2022.105398>
- Mafakheri B., N., Lin, W., Yousefi, F., 2021. Using the combination of conventional logs, borehole image log, and six-arm caliper for determining the orientation and magnitude of principal in-situ stresses: A case study in Zagros suture zone in Kurdistan Region of Iraq, in: *Proceedings of the 14th SEGJ International Symposium*. 218–221. <https://doi.org/10.1190/segj2021-058.1>

- Moos, D., Peska, P., Zoback, M.D., 1998. Predicting the Stability of Horizontal Wells and Multi-Laterals - The Role of In Situ Stress and Rock Properties. *SPE International Conference on Horizontal Well Technology*. <https://doi.org/10.2118/50386-MS>
- Navabpour, P., Angelier, J., Barrier, E., 2008. Stress state reconstruction of oblique collision and evolution of deformation partitioning in W-Zagros (Iran, Kermanshah) 755–782. <https://doi.org/10.1111/j.1365-246X.2008.03916.x>
- Obaid, A.K., Allen, M.B., 2017. Landscape maturity, fold growth sequence and structural style in the Kirkuk Embayment of the Zagros, northern Iraq. *Tectonophysics* **717**, 27–40. <https://doi.org/10.1016/j.tecto.2017.07.006>
- Peska, P., Zoback, M.D., 1995. Compressive and tensile failure of inclined well bores and determination of in situ stress and rock strength. *J Geophys Res Solid Earth* **100**, 12791–12811. <https://doi.org/10.1029/95JB00319>
- Radwan, A., Sen, S., 2021a. Stress Path Analysis for Characterization of In Situ Stress State and Effect of Reservoir Depletion on Present-Day Stress Magnitudes: Reservoir Geomechanical Modeling in the Gulf of Suez Rift Basin, Egypt. *Natural Resources Research* **30**, 463–478. <https://doi.org/10.1007/s11053-020-09731-2>
- Radwan, A., Sen, S., 2021b. Characterization of in-situ stresses and its implications for production and reservoir stability in the depleted El Morgan hydrocarbon field, Gulf of Suez rift basin, Egypt. *J Struct Geol* **148**, 104355. <https://doi.org/10.1016/j.jsg.2021.104355>
- Regard, V., Bellier, O., Thomas, J.C., Abbassi, M.R., Mercier, J., Shabanian, E., Feghhi, K., Soleymani, S., 2004. Accommodation of Arabia-Eurasia convergence in the Zagros-Makran transfer zone, SE Iran: A transition between collision and subduction through a young deforming system. *Tectonics* **23**, 1–25. <https://doi.org/10.1029/2003TC001599>
- Reif, D., Grasemann, B., Faber, R.H., 2011. Quantitative structural analysis using remote sensing data: Kurdistan, northeast Iraq. *Am Assoc Pet Geol Bull* **95**, 941–956. <https://doi.org/10.1306/11151010112>
- Tingay, M., Reinecker, J., Müller, B., 2008. Borehole breakout and drilling-induced fracture analysis from image logs. *World stress map* 1–8. http://dc-app3-14.gfz-potsdam.de/pub/guidelines/WSM_analysis_guideline_breakout_image.pdf

- Vernant, P., Nilforoushan, F., Hatzfeld, D., Abbassi, M.R., Vigny, C., Masson, F., Nankali, H., Martinod, J., Ashtiani, A., Bayer, R., Tavakoli, F., Chéry, J., 2004. Present-day crustal deformation and plate kinematics in the Middle East constrained by GPS measurements in Iran and northern Oman. *Geophys J Int* **157**, 381–398. <https://doi.org/10.1111/j.1365-246X.2004.02222.x>
- Wang, H.F., 2017. Theory of Linear Poroelasticity with Applications to Geomechanics and Hydrogeology. *Princeton University Press*. <https://doi.org/doi:10.1515/9781400885688>
- Zoback, M.D., 2007. Reservoir Geomechanics, *Cambridge University Press*. <https://doi.org/10.1017/CBO9780511586477>
- Zoback, M.D., Moos, D., Mastin, L., Anderson, R.N., 1985. Well Bore Breakouts and in Situ Stress. *J Geophys Res* **90**, 5523–5530. <https://doi.org/10.1029/JB090iB07p05523>

Chapter 5

Stress state of southeastern Zagros suture zone

5.1 Background

Complex structures with different stress regimes pose challenges in tectonic studies and have implications for the oil and gas industry. The analysis of in-situ stress state and natural fractures in the Dezful Embayment, the southwestern part of the Zagros fold and thrust belt (ZFTB) in Iran, and their implications for tectonic and oil field development are poorly understood. This study investigated the stress profiles for eight wellbores of the Asmari reservoir, located in two oil fields in southwestern Iran (Figure 2-7). The studied fields are located in the low-folded ZFTB. According to several previous studies, reverse faulting and fault propagation folds caused a reverse stress regime in several depths in this area (e.g., Berberian, 1995; Derikvand et al., 2018; Lacombe et al., 2011). Nevertheless, little attention was paid to the present-day state of stress, geological factors resulting in stress variation, and stress distribution patterns in the studied region and their impact on hydrocarbon resource management.

By analyzing the shape and orientation of multiple borehole breakouts, geologists can use statistical techniques to determine the most likely orientation of the maximum horizontal stress direction. This information can help plan the drilling of additional boreholes or understand the behavior of rock formations in the subsurface. Due to the complexity of implementation and high cost, direct method tests are rarely applicable, especially in deeper wells. In addition, these tests do not result in a continuous value for the magnitude of in situ stress. Indirect methods are widely used to determine profiles of stresses with respect to depth (Baouche et al., 2022; Lin et al., 2011; Mafakheri B. et al., 2022; Oohashi et al., 2017; Radwan and Sen, 2021b; Tang et al., 2021; Wang, 2017; Zoback et al., 2003).

5.2 Methodology

5.2.1 Workflow

The data presented in this analysis has been generously provided by a prominent oil company, though specific details regarding the exact fields and locations remain undisclosed to protect proprietary and sensitive information. This study's methodology includes four concurrent Processes. First, determining the lithology of the study formations to assist further interpretation and discussion. Second, data preparation includes conventional wireline logs, acoustic image logs, and resistivity image logs. Third, classify the breakouts (BO) and drilling induced tensile fractures (DITF) using the world stress map approach. Fourth, determining the magnitudes and orientations of in-situ principal stresses using a combination of conventional logs, such as natural gamma-ray (GR), density (RHOB), porosity (NPHI), compressional wave (DT), and resistivity logs (LLS, LLD, and MSFL), as well as borehole image logs (UBI, OBMI, and FMI) and mechanical caliper data (CAL1-CAL6). Citing security and confidentiality concerns, the data used in this report comes from a notable oil company. However, precise details about the fields and locations are withheld to safeguard proprietary and sensitive information. Figure 5-1 shows the overall workflow used in this study. Each component was required to fulfill the associated requirements for interpretation to be effective. Two streams of actions are required to determine the magnitude and orientation of in situ stresses. One line of action provides the rock's physical properties and wellbore deformation measurements, such as BO and DITF. On the other hand, the second line uses empirical equations to determine vertical stress and pore pressure. A combination of both streams meets at the end to determine the magnitude and orientation of in situ stresses.

The density logs were used to calculate the vertical stress for all the wellbores. The geomechanical data, such as the Poisson ratio, Young's modulus, and uniaxial compressive strength, were calculated using empirical equations. The equations are mostly based on petrophysical data such as the slowness of shear and compression waves (Δt_s and Δt_c), density (RHOB), and neutron (NPHI).

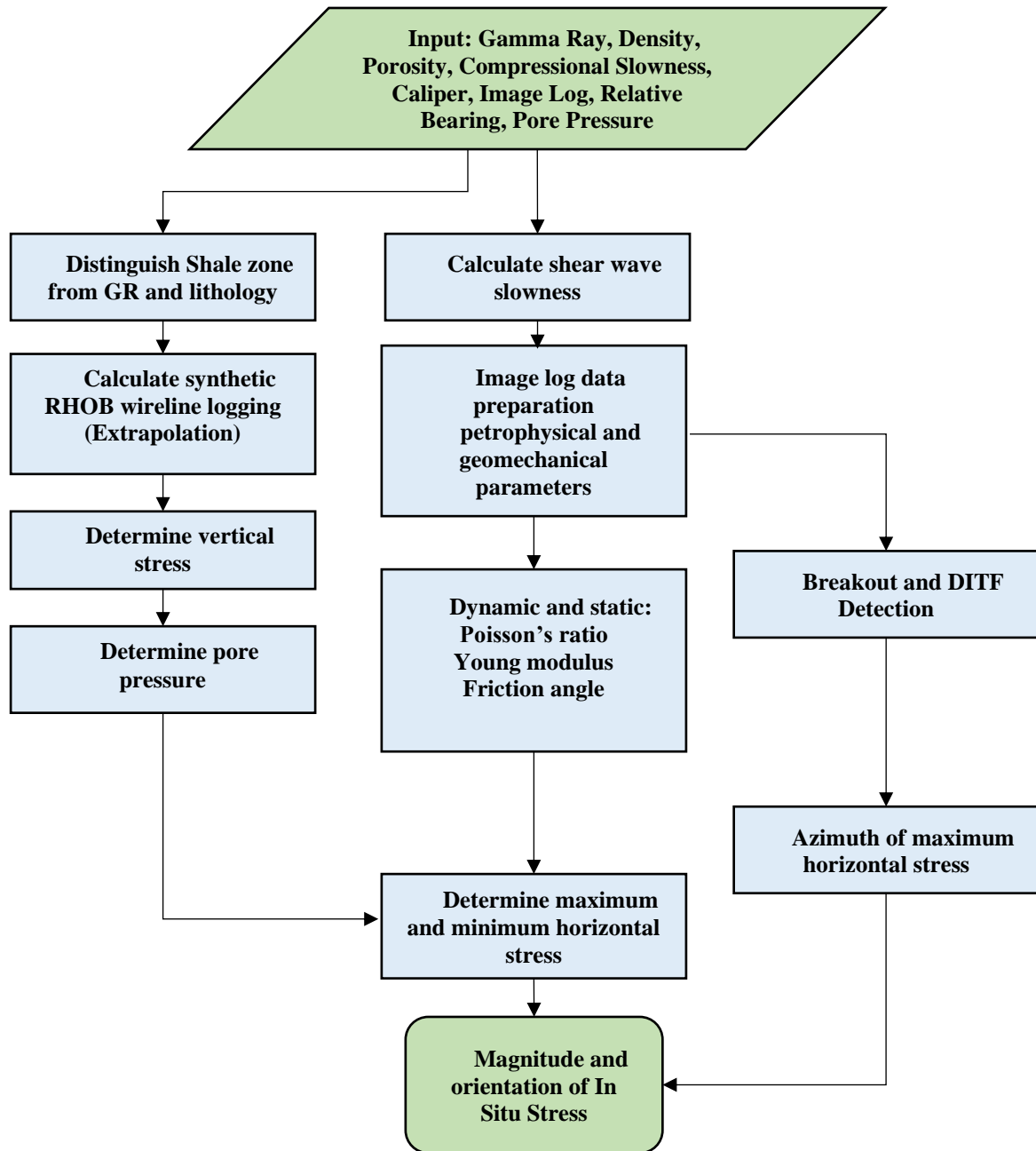


Figure 5-1. Workflow of determining magnitude and orientation of in situ stresses based on the poroelastic strain method and BOs and DITFs results. After Mafakheri B. et al. (2024).

5.2.2 Lithology

As mentioned earlier, determining lithology is crucial for interpreting the stress distribution in the study area. Therefore, several cross-plots were conducted using conventional logs to assist in the lithology determination. First, as shown in Figures 5-2a and 5-2b, the neutron-density and density-photoelectric effect (PEF) cross-plots suggest that the dominant lithologies are limestone and dolomite, and a relatively high shale content exists in the formation. Next, Considering the high content of clay in the Asmari Formation, a thorium-potassium cross-plot (K/THOR) distinguished the clay type as dominantly Illite and its mixtures with montmorillonite (Figure 5-2c). Eventually, using the combination of conventional logs such as gamma-ray, neutron porosity, density, resistivity, and several cross-plots, the lithology of the Asmari Formation was determined and evaluated.

5.2.3 Data Preparation

Data preparation is crucial to any reservoir geomechanical study, particularly breakout analysis. Once the data has been collected, it must be processed and analyzed to ensure accuracy and reliability. Therefore, the data preparation was carried out meticulously to satisfy the appropriate criteria, ultimately leading to a fruitful interpretation of the results. This study evaluated seven wells from oil Field A and one from oil Field B. The average true vertical depth (TVD) of wells in Field A is 3930 m, and in Field B it is 1350 m. After the data quality control, dynamic and static borehole images were prepared for interpretation using the Techlog software from Schlumberger to visualize and analyze the data.

The orientation of maximum horizontal stress is associated with borehole deformations such as BO and DITF. BOs are typically identified as elongated, concave-shaped features in the borehole wall that occur perpendicular to the orientation of maximum horizontal stress. At the same time, DITFs are fractures that occur in the rock formation surrounding a borehole during drilling operations, and they are parallel to the orientation of maximum horizontal stress. Identifying a BO or DITF from borehole image logs generally involves analyzing the shape and orientation of the features in the

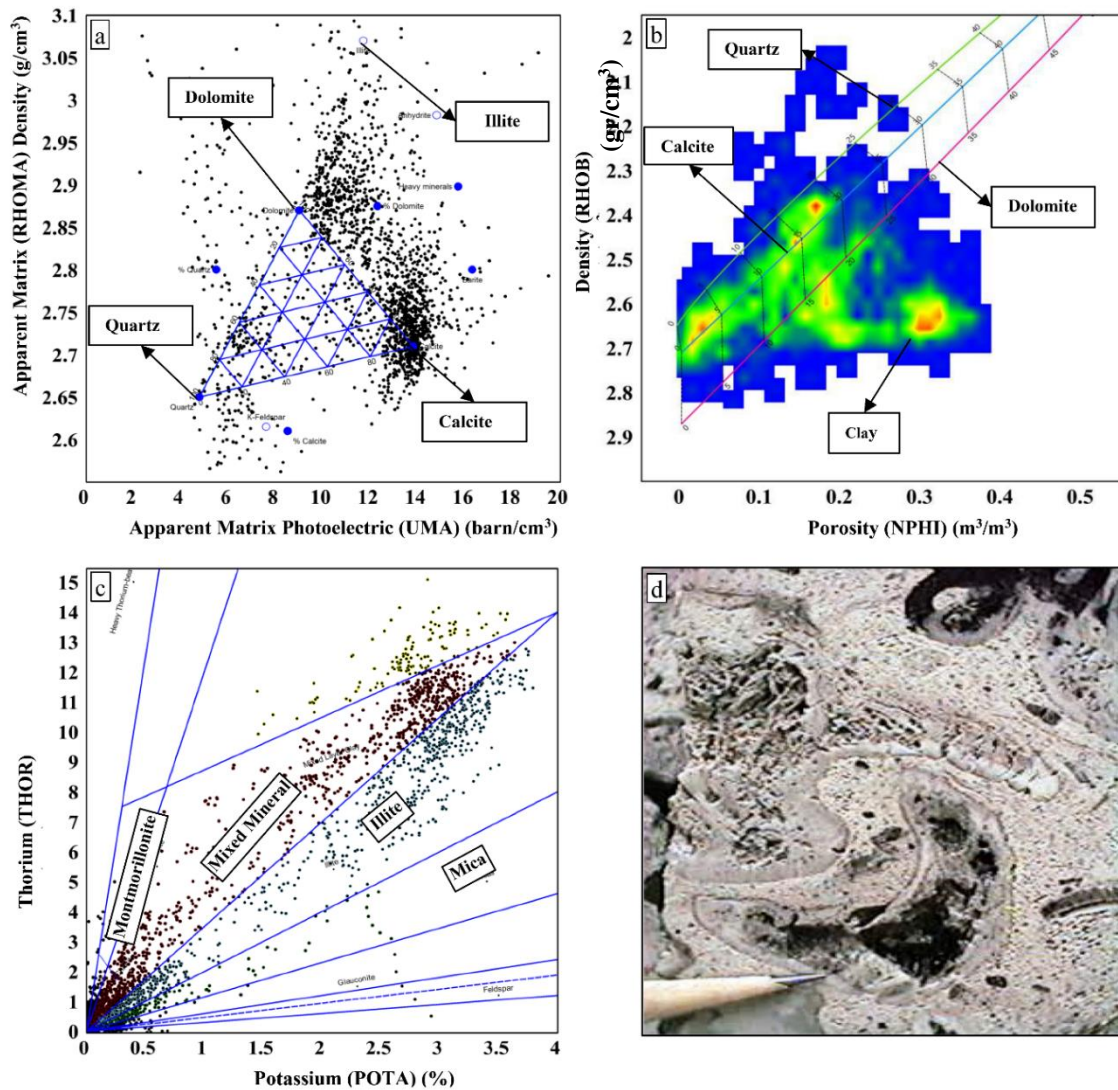


Figure 5-2. Lithology identification of Asmari formation for well A2. a) Apparent matrix Density-Apparent matrix volumetric Photoelectric factor cross-plot (RHOMA-UMA) showing the frequency of several minerals. b) Porosity-Density cross-plot showing Calcite, Dolomite, Quartz, and Clay content for entire studied interval. Colors show the density of points on the cross-plots. Red show higher density and blue spectrums show lower density of points. c) Thorium-Potassium (THOR/K) cross-plot determining the majority the type of clay content. d) Sample of vuggy carbonate from upper Asmari Formation. After Mafakheri B. et al. (2024).

borehole image logs. Therefore, first, the borehole image logs should be identified in combination with the caliper log. For example, Figures 5-3a, 5-3b, and 5-3c show several breakouts detected in acoustic and resistivity borehole image logs in wells A5 and B1. Then, to ensure the accuracy of the breakout analysis, the spiral plot was used to create a vertical-horizontal section of the borehole in several depths, clearly showing the wellbore diameters for a specific interval (Figure 5-3c). Then, as shown in the workflow of this research in Figure 5-1, the poroelastic horizontal strain theory method was used to determine the magnitudes of the principal stresses.

5.2.4 Fracture analysis

The picking of natural fractures and bedding planes was done manually. Natural fractures were identified on borehole images by dark or bright and continuous or discontinuous sinusoidal wave appearances, depending on the conductivity of borehole fluids and the cement degree of fractures (Lai et al., 2018; Marghani et al., 2023; Radwan et al., 2021). Image logs from wells drilled using water-based drilling muds can reveal whether fractures are electrically conductive or not, and electrically conductive fractures are typically thought to be open (Lai et al., 2018). On borehole images, bedding planes might also seem sinusoidal. They do, however, occur as interfaces between lithological units that show various colors on borehole images due to conductivity contrast and can thus be identified from natural fractures.

5.2.5 Breakout and Drilling Induced Tensile Fracture Quality Ranking

The azimuth of the maximum horizontal stress is an essential parameter for any geomechanical study, and one method to determine it is the BO or DITF azimuth method (Zoback, 2007). This section discusses the equations used to calculate the standard deviation, mean BO, or DITF azimuth according to the world stress map approach (Tingay et al., 2008) for each well and also the average azimuth of maximum horizontal stress for the entire field. The azimuth of identified BOs and DITFs is identical on both sides of the wellbore for each well, as shown in Figure 5-3.

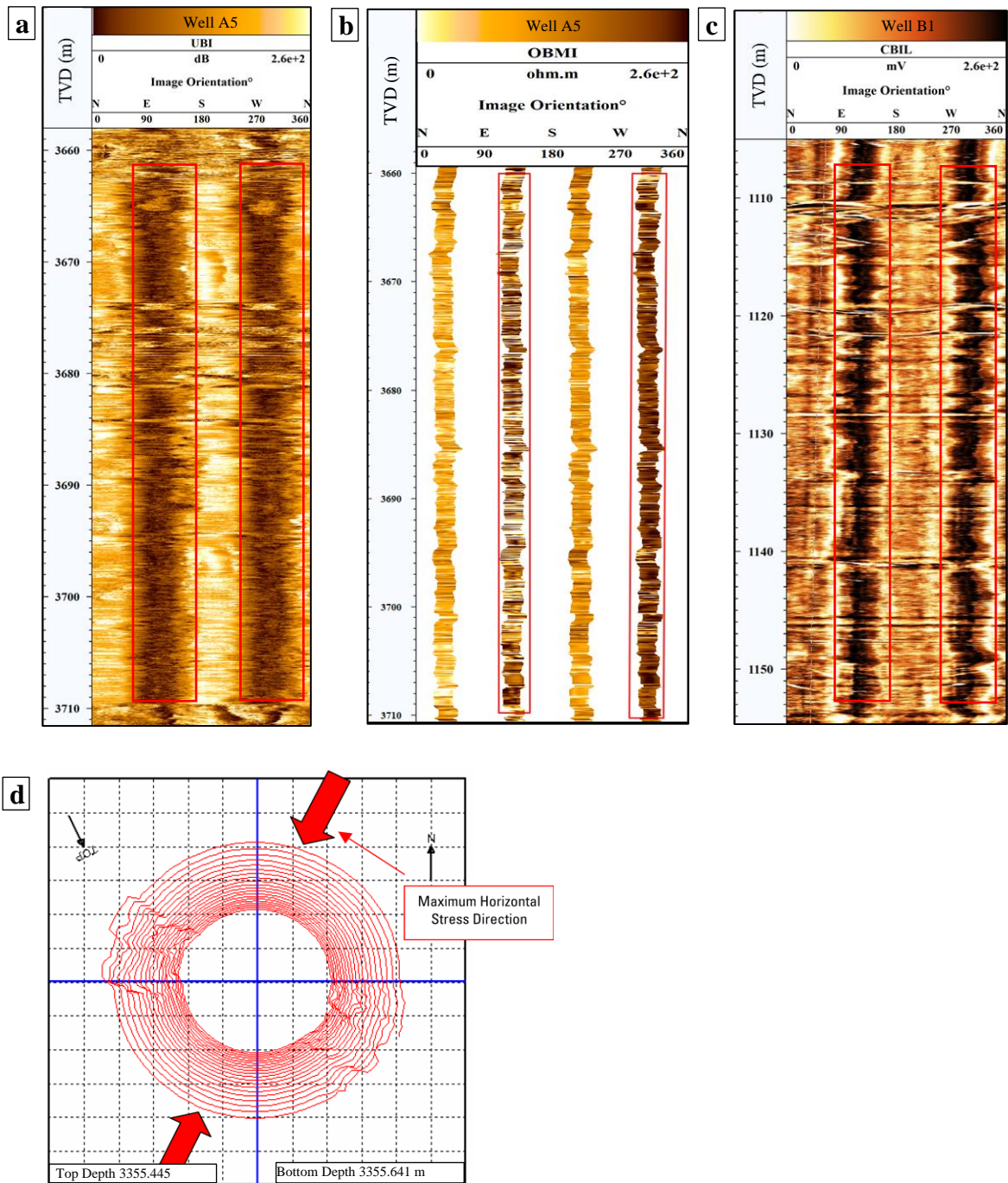


Figure 5-3. Presentation of image logs in wells A5 and B1. a) Identification of breakouts from acoustic image log (UBI) in well A5. b) Identify breakouts from the resistivity image log (OBMI) in well A5. c) Identification of breakouts from acoustic image log (UBI) in well B1. d) Hole shape analysis using a spiral plot around a depth of 3355 m. Each red circle is representing an upscaled diameter of the hole. Two identical deformed zones indicate the presence of breakouts. Red arrows show the azimuth of maximum horizontal stress based on each side of the breakout. After Mafakheri B. et al. (2024).

Therefore, the identical BOs and DITFs on both sides of the borehole are equivalent. Thus, θ_i is the orientation of just one parallel BO or DITF, and $\theta_i^* = 2 \theta_i$. First, the length (height)-weighted mean azimuths for each well were calculated based on length weighted according to Equations 4-3, 4-4, and 4-5. Where l_i is the length of each BO or DITF, and L is the total length (height) of the BOs or DITFs. On the other hand, the mean azimuth and standard deviation were calculated based on 4-6, 4-7, and 4-8. In these equations θ_m is the mean azimuth of the BOs or DITFs and S_o is the standard deviation. Eventually, to encounter both BO and DITF in the average azimuth of maximum horizontal stress for the entire field, the following number-weighted equations are suggested for this study:

$$\theta_{m(\text{ave})} = \theta_{m(\text{BO})} + \left(\frac{\theta_{m(\text{BO})} - (\theta_{m(\text{DITF})} + 90)}{\frac{N_{\text{DITF}}}{N_{\text{BO}} + N_{\text{DITF}}}} \right) + 90 \quad (5-1)$$

$$\theta_{m(\text{total})} = \frac{\Sigma[\theta_{m(\text{ave})j} * (N_{\text{BO}j} + N_{\text{DITF}j})]}{\Sigma(N_{\text{BO}j} + N_{\text{DITF}j})} \quad (5-2)$$

where in Equation 5-1, $\theta_{m(\text{ave})}$ is the average azimuth of maximum horizontal stress for each well, $\theta_{m(\text{BO})}$ and $\theta_{m(\text{DITF})}$ mean azimuth based on BO and DITF, respectively. N_{BO} and N_{DITF} are the number of BOs and DITFs for each well. Since the length of BOs and DITFs are similar the weighted average was calculated. In Equation 5-2, $\theta_{m(\text{total})}$ is the number weighted average azimuth of maximum horizontal stress for the entire field and $\theta_{m(\text{ave})j}$ is the azimuth of maximum horizontal stress for well j^{th} . On the other hand, $N_{\text{BO}j}$ and $N_{\text{DITF}j}$ are the number of BOs and DITFs for well j^{th} .

5.2.6 Magnitudes of In-Situ Principal Stresses

In this study, to determine the magnitude of horizontal stresses based on the poroelastic horizontal strain method, vertical stress, pore pressure, and the physical properties of the rocks should be calculated beforehand. Estimating the vertical stress is the first step of any geomechanical study. At a certain depth (m), the vertical stress is determined according to Equation 4-16 where S_v is the vertical in-situ stress (MPa), RHOB is the density log (g/cm^3), and g (gravitational acceleration) is 9.8 m/s^2 . The next required parameter is pore pressure (P_p), which is the pressure exerted by fluids trapped

within the pores of rock formation. In this study, pore pressure was estimated from sonic logs and downhole drilling data using Eaton's method (Eaton, 1975):

$$P_p = S_v - (S_v - P_{\text{hyd}}) * \left(\frac{DT_n}{DT} \right)^3 \quad (5-3)$$

DT is the compressional sonic slowness ($\mu\text{sec/m}$); DT_n is the sonic travel time in shales ($\mu\text{sec/m}$), and P_{hyd} is the hydrostatic pressure in MPa. There are several empirical correlations adapted for Asmari Formation to establish the relation between static and dynamic elastic moduli and rock mechanics properties. In this study the static Young's modulus (E_s), dynamic Young's modulus (E_d), and Poisson's ratio (ν) were estimated by the method of Najibi et al. (2015) and Biot's coefficient (α) was estimated by the method of Wu et al. (2001). Poisson's ratio (ν) and Biot's coefficient (α) are estimated based on Equations 4-21 and 4-22, respectively and Young's modulus as follow:

$$E_s(GPa) = 0.014E_d^{1.96} \quad (5-4)$$

$$E_d(GPa) = 0.169V_p^{3.32} \quad (5-5)$$

where V_p is the compressional wave velocity. According to Fjær et al. (2008), the poroelastic horizontal strain model considers the rock strains to determine anisotropic horizontal stresses. This approach has been used frequently to determine principal in-situ stresses (Amiri et al., 2019; Baouche et al., 2020; Javani et al., 2017; Radwan and Sen, 2021b, 2021a). The equations of vertical stress and maximum and minimum horizontal stresses are calculated based on Equations 4-17 and 4-18. where S_H and S_h are the maximum and minimum horizontal in-situ stress, respectively. In addition, ε_x and ε_y are two horizontal strain components along the S_H and S_h , respectively, and might be compressional or extensional according to the tectonic stresses. Therefore, they would account for calibration factors and would be expected to match estimations from rock failure. The variables ε_y and ε_x were estimated based on Equations 4-23 and 4-24.

5.3 Results of stress analysis

5.3.1 Borehole Failure

As shown in Table 5-1, the Asmari Formation in well A5 of Field A ranges averagely from 3348 m to 3760 m, and the maximum top formation difference among all seven wells is less than 65 m. The formation in the well in Field B ranges from 1020 m to 1210 m. Several sets of BOs, as shown in Figure 5-3, were identified from UBI, OBMI, CBIL and FMI, which assisted with lithology, Caliper logs, and spiral plots. Also, additional considerations, such as shale zones, were evaluated to avoid misinterpretation among other deformations, such as washout and keyseat resulting from shale swelling. As shown in Tables 5-1 and 5-2, 54 distinct zones, including 207 pairs of BOs and 39 pairs of DITFs, were detected from a total of 3.2 km of image logs from all wells in both fields. There are seven wells from Field A spread all along the western culmination of the anticline, and their target reservoir is the Asmari Formation (Figure 5-4).

Table 5-1. Data catalogue and results of breakout and drilling induced tensile fracture for all wells. The average azimuth of maximum horizontal stress considering results of both breakout and drilling induced tensile fracture is reported. After Mafakheri B. et al. (2024).

Well no.	Type	Asmari Top (m)	Breakout		DIF		Azimuth of S_H
			$\theta_{m(BO)}$	No.	$\theta_{m(DITF)}$	No.	$\theta_{m(ave)j}$
A1	UBI and OBMI	3382	N65W	9	No	No	N35E
A2	UBI and FMI	3356	N35W	8	N67E	2	N58E
A3	UBI and OBMI	3336	N75W	8	No	No	N15E
A4	UBI and OBMI	3316	N60W	78	N41E	2	N31E
A5	UBI and OBMI	3348	N75W	20	N28E	14	N22E
A6	UBI and OBMI	3332	N80W	56	N17E	10	N11E
A7	UBI and OBMI	3370	N45W	17	N53E	11	N48E
B1	CBIL	1020	N55W	11	No	No	N25E

Table 5-2. World Stress Map quality ranking criteria (Tingay et al., 2008) for breakouts interpreted from image logs. Characteristic of analyzed breakout data, including mean breakout azimuth and standard deviation (S_o). After Mafakheri B. et al. (2024).

A-Quality	B-Quality	C-Quality	D-Quality	E-Quality
≥10 distinct breakout zones and combined length ≥ 100 m in a single well with $S_o \leq 12^\circ$	≥ 6 distinct breakout zones and combined length ≥ 40 m in a single well with $S_o \leq 20^\circ$	≥4 distinct breakout zones and combined length ≥20 m in a single well with $S_o \leq 25^\circ$	< 4 distinct breakout zones or < 20 m combined length with $S_o \leq 40^\circ$	Wells without reliable breakouts or with $S_o > 40^\circ$

Well no.	Standard Deviation S_o	Total length (m)	Number of distinct zones	Quality
A1	40.3	24	5	C
A2	9.2	53	6	B
A3	23.7	67	5	B or C
A4	13.6	165	11	A
A5	16.4	48	8	B
A6	12.5	107	9	A or B
A7	9.6	39	6	B
B1	14.8	35	4	C

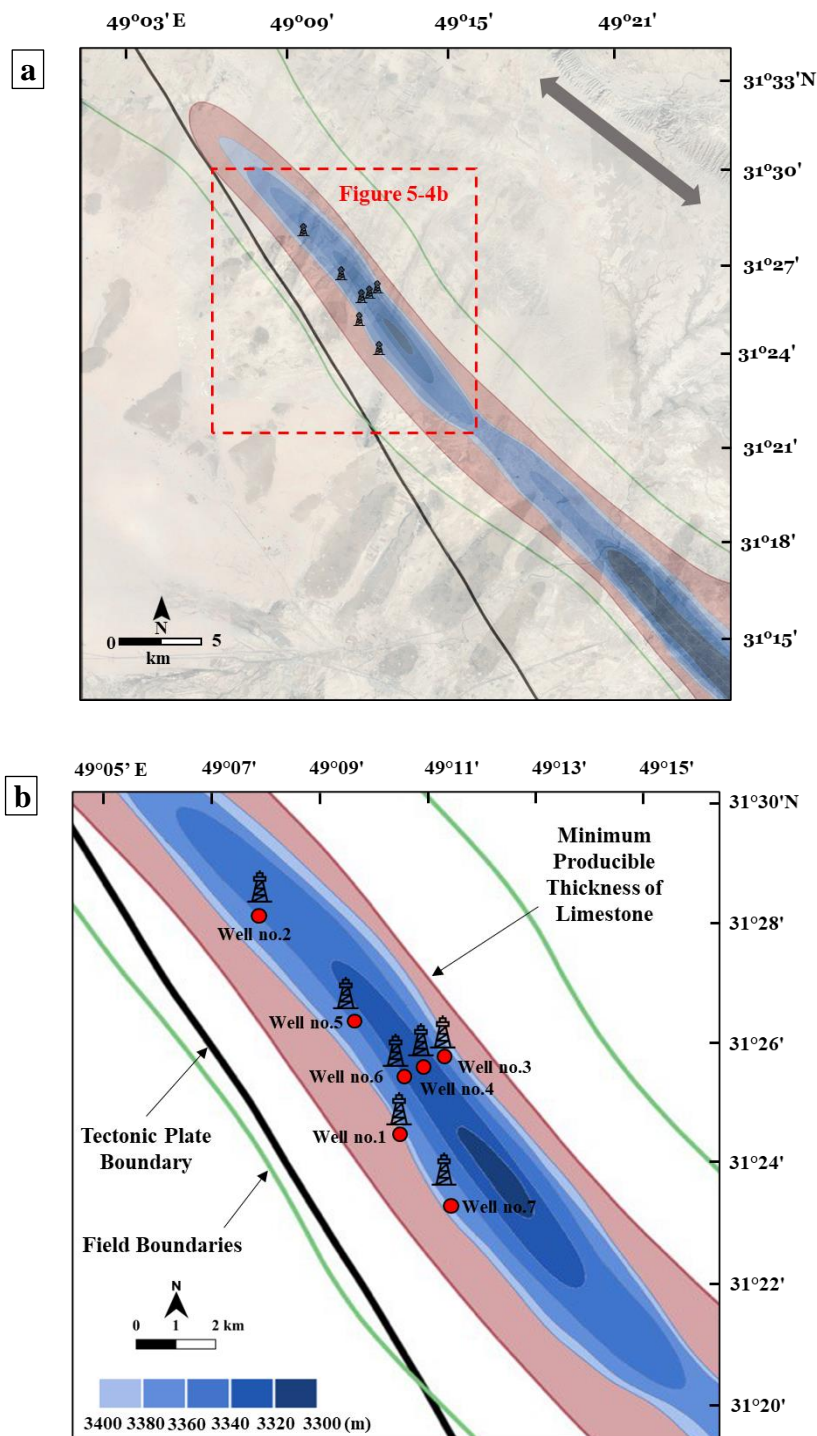


Figure 5-4. Underground contour map of top formation of Asmari in Filed A. The numbers below the well number are the depth of top formation of the Asmari Formation. Different shades of blue bars show different depths of top formation. Red circles show the position of seven wells. The black line shows the tectonic plate boundary between the Arabian and Eurasian Plates, and the green line is the field boundary. A Grey double-sided arrow in (a) shows the closest mountain string on the NE of the Field. After Mafakheri B. et al. (2024).

5.3.2 Maximum horizontal stress orientation

After identifying the BOs and DITFs, since there is a significant difference between the length and number of BOs and DITFs, in the first step, Equations 4-3, 4-4, 4-5, and 4-6 were used to determine the mean azimuth of the BOs or DITFs separately θ_m . The results of $\theta_{m(\text{BO})}$ and $\theta_{m(\text{DITF})}$ for all wells are presented in Table 5-1. The quality ranking is another important factor in determining the orientation of maximum horizontal stress from BO and DITF. Since the number of BOs is significant in this study, the ranking was conducted merely according to the BO. Based on the world stress map standard (Heidbach et al., 2016; Tingay et al., 2008), several parameters, such as standard deviation, mean breakout azimuth and the number of distinct zones, were considered for the ranking (Table 5-2).

According to Equations 4-3, 4-4, 4-5, 4-6, 4-7, and 4-8, the quality of all eight wells was ranked based on the distinct number of breakout zones, standard deviation, and total length of BOs. Considering the significant total lengths of 586 m with a low standard deviation in some depths and 54 distinct zones, there are two sets of BOs with A quality, and the rest ranked as B and C, which show the high certainty of the results. Then, as mentioned in the methodology, by combining the results from BO and DITF for each well and employing proposed Equations 5-1 and 5-2, the azimuth of maximum horizontal stress for each well ($\theta_{m(\text{ave}j)}$) was determined and presented in Table 5-2. Eventually, the total number for the azimuth of maximum horizontal stress considering both BO and DITF was determined as $\theta_{m(\text{total})}$ for the entire field. The results of Fields A and B show N32°E and N55°E, respectively. The results of BOs and DITFs are presented in Figure 5-5. BOs were detected in all seven wells, but only in five wells DITFs were detected.

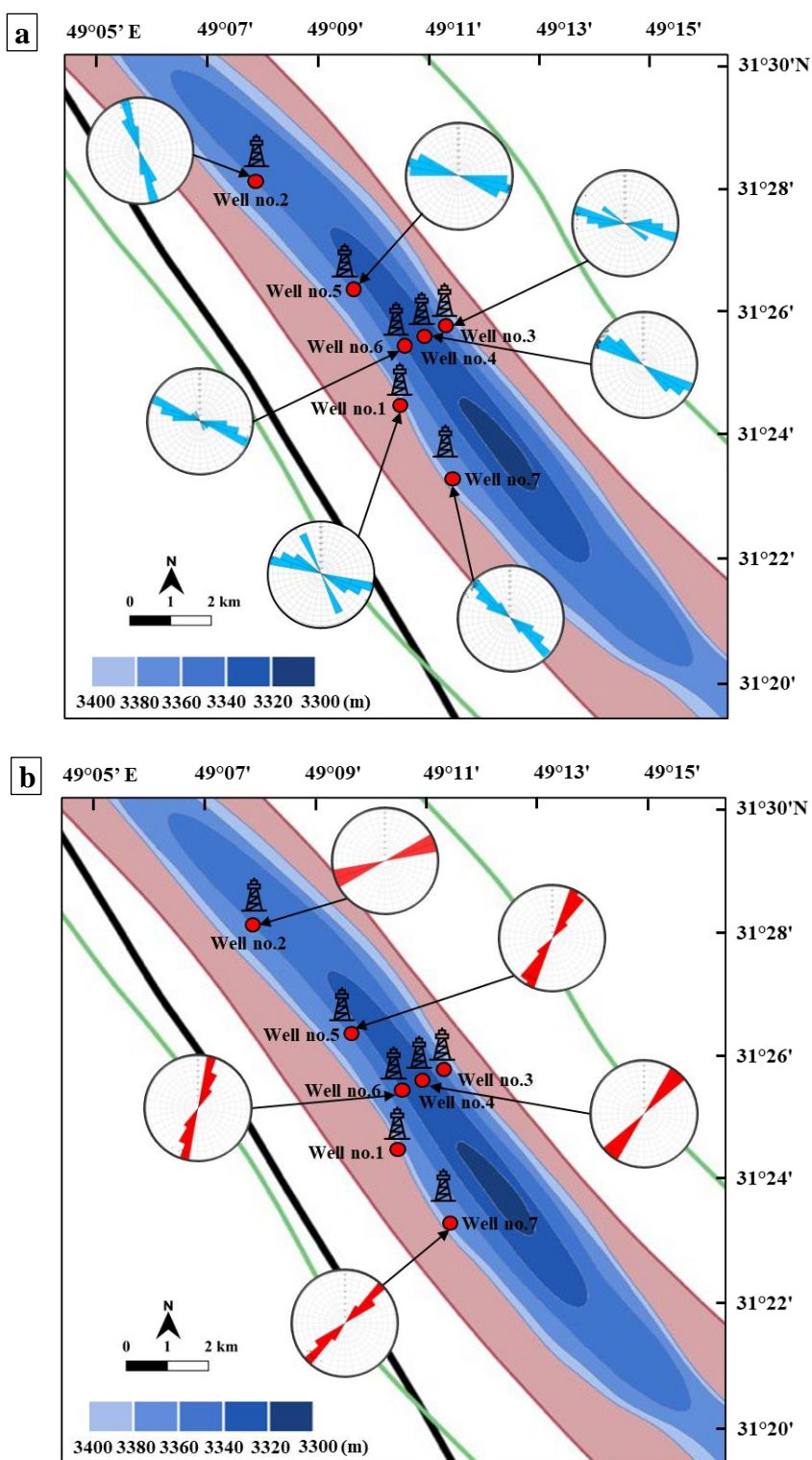


Figure 5-5. a) The rose diagram presents the breakouts for each well. Blue petals show the azimuth of breakouts. b) The rose diagram presents each well's drilling-induced tensile fractures (DITFs). Red petals show the azimuth of DITFs. After Mafakheri B. et al. (2024).

5.3.3 Natural Fracture Analysis

To assist the stress analysis, several sets of natural fractures have been identified for well A2 (Figure 5-6). Natural fractures are common in the Asmari Formation (Khoshbakht et al., 2009) and are displayed as continuous/discontinuous sinusoidal waves on the image logs. Fracture sets within a geological formation are closely related to the orientation of the maximum horizontal stress (S_H) (Heffer and Lean, 1993; Queen and Rizer, 1990). Stress in the Earth's crust, resulting from tectonic forces, tends to create tensional natural fractures in the direction perpendicular to the minimum stress (S_h), as usually rock failure is more likely to occur where the stresses are lowest. Therefore, the most frequently occurring tensional fracture orientation usually aligns approximately parallel to the S_H direction. As shown in Figure 5-6, in well A2, most fractures in set 2 are subparallel with the orientation of maximum horizontal stresses and confirm the results of BOs and DITFs from Table 5-2.

5.3.4 Pore pressure

The values of P_p were estimated by Equation 5-3 from the compressional sonic slowness logs (DT) and compared with values from previous literature that measured pore pressure by hydraulic fracturing tests in the Asmari Formation (Haghi et al., 2018). The estimated average pore pressure for the Asmari Formation in Field A is 37.1 MPa at 3360 m depth and 41.6 MPa at 3780 m depth, which is consistent with the results of Haghi et al. (2018). For Field B, P_p ranges from 10.6 MPa at 1050 m depth to 11.6 MPa at 1150 m depth. The mean P_p gradient is 10.7 MPa/km and 10 MPa/km in Fields A and B, respectively. As shown in Figure 5-6, shale was encountered at 3590 m, and Figure 5-7 demonstrates a higher-pressure regime with an average gradient of 12.1 MPa/km below the oil-water contact. Overpressure behavior is probably caused by fast compaction in Early Miocene shales, where sedimentation rates were so fast that the pore fluids could not release the pressure, and another reason could be the transition from the oil zone to the aquifer. The wells were drilled with overbalanced oil-based mud. According to the drilling reports from field A, no serious incidents of formation fluid influx above or below 3590 were reported, implying greater confidence in pore pressure interpretation.

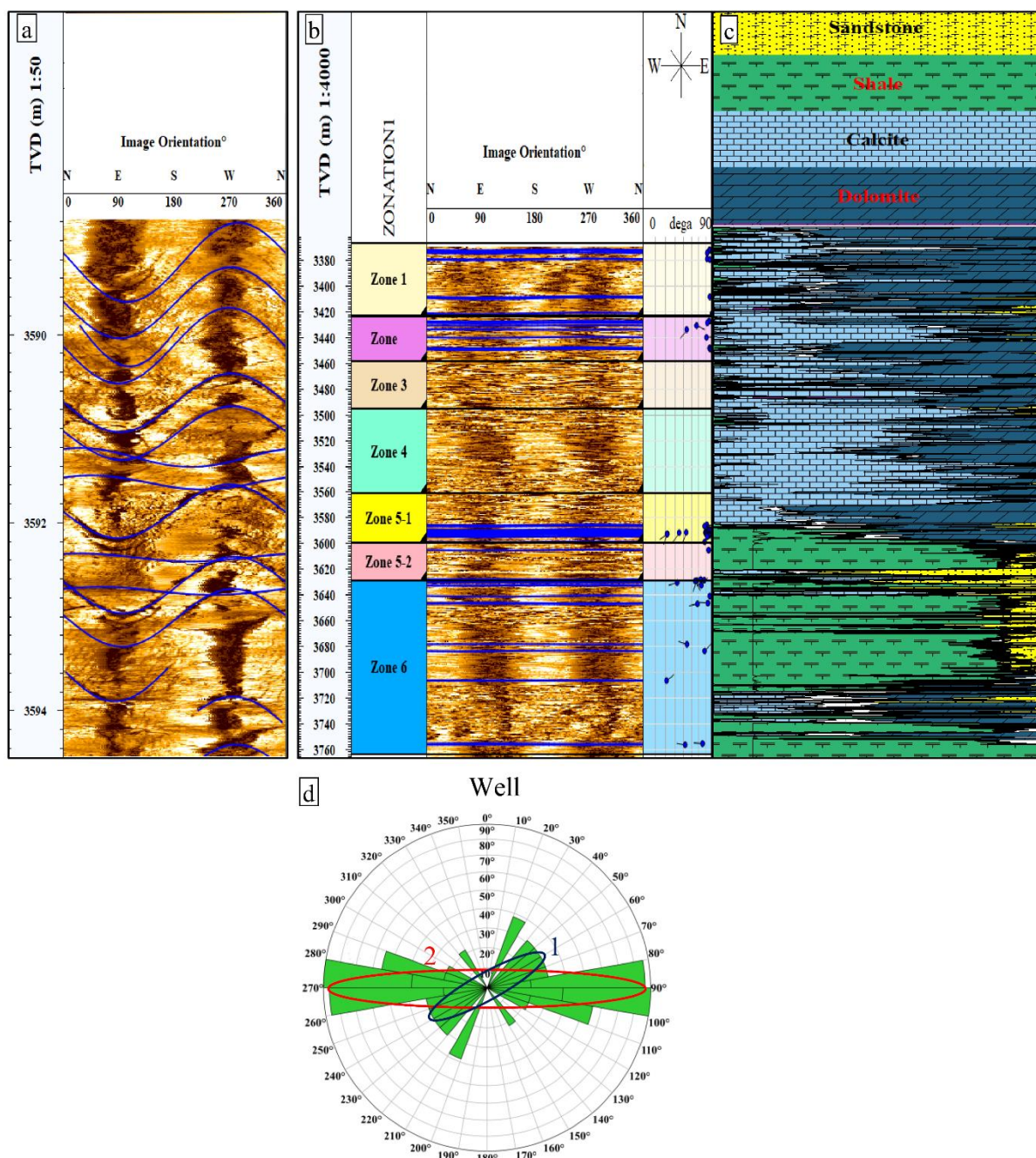


Figure 5-6. Results of image log analysis for fracture identification in well A2. a) Example of detected fractures in approximately 6 m intervals. b) Identified fractures for the entire Amari formation in well A2. c) Lithology Column of Asmari Formation. d) Results of fracture analysis of Well A2 are presented in the rose diagram. Two distinct sets of fractures were detected. After Mafakheri B. et al. (2024).

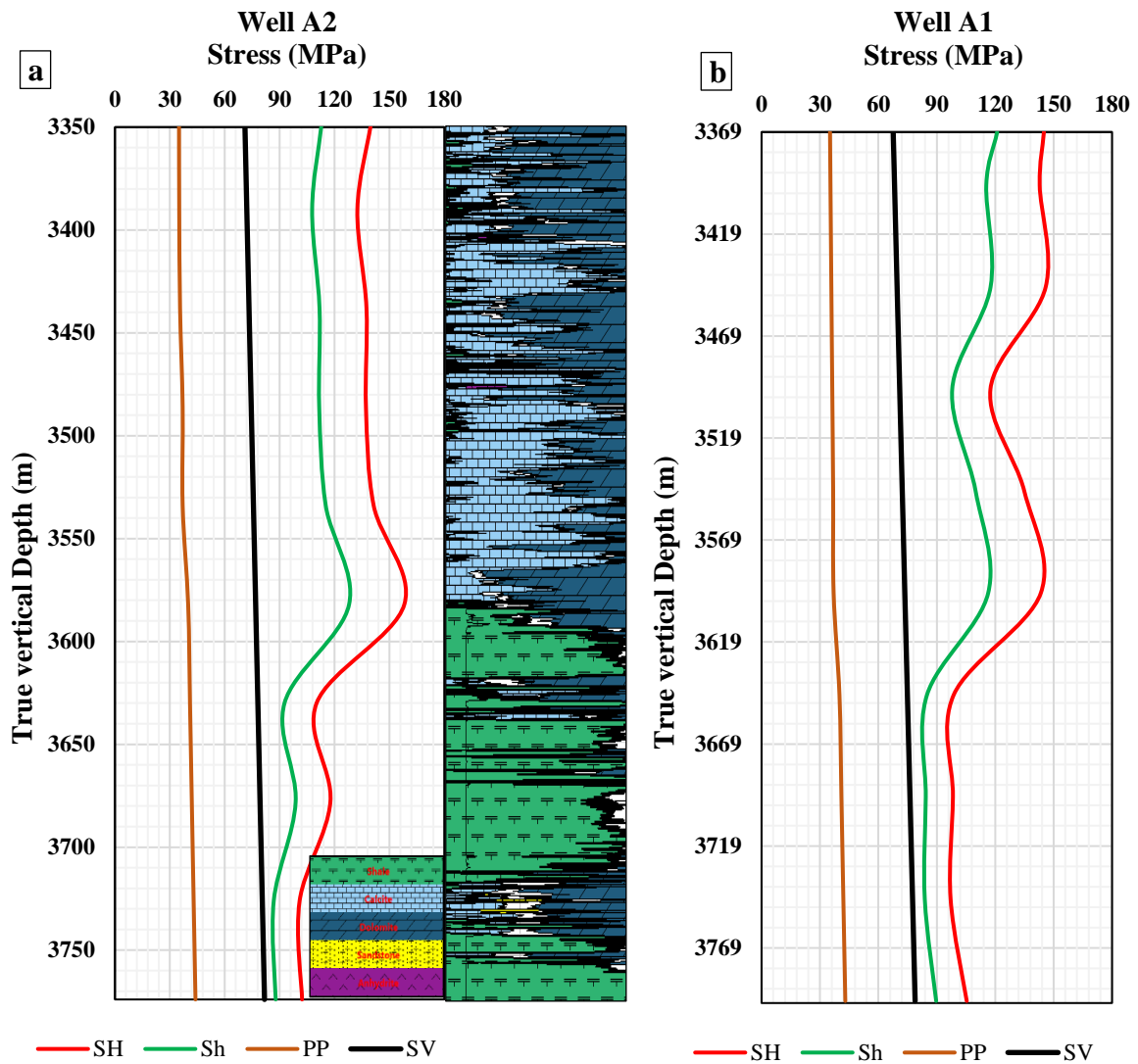


Figure 5-7. Profile of in situ stresses including SV, SH, Sh and pore pressure Pp for both fields. a) Stress profile and lithology column for well A2. b) Stress profile for well A.1 c) Stress profile for well A7. d) Stress profile for well B1. e) Extrapolated stress profile based on the well B1. f) Extrapolated stress profile based on the well A2. After Mafakheri B. et al. (2024).

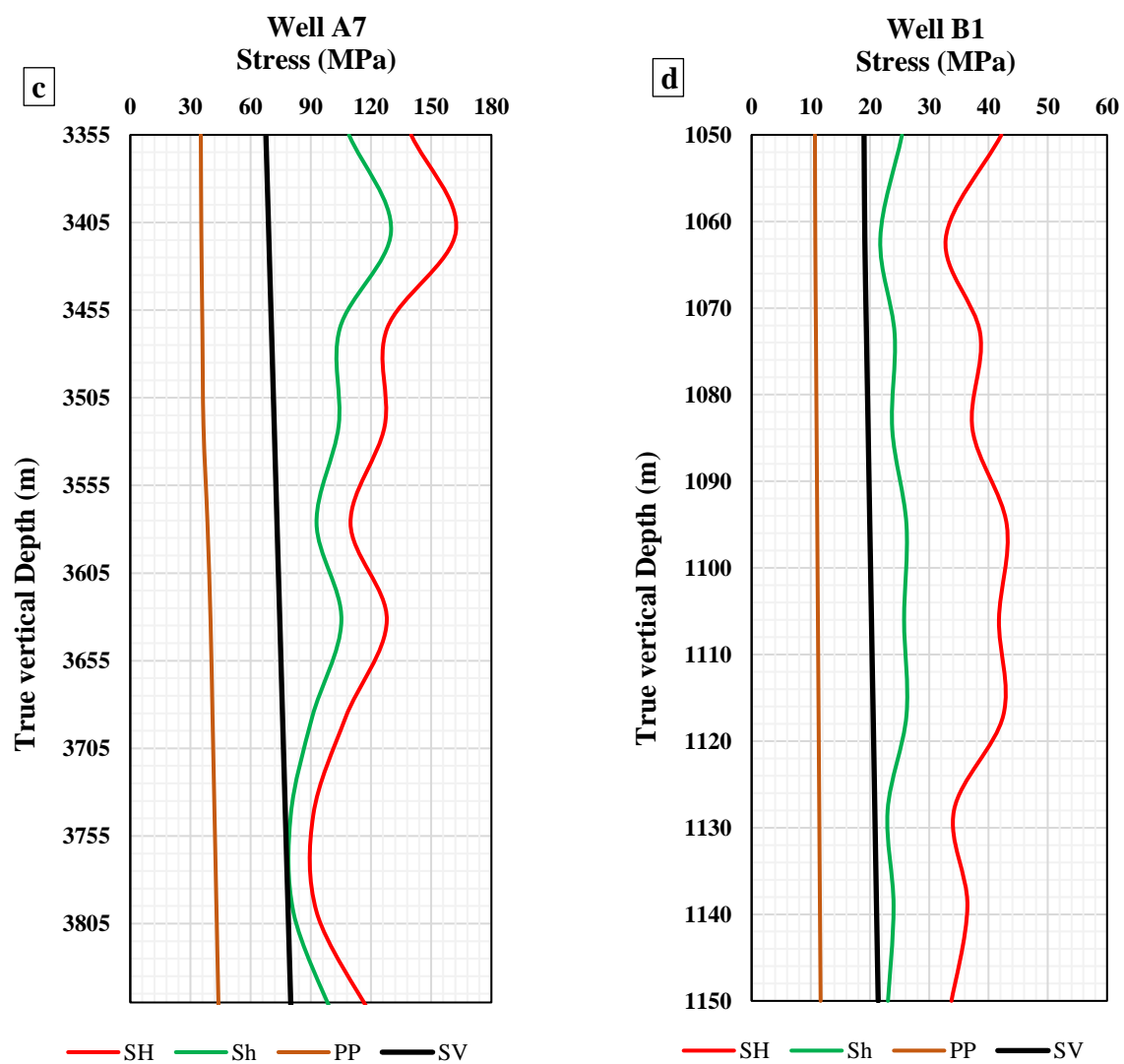


Figure 5-7. Continued.

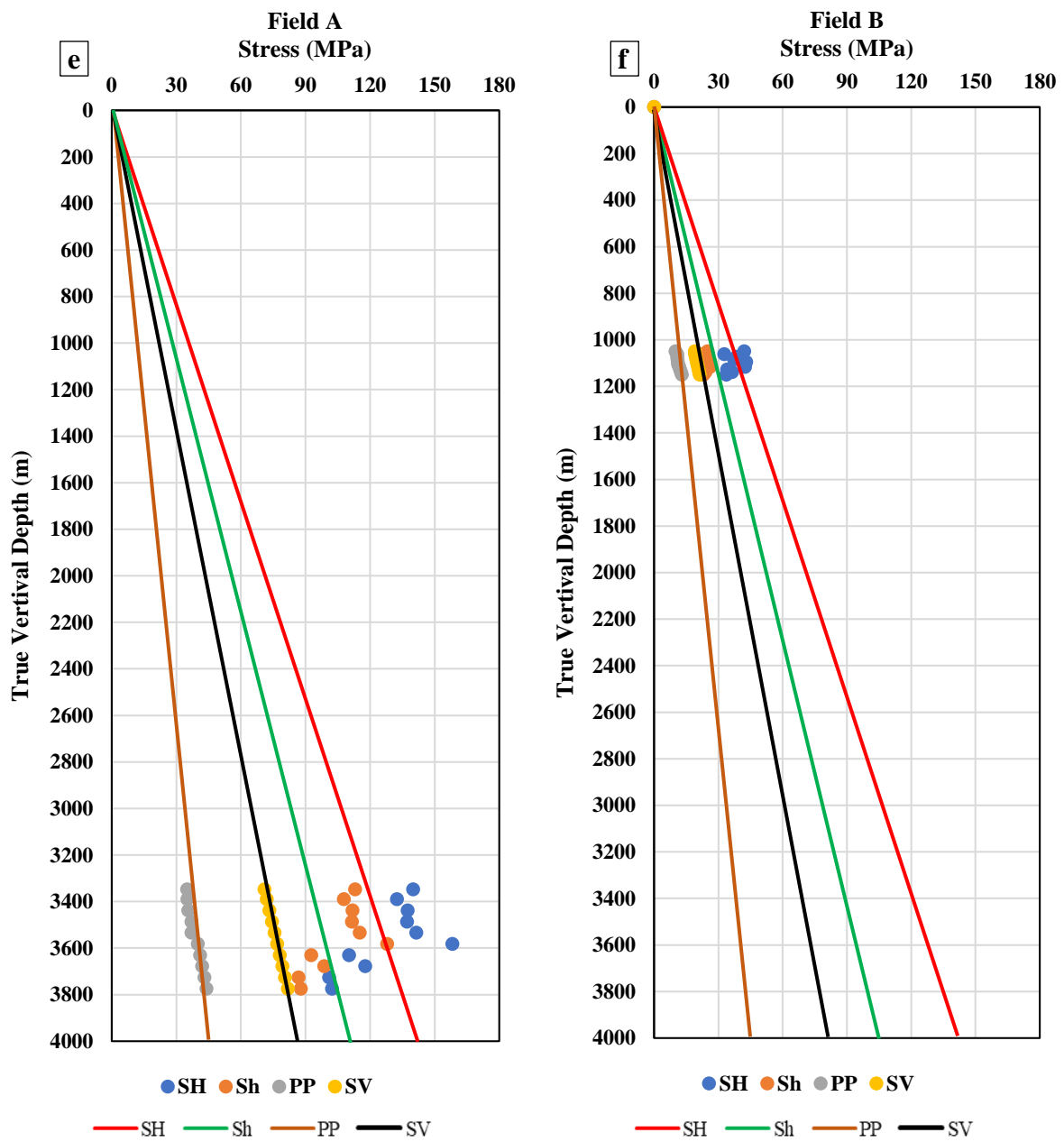


Figure 5-7. Continued.

5.3.5 Stress Magnitude

Figure 5-7 depicts the magnitudes of the principal in-situ stresses for wells A1, A2, A7, and B1, including vertical and maximum and minimum horizontal stresses, as determined using the methods described in Methodology. The vertical stress (S_v) was determined by integrating a synthetic shallow density profile and bulk density log based on Equation 4-16. No significant differences are detected between the results of each well from the same field. For the Asmari Formation, according to available data, estimated average S_v values in Field A range from 69.8 MPa at 3360 m depth to 80.4 MPa at 3780 m depth, and for Field B, they range from 18.9 MPa at 1050 m depth to 21.3 MPa at 1150 m depth. The mean S_v gradient is 25.4 MPa/km and 24 MPa/km in Fields A and B, respectively. The magnitude of both horizontal stresses was estimated by Equations 4-17 and 4-18 based on the Poroelastic strain model. The results for three wells from different locations in Field A showed moderate differences. Two obvious trends exist in the horizontal stresses above and below 3580 m. The average value of estimated average S_h above this depth in Field A ranges from 112.2 MPa at 3360 m depth to 128.3 MPa at 3580 m, and for S_H , it varies from 131.3 MPa at 3360 m depth to 148.1 MPa at 3580 m. The estimated S_h and S_H gradients, above 3590 m, are 69.8 MPa/km and 73.1 MPa/km, whereas, at the deeper level below 3590 m, there is a sharp decline in both horizontal stresses, and for the rest of the studied interval results show relatively constant values.

5.3.6 Stress Regime

Stress polygons are commonly used to identify and understand the principal stress components in critically stressed boundary conditions (Figure 5-8). Estimated magnitudes of the principal stresses (S_v , S_h , and S_H) define the stress regime in Field A. The plotted stress polygon depicts the magnitudes of S_h and S_H for a particular depth with known S_v and P_p values (Figure 5-8). Two depth points have been plotted for Field A. As shown in Figures 5-7 and 5-8, based on the relationship between the magnitudes of the in-situ stress in Field A, in the depths above 3590 m, the stress regime is thrust faulting ($S_H > S_h > S_v$). In contrast, below this depth, there is a sharp decrease in the horizontal stresses, and the S_h line overlaps with S_v , which is more likely explainable

with the shifting toward a strike-slip regime ($S_H > S_v \geq S_h$). Shallow depth points are located within the thrust faulting environment, whereas deeper depth points are located within the border between the strike-slip and thrust faulting stress regimes. It is worth mentioning that these results for all the studied wells were almost consistent. On the other hand, however, for Field B, since the studied interval did not cross the oil-water contact (OWC), in the entire studied interval, the dominant stress regime is thrust faulting ($S_H > S_h > S_v$) with no dramatic change in the estimated stresses.

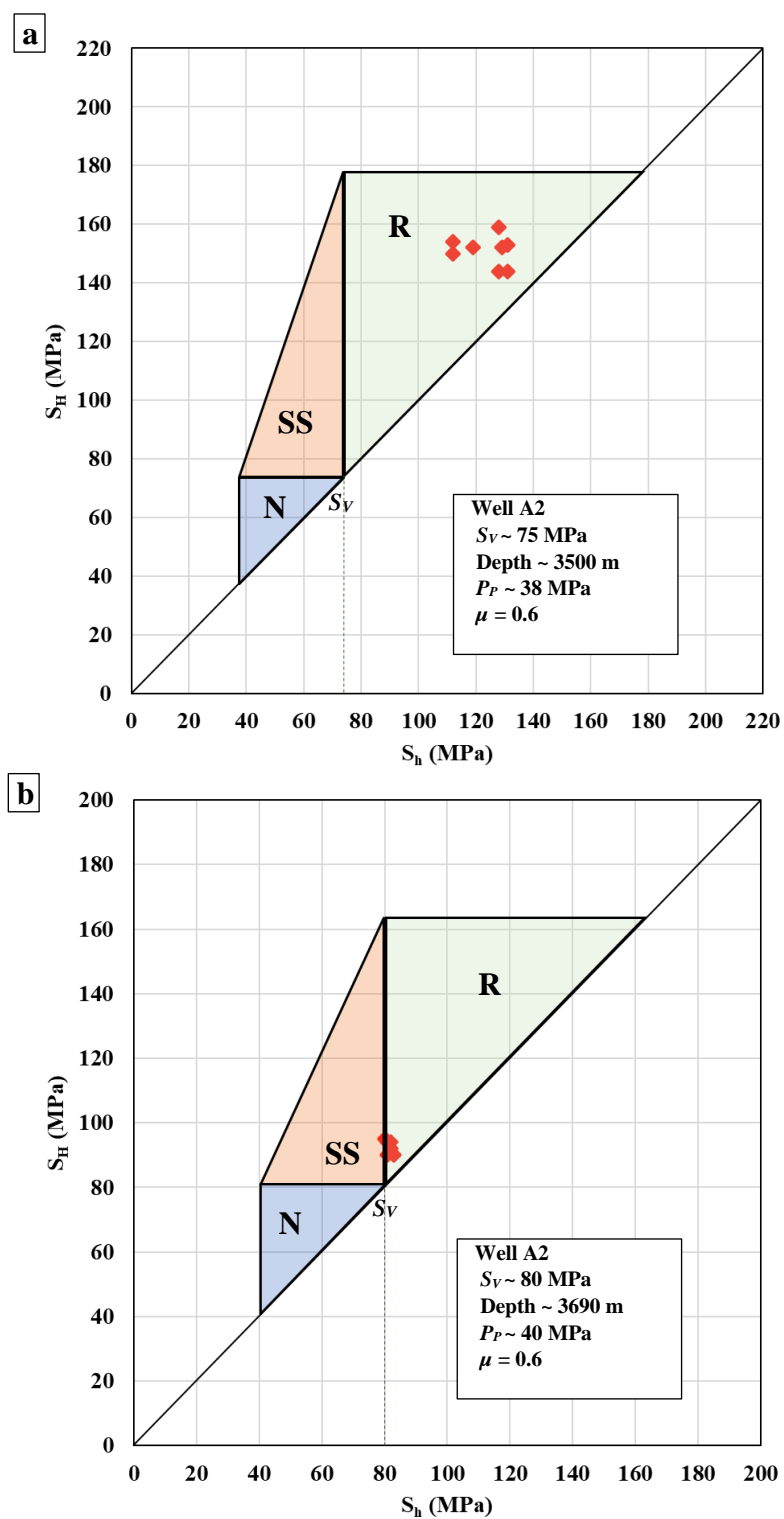


Figure 5-8. Stress polygon for two different depths in Well A2. a) Plotted stress polygon for the reverse faulting regime (R). b) Plotted stress polygon shows the shifting from reverse faulting (R) to strike-slip (SS) stress regime. After Mafakheri B. et al. (2024).

5.4 Interpretation of in situ stress analysis (SE Zagros suture zone)

5.4.1 Horizontal stress magnitude and orientation

As shown in Figure 5-9, the overall trend for maximum horizontal stress orientation is NE-SW. The estimated mean azimuth for the entire Field A is N32°E and for Field B is N55°E. For Field A, the standard deviation between seven wells is 17°, which is relatively moderate and implies the reliability of the results. In Field A, the average difference between the azimuth of S_H derived from BOs and DITFs is 10.2°, which is considerable, and it is a significant clue that the stress state is in a complex condition. The greatest difference in the azimuth of S_H derived from BOs and DITFs is reported in wells A5 and A2 with 13° and 12°, respectively. Both wells are along the extension of the northwestern limb of the anticline with low standard deviation (Tables 5-1 and 5-2; Figure 5-4). On the other hand, wells A6 and A7 show the lowest difference in the azimuth of S_H from BOs and DITF, with 2°. Figures 5-4 and 5-5 show that A5 and A2 are far from the hinge line and center of the anticline, and A6 and A7 are closer to the center. One hypothesis suggested for this phenomenon is that the difference in the degree of folding in the Asmari Formation, and consequently, the difference in extension forces on the formation can cause a greater difference between results from BOs in different well locations (Figure 5-10). Other recommended reasons behind the stress deflections are lateral deformability/strength contrasts, flexural stresses, and geological structures such as faults (Sonder, 1990).

Since the difference between the Asmari top formation from different wells is relatively low, and no dramatic horizontal change in the rock properties is reported, the inconsistency between the azimuth results of BO and DITF is likely irrelevant to the density and strength contrast. Also, since the anticline is relatively subparallel to the mountain ranges in the area, surface structure and their geological features (Figures 5-4 and 5-9) are most likely not effectively causing the differences. However, as shown in Figures 2-12 and 5-5 in the southwestern culmination of the anticline in Field A, there are three thrust faults, including a major fault, and possibly they affect the state of stress in wells closer to the faults (A1, A2, A5, and A7) and can cause differences between the results of BO and DITF. As presented in Figures 5-4 and 5-9, the wells

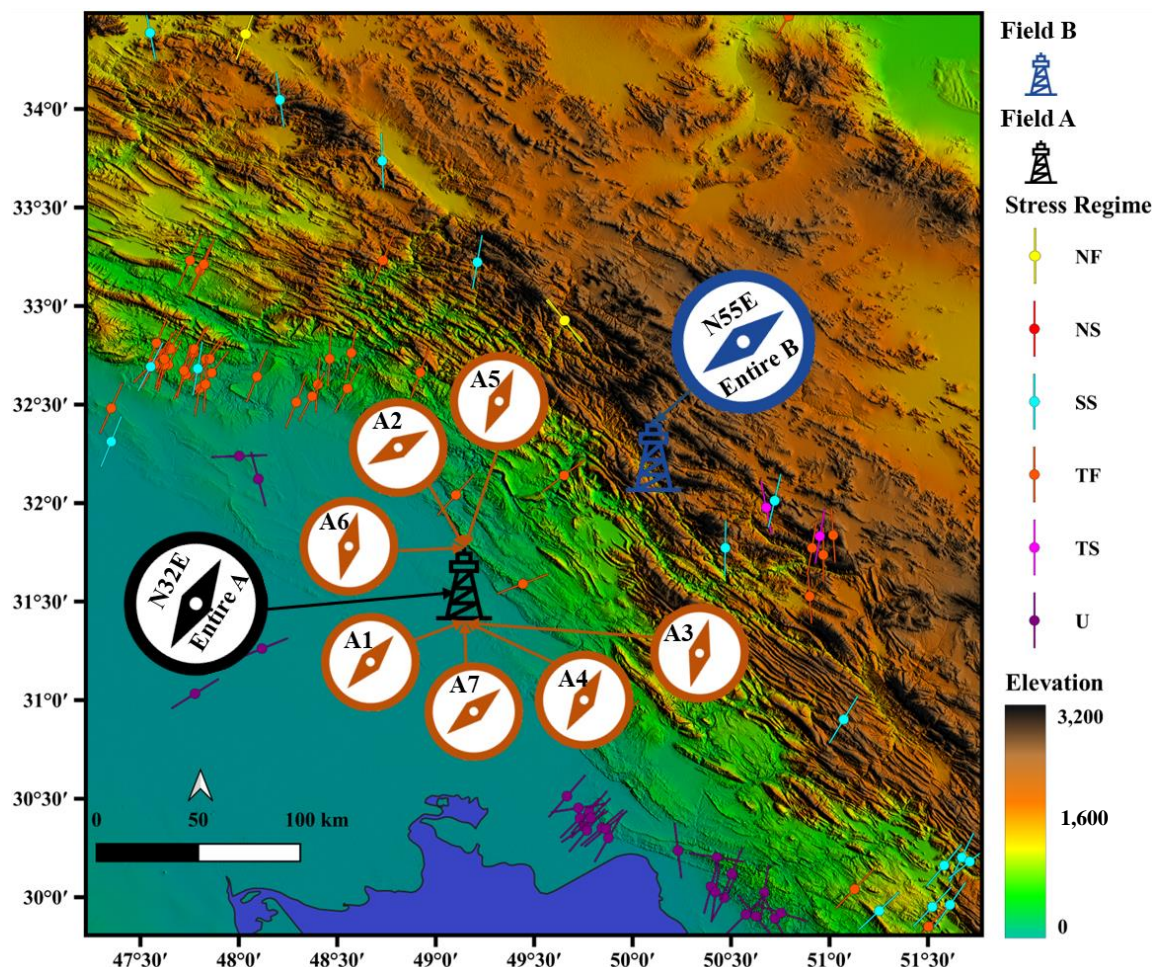


Figure 5-9. The mean azimuth of maximum horizontal stress based on combination of results of BOs and DITFs plotted on a digital elevation map of the study area. Colorful lines show the orientation of maximum horizontal stress, based on world stress map data. Brown compasses show the mean azimuth of the maximum horizontal stress for each well ($\theta_{m(ave)}$) based on the results of both breakouts and DITF. Black and Blue compasses show the average azimuth of maximum horizontal stress for the entire field ($\theta_{m(total)}$) for Field A and azimuth of maximum horizontal stress based on well B1 in the Field B, respectively. After Mafakheri B. et al. (2024).

closer to the boundary of the anticline have a closer azimuth of BOs compared to those closer to the Hing line.

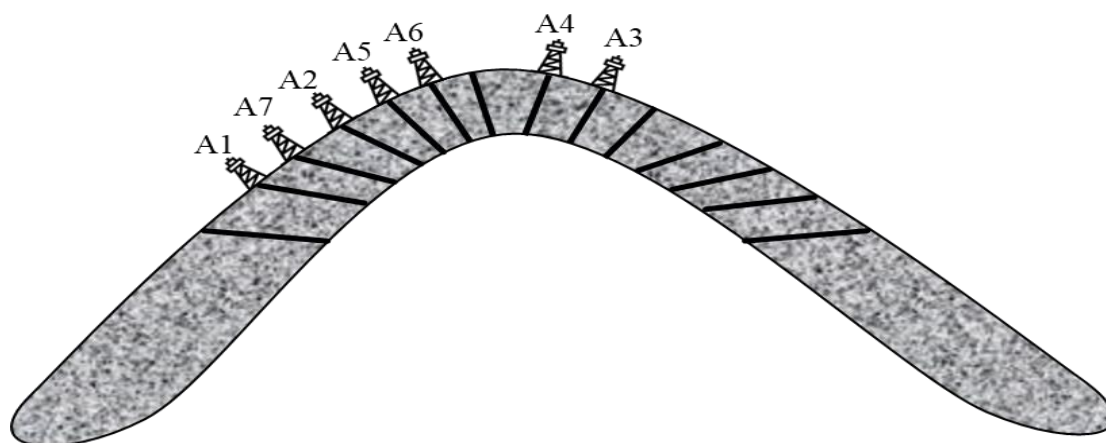


Figure 5-10. Schematic anticline folding degree scale. Each well is located on different part of the anticline, and it cause different tensional forces. Black lines show the schematic illustration of tension in the interval. After Mafakheri B. et al. (2024).

Table 5-3. Magnitude of in situ stress and pore pressure results for different zones of Asmari formation estimated from well A2. After Mafakheri B. et al. (2024).

Asmari Zones	Depth Range TVD (m)	Stress Magnitude (MPa)			
		P _p	S _v	S _H	S _h
Zone 1	3356 – 3415	35.2	72.1	136.7	110.9
Zone 2	3405 – 3455	36.3	73.9	137.3	111.7
Zone 3	3455 – 3501	37.0	75.1	139.3	113.4
Zone 4	3501 – 3547	37.0	75.7	141.4	115.2
Zone 5-1	3547 – 3571	38.5	76.3	149.8	121.6
Zone 5-2	3571 – 3599	40.5	77.5	134.2	110.3
Zone 6	3584 – 3775	42.5	79.9	107.8	91.5

According to Hol et al. (2018) production from mature basins leads to critical changes in the stress state and causes reservoir depletion that results from fluid draw-down. Field A has produced oil since 1984 for 25 years before the first studied well was drilled in 2009. Pore pressure drawdown is expected, and according to the company's report, the gas cap experienced the highest-pressure decline, followed by and then the oil zone. As shown in Figure 5-7 and Table 5-3, the P_p values of the gas cap are the lowest and, beyond the oil-water contact in the aquifer, are the greatest. Another possible reason is the change in lithology of different zones in the Asmari Formation. In addition, the lower zones of Asmari contain more clay. As mentioned earlier, in the shaly zones in this region, there is more trapped connate water due to rapid formation compaction, which is an additional explanation for the P_p difference. In addition, as shown in Figure 2-11b, the OWC is at 3600m, which agrees with the horizontal stress shifting in Figure 5-7.

Regarding the magnitude of the horizontal stresses, as presented in Figure 5-7 and Table 5-3, the stress value difference between S_H and S_h is not very high compared to their differences with S_v . Also, the revelation of this fact is reflected in the gradient differences. Since S_h increases with P_p , these variations in the S_h gradient with depth can be explained by the P_p distribution across the drilled strata. Moreover, the shale intervals have even higher pore pressure than shallow sediments; thus, the estimated S_h shows a higher gradient.

5.4.2 Links to regional stress state and tectonic setting

In the collision between the Arabian and Eurasian plates, dominant stress regimes in the middle to deep depths are dominantly thrust faulting to strike-slip regimes, and they were mostly activated in the late Miocene (Alavi, 2007; Derikvand et al., 2018). As shown in Figure 5-9 and presented in world stress map Heidbach et al. (2016), the azimuth of S_H in the Zagros region, based on the world stress map database, is consistent with the result of this study and with the relative plate motion of the Arabian plate with respect to the Eurasian plate in Figure 2-7. This consistency suggests that large tectonic forces play a dominant role in the current stress pattern. Fields A and B locations were

close to the collision boundary and Zagros Suture zone. Therefore, the results can contribute to our understanding of the in-situ stresses in the region.

On the other hand, according to Sonder (1990), the difference in horizontal stress determines stress anomalies in the folded and faulted sedimentary cover. A moderate to high difference between horizontal stresses can result in stress deflection in the sedimentary rock where the stress state is on the border between thrust faulting and strike-slip faulting regimes.

In several studies (Ahlers et al., 2018; Cornet and Röckel, 2012; Fritz et al., 2023; Sonnette et al., 2014), it is mentioned that deep formations (5 km) with high temperatures and a ductile nature can cause decoupling of the stress between upper and lower structures. Therefore, the existence of the shaly formations at the bottom of the Asmari Formation at a depth of 3700 m could be one of the reasons behind the stress variation in Field A. Conversely, since in Field B, the Asmari formation is not deep enough, this change in stress state is not expected.

According to Yaghoubi et al. (2021) most faults are critically stressed in the Dezful Embayment since the most pre-existing faults are reverse faulting regimes (NW-SE) and their strikes are perpendicular to the azimuth of present-day S_H . As a result, the stress in the sedimentary cover cannot be as strong as the compressional stress in the basement. Even though the horizontal stress is exponentially increasing in deeper depths close to the basement, the compressional stress in the basement is coupled with middle depths in Fields A and B. Consequently, the existence of transverse faults suggested by previous literature is possible to be a dominant stress state. However, since the evaporates of the Gachsaran Formation, according to Khodabakhsh Nezhad et al. (2016) formed a strong detachment horizon, there is a possibility that stress above the Asmari Formation can be detached from below formations.

On a regional scale, as shown in Figure 5-9 from the southeast of the study area in Figure 2-9, the azimuth of S_H is shifting from $N32^\circ E$ in Field A to $N55^\circ E$ in Field B. Therefore, the orientation of compressional forces shifts eastward as it gets closer to the high folded zone. But in this area, the azimuth of S_H based on EFM results from WSM (Heidbach et al., 2018) in deeper depths shifted northward and they are contradicted with the eastward shifting of S_H based on BO and DITF in the shallower depths. For instance, on the southeast of well B1, the results of EFM from the closest earthquake

also show a northward shifting in the S_H orientation. Therefore, the orientation of S_H in the shallower depths near the high folded zone is not under the great influence of basement compressional forces. Probably, the basement topography of the area and mountain range caused the transversion of the orientation of S_H . In addition, several contradictory results in the East of well A3 emphasize the complexity of the area closer to the Zagros suture zone. According to previous studies in Table 2-2, based on different sources, this area's most frequent stress regime is thrust faulting for the shallow to deeper depths. According to a GPS study (Vernant et al., 2004), the surface displacement in Field A is higher than average relative to nearby areas. The closest GPS station to the collision border shows 25 mm y^{-1} , while the one on the high Zagros folded zone shows 20 mm y^{-1} . On the other hand, by going toward central Iran, the number declined to 14 mm y^{-1} . From the surface displacement point of view, this is evidence that compressional forces are still active and northeastward, and there are no big changes from the collision border toward the Zagros suture zone and mountain range.

In terms of seismicity, according to Yaghoubi (2021) and the WSM map in Figure 5-9, the results show that the area is an active seismic zone, and the present-day compressional forces are relatively consistent with the estimated azimuth of S_H . The closest studied EFM result to Field A is significantly consistent with the breakout result in this study. Therefore, the interpreted data from depths deeper than 10 km still meets the medium to shallow results of oil wells.

5.4.3 Regional and local origin of present-day stress field

The studied oil field is in the Zagros foothills. The oil field is located around the crest of a slightly asymmetric anticline, which is trending NW–SE (Figure 5-5). The findings of this study suggest that Jurassic thrust faulting, situated at the boundary of the collision zone and the Zagros folded zone, points to a compressional stress state. However, these anticlines are typically expected to align in a slanted position relative to a thrust fault. The reservoir in Field A is placed next to a local blind major thrust fault and two minor faults, which makes the field isolated from the outer arc at the collision border of the Arabian and Eurasian plates. Field B is surrounded by three major thrust faults, which isolate it from the outer arc and deeper formations (Figures 2-12 and 5-5).

However, these faults initially were suspected of playing a role in decoupling the studied block from deeper compressional forces and causing shifting of the stress regime, but according to the result presented in Figure 5-7, since the compressional stress regime in the basement has not changed and remains thrust faulting even in shallower depths in well B1, most likely the inner arc is coupled with the outer arc and even deeper formations. Therefore, the stress regime in both fields is probably influenced by the far-field stress regime in the outer arc and is approximately consistent with the plate convergence reported by (Ghafur et al., 2023; Vernant et al., 2004).

5.4.4 Implications for field development and wellbore stability

Usually, mitigating breakouts requires a higher mud weight above the formation collapse pressure. It should be highlighted that when there is a strong horizontal stress contrast in thrust faulting to a strike-slip stress regime, many failures are likely to occur, and as shown in Figure 5-9 and Table 5-1, a significant number of breakouts with significant lengths were discovered in all of the wells. Regarding oil well stability in such a stress regime, deviated and horizontal wells can often be more stable than vertical wells because the orientation of these wells can be planned to coincide with the direction of the S_H . In this situation, drilling in the direction of the S_h can minimize the difference between the stresses acting on the wellbore and reduce the chance of wellbore failure due to tensile or shear stresses. However, other factors, such as the presence and orientation of existing fractures, faults, or bedding planes, can also influence wellbore stability and must be considered when planning the well trajectory. In practice, well trajectory planning often involves a combination of geomechanical modeling, seismic data, and other geophysical and geological information to optimize wellbore stability and maximize productivity. As shown in Figure 5-6, there are two sets of natural fractures. Set 2, which contains the majority of fractures in the Asmari formation in well A2, is paralleled to the orientation of S_H and probably formed during the present stress state and under the same compressional force. Set 2 probably formed during the previous stress state in the Dezful Embayment. From a production point of view, the best horizontal well should cross most of the natural fractures. Since most of the fractures are aligned to the orientation of S_H , the most productive horizontal wells

should be drilled parallel to S_h in the Dezful embayment, which in the SW sector is $N58^\circ W$ around Fields A and in the NE sector is $N35^\circ W$ around Field B. In addition, the hydraulic fractures will propagate along many natural fractures parallel to the orientation of S_H and effectively create a transverse fracture network within the Asmari reservoirs, which typically have low permeability. Therefore, optimization in the thrust faulting stress regime, as seen in the studied fields, should be guided by detailed geomechanical assessments. In the case of overbalanced drilling for horizontal wells, the existence of open fractures in the Asmari Formation can cause serious formation damage and excessive acidizing and fracturing. Therefore, the mud weight should be designed carefully to prevent formation damage. The mud weight for drilling the Asmari Formation should be increased gradually, and the mud loss should be monitored carefully.

5.5 Integration of two study area

To effectively integrate and compare the results from NW and SE of Zagros suture zone there are several aspects to be considered such as the orientation and magnitude of maximum horizontal stresses. The results from both studies collectively illuminate the complex geomechanical dynamics across the Zagros belt. These findings underscore the critical need for region-specific stress analysis in oil field development, addressing both geological and geomechanical challenges. This integrated perspective enhances our understanding of the Zagros suture zone's geomechanical environment, vital for efficient and safe hydrocarbon exploration and production.

This study suggests that the present dominant stress regime in the NW and SE of Zagros suture zone in different depths is a reverse (thrust) faulting stress regime. However complexity of the geology and tectonics of each area in different depths, locally transformed into strike-slip stress regime. Noteworthy, duration of oil production might have impacted the formation pressure and consequently changed the local in-situ stresses and eventually the stress regime. Despite occasional transformation in the stress regime, the collision between tectonic plates controls the pattern of the stress field all along the Zagros suture zone and the convergence between the Arabian and Eurasian plate is active and responsible for the stress regime. In terms of hydrocarbon production this study reveals that these variations in stress regime can impact wellbore stability and should be carefully considered during drilling operations and well planning.

On the other hand even though surface displacement is inconclusive to determine the deeper stress state but the overall orientation of maximum horizontal stress along the Zagros suture zone is NE-SW and is aligned with the current surface observation of tectonic movement of Arabian Plate and probably shows the strong attachment of the surface and basement. However the result in three different oil fields in different depths are showing moderately different values. As shown in Figure 5-11, the mean azimuth of maximum horizontal stress in NW part of Zagros suture zone is $N72^{\circ}E$, while in the SE part of Zagros suture zone varying from $N32^{\circ}E$ in the Filed A to $N55^{\circ}E$ in the field B. The difference between the azimuth of maximum horizontal stress in the two areas in the NW and SE of Zagros suture zone, can be explained by several hypotheses.

One reason behind the differences between azimuth of maximum horizontal stress is probably related to the complexity of the folded zone shown in Figure 2-3 and 2-10. Folding and faulting along the Zagros suture zone caused a disturbance in the stress regime and consequently changed the azimuth of maximum horizontal stress. On the other hand, in a bigger picture, the relative tectonic movement of Arabian, Eurasian and Anatolian plate can cause the difference between the azimuth of maximum horizontal stress in the NW part of Zagros suture zone compare the SE part (Kaban et al., 2018, Stren and Johnson, 2010). the Arabian plate is pushing the Anatolian plate with different rate compared to the Eurasian plate. The average rate of Arabian plate movement toward the Eurasian plate is 10 mmy^{-1} , while the average rate of Anatolian plate movement westward is 20 mmy^{-1} (Kokum and Özcelik, 2020; Vernant et al., 2004). Furthermore, the main Eurasian plate movement is align with SE and in the NW part of the Zagros that Iranian block does not have important presence, the impact of Eurasian plate movement is increasing. Therefore the eastward element of collision of Arabian, Eurasian and Anatolian plate tectonic forces is more dominant in the NW part of the Zagros suture zone compared to the SE part and consequently the azimuth of maximum horizontal stress is shifting from $N72^{\circ}E$ to $N32^{\circ}E$.

In this study, in terms of regional structural geology, reveals that deeper formations with ductile nature can cause decoupling of stress between upper and lower structures in both study areas. On the other hand, the alignment of azimuth of horizontal stresses reveals the complex regional influences, with stress in shallower depths potentially influenced by basement topography and mountain range. Further research and ongoing monitoring of stress conditions will continue to refine our understanding and enhance exploration and production strategies in the future.

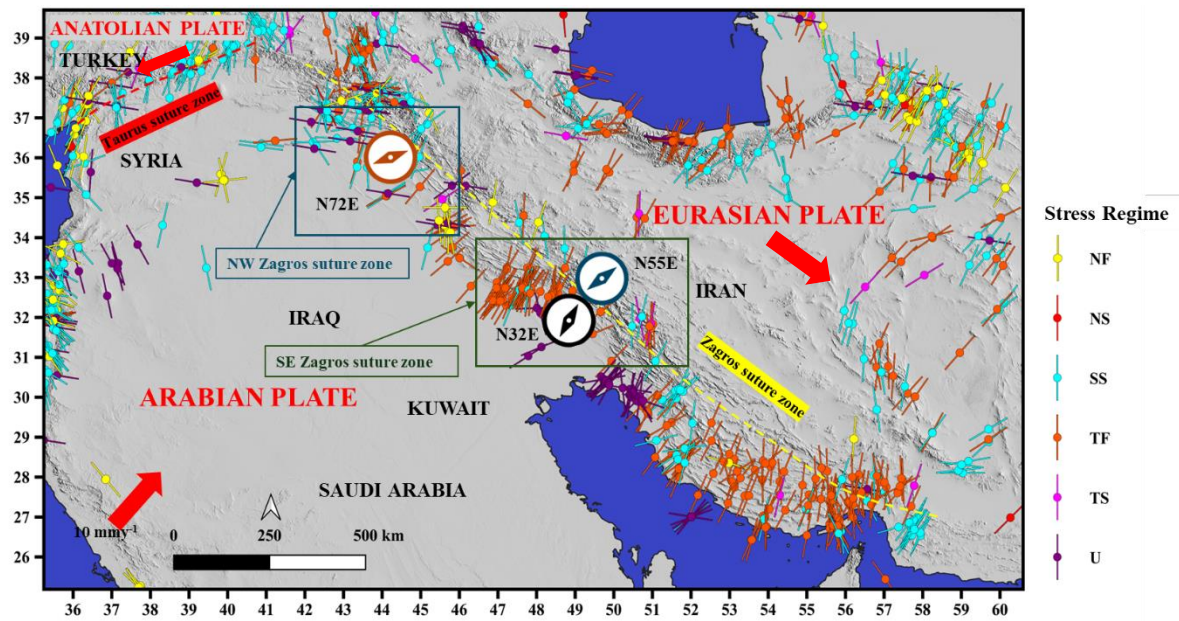


Figure 5-11. Integration of two study areas in the northwestern and southeastern Zagros plotted suture zone plotted on a digital elevation map of world stress map (Heidbach et al., 2018). The blue box shows the northwestern Zagros suture zone in Chapter 4, and the green square box shows the southeastern Zagros suture zone in Chapter 5. Schematic compass icons show the orientation of maximum horizontal stress in each filed and colorful lines represent different stress regimes based on world stress map data. The red arrow shows the estimated Arabian tectonic plate movement toward the Eurasian plate.

5.6 Summary

This chapter, utilizing a combination of conventional and image logs, offers valuable insights into the tectonic and geomechanical characteristics of the ZFTB. A comprehensive analysis was conducted on stress orientations, natural fractures, pore pressure, and stress regime across two oil fields in the Zagros foothills. The findings have significant implications for energy field development, including optimizing drilling practices, wellbore stability, and reservoir management in similar geological settings. This contributes to the overall efficiency and productivity of oil and gas operations in the region.

This study identified 54 distinct zones from a total of 3.2 km of image logs, encompassing 207 pairs of BOs and 39 pairs of DITFs across all wells in both fields.

The study revealed that the maximum horizontal stress orientations in Field A and Field B were N32°E and N55°E, respectively. The natural fractures' orientation closely aligns with azimuth of maximum horizontal stresses, confirming the reliability of the stress analysis and proving crucial for optimizing wellbore stability, productivity, and designing hydraulic fracturing operations.

Furthermore, the study highlighted the complex nature of stress distribution in the area. The increasing differences in the azimuth of maximum horizontal stress, as indicated by breakouts and drilling-induced tensile fractures with increasing depth, suggest variations in stress states and complexities in the subsurface stress regime. These variations can significantly impact wellbore stability and should be carefully considered during drilling operations and well planning. In terms of stress magnitudes and regimes, Field A showed a transition from a distinct thrust faulting regime to a crossover of thrust and strike-slip faulting regimes with increasing depth. In contrast, Field B maintained a consistent thrust faulting stress regime throughout.

Eventually this chapter tried to explain the regional and overall dynamics of plate movement and stress analysis in the Zagros suture zone. It specifically addresses the orientation and magnitude of maximum horizontal stresses, variations in the stress regime due to geological and tectonic complexities, and the influence of tectonic plate movements on stress patterns in this region.

References

- Ahlers, S., Hergert, T., Henk, A., 2018. Numerical modelling of salt-related stress decoupling in sedimentary basins—motivated by observational Data from the North German Basin. *Geosciences* **9**, 19. <https://doi.org/10.3390/GEOSCIENCES9010019>
- Alavi, M., 2007. Structures of the Zagros fold-thrust belt in Iran. *Am J Sci* **307**, 1064–1095. <https://doi.org/10.2475/09.2007.02>
- Amiri, M., Lashkaripour, G.R., Ghabezloo, S., Moghaddas, N.H., Tajareh, M.H., 2019. Mechanical earth modeling and fault reactivation analysis for CO₂-enhanced oil

- recovery in Gachsaran oil field, south-west of Iran. *Environ Earth Sci* **78**, 1–22. <https://doi.org/10.1007/s12665-019-8062-1>
- Bailin, W., 2001. Boit's Effective Stress Coefficient Evaluation: Static And Dynamic Approaches. *ISRM International Symposium - 2nd Asian Rock Mechanics Symposium*.
- Baouche, R., Sen, S., Ferial, H.A., Radwan, A.E., 2022. Estimation of horizontal stresses from wellbore failures in strike-slip tectonic regime: A case study from the Ordovician reservoir of the Tinzaouatine field, Illizi Basin, Algeria. *Interpretation* **10**, SF37–SF44. <https://doi.org/10.1190/INT-2021-0254.1>
- Baouche, R., Sen, S., Ganguli, S.S., 2020. Pore pressure and in-situ stress magnitudes in the Bhiret Hammou hydrocarbon field, Berkine Basin, Algeria. *Journal of African Earth Sciences* **171**, 103945. <https://doi.org/10.1016/j.jafrearsci.2020.103945>
- Berberian, M., 1995. Master “blind” thrust faults hidden under the Zagros folds: active basement tectonics and surface morphotectonics. *Tectonophysics* **241**, 193–224. [https://doi.org/10.1016/0040-1951\(94\)00185-C](https://doi.org/10.1016/0040-1951(94)00185-C)
- Cornet, F.H., Röckel, T., 2012. Vertical stress profiles and the significance of “stress decoupling.” *Tectonophysics* **581**, 193–205. <https://doi.org/10.1016/J.TECTO.2012.01.020>
- Derikvand, B., Alavi, S.A., Fard, I.A., Hajjalibeigi, H., 2018. Folding style of the Dezful Embayment of Zagros Belt: Signatures of detachment horizons, deep-rooted faulting and syn-deformation deposition. *Mar Pet Geol* **91**, 501–518. <https://doi.org/10.1016/j.marpetgeo.2018.01.030>
- Eaton, B.A., 1975. The Equation for Geopressure Prediction from Well Logs, in: Fall Meeting of the Society of Petroleum Engineers of AIME, Dallas, Texas. <https://doi.org/10.2118/5544-MS>
- Fjær, E., Holt, R.M., Horsrud, P., Raaen, A.M., Risnes, R., 2008. Petroleum Related Rock Mechanics. *Elsevier*. [https://doi.org/10.1016/S0376-7361\(07\)53013-X](https://doi.org/10.1016/S0376-7361(07)53013-X)
- Fritz, H., Tenczer, V., Hauzenberger, C., 2023. Fold interference pattern and crustal decoupling in northern Tanzania. *Journal of African Earth Sciences* **202**, 1464–343. <https://doi.org/10.1016/j.jafrearsci.2023.104940>

- Ghafur, A.A., Sissakian, V.K., Al-Ansari, N., Omer, H.O., Abdulhaq, H.A., 2023. Tectonic development of northeastern part of the Arabian Plate: Examples from Pirmam and Bana Bawi anticlines in the Kurdistan region of north Iraq. *Results in Geophysical Sciences* **14**, 2666–8289. <https://doi.org/10.1016/j.ringps.2023.100054>
- Haghi, A.H., Chalaturnyk, R., Ghobadi, H., 2018. The state of stress in SW Iran and implications for hydraulic fracturing of a naturally fractured carbonate reservoir. *International Journal of Rock Mechanics and Mining Sciences* **105**, 28–43. <https://doi.org/10.1016/j.ijrmms.2018.03.002>
- Heffer, K., Lean, J.C., 1993. Earth stress orientation - a control on, and guide to, flooding directionality in a majority of reservoirs, *Reservoir Characterization III*. PennWell Books, Tulsa, Oklahoma.
- Heidbach, O., Barth, A., Müller, B., Reinecker, J., Stephansson, O., Tingay, M., Zang, A., 2016. WSM quality ranking scheme, database description and analysis guidelines for stress indicator. *GFZ German Research Centre for Geosciences* 40–41. <https://doi.org/10.2312/wsm.2016.001>
- Heidbach, O., Rajabi, M., Cui, X., Fuchs, K., Müller, B., Reinecker, J., Reiter, K., Tingay, M., Wenzel, F., Xie, F., Ziegler, M.O., Zoback, Mary Lou, Zoback, Mark, 2018. The World Stress Map database release 2016: Crustal stress pattern across scales. *Tectonophysics* **744**, 484–498. <https://doi.org/10.1016/j.tecto.2018.07.007>
- Hol, S., van der Linden, A., Bierman, S., Marcelis, F., Makurat, A., 2018. Rock Physical Controls on Production-induced Compaction in the Groningen Field. *Sci Rep* **8**, 7156. <https://doi.org/10.1038/s41598-018-25455-z>
- Javani, D., Aadnoy, B., Rastegarnia, M., Nadimi, S., Aghighi, M.A., Maleki, B., 2017. Failure criterion effect on solid production prediction and selection of completion solution. *Journal of Rock Mechanics and Geotechnical Engineering* **9**, 1123–1130. <https://doi.org/10.1016/j.jrmge.2017.07.004>
- Kaban, M. K., Petrunin, A. G., El Khrepy, S., & Al-Arifi, N. (2018). Diverse continental subduction scenarios along the Arabia-Eurasia collision zone. *Geophysical Research Letters* **45**, 6898–6906. <https://doi.org/10.1029/2018GL078074>

- Khodabakhshnezhad, A., Arian, M., Khodabakhshnezhad, A., Arian, M., 2016. Salt Tectonics in the Southern Iran. *International Journal of Geosciences* **7**, 367–377. <https://doi.org/10.4236/IJG.2016.73029>
- Kokum, M., Özcelik, F., 2020. An example study on re-evaluation of historical earthquakes: 1789 Palu (Elazığ) earthquake, Eastern Anatolia, Turkey. *Bulletin of the Mineral Research and Exploration* **161**, 157–170.
- Lacombe, O., Bellahsen, N., Mouthereau, F., 2011. Fracture patterns in the Zagros Simply Folded Belt (Fars, Iran): Constraints on early collisional tectonic history and role of basement faults. *Geol Mag* **148**, 940–963. <https://doi.org/10.1017/S001675681100029X>
- Lai, J., Wang, G., Wang, S., Cao, J., Li, M., Pang, X., Han, C., Fan, X., Yang, L., He, Z., Qin, Z., 2018. A review on the applications of image logs in structural analysis and sedimentary characterization. *Mar Pet Geol* **95**, 139–166. <https://doi.org/10.1016/j.marpetgeo.2018.04.020>
- Lin, W., Saito, S., Sanada, Y., Yamamoto, Y., Hashimoto, Y., Kanamatsu, T., 2011. Principal horizontal stress orientations prior to the 2011 Mw 9.0 Tohoku-Oki, Japan, earthquake in its source area. *Geophys Res Lett* **38**. <https://doi.org/10.1029/2011GL049097>
- Mafakheri B., N., Lin, W., Murata, S., Yousefi, F., Radwan, A.E., 2022. Magnitudes and orientations of present-day in-situ stresses in the Kurdistan region of Iraq: Insights into combined strike-slip and reverse faulting stress regimes. *J Asian Earth Sci* **239**, 105398. <https://doi.org/10.1016/j.jseaes.2022.105398>
- Marghani, M.M.A., Zairi, M., Radwan, A.E., 2023. Facies analysis, diagenesis, and petrophysical controls on the reservoir quality of the low porosity fluvial sandstone of the Nubian formation, east Sirt Basin, Libya: Insights into the role of fractures in fluid migration, fluid flow, and enhancing the permeability of low porous reservoirs. *Mar Pet Geol* **147**, 105986. <https://doi.org/10.1016/J.MARPETGEO.2022.105986>
- Najibi, A.R., Ghafoori, M., Lashkaripour, G.R., Asef, M.R., 2015. Empirical relations between strength and static and dynamic elastic properties of Asmari and Sarvak limestones, two main oil reservoirs in Iran. *J Pet Sci Eng* **126**, 78–82. <https://doi.org/10.1016/J.PETROL.2014.12.010>

- Oohashi, K., Lin, W., Wu, H.Y., Yamaguchi, A., Yamamoto, Y., 2017. Stress State in the Kumano Basin and in Slope Sediment Determined From Anelastic Strain Recovery: Results From IODP Expedition 338 to the Nankai Trough. *Geochemistry, Geophysics, Geosystems* **18**, 3608–3616. <https://doi.org/10.1002/2017GC007137>
- Queen, J.H., Rizer, W.D., 1990. An integrated study of seismic anisotropy and the natural fracture system at the Conoco borehole test facility, Kay County, Oklahoma. *J Geophys Res* **95**. <https://doi.org/10.1029/JB095IB07P11255>
- Radwan, A., Abdelghany, W.K., Elkhawaga, M.A., 2021. Present-day in-situ stresses in Southern Gulf of Suez, Egypt: Insights for stress rotation in an extensional rift basin. *J Struct Geol* **147**, 104334. <https://doi.org/10.1016/j.jsg.2021.104334>
- Radwan, A., Sen, S., 2021a. Characterization of in-situ stresses and its implications for production and reservoir stability in the depleted El Morgan hydrocarbon field, Gulf of Suez rift basin, Egypt. *J Struct Geol* **148**, 104355. <https://doi.org/10.1016/j.jsg.2021.104355>
- Radwan, A., Sen, S., 2021b. Stress Path Analysis for Characterization of In Situ Stress State and Effect of Reservoir Depletion on Present-Day Stress Magnitudes: Reservoir Geomechanical Modeling in the Gulf of Suez Rift Basin, Egypt. *Natural Resources Research* **30**, 463–478. <https://doi.org/10.1007/s11053-020-09731-2>
- Sonder, L.J., 1990. Effects of density contrasts on the orientation of stresses in the lithosphere: Relation to principal stress directions in the Transverse Ranges, California. *Tectonics* **9**, 761–771. <https://doi.org/10.1029/TC009I004P00761>
- Sonnette, L., Humbert, F., Aubourg, C., Gattacceca, J., Lee, J.C., Angelier, J., 2014. Significant rotations related to cover–substratum decoupling: Example of the Dôme de Barrôt (Southwestern Alps, France). *Tectonophysics* **629**, 275–289. <https://doi.org/10.1016/J.TECTO.2014.04.009>
- Stern, R., Johnson, P., 2010. Continental lithosphere of the Arabian Plate: A geologic, petrologic, and geophysical synthesis. *Earth-Science Reviews* **101**, 29–67, <https://doi.org/10.1016/j.earscirev.2010.01.002>.

- Tang, Z., Kong, X., Duan, W., Gao, J., 2021. Wellbore breakout analysis and the maximum horizontal stress determination using the thermo-poroelasticity model. *J Pet Sci Eng* **196**, 107674. <https://doi.org/10.1016/j.petrol.2020.107674>
- Tingay, M., Reinecker, J., Müller, B., 2008. Borehole breakout and drilling-induced fracture analysis from image logs. *World stress map* 1–8. http://dc-app3-14.gfz-potsdam.de/pub/guidelines/WSM_analysis_guideline_breakout_image.pdf
- Vernant, P., Nilforoushan, F., Hatzfeld, D., Abbassi, M.R., Vigny, C., Masson, F., Nankali, H., Martinod, J., Ashtiani, A., Bayer, R., Tavakoli, F., Chéry, J., 2004. Present-day crustal deformation and plate kinematics in the Middle East constrained by GPS measurements in Iran and northern Oman. *Geophys J Int* **157**, 381–398. <https://doi.org/10.1111/j.1365-246X.2004.02222.x>
- Wang, H., 2017. Theory of linear poroelasticity with applications to geomechanics and hydrogeology. *Princeton University Press*. <https://doi.org/10.1515/9781400885688>
- Yaghoubi, A., Mahbaz, S., Dusseault, M.B., Leonenko, Y., 2021. Seismicity and the state of stress in the Dezful embayment, Zagros fold and thrust belt. *Geosciences* **11**, 254. <https://doi.org/10.3390/geosciences11060254>
- Zoback, M.D., 2007. Reservoir Geomechanics, 1st edition, *Cambridge University Press*. <https://doi.org/10.1017/CBO9780511586477>
- Zoback, M.D., Barton, C.A., Brudy, M., Castillo, D.A., Finkbeiner, T., Grollimund, B.R., Moos, D.B., Peska, P., Ward, C.D., Wiprut, D.J., 2003. Determination of stress orientation and magnitude in deep wells. *International Journal of Rock Mechanics and Mining Sciences* **40**, 1049–1076. <https://doi.org/10.1016/j.ijrmms.2003.07.001>

Chapter 6

Application of AI in borehole breakout analysis

6.1 Background

Borehole breakouts, a form of wellbore instability, are local enlargements of the borehole diameter usually associated with in-situ stress and formation strength. They create an unstable wellbore condition that, in the worst-case scenario, can result in a complete wellbore collapse if not promptly addressed (Moore et al., 2012; Neeamy and Selman, 2020). Borehole breakouts cause problems in drilling operations such as excessive non-productive time due to stuck pipe incidents, wellbore collapse, or the need for remedial operations, mud loss and sand production (Cheatham, 1984; Kovacich and Haimson, 2000; Najibi et al., 2017).

In addition, detecting breakouts is a crucial step in well-completion design. Information about breakouts, such as their location and size, can help to optimize the completion design to mitigate their effects (Xia et al., 2020). Additionally, understanding the causes behind the breakouts can assist in planning effective sand control measures or devising suitable hydraulic fracturing strategies (Xia et al., 2020). Breakouts are also important features in evaluation of stress state in the wellbore (Zoback et al., 1985).

Traditionally, breakouts are identified through the visual interpretation of borehole image logs, including acoustic or resistivity images of the borehole wall. This approach, although effective, can be time-consuming, subject to human error, and demands considerable expertise (Dias et al., 2020). Despite recent progress in advanced artificial intelligence (AI) techniques in image processing to detect breakouts from image logs automatically, so far, human supervision is inevitable in the procedure.

Table 6-1. Comparison between image logs and conventional logs.

Image Log	Conventional log
High resolution	Low resolution
High accuracy borehole deformation detection	Low accuracy borehole deformation detection
High cost	Low cost
Not frequently used in drilled wells	Frequently used
Not available in most of wells	Available in most of wells
Low successful operation rate	High successful operation rate
Difficult interpretation for resistivity image log	Relatively related to physical parameters of rock

As shown in Table 6-1, the conventional wireline log is compared with the image logs. However, borehole image logs have much higher resolution than conventional logs, but they are not always available due to their high acquisition cost and low successful operation rate, limiting their widespread use in routine drilling operations. Moreover, image logs were unavailable for hundreds of boreholes drilled before such technology was introduced in the 1980s (Soroush et al., 2010). On the other hand, conventional log data, such as radioactivity, neutron porosity, resistivity, density, and sonic logs, are widely collected during and after drilling operations. They contain valuable information about the geological formations traversed by the borehole and are readily available for most wells (Mousavipour et al., 2020).

In recent years, machine learning (ML) has revolutionized how geoscientists and engineers approach the analysis of subsurface data. ML has been increasingly applied in various aspects of oil and gas operations due to its ability to process large volumes of data, recognize complex patterns, and make accurate predictions (e.g., Bergen et al., 2019; Morgenroth et al., 2019; Osarogiagbon et al., 2021; Zhong et al., 2022).

Classification, a significant branch of AI, categorizes data into distinct classes based on certain attributes. In the context of identifying borehole breakouts, classification models can be trained to recognize patterns in conventional log data that indicate the presence of breakouts (e.g., Soroush et al., 2010; Xia et al., 2020). Therefore, developing an ML classification model to predict borehole breakouts using conventional log data could significantly enhance the efficiency and cost-effectiveness of breakout detection, thereby improving wellbore stability management. Supervised ML employs algorithms that learn from labeled training data to make predictions or decisions without being explicitly programmed to perform the task (Osarogiagbon et al., 2021).

The study in this chapter aims to explore the application of various supervised ML classification models, including K-Nearest Neighbors (KNN), Decision Tree (DT), Random Forest (RF), Support Vector Machine (SVM), and Extreme Gradient Boosting (XGBoost) for identifying borehole breakouts in carbonate reservoirs based on conventional log data and borehole image logs. Each model has unique strengths and suits different data types and problem domains.

The comparative analysis of these models on the given dataset will provide insights into their performance and suitability for the task. Through a rigorous evaluation of these models, this study aims to develop a more effective, accurate, and automated tool for borehole breakout identification, facilitating improved wellbore stability management and safer drilling and well-completion operations with the application of only conventional logs.

6.2 ML Classification Methodology

6.2.1 Workflow

This study employed a systematic approach to explore the potential of supervised ML models in identifying borehole breakouts using conventional well logs (Mafakheri B. et al., Under review, Mafakheri B. et al. in-preparation). Two data sets, including input and dependent variables, are required for supervised classification. This study used conventional wireline logs as the input variable and identified breakout zones as the dependent variable (labels). The methodology followed a structured workflow encompassing five main steps (Figure 6-1). First, suitable well logs were investigated to identify the corresponding well logs to borehole enlargements. This objective was achieved by analyzing the distribution of well logs for breakout and non-breakout zones to identify the best candidates. Next, based on the previous study from Mafakheri et al. (2022), visual observation of a six-pad resistivity image log and six-pad caliper was used for recording the breakout zones and set as the dependent variable for supervised machine learning classification models (Figure 6-2). The results were recorded in digital format. The Breakout zone was labeled 1, and the non-breakout zone 0. Since the breakout was recorded continuously as length, but the well-log data are available for only certain depths, all logs and breakout zones were matched up.

Therefore, each value of the well log has a corresponding value from the detected breakouts from image logs. Second, as shown in Figure 6-1, a range of ML classification models, including KNN, DT, and RF, were evaluated for this study. These models were selected based on their potential applicability and performance in geological and petroleum industry-related classification tasks (Karpatne et al., 2019; Morgenroth et al., 2019; Zhong et al., 2022). Third, the input data were prepared to adopt the data to get the best performance of classification models (Figure 6-1). After that, an initial evaluation was conducted to assess the accuracy of each selected model. This step provided a preliminary insight into the models' capability to correctly identify borehole breakouts from the provided well-log data. Fourth, optimum hyperparameters for each model were determined through a systematic tuning process to enhance the models' performance (Figure 6-1). Also, overfitting problems were evaluated to validate each model's robustness and reliability in different data scenarios. Finally, a

comparative analysis was performed to evaluate the models compared to each other based on metrics such as Accuracy, Precision, Recall, and F1-Score. This step can highlight each model's relative strengths and weaknesses (Figure 6-1).

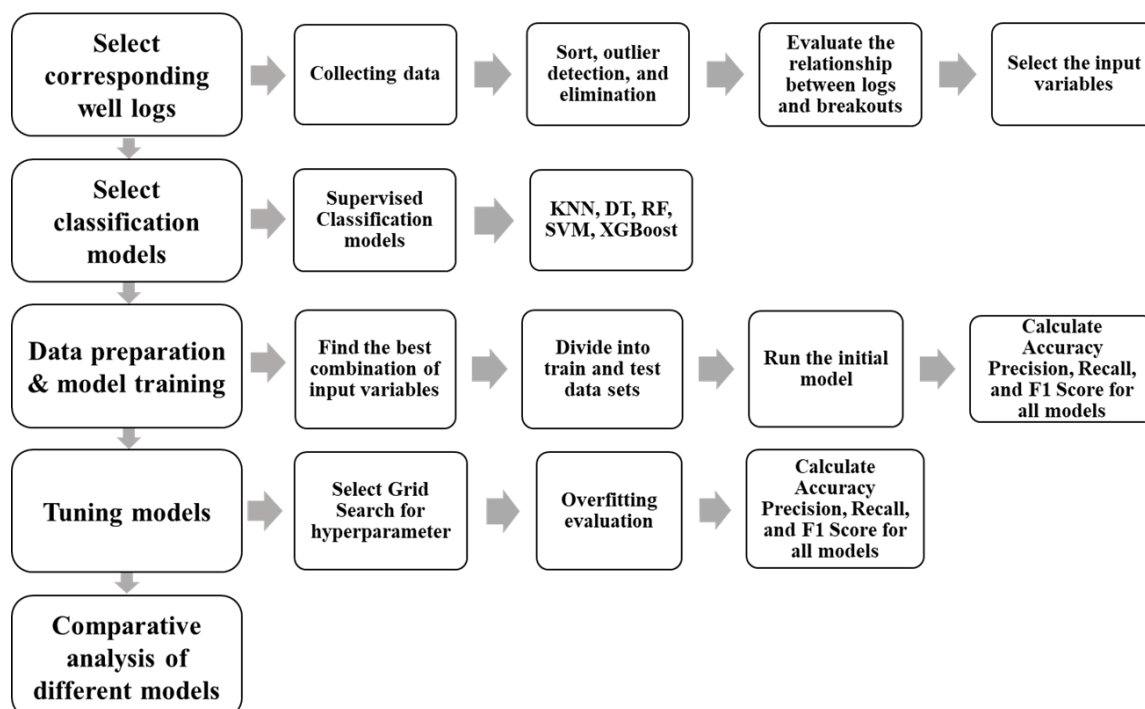


Figure 6-1. Workflow of a systematic approach to explore the potential of supervised machine learning (ML) in identifying breakout.

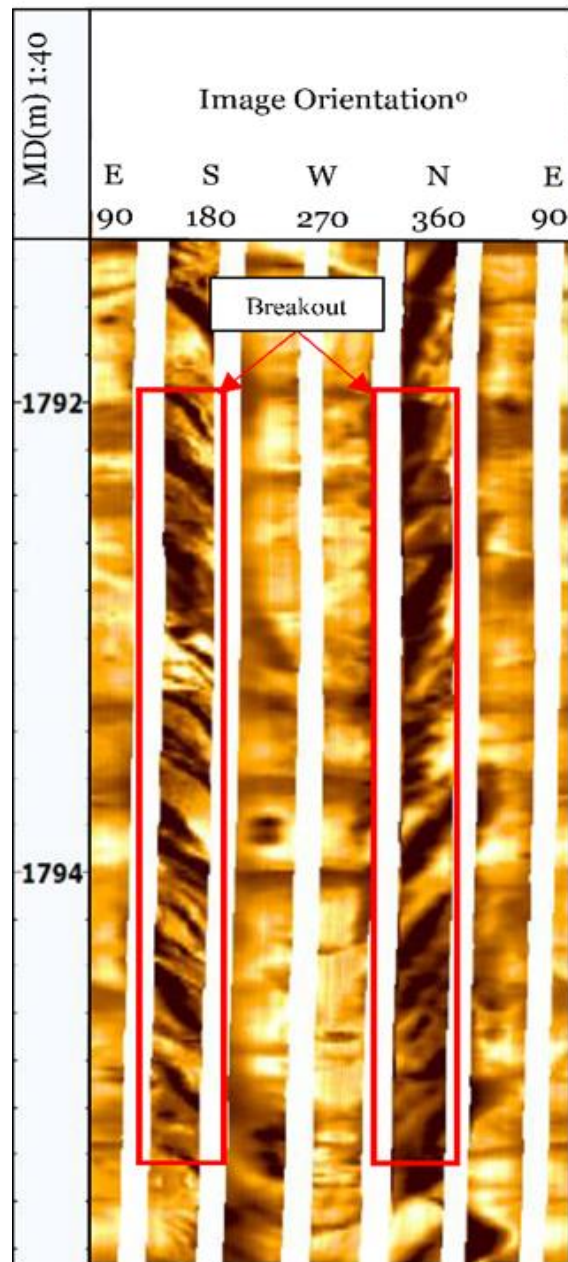


Figure 6-2. Visual observation of a six-pad resistivity image log to identify breakouts. After Mafakheri B. et al. (2022).

6.2.2 Petrophysical logs correspond to borehole geometry.

The primary objective of the initial phase of this study was to assess the employing conventional petrophysical logs to identify borehole breakouts. Initially, a list of available logs in the study area and their possible physical relation to the borehole geometry were considered. The well-log data were obtained from Mafakheri B. et. al (2022). The studied well is located in the Kurdistan region of Iraq, and the depth was between 1680 m and 2000 m in a single well. The dominant lithological unit in this study is Carbonate, including both Limestone and Dolomite. However, there are shale and marl in different intervals. The endeavor was to comprehend the varying responses of different logs corresponding to the breakout and non-breakout zones. Then, each well log was evaluated individually to find potential correlations between a particular petrophysical log and the occurrence of breakouts, preliminary in carbonate rocks. As shown in Figures 6-3a, b, c, d, e, f and g, histograms of each well log for breakout zones and non-breakout zones were plotted to evaluate the impact of borehole geometry on the wireline logs. Some of the logs indicate a better correlation than others. In the histogram, if the distribution of well log values for breakout and non-breakout zones has a similar trend, there is a low chance that there is a good correlation with the occurrence of breakouts. For example, density-related logs such as neutron porosity (NPHI), bulk density (RHOB), sonic, and density correction (DRHO) show a higher potential than gamma ray-related logs such as gamma-ray (GR), thorium (Th), potassium (K), uranium (U), and photoelectric factor (PEF). In addition, deeper resistivity logs, such as deep lateral (LLD) and shallow lateral (LLS), show a better correlation than wellbore wall resistivity logs, such as mud cake resistivity (MSFL).

Based on the histograms depicted in Figure 6-3, a higher caliper (CAL) value is associated with the existence of the BO zones. The frequency of breakout zones is higher in the medium GR, low LLD, and higher sonic log slowness, which is probably associated with clay content or thin layers of shale in the carbonates. According to the drilling report, water formation resistivity was lower than drilling fluid, and for water-based drilling fluid in this study, invasion into shaly intervals is lower than carbonates. Besides, in higher RHOB and NPHI, the breakout is more likely to occur. However,

DRHO did not exhibit a discernible correlation with the occurrence of breakouts in this analysis.

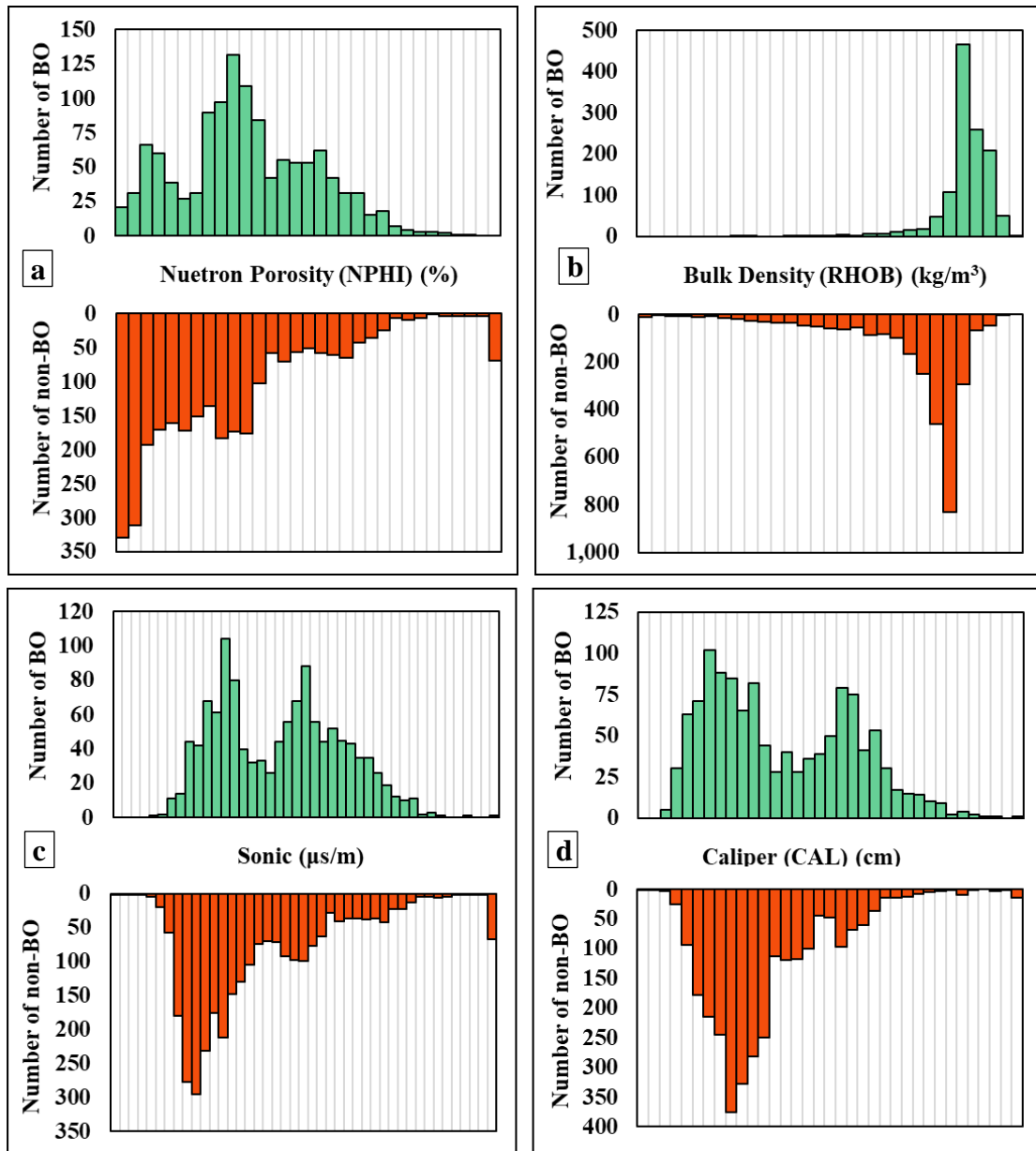


Figure 6-3. a, b, c, d, e, f, g) Effect of the presence of breakout zones on petrophysical well logs by plotting their histogram. Orange bars represent the histogram bar of non-breakout zones (non-BO), and green bars represent the histogram of breakout zones (BO). h) Blue squares represent breakout zones, and red squares represent non-breakout zones for the CAL-RHOB graph, and the green frame shows two distinct areas in the graph in which the occurrence of breakout is more frequent. i) Blue squares represent breakout zones, and red squares represent breakout zones for the NPHI-CAL-RHOB graph.

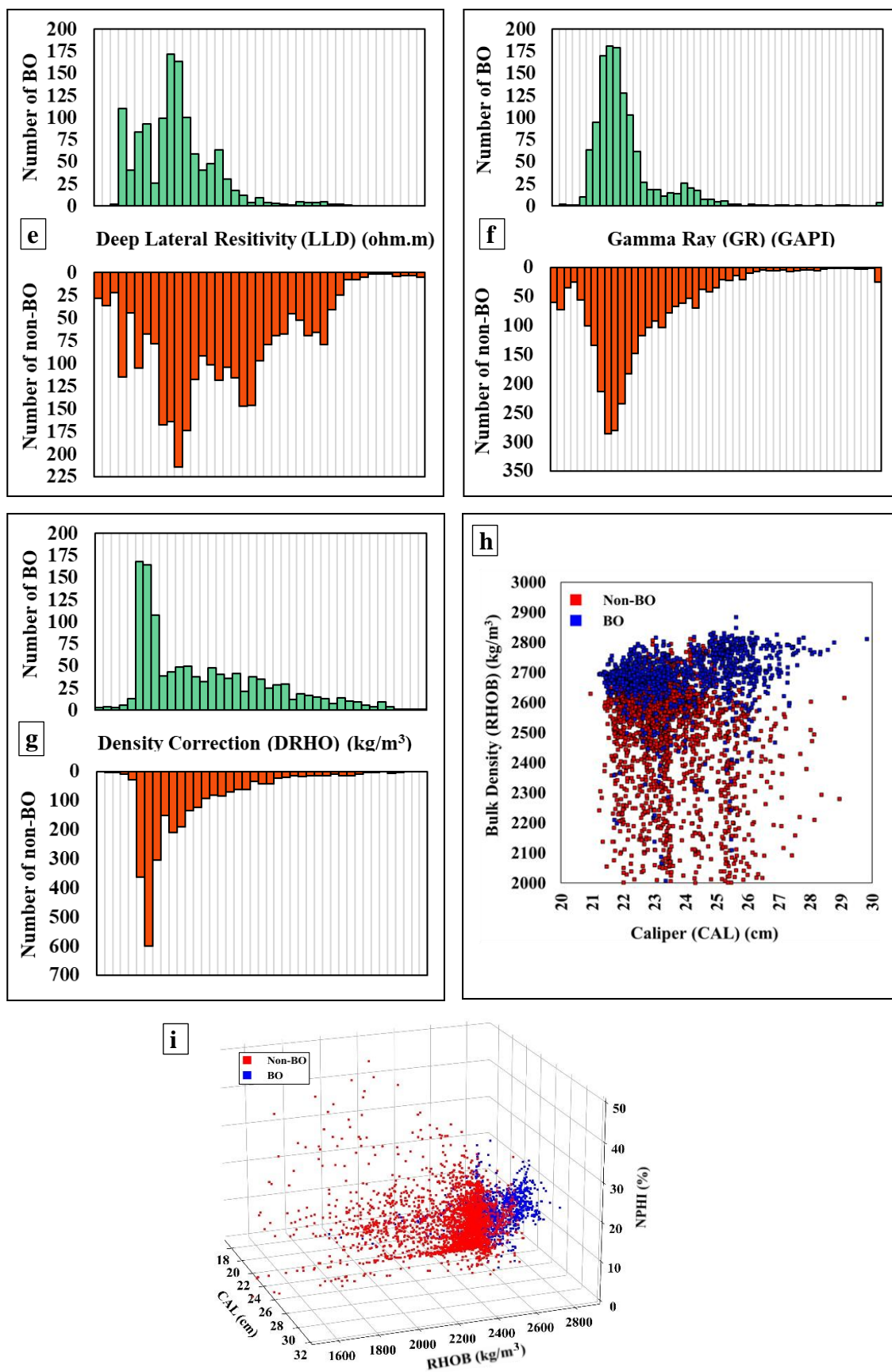


Figure 6-3. Continued.

As shown in Table 6-2, 12 logs were selected for this analysis. Input logs were categorized into four categories. First, density-related logs (NPHI, Sonic, RHOB, and DRHO), second, gamma ray-related logs (GR, Th, K, and U), third, resistivity-related logs (LLD, LLS, MSFL), and finally, CAL as the last category.

The outcomes of the single well log analysis underscored that while certain individual logs might exhibit a response to the presence or absence of breakout zones to some extent, detecting breakout zones merely by individual logs is not reliable due to the complexity of the rock properties and geomechanical parameters. Therefore, applying multiple well logs to the borehole breakout is the next step. Figures 6-3h and 6-3i show two and three-log cross-plots based on the breakout and non-breakout zones. Evidently, both plots are more capable of distinguishing the breakout and non-breakout zones and portray an improvement in separation by incorporating a second variable. For instance, the CAL-RHOB plot shows a more distinctive border between the two zones (Figure 6-3h). However, extending the dimensionality of the analysis to three by including the NPHI log in a three-dimensional plot (RHOB-CAL-NPHI) shows a better capacity to separate the different zones (Figure 6-3i). This fact intrigued this study to evaluate the possibility of using a multivariable plot in a higher dimensional space. Therefore, several different hyperdimensional models from 4 dimensions to 12 dimensions were evaluated in this study. The next section will present a workflow for identifying borehole breakout zones based on proposed classification models.

Table 6-2. List of input variables and dependent variables. Values at ten depths are shown as examples for the input and dependent variables.

Variables	Input Variables												Dependent Variable
	Neutron Porosity	Sonic Travel Time	Bulk Density	Density correction	Gamma Ray	potassium content	Thorium content	Uranium Content	Deep Resistivity	Shallow Resistivity	micro-spherically focused log	Average Caliper	Breakout occurrence
Symbol	NPHI	DT	RHOB	DRHO	GR	POTA	THOR (ppm)	U	LLD	LLS	MSFL	CAL	BO
Units	%	us/m	kg/m ³	kg/m ³	GAPI	kg/m ³	ppm	ppm	OHMM	OHMM	OHMM	cm	1= BO 0=NBO
1616.51	13.96	62.29	2500	90	8.94	0.53	2.50	1.67	9.89	10.78	2.72	27.56	0
1616.66	13.87	61.85	2340	50	7.57	0.532	2.33	1.73	9.60	10.43	3.56	26.01	0
1616.82	17.15	63.49	2150	50	8.53	0.53	2.14	1.78	9.47	10.23	17.06	25.91	0
1616.97	20.03	64.19	2040	90	7.66	0.521	2.03	1.83	9.61	10.38	3.64	25.83	0
1617.12	23.05	63.81	2010	130	8.22	0.473	2.01	1.85	10.11	10.91	3.03	26.26	0
1617.27	20.64	64.98	2080	110	7.31	0.449	2.08	1.86	10.74	11.62	1.88	27.81	1
1617.43	16.97	65.48	2250	110	6.69	0.446	2.25	1.92	11.33	12.30	0.38	29.18	0
1617.58	14.78	64.08	2490	100	6.99	0.439	2.49	1.91	11.72	12.85	0.32	30.30	1
1617.73	11.63	63.79	2540	50	6.06	0.427	2.55	1.94	11.72	13.04	0.21	30.28	1
1617.88	11.14	64.53	2550	0	7.43	0.475	2.55	1.96	11.33	12.83	0.34	30.91	0

6.3 Classification Models

6.3.1 Model selection

As shown in Table 6-3, five classification models were selected according to previous literature. Each model has some merits and disadvantages. The choice between them would depend on the specific requirements of the task, such as the nature of the data, the computational resources available, and the level of interpretability required. As presented in Table 6-3, the KNN is a simple and intuitive instance-based learning algorithm based on the majority class of its K nearest neighbors in the feature space, though it can struggle with high-dimensional data and requires a meaningful distance metric. (Ghenabzia et al., 2020). A DT model is a flowchart-like tree structure where each node represents a feature, each branch represents a decision rule, and each leaf node represents the outcome. DT models are highly interpretable and easy to implement, but they are prone to overfitting and can be sensitive to small variations in the data (Alshaikh et al., 2018). RF is an ensemble learning method that constructs multiple decision trees during training and outputs the class mode of the classes output by individual trees. RF addresses some of the overfitting issues of a single decision tree and often provides better generalization performance, but at the cost of increased complexity and decreased interpretability (Gupta et al., 2019). SVM is a powerful classification algorithm that finds the optimal hyperplane separating different classes in the feature space. SVM excels in high-dimensional spaces and is robust to outliers. Still, they can be computationally intensive and may require careful tuning of the kernel and parameters (Abdelgawad et al., 2018). Lastly, XGB is a powerful ensemble method that can handle various data types and often delivers superior predictive performance. XGBoost is an advanced implementation of a gradient-boosting algorithm that has shown better accuracy in many machine-learning tasks. Still, it can be computationally intensive and may require careful tuning of hyperparameters (Gupta et al., 2019).

Table 6-3. Comparison between the supervised machine learning classification.

Algorithm	Strengths	Weaknesses
KNN	<ul style="list-style-type: none"> • Simple to understand and easy to implement • Makes no assumptions about the distribution of the underlying data • Interpretable results 	<ul style="list-style-type: none"> • sensitive to irrelevant or redundant features • computationally expensive and slow • Selecting the optimal number of neighbors (K) can be challenging
DT	<ul style="list-style-type: none"> • easy to interpret and visualize • require less data preprocessing • flexibility to handle data with non-linear relationships 	<ul style="list-style-type: none"> • Prone to overfitting, especially when a tree is particularly deep • not perform well on small datasets • The algorithm makes greedy decisions at each node to reduce the impurity
RF	<ul style="list-style-type: none"> • No effort for data preparation • Able to rank feature importance • Works well in high-dimensional spaces 	<ul style="list-style-type: none"> • Lack of interpretability if tree quantity is large • May overfit if data is noisy
SVM	<ul style="list-style-type: none"> • Works well in complicated domains • Works well with outliers • Effective in High Dimensional Spaces 	<ul style="list-style-type: none"> • Requires data preparation • Kernel selection can be hard • Poor performance and long computation time if the dataset is large and noisy
XGBoost	<ul style="list-style-type: none"> • No effort for data preparation • Able to rank feature importance • State-of-the-art accuracy in many regression and classification problems 	<ul style="list-style-type: none"> • Lack of interpretability • Poor performance on some tasks, such as image and text recognition

6.3.2 K-Nearest Neighbors (KNN):

The KNN algorithm begins by selecting the number of neighbors (K) (Figure 6-4). The most popular distance weigh option is the Euclidean distance, while other options include the Manhattan distance and the Minkowski distance, which could be useful in some other cases. The formula for Euclidean distance is as follows (Mucherino et al., 2009):

$$d(p, q) = \sqrt{(p_1 - q_1)^2 + (p_2 - q_2)^2 + \dots + (p_n - q_n)^2} \quad (6-1)$$

where $d(p, q)$ is the Euclidean distance between points p and q and n is the total number of dimensions. The method calculates the distance between each observation and every other point in the training dataset, ranks the distances in ascending order, and selects the first K points to classify. For classification, a majority vote is conducted, counting the times each class appears among the K -nearest neighbors and assigning the most common class to the observation. The majority-weighted vote equation is (Mucherino et al., 2009):

$$\hat{y} = \arg \max_c \sum_{i=1}^K w_i \cdot I(y_i = c) \quad (6-2)$$

where \hat{y} is the predicted class label, and c is the class label. K is the number of the nearest neighbors considered, and I is the indicator function. On the other hand, w_i is the weight assigned to the i^{th} nearest neighbor. The algorithm outputs the class label for classification tasks. Optionally, the model's error can be evaluated on a validation set to tune hyperparameters like the number of neighbors (K) and the distance metric.

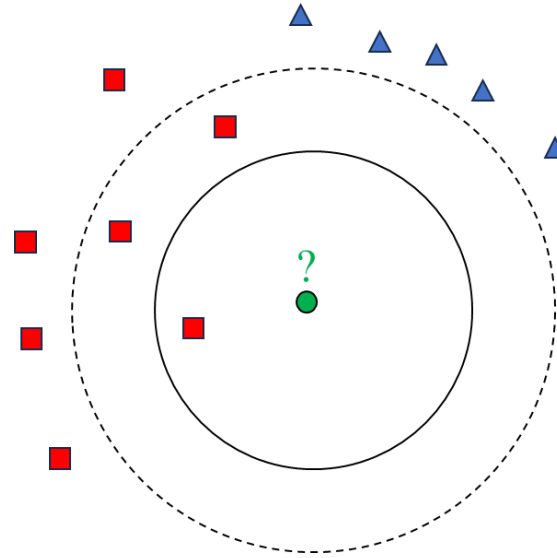


Figure 6-4. KNN classification conceptual image. Classification depends on the distance between the input data point (green circle) and different classes (red squares and blue triangles).

6.3.3 Decision Tree (DT):

A DT for classification is a supervised learning algorithm that predicts a target by learning decision rules inferred from the data features (Figure 6-5). The target variable is categorical, denoting the class label. The algorithm selects the attribute that best divides the dataset using a feature selection measure like Gini impurity or Information gain/entropy. Gini impurity is calculated as (Webb et al., 2011):

$$\text{Gini}(p) = 1 - \sum (p_i)^2 \quad (6-3)$$

where p_i is the proportion of samples belonging to class i at a given node. On the other

$$\text{IG}(D_p, f) = I(D_p) - \sum_{j=1}^m \frac{N_j}{N} I(D_j) \quad (6-4)$$

hand, Information gain (IG) is calculated using (Webb et al., 2011):

where I is the entropy of the dataset, D_p is for the parent, D_j is for the j -th child node, N is the total number of samples, and f is the feature that maximizes information gain or minimizes Gini impurity to split the dataset into subsets. This process goes back and forth,

making a tree structure with decision nodes and leaf nodes. When there are no more attributes to split, and the tree has reached its deepest point, the growth will stop at this point. The key hyperparameter in a DT classifier is whether Gini or entropy for the purity of a node. The maximum depth of the tree, the minimum number of samples required to split an internal node, and the minimum number of samples required for a leaf node are among other important hyperparameters for tuning DT models.

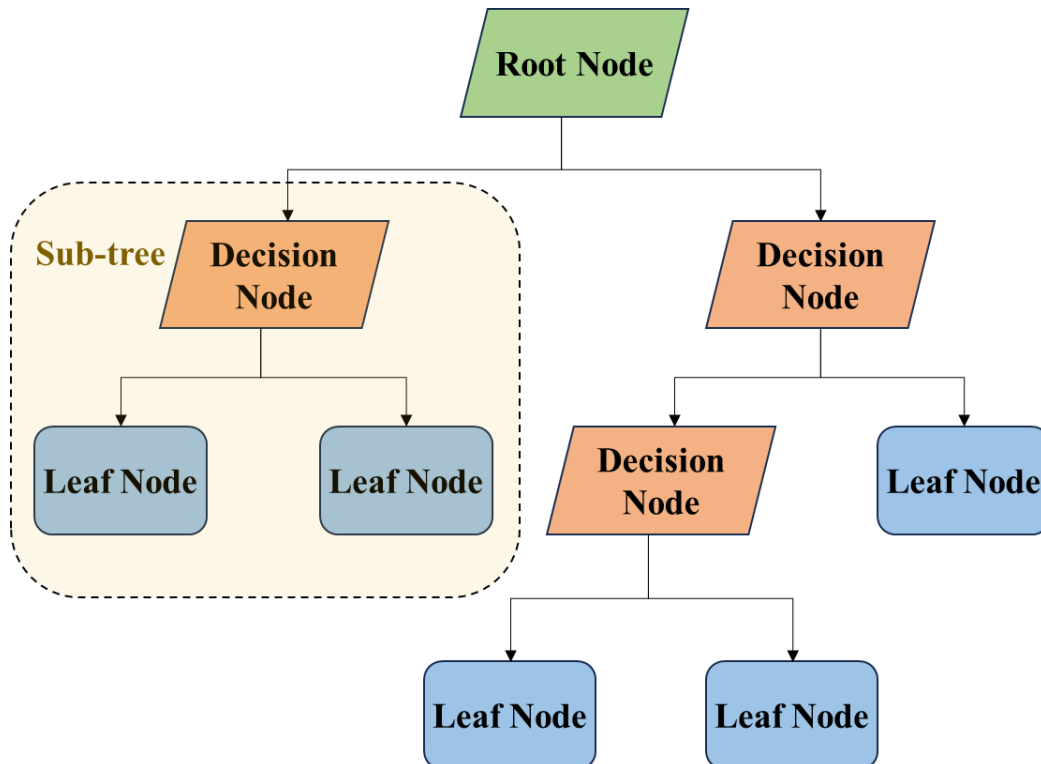


Figure 6-5. Illustration of a simple DT algorithm. Decision nodes will continue to the next node, and in the leaf node, the tree will be ended.

6.3.4 Random Forest (RF):

RF is an ensemble learning method that operates by constructing multiple decision trees during training and outputting the class, that is, the mode of the classes output by individual trees. Initially, several trees will be built in the forest as the number of estimators. A bootstrap sample from the training data for each tree will be selected. Each tree is grown to the fullest extent possible, without pruning, on this bootstrap sample (Figure 6-6). However, a random subset of features is chosen to split the node at each node rather than considering all features. This randomness in feature selection helps to make the model robust to outliers and noisy data and also helps to decrease the correlation between trees in the forest, making the ensemble model more robust. Each tree in the forest is built independently of the others. For classification tasks, the Gini impurity or entropy is often used as the criterion for making splits in the decision trees. The Gini impurity, entropy and information gain (IG) are calculated as follows (Fawagreh et al., 2014; Liu et al., 2012):

$$\text{Gini}(p) = 1 - \sum(p_i)^2 \quad (6-5)$$

$$\text{Entropy} = - \sum_{i=1}^J p_i \log_2(p_i) \quad (6-6)$$

$$\text{Information Gain} = \text{Entropy}_{parent} - \sum_j \frac{N_{child_j}}{N_{parent}} \text{Entropy}_{parent_j} \quad (6-7)$$

where p_i is the probability of an item with label i . Once all the trees have been built, predictions can be made by passing the input data through all the trees in the forest and aggregating their predictions. The class with the most votes is returned for classification. Entropy_{parent} is the entropy of the parent node before the split, N_{child_j} is the number of samples in the j -th child node after the split, N_{parent} is the number of samples in the parent node, and $\text{Entropy}_{parent_j}$ is the entropy of the j -th child node. Hyperparameters like the maximum depth of the tree, the minimum number of samples required to split a node, and the number of estimators should be tuned to control the complexity of the individual trees in the forest.

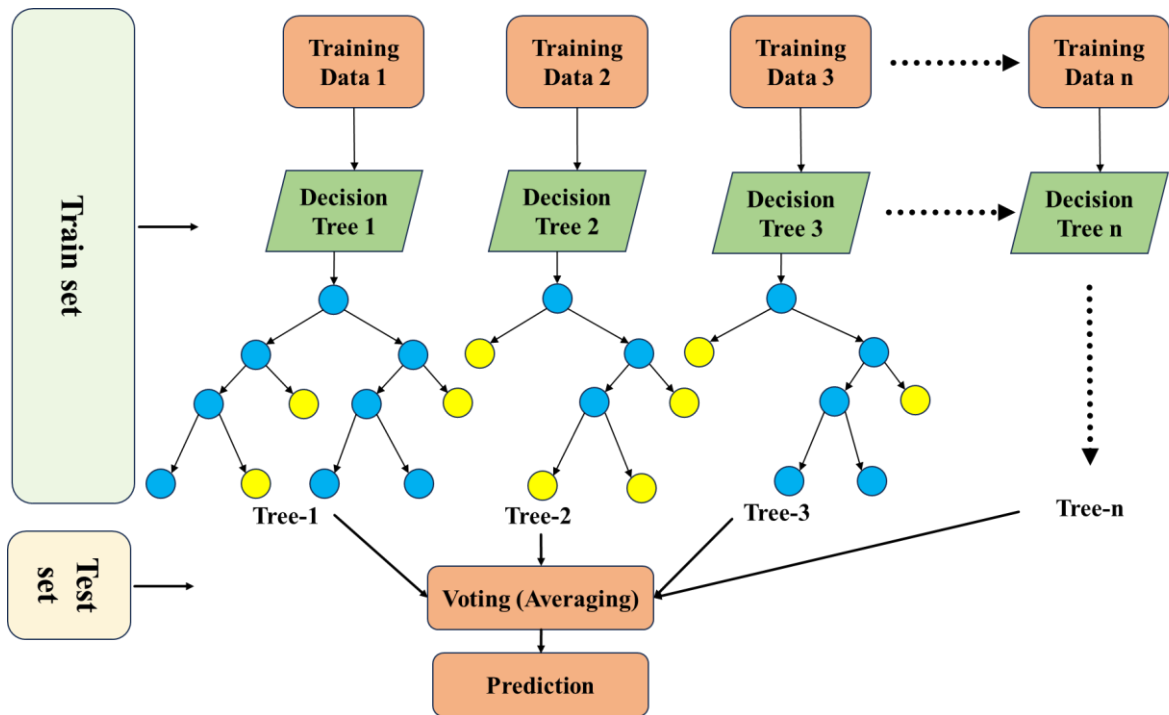


Figure 6-6. Schematic illustration of RF algorithm. Blue circles represent decision nodes and yellow circles represent leaf nodes. The train and test set are separated by two-time spans on the left side.

6.3.5 Support Vector Machine (SVM)

SVM is a supervised machine learning algorithm widely used for classification tasks such as finding the optimal hyperplane that categorizes the dataset into distinct classes with the maximum margin (Figure 6-7a). The kernel function is a vital element in SVM, facilitating the transformation of input data into a higher-dimensional space to enable the separation of classes by a hyperplane (Figure 6-7b). The choice of kernel is crucial, with options such as the radial basis function (RBF) kernel (Cristianini and Ricci, 2008):

$$K(x_i, x_j) = \exp(-\gamma \|x_i - x_j\|^2) \quad (6-8)$$

Where K is the kernel function, x_i and x_j are two feature vectors in the input space, and γ is a parameter that sets the kernel's spread, determining how much influence a single training example has. The decision function for classifying a new instance is:

$$f(x) = \text{sgn} \left(\sum_{i=1}^n \alpha_i y_i K(x_i, x) + b \right) \quad (6-9)$$

K is the kernel function, α_i is the Lagrange multipliers, and "sgn" is the sign function. The parameters α_i are derived from the dual problem, which is maximized under the conditions $\sum_{i=1}^n \alpha_i y_i = 0$ and $\alpha_i \geq 0$. The y_i represents the label of the i -th training example. The b is considered a bias of the model and serves as an intercept term in the decision function. Gamma is one of the most important hyperparameters. The larger the gamma, the closer other examples must be affected. In addition, Hyperparameters in regularization parameter C , which balances the trade-off between a low training error and a smooth decision boundary, and the kernel coefficient γ , determine the influence of individual training examples. High values of C can lead to overfitting, while low values may result in underfitting.

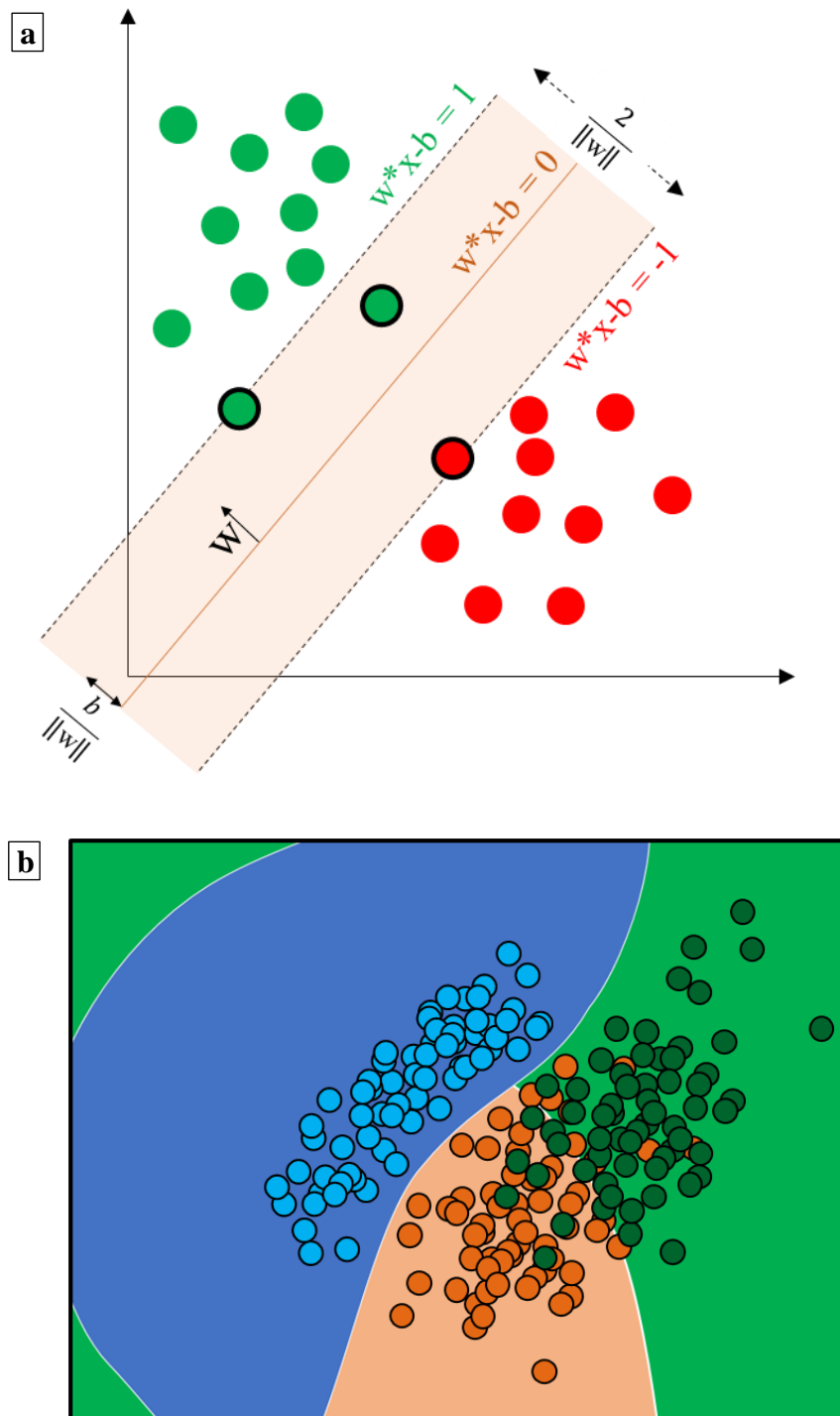


Figure 6-7. SVM classification conceptual image. Green and red circles represent two different classes. New cases (Green and red circles with black borders) get classified depending on their distance from the separation line. b) Schematic illustration of RBF kernel. Different classes get separated based on the radial distance from the hyperplane.

6.3.6 Extremely Gradient boosting (XGBoost)

XGBoost is an efficient and powerful implementation of gradient boosting widely used for classification tasks (Figure 6-8). XGBoost is a supervised learning algorithm based on ensemble trees. It aims at optimizing the cost objective function composed of a loss function (d) and a regularization term (β): It minimizes a regularized objective function that combines a loss function with a regularization term to control overfitting (Chen and Guestrin, 2016; Cherif and Kortebi, 2019):

$$\Omega^{(t)} = \sum_{i=1}^n \left[d(y_i, \hat{y}_i^{(t-1)}) + g_i f_t(x_i) + \frac{1}{2} h_i f_t^2(x_i) \right] + \beta(f_t) \quad (6-10)$$

where $\Omega^{(t)}$ represents the regularized objective at iteration t . It is the function that XGBoost tries to minimize when adding the new tree f_t . n is the number of training examples. y_i is the true label for the i -th training example. $\hat{y}^{(t-1)}$ is the prediction for the $(t-1)$ -th iteration before adding the new tree. h_i is the second derivative of the loss function with respect to the prediction $\hat{y}^{(t-1)}$. XGBoost uses both the gradient of the loss function g_i and h_i , which is computed for each instance of i as:

$$g_i = \partial_{\hat{y}^{(t-1)}} l(y_i, \hat{y}^{(t-1)}) \quad (6-11)$$

$$h_i = \partial_{\hat{y}^{(t-1)}}^2 l(y_i, \hat{y}^{(t-1)}) \quad (6-12)$$

The model is an ensemble of trees, where each tree is added iteratively to correct the residuals of the previous trees. The prediction at step t is updated as:

$$\hat{y}^{(t)} = \hat{y}^{(t-1)} + \eta f_t(x) \quad (6-13)$$

where, $f_t(x)$ representing the new tree and η as the learning rate. XGBoost enhances the model by adding trees that reduce the objective function, which involves selecting split points that provide the most significant gain after accounting for the loss function reduction and the regularization penalty. Trees are grown to the maximum depth and then pruned back if the gain is negative after regularization. Key hyperparameters are

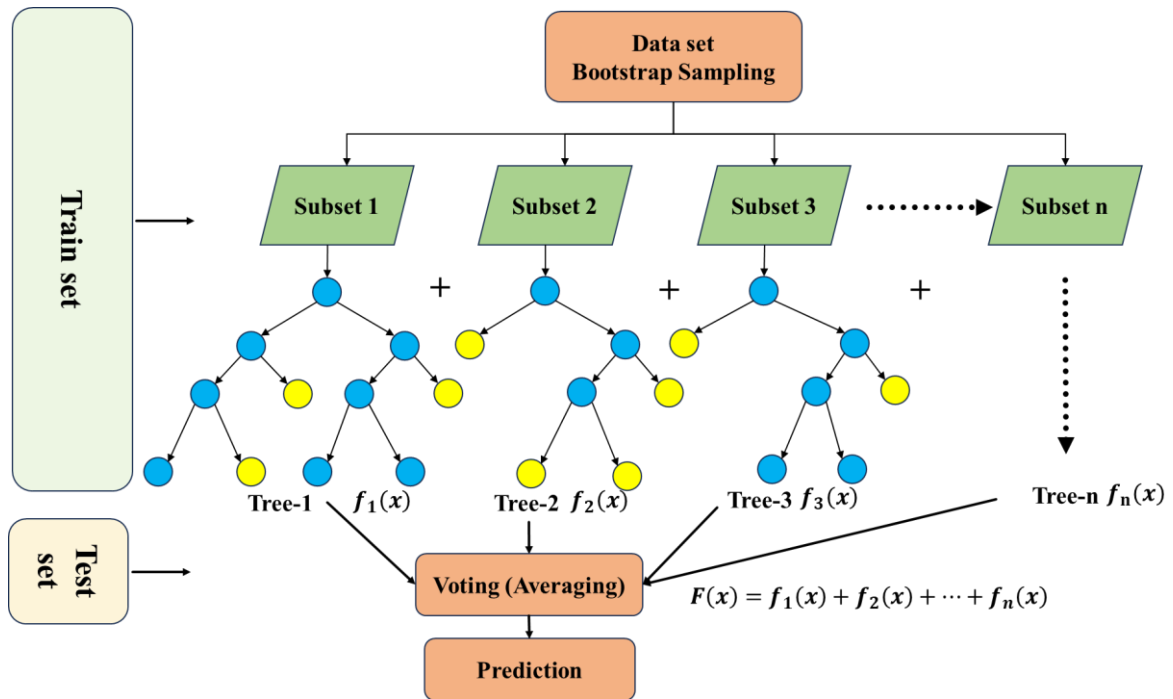


Figure 6-8. Schematic illustration of XGBoost algorithm. Blue circles represent decision nodes, and yellow circles represent leaf nodes. The train and test set are separated by two-time spans on the left side.

the learning rate η , which shrinks each tree's contribution; the maximum depth of the trees; and the number of estimators.

6.4 Evaluation metrics

In classification tasks, it is crucial to have metrics to evaluate the model's performance. Four metrics are commonly used to evaluate the performance of classification models, including Accuracy, Precision, Recall, and F1 Score. The metrics are as follows (Goutte and Gaussier, 2005):

$$\text{Accuracy} = \frac{T_p + T_n}{T_p + T_n + F_p + F_n} \quad (6-14)$$

$$\text{Precision} = \frac{T_p}{T_p + F_p} \quad (6-15)$$

$$\text{Recall} = \frac{T_p}{T_p + F_n} \quad (6-16)$$

$$\text{F1 Score} = \frac{2 * \text{Precision} * \text{Recall}}{\text{Precision} + \text{Recall}} \quad (6-17)$$

where T_p is true positive, T_n is true negative, F_p is false positive, and F_n is false negative (Table 6-4). T_p occurs when the model correctly predicts the positive class. In other words, the actual class of the instance is positive, and the model also predicts the positive class. T_n occurs when the model correctly predicts the negative class. In other words, the actual class of the instance is negative, and the model also predicts the negative class. F_p is when the actual class is negative but predicted as positive, and F_n is when the actual class is positive but predicted as negative. Accuracy is the ratio of correctly predicted instances to the total instances in the dataset, and Precision is the ratio of correctly predicted positive observations to the total predicted positives. The Recall is the ratio of correctly predicted positive observations to all observations in the actual class, and the F1 Score is the weighted average of Precision and Recall that tries to find the balance between them. In the context of a binary classification task, where the goal is to separate instances into one of two classes (often labeled as "positive" or "negative"), all metrics depend on the four conditions mentioned above. These metrics provide a more comprehensive understanding of the model performance, especially in cases where the data is imbalanced or false positives and negatives carry different costs.

These terms are fundamental in understanding the performance of a classification model, and they form the basis for many evaluations. Eventually, the combination of these metrics forms a confusion matrix, which is a specific table layout that allows visualization of the performance of a supervised learning algorithm on a set of data. As mentioned in section 2.3, after selecting the classification models, each model's principles will be evaluated based on the evaluation metrics. Furthermore, understanding these metrics is crucial for fine-tuning models, as it helps identify areas where the model may be underperforming, such as in cases of class imbalance or biased data. Additionally, these metrics serve as guidelines for model selection, where different scenarios may require prioritizing one metric over others.

In evaluating supervised machine learning models for detecting borehole breakouts, all four metrics are employed to assess performance, each offering unique insights. Accuracy measures the proportion of total correct predictions, providing a general sense of model effectiveness. However, accounting only on Accuracy can be misleading in this case for detecting breakout occurrence using an imbalanced dataset (breakout zones are less frequent than non-breakout zones). Precision is critical in this case, indicating the proportion of correct predicted breakouts, thus assessing the model's ability to avoid false positives. Even though high Precision is crucial for minimizing unnecessary interventions due to the nature of the data set and because detecting the breakout zones is more important than non-breakout zones, Recall is more important. Recall measures the model's ability to detect all actual breakouts, which avoids potentially dangerous oversights. Lastly, the F1 Score harmonizes Precision and Recall into a single metric, giving an overall performance measure where neither false positives nor false negatives are disproportionately penalized. While all metrics provide valuable information, having all four metrics close to each other in this study is important, and a big gap between them might show an unreliable classification model.

Table 6-4. Four parameters define the evaluation metrics.

	Predicted: No	Predicted: Yes
Actual: No	True Negative (T_n)	False Positive (F_p)
Actual: Yes	False Negative (F_n)	True Positive (T_p)

6.5 Results and interpretation of classification models

6.5.1 Overview

In this study, Python programming language has been used to conduct classification models. The Python code used a comprehensive approach to machine learning classification, leveraging various libraries for data processing, model training, and evaluation. First, for data preparation Pandas library is used for reading data from an Excel file and converting it to NumPy arrays, which is facilitated by NumPy library. For the machine learning part, Python code employed Sklearn library for different purposes including splitting the dataset into training and testing sets, training different classification models and evaluating their performance through metrics like Accuracy, Precision, Recall, and F1-Score. Overall, this script followed the workflow shown in Figure 6-1.

Initially, based on previous studies, from 4099 interval points, the test data size was set as 20% of all data, 819 interval points, and the train data size was set as 80%, which is 3280 points. Based on the data selection, all the data points were divided based on the shuffle mode. Therefore, every time the models were run, the depth of data selected for training and testing was changed randomly. Consequently, the results of the evaluation metrics were slightly different in different training by less than 1%.

After conducting the classification modeling for five classification models, the visual results for the entire studied well presented in Figure 6-9. T_p , T_n , F_p , and F_n were determined, and the results were used to calculate the evaluation metrics. These parameters, including Accuracy, Precision, Recall, and F1 Score, were used to evaluate the performance of each model (Figure 6-10). According to the initial results for 20%

test data size and based on all input data, the training Accuracy, Precision, Recall, and F1 Score are almost 100%, except for the DT classification model, the Accuracy is 78%. On the other hand, for the test results, as shown in Figure 6-10, the RF and XGBoost show the highest metrics, and the DT shows the lowest. The RF and XGBoost models demonstrated superior performance, with metrics nearing the 92% mark, indicating a robust ability to generalize and accurately classify borehole breakouts.

The consistency across Accuracy, Precision, Recall, and F1 Score for these two models suggests that they are well-calibrated for this task, benefiting from their ensemble approaches that combine multiple decision trees to reduce overfitting and enhance predictive power.

On the other hand, while achieving an overall Accuracy of around 83%, the SVM model exhibited a markedly lower Precision of 55%. This fact suggests that while the model is fairly good at identifying true breakouts, it is also prone to a higher rate of false positives. This discrepancy could be due to SVM's sensitivity to the choice of kernel and the hyperplane margin's fitting, which might not be optimal for the dataset's distribution.

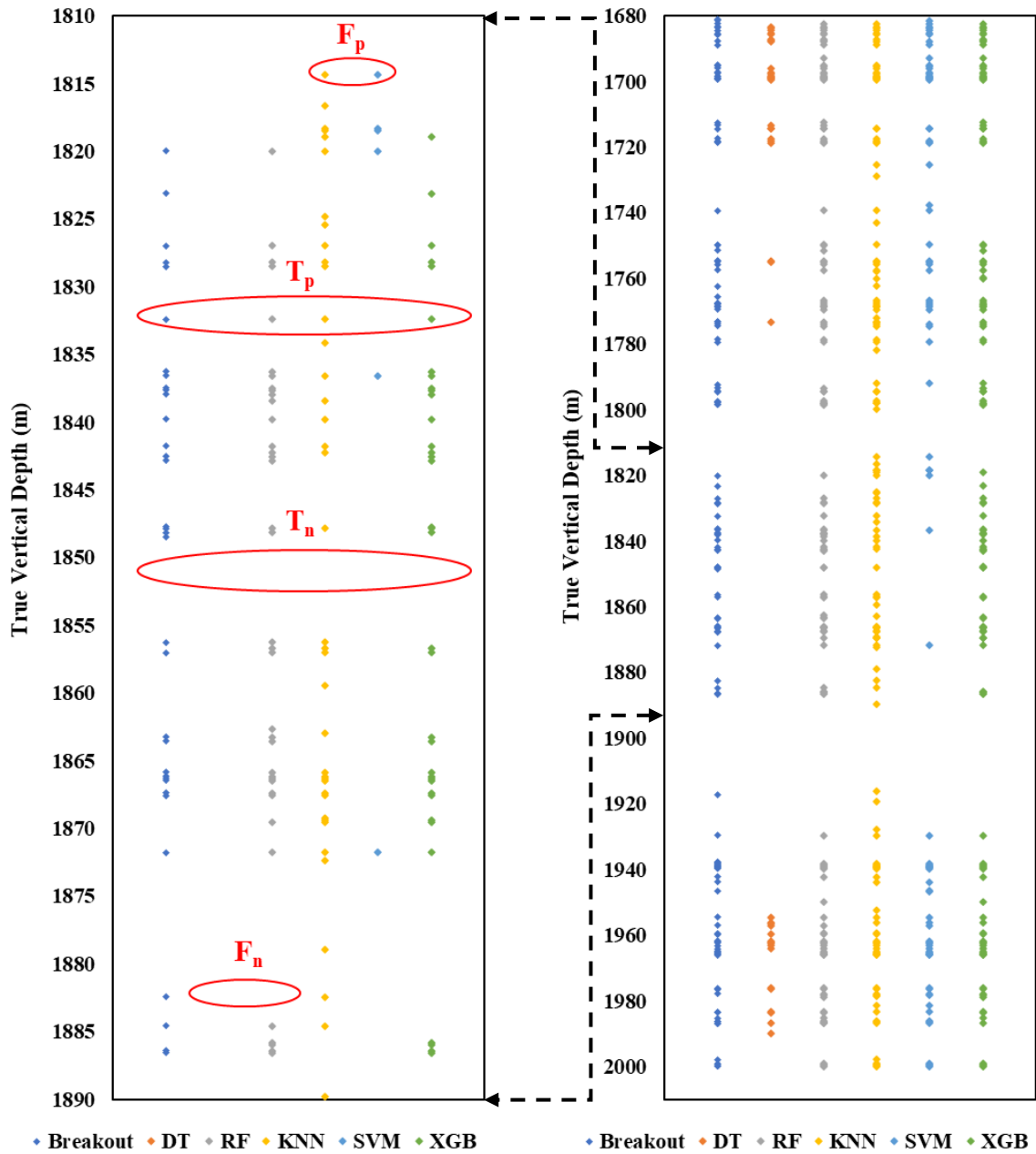


Figure 6-9. Visualized results of predicted breakouts for the studied intervals based on KNN, DT, RF, SVM, and XGBoost compare with the real breakout identified from image logs which is shown as dark blue boxes. Four conditions of the results, including true positive (T_p), true negative (T_n), false positive (F_p), and false negative (F_n) illustrated on the plot. The dashed arrow shows the scale-up of the right graph to the left graph.

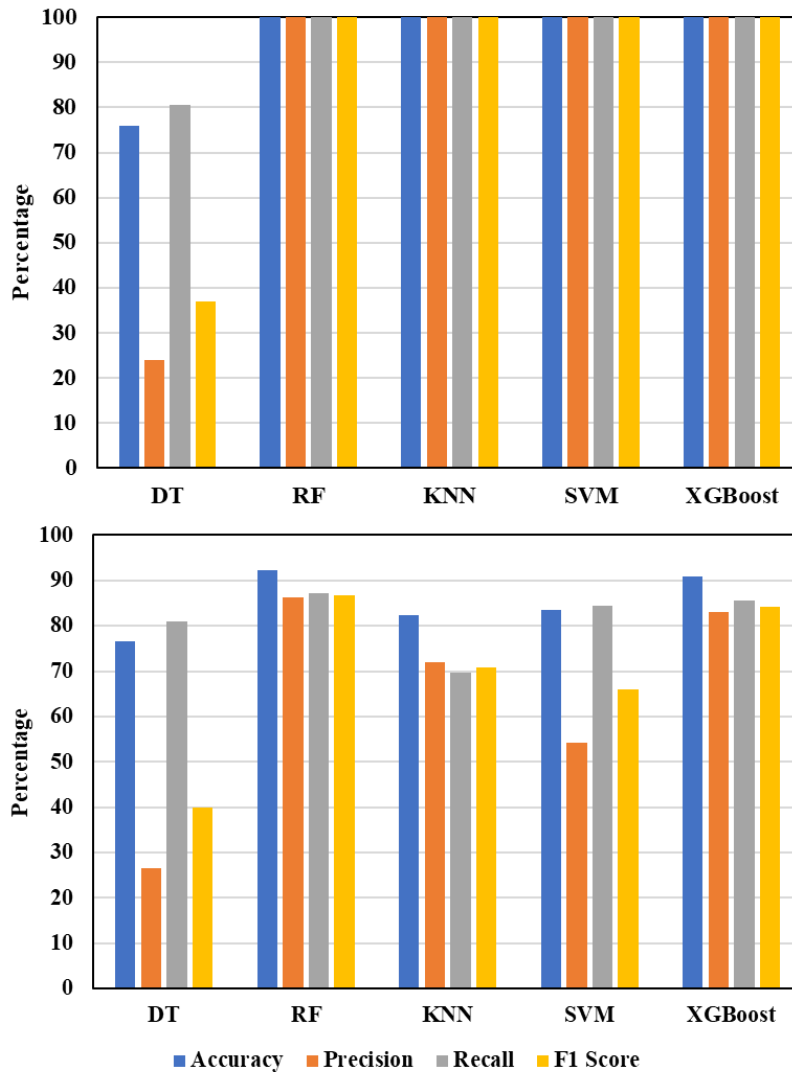


Figure 6-10. Model evaluation metrics for training data (80%) for KNN, DT, RF, SVM, and XGBoost classification models. b) Model evaluation metrics for test data (20%) for KNN, DT, RF, SVM, and XGBoost.

In addition, while achieving an overall Accuracy of around 78%, the DT model exhibited a markedly lower Precision of 26%. This fact suggests that while the model is fairly good at identifying true breakouts, it is also prone to a higher rate of false positives. The DT model showed a stark contrast between a high Recall of 80% and a very low Precision of 26%. The number of F_n points are much less than T_p , which explains the high Recall. This fact implies that the model was not capable of identifying most actual breakouts. Despite the fact that the DT model predicted non-breakout zones correctly, the low precision shows that the model is not good at predicting the breakout

zones. This problem could be due to the DT's susceptibility to overfitting the training data, leading to poor generalization to unseen data.

The KNN model's performance metrics hovering around 70% indicate moderate effectiveness. KNN's reliance on feature space proximity may lead to challenges in a high-dimensional context like borehole image logs, where the distinction between classes may not be clearly defined by nearness alone.

These insights suggest that when selecting a model for identifying borehole breakouts, it is crucial to consider the trade-offs between different types of errors. In the context of carbonate reservoirs, where the accurate identification of breakouts is critical for operational safety and cost management, the balanced performance of RF and XGBoost makes them favorable.

In identifying borehole breakouts, it is crucial to acknowledge the spatial distribution and scale of these features within the reservoir. True negative predictions of non-breakout intervals correctly identified as non-breakouts sometimes occur among sequences of true positive intervals, where breakouts have been correctly identified. Given that breakouts are generally extensive and tend to be connected across intervals, the occurrence of a true negative within a cluster of true positives could potentially be reclassified as a breakout, owing to the overarching presence of breakout features in the vicinity. This phenomenon suggests that some true negatives might represent a pause in the continuity of breakouts rather than an absolute absence. Reclassifying these isolated true negatives within a breakout zone as a breakout could possibly increase the predictive metrics, improving Precision and Recall by reducing false negatives and false positives. Therefore, this consideration could mean a more nuanced prediction in detecting borehole breakouts in all models.

6.5.2 Analysis of Input Parameters

It is important to find the most effective input parameters. As shown in Figure 6-11, input data were separated into seven different classes. Density-related logs such as NPHI, RHOB, DRHO, and sonic were selected as one class, and resistivity-related logs such as LLD, LLS, and MSFL were selected as another. Also, radioactivity-related logs such as GR, K, Th, and U were considered as another class. Then, combining these

three classes with CAL formed another three classes. Eventually, combining all the input data was considered the last class. The analysis indicated that the integration of all input data yielded the highest performance metrics, suggesting that the synergistic effect of combining all log types is crucial for accurate breakout detection. The classes that combined the three log types with CAL data showed strong results, underscoring the caliper's significant role in enhancing model predictions. Surprisingly, when considered individually, resistivity logs outperformed density logs, which could be attributed to their direct relation to fluid and rock properties affecting breakout formation. Radioactivity logs alone were not accurate, potentially due to their indirect relation to mechanical rock properties relevant to breakout occurrence. These insights could guide the selection of suitable well logs in future borehole evaluations.

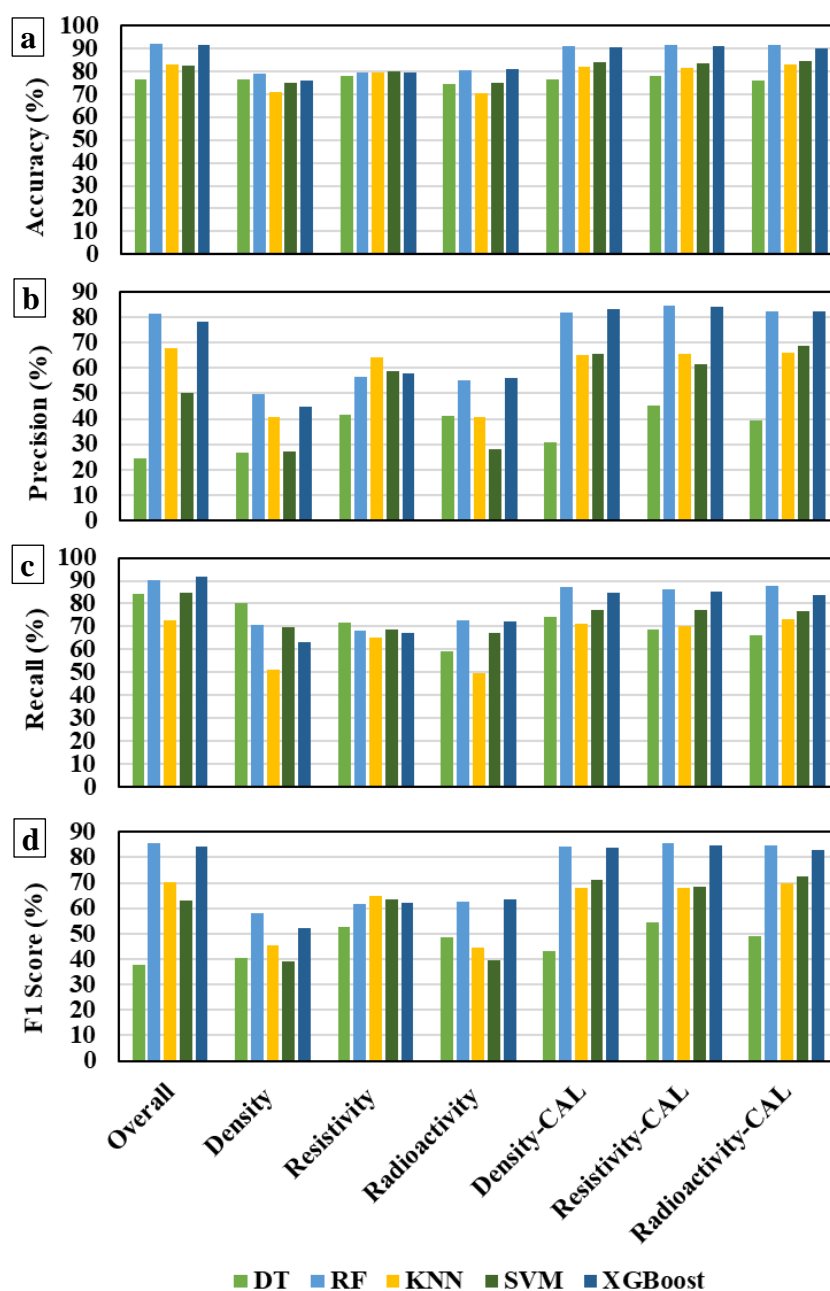


Figure 6-11. Seven different combinations of well logs were evaluated for KNN, DT, RF, SVM, and XGBoost classification models. Different color bars represent different classification models. a) Results of Accuracy for different set of input variables. b) Results of Precision for different set of input variables. c) Results of Recall for different set of input variables. d) Results of F1 Score for different set of input variables

6.5.3 Tuning hyperparameters

Overall, considering the high value of metrics for training, the results underscore the need for a nuanced approach to model selection and also the careful tuning of hyperparameter settings that determine the structure and behavior of the machine learning models to enhance each model's performance by tailoring them to the unique characteristics of borehole breakout identification. This tuning process involves adjusting the parameters that are not directly learned from the data but govern the learning process itself, which can significantly affect the model's ability to generalize from training data to unseen data. The implications of misclassification and the operational context within the carbonate reservoirs must be considered when fine-tuning these settings. Therefore, several of the most common hyperparameters were selected for all models.

For the KNN classification model, the number of neighbors, denoted by K , is the most crucial hyperparameter, directly affecting the model by determining the number of nearest points to consider when making a prediction. As shown in Figure 6-12, a K value around 6 demonstrates the optimal balance between bias and variance, providing the best generalization from training to test data.

For the DT classification model, the maximum depth of trees, the maximum number of splits, and the minimum samples per leaf are common hyperparameters, and they were tuned. As presented in Figure 6-13, a maximum depth of trees above 10 showing no improvement in the metrics suggests that increasing the tree's depth beyond this point does not contribute to better performance and likely represents the optimal depth for this model. A minimum split number of around 10 and minimum samples per leaf of around 5 appear to be the optimum, balancing the model's ability to capture sufficient details in the data while avoiding overfitting.

The RF classification model has hyperparameters, including the number of trees in the forest (estimators), the maximum depth of the trees, and the minimum samples required to split a node. None of these parameters significantly affect the metrics beyond certain thresholds. As shown in Figure 6-14, the number of estimators of around 150, the maximum number of splits of around 20, and the minimum samples for a split

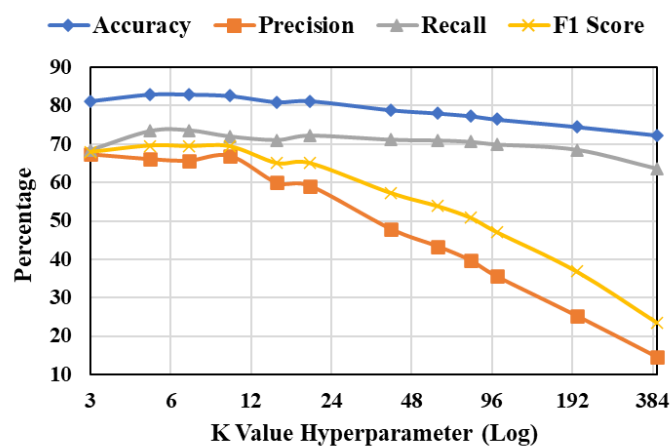


Figure 6-13. Tuning K value hyperparameter for the KNN classification model. The x-axis is logarithmic to present the bigger numbers of the K value. Colorful lines represent the different evaluation metrics.

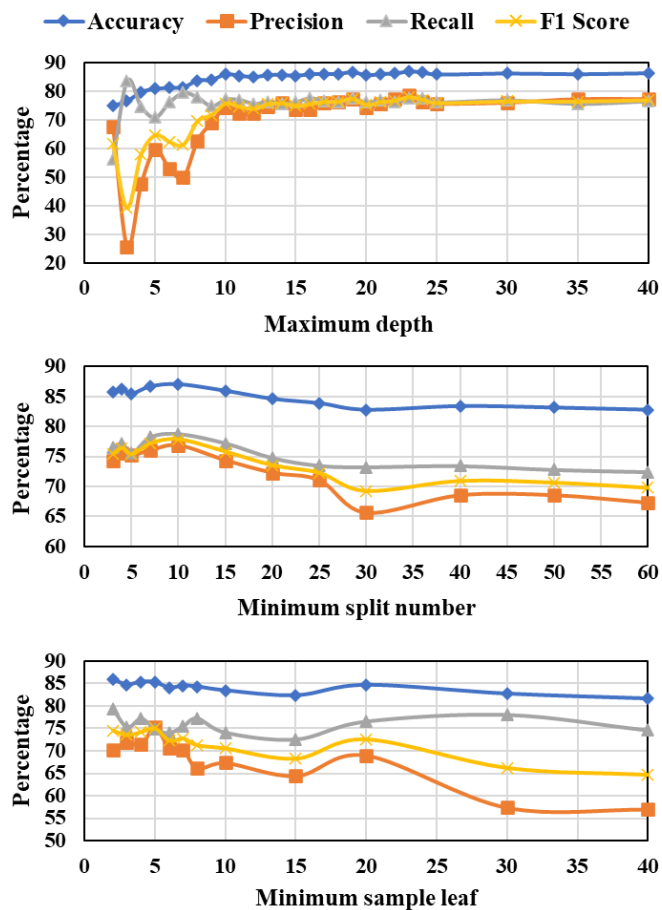


Figure 6-13. Tuning hyperparameters for DT classification model including maximum depth of the tree, minimum split number of the nodes and minimum sample leaf. Colorful lines represent the different evaluation metrics.

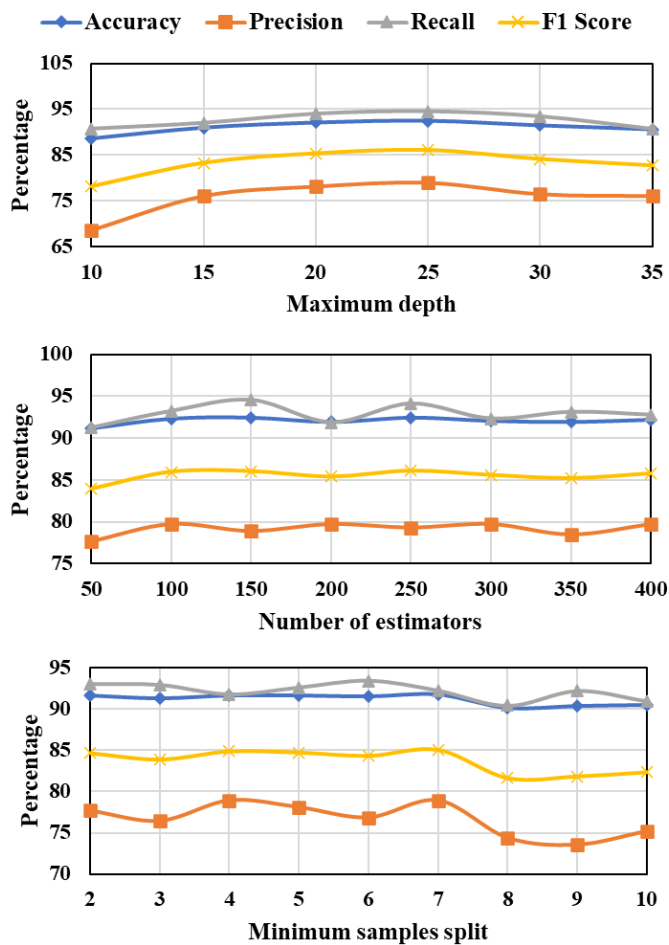


Figure 6-14. Tuning hyperparameters for RF classification model including maximum depth of the tree, number of estimator and minimum sample split. Colorful lines represent the different evaluation metrics.

of around 6 demonstrate the optimum values, which optimize both the diversity and depth of the trees for accurate and robust predictions.

For the SVM classification model, gamma is a hyperparameter that represents the influence of a single training example, with lower values meaning 'far' and higher values meaning 'close'. The kernel function, especially the Radial Basis Function (RBF), impacts how the data is transformed to find the optimal boundary between classes. As presented in Figure 6-15, a gamma value around 0.01 provides the right balance for the model to generalize without overfitting the training data.

Finally, for the XGBoost classification model, common hyperparameters include the learning rate, which controls the contribution of each tree in the ensemble; the maximum depth of the trees, affecting the model complexity; and the number of trees

or estimators. Similar to the RF model, no significant impact was observed for hyperparameters beyond certain values. As shown in Figure 6-16, the learning rate of around 0.2, the maximum depth of around 7, and the number of estimators of around 250 demonstrate the optimum values, balancing the speed and Accuracy of the learning process to prevent overfitting while maintaining high predictive performance.

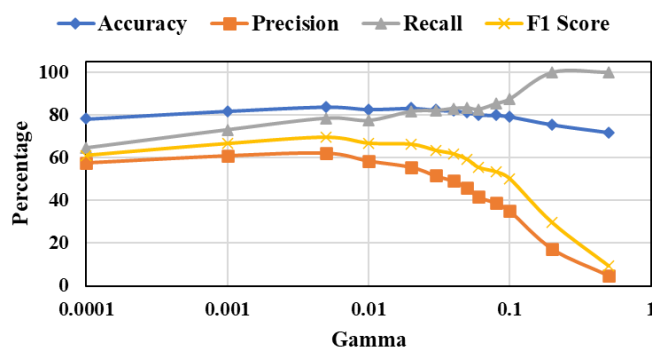


Figure 6-15. Tuning gamma hyperparameter for the SVM classification model. The x-axis is logarithmic to present the different numbers of gamma. Colorful lines represent the different evaluation metrics.

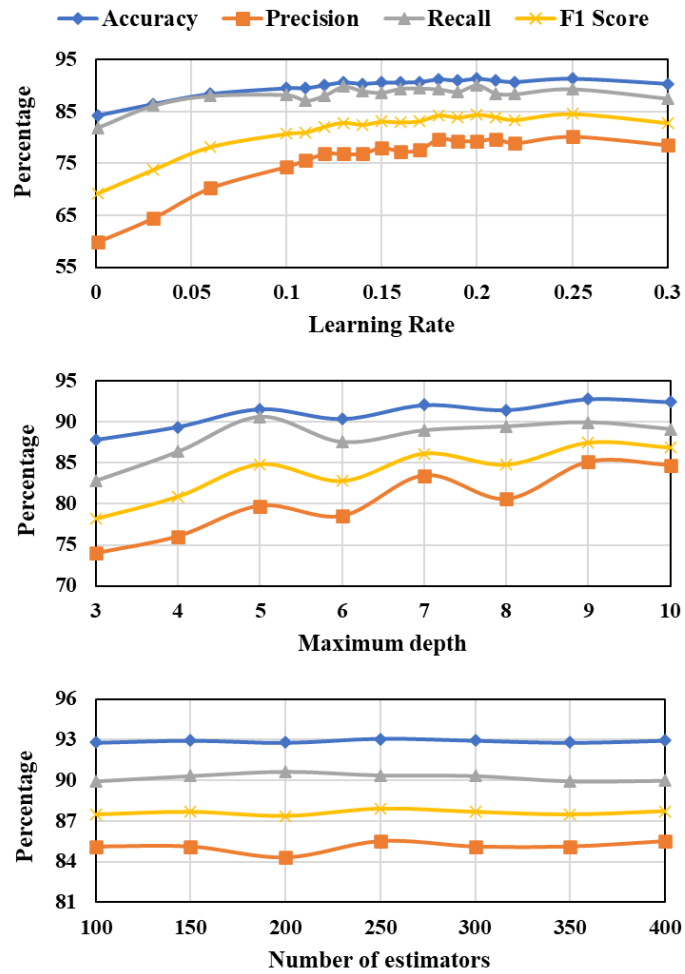


Figure 6-16. Tuning hyperparameters for XGBoost classification model including maximum depth of the tree, learning rate and the number of estimators. Colorful lines represent the different evaluation metrics.

6.5.4 Robustness

The robustness of classification models in detecting borehole breakouts was further scrutinized by examining their robustness against overfitting, a common pitfall where a model learns the training data too well and fails to generalize to new data. To address this, models under different data test sizes were evaluated. As mentioned earlier, a conventional split of 80% training and 20% testing data was initially employed, providing a baseline for performance metrics. Subsequently, the test size was changed from 1% to 40%, reducing the training data proportionately. As Shown in Figure 6-17,

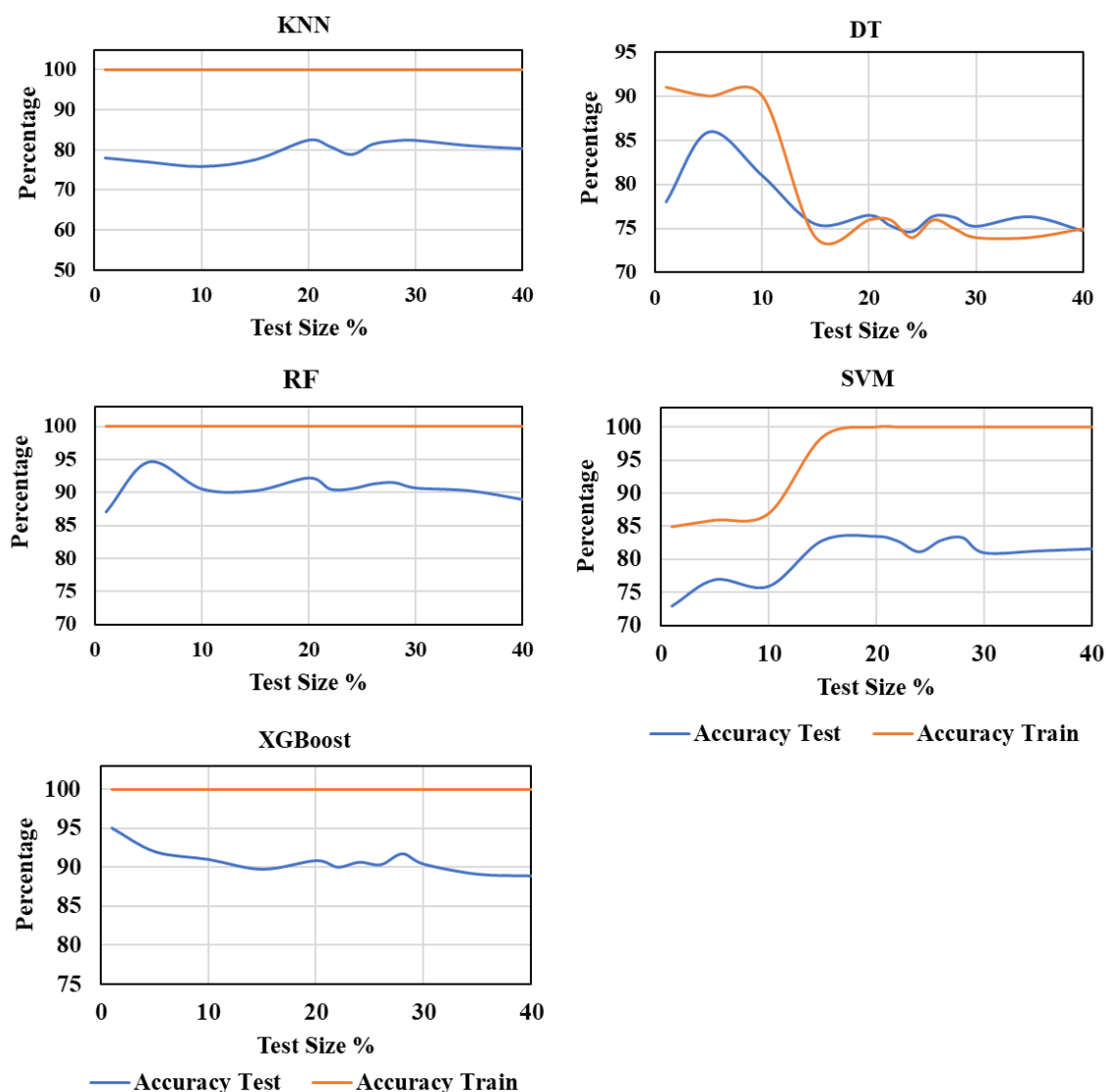


Figure 6-17. Evaluation of Accuracy of test and train data for KNN, DT, RF, SVM, and XGBoost based on different test size data between 1% and 40%. Variation between the training and test evaluation metrics, emphasizes the robustness of the model.

with each increase in test data size, Accuracy was monitored. Notably, a model that maintains performance metrics as the test size increases demonstrates resilience against overfitting.

Conversely, a significant drop in performance would suggest the model's vulnerability to overfitting or show the general incapability of the model. The RF model, which exhibited the highest performance in initial evaluations, was found to sustain predictive Accuracy, indicating that the method effectively generalized beyond

the training dataset. In addition, the splitting data size was set on shuffle mode to avoid overfitting on the same part of the data. This exercise validated the robustness of models and reinforced the reliability of the results under varying conditions, ensuring that the models are truly effective for practical applications in identifying breakouts in carbonate formations.

6.5.5 Well log selection for future cases

The main challenges for future application of the methods discussed in this chapter primarily involve the evolving nature of machine learning and well log analysis. Selecting the best well logs is the biggest challenge. The protocol for selecting well logs and finding the best combination of well logs as input variables depends on understanding the specification of each well log.

Different well logs respond to the occurrence of breakouts on the wellbore wall due to their varied sensitivities to different physical properties and conditions within the borehole environment. The correlation between the occurrence of breakouts and well logs can be directly related to the parameters measured by the well logs, such as resistivity, radiation, and density. On the other hand, borehole breakout can cause anomalies in the measurements of the well-log tools based on the tool's geometry and placement of the tool relative to the borehole wall. For example, resistivity logs slide on the borehole wall, and any change, such as breakout, can cause an error in the measured resistivity and appear as the anomaly, leading the classification models to find a correlation between the resistivity anomaly and breakout occurrence. Other well logs, such as acoustic log, RHOB and NPHI should be centralized in the center of the well, and any variation in the distance between the tool and the borehole wall can cause an error in their measurement. Therefore, breakouts can possibly cause an error and consequently appear as an anomaly in the measurements and lead classification models to find a correlation between breakouts and errors. As shown in Figure 6-2, even though there is a correlation between breakout zones and measurements of a single well log but there are no clear criteria to predict the breakout zones. In addition, in this study we could not establish a classification model with a reasonable accuracy based on merely

a single well. Therefore only hyperdimensional spaces with at least four dimensions based on four well logs can be used.

On the other hand, one of the biggest disadvantages of using AI classification models in a hyperdimensional state is the low interpretability of the results. Therefore there is no clear understanding behind the accuracy of combination of well logs in Figure 6-11. Furthermore, the combination of all well logs together demonstrates a better performance. These logs are the most common and accessible logs among the oil fields and this study suggests to select the highest number of well logs to get the best performance of the classification model. Since the reasons behind the correlation of each combination is not clear and can be only locally interpreted, in new cases with different lithology and geology, using a higher number of well logs can collectively increase the chance of predicting the breakout zones.

For future studies, testing a higher number of combinations is recommended. In this sort of task that the results could be affected by a specific factor such as lithology and geology, keeping the protocol dynamic is important. As new well logs or data become available, or as the objectives of the analysis evolve, revisit, and revise the selection protocol could be beneficial.

6.6 Summary

This chapter highlights borehole breakouts as an important tool for geoscientists and geoengineers. It explores using ML for identifying borehole breakouts in carbonate reservoirs by conventional logs. For this purpose it compares various ML classification models including KNN, DT, RF, SVM, and XGBoost. The chapter also evaluates these models' effectiveness using metrics like accuracy, precision, recall, and F1 score. The RF and XGBoost classification models, with an accuracy of about 92%, emerged as the most robust and accurate models, maintaining high performance and high evaluating metrics, which is crucial for the reliability of identification of breakouts.

RF and KNN models, with their ensemble approaches, have demonstrated good robustness, further validated by testing across different data sizes and the employment of shuffle mode to enhance the generalizability of the results. The detailed examination of input parameters revealed that combining all available data classes, including density, resistivity, radioactivity logs, and caliper data, substantially improved model performance, underscoring the value of leveraging a multifaceted approach to data integration for breakout detection. Moreover, careful tuning of hyperparameters was conducted to optimize each model's ability to distinguish between breakout and non-breakout intervals effectively. The methodologies and insights derived herein can be a benchmark for future research and practical applications in geomechanics and petroleum engineering.

References

- Abdelgawad, K., Elkatatny, S., Mousa, T., Mahmoud, M., Patil, S., 2018. Real Time Determination of Rheological Properties of Spud Drilling Fluids Using a Hybrid Artificial Intelligence Technique. Society of Petroleum Engineers - *SPE* Kingdom of Saudi Arabia Annual Technical Symposium and Exhibition 2018, SATS 2018. <https://doi.org/10.2118/192257-MS>
- Alshaikh, A.A., Albassam, M.K., Al Gharbi, S.H., Al-Yami, A.S., 2018. Detection of Stuck Pipe Early Signs and the Way Toward Automation. Society of Petroleum Engineers - Abu Dhabi International Petroleum Exhibition and Conference 2018, *ADIPEC* 2018.
- Bergen, K.J., Johnson, P.A., De Hoop, M. V., Beroza, G.C., 2019. Machine learning for data-driven discovery in solid Earth geoscience. *Science* **363**. <https://doi.org/10.1126/science.aau0323>
- Cheatham, J.B., 1984. Wellbore Stability. *Journal of Petroleum Technology* **36**, 889–896. <https://doi.org/10.2118/13340-PA>
- Chen, T., Guestrin, C., 2016. XGBoost: A Scalable Tree Boosting System. Proceedings of the *ACM SIGKDD* International Conference on Knowledge Discovery and Data Mining, 785–794. <https://doi.org/10.1145/2939672.2939785>
- Cherif, I.L., Kortebi, A., 2019. On using eXtreme Gradient Boosting (XGBoost) Machine Learning algorithm for Home Network Traffic Classification. *IFIP Wireless Days*, UK. <https://doi.org/10.1109/WD.2019.8734193>
- Cristianini, N., Ricci, E., 2008. Support Vector Machines. *Encyclopedia of Algorithms* 928–932. https://doi.org/10.1007/978-0-387-30162-4_415
- Dias, L.O., Bom, C.R., Faria, E.L., Valentín, M.B., Correia, M.D., de Albuquerque, Márcio P., de Albuquerque, Marcelo P., Coelho, J.M., 2020. Automatic detection of fractures and breakouts patterns in acoustic borehole image logs using fast-region convolutional neural networks. *J Pet Sci Eng* **191**, 107099. <https://doi.org/10.1016/j.petrol.2020.107099>
- Fawagreh, K., Gaber, M.M., Elyan, E., 2014. Random forests: from early developments to recent advancements. *Systems Science & Control Engineering* **2**, 602–609. <https://doi.org/10.1080/21642583.2014.956265>

- Ghenabzia, A., Kazar, O., Merizig, A., Sayah, Z., Zoubeidi, M., 2020. Drilling stuck pipe prediction in Algerian oil fields: time series forecasting approach. *Advances in Intelligent Systems and Computing* **1104**, 262–275. https://doi.org/10.1007/978-3-030-36671-1_23
- Goutte, C., Gaussier, E., 2005. A Probabilistic Interpretation of Precision, Recall and F-Score, with Implication for Evaluation. *Lecture Notes in Computer Science* 3408, 345–359. https://doi.org/10.1007/978-3-540-31865-1_25
- Gupta, S., Chatar, C., Celaya, J.R., 2019. Machine Learning Lessons Learnt in Stick-Slip Prediction. Society of Petroleum Engineers - Abu Dhabi International Petroleum Exhibition and Conference 2019, ADIP 2019.
- Karpatne, A., Ebert-Uphoff, I., Ravela, S., Babaie, H.A., Kumar, V., 2019. Machine Learning for the Geosciences: Challenges and Opportunities. *IEEE Trans Knowl Data Eng* **31**, 1544–1554. <https://doi.org/10.1109/TKDE.2018.2861006>
- Kovacich, J.R., Haimson, B.C., 2000. Factors affecting borehole breakout dimensions, and the potential for sand production in high porosity Berea sandstone, in: Girard, J., Liebman, M., Breeds, C., Doe, T. (Eds.), *4th North American Rock Mechanics Symposium*, USA, Washington. 271–277.
- Liu, Y., Wang, Y., Zhang, J., 2012. New machine learning algorithm: Random forest. *Lecture Notes in Computer Science* (including subseries Lecture Notes in Artificial Intelligence and Lecture Notes in Bioinformatics) 7473 LNCS, 246–252. https://doi.org/10.1007/978-3-642-34062-8_32
- Mafakheri B., N., Lin, W., Ishitsuka, K., 2024a. Application of supervised machine learning classification models to identify borehole breakouts in carbonate reservoirs based on conventional log data. *International Journal of the JSRM* (Under revision).
- Mafakheri B., N., Lin, W., Ishitsuka, K., 2024b. Utilizing artificial intelligence algorithms for detecting borehole breakouts by conventional logging data. in preparation.
- Mafakheri B., N., Lin, W., Murata, S., Yousefi, F., Radwan, A.E., 2022. Magnitudes and orientations of present-day in-situ stresses in the Kurdistan region of Iraq: Insights into combined strike-slip and reverse faulting stress regimes. *J Asian Earth Sci* **239**, 105398 . <https://doi.org/10.1016/j.jseas.2022.105398>

- Moore, J.C., Chang, C., McNeill, L., Thu, M.K., Yamada, Y., Huftile, G., 2012. Growth of borehole breakouts with time after drilling: Implications for state of stress, NanTroSEIZE transect, SW Japan. *Geochemistry, Geophysics, Geosystems* **12**. <https://doi.org/10.1029/2010GC003417>
- Morgenroth, J., Khan, U.T., Perras, M.A., 2019. An overview of opportunities for machine learning methods in underground rock engineering design. *Geosciences* **9**, 504. <https://doi.org/10.3390/geosciences9120504>
- Mousavipour, F., Ali, M., Hamed, R., Moghanloo, G., 2020. Prediction of in situ stresses, mud window and overpressure zone using well logs in South Pars field. *J Pet Explor Prod Technol* **10**, 1869–1879. <https://doi.org/10.1007/s13202-020-00890-9>
- Mucherino, A., Papajorgji, P.J., Pardalos, P.M., 2009. k-Nearest Neighbor Classification. *Springer*, New York, NY, pp. 83–106. https://doi.org/10.1007/978-0-387-88615-2_4
- Najibi, A.R., Ghafoori, M., Lashkaripour, G.R., Asef, M.R., 2017. Reservoir geomechanical modeling: In-situ stress, pore pressure, and mud design. *J Pet Sci Eng* **151**, 31–39. <https://doi.org/10.1016/j.petrol.2017.01.045>
- Neeamy, A.K., Selman, N.S., 2020. Wellbore Breakouts Prediction from Different Rock Failure Criteria. *Journal of Engineering* **26**, 55–64. <https://doi.org/10.31026/j.eng.2020.03.05>
- Osarogiagbon, A.U., Khan, F., Venkatesan, R., Gillard, P., 2021. Review and analysis of supervised machine learning algorithms for hazardous events in drilling operations. *Process Safety and Environmental Protection* **147**, 367–384. <https://doi.org/10.1016/J.PSEP.2020.09.038>
- Soroush, H., Rasouli, V., Tokhmechi, B., 2010. A data processing algorithm proposed for identification of breakout zones in tight formations: A case study in Barnett gas shale. *J Pet Sci Eng* **74**, 154–162. <https://doi.org/10.1016/j.petrol.2010.08.012>
- Webb, G.I., Fürnkranz, J., Fürnkranz, J., Fürnkranz, J., Hinton, G., Sammut, C., Sander, J., Vlachos, M., Teh, Y.W., Yang, Y., Mladeni, D., Brank, J., Grobelsnik, M., Zhao, Y., Karypis, G., Craw, S., Puterman, M.L., Patrick, J., 2011. Decision Tree. *Encyclopedia of Machine Learning* 263–267. https://doi.org/10.1007/978-0-387-30164-8_204

- Xia, W., Li, Z., Zhang, Y., Zhao, W., 2020. Breakout detection for fast EDM drilling by classification of machining state graphs. *International Journal of Advanced Manufacturing Technology* **106**, 1645–1656. <https://doi.org/10.1007/s00170-019-04530-3>
- Zhong, R., Salehi, C., Johnson, R., 2022. Machine learning for drilling applications: A review. *J Nat Gas Sci Eng* **108**, 104807. <https://doi.org/10.1016/j.jngse.2022.104807>
- Zoback, M.D., Moos, D., Mastin, L., Anderson, R.N., 1985. Well bore breakouts and in situ stress. *J Geophys Res Solid Earth* **90**, 5523–5530. <https://doi.org/10.1029/JB090IB07P05523>

Chapter 7

Conclusion

Using a combination of conventional and image logs, this dissertation provides valuable insights into the tectonic and geomechanical characteristics of the Zagros suture zone. The study comprehensively analyzed stress magnitude and orientations, natural fractures, pore pressure, and stress regime in two oil fields located in the southwestern Zagros suture zone and one oil field in the northwestern Zagros suture zone. The findings of this study have significant implications for energy field development, optimizing drilling practices, wellbore stability, and reservoir management in similar geological settings, ultimately improving the efficiency and productivity of oil and gas operations in the region. The main conclusions obtained from each chapter except Chapter One and Seven are described below.

Chapter Two focuses on the geology and tectonic background of the northwestern and southeastern part of the Zagros suture zone where my study area is located, specifically in the Kurdistan region of Iraq and the Dezful embayment southwest of Iran. It discusses how different tectonic forces have shaped the geology of the Zagros suture zone over various eras, with the current tectonic setting largely influenced by the collision of the Arabian and Eurasian plates. This chapter details the tectonic evolution of the Zagros suture zone, formed through various geological stages, and outlines the distinct geological structures and formations resulting from this evolution. These include the development of the Zagros fold and thrust belt and its trends, the role of different rock formations in the area's geology, and the impact of these structures on regional tectonic activity.

Chapter Three gave an overview of existing methods of determining and measuring in situ stress, classifying them into direct and indirect methods. This chapter explains that each stress measurement method has different merits and disadvantages and is applicable only under certain conditions. It discusses the reliability of different methods for this purpose, highlighting that breakout data from image logging can provide more accurate stress orientations and magnitudes than Earthquake Focal Mechanisms (EFMs) at

intermediate depths. The chapter suggested that when combined with actual measurements from wellbore data, theoretical methods, such as the poroelastic strain model, can yield valuable insights about stress states in active tectonic regions.

Chapter Four investigated the present-day stress state of the northwestern section of the Zagros suture zone in the Kurdistan region of Iraq. In addition, it explains a comprehensive methodology for applying the breakout approach and poroelastic strain model to determine the orientation and magnitude of horizontal stresses. The stress pattern was determined by combining image logs and conventional logs collected in northern Iraq and surrounding regions. The results showed that the stress regime below the depth of 1600 m is thrust faulting, and above this depth, it transforms into a strike-slip fault regime. The mean azimuth of the maximum horizontal in-situ stress, $N72^{\circ}E$, is consistent with the tectonic movement and previous studies in the nearby Zagros suture zone. Regarding drilling implications, the redistribution of stresses and the transition from a strike-slip faulting stress regime to a reverse fault stress regime are critical and will undoubtedly affect hole stability in the drilled wells throughout the field. The pattern of tectonic stress fields in northern Iraq was found to be mainly controlled by the collision between the Arabian and Eurasian plates.

Chapter Five provides a detailed analysis of the stress state in the southeastern Zagros suture zone, underlining the complex interplay between thrust faulting and strike-slip regimes. The study comprehensively analyzed the magnitude and orientations of in situ stress, natural fractures, and pore pressure in two oil fields in the Zagros foothills. The findings of this study have significant implications for energy field development, optimizing drilling practices, wellbore stability, and reservoir management in similar geological settings. A total of 3.2 km length of images and conventional logs from seven wells in both fields were used to determine the magnitude and orientation of in situ stresses. The results revealed that the azimuth of maximum horizontal stress in Field A and Field B were $N32^{\circ}E$ and $N55^{\circ}E$, respectively. Field A is located in the SW sector of Dezful embayment which is 60 Km away from the Field B in the NE sector of Dezful embayment. The orientation of natural fractures was found to be closely aligned with the maximum horizontal stresses, confirming the reliability of the stress analysis. Increasing differences between the azimuth of maximum horizontal stress based on breakout and drilling-induced tensile fractures with increasing depth indicated the complexities in the

subsurface stress regime. The assessment of stress regimes highlighted its variations with depth. Field A transitioned from a distinct thrust faulting regime to a cross-over of thrust and strike-slip faulting regimes with increasing depth, whereas Field B maintained a consistent thrust faulting stress regime.

Chapter Six provides significant insights into the effectiveness of various supervised machine-learning classification models for identifying borehole breakouts by conventional logs. This chapter highlights the application of various supervised machine learning (ML) models, including K-Nearest Neighbors (KNN), Decision Tree (DT), Random Forest (RF), Support Vector Machine (SVM), and Extreme Gradient Boosting (XGBoost) for identifying borehole breakouts. With their ensemble approaches, the RF and XGBoost models demonstrated an accuracy of 92% and emerged as the most robust and accurate, maintaining high-performance metrics. In addition, this chapter provides a detailed examination of input parameters, revealing that combining all available well logs as input data improved the model's performance. Moreover, careful tuning of hyperparameters was vital in optimizing each model's ability to discern between breakout and non-breakout intervals effectively. The robustness evaluation process, employing a varying test data size and shuffle mode, has demonstrated the models' consistency and reliability, a testament to the robustness of the methodologies applied.

In summary, this dissertation makes a substantial contribution to the field of structural geology and petroleum engineering by providing a comprehensive analysis of the tectonic and geomechanical dynamics of the Zagros suture zone. By integrating findings from various methodologies, including conventional and image logs, breakout analysis, and advanced machine learning techniques, this study offers a nuanced understanding of stress regimes, fracture patterns, and wellbore stability in key oil fields of this region. However, it is important to acknowledge the limitations inherent in the scope of the data and methods used. Future research could expand upon this work by incorporating a broader range of geological settings within the Zagros suture zone, employing emerging data acquisition and analysis technologies, and further refining machine learning algorithms to enhance predictive accuracy. Such advancements would improve our understanding of the Zagros suture zone and provide valuable insights applicable to similar geological contexts globally.

Ph D. Dissertation

In-situ stress analysis and fracture characterization
in oil reservoirs with complex geological settings:
A multi-methodological approach in the Zagros fold and thrust belt

Nazir Mafakheri Bashmagh

Laboratory of Earth and Resource System
Department of Urban Management
Graduate School of Engineering
Kyoto University

Kyoto University, Room C1-1-118
Kyotodaigaku-Katsura, Nishikyo-ku, Kyoto, 615-8540, Japan
